Design, Analysis, and Application of Immersed Finite Element Methods

Ruchi Guo

Thesis submitted to the Faculty of the
Virginia Polytechnic Institute and State University
in partial fulfillment of the requirements for the degree of

Doctor of Philosophy
in
Mathematics

Tao Lin, Chair
Slimane Adjerid
Timothy Warburton
Pengtao Yue

April 16, 2019
Blacksburg, Virginia

Keywords: Elliptic Interface Problems, Elasticity Interface Problems, Unfitted Meshes, Immersed Finite Element, High-order Discontinuous Galerkin methods, Error Analysis, Interface Inverse Problems, Shape Optimization

Design, Analysis, and Application of Immersed Finite Element Methods

Ruchi Guo

(ABSTRACT)

This dissertation consists of three studies of immersed finite element (IFE) methods for interface problems related to partial differential equations (PDEs) with discontinuous coefficients. These three topics together form a continuation of the research in IFE method including the extension to elasticity systems, new breakthroughs to higher degree IFE methods, and its application to inverse problems.

First, we extend the current construction and analysis approach of IFE methods in the literature for scalar elliptic equations to elasticity systems in the vector format. In particular, we construct a group of low-degree IFE functions formed by linear, bilinear, and rotated Q_1 polynomials to weakly satisfy the jump conditions of elasticity interface problems. Then we analyze the trace inequalities of these IFE functions and the approximation capabilities of the resulted IFE spaces. Based on these preparations, we develop a partially penalized IFE (PPIFE) scheme and prove its optimal convergence rates.

Secondly, we discuss the limitations of the current approaches of IFE methods when we try to extend them to higher degree IFE methods. Then we develop a new framework to construct and analyze arbitrary p-th degree IFE methods. In this framework, each IFE function is the extension of a p-th degree polynomial from one subelement to the whole interface element by solving a local Cauchy problem on interface elements in which the jump conditions across the interface are employed as the boundary conditions. All the components in the analysis, including existence of IFE functions, the optimal approximation capabilities and the trace inequalities, are all reduced to key properties of the related discrete extension operator. We employ these results to show the optimal convergence of a discontinuous Galerkin IFE (DGIFE) method.

In the last part, we apply the linear IFE methods in the literature together with the shape optimization technique to solve a group of interface inverse problems. In this algorithm, both the governing PDEs and the objective functional for interface inverse problems are discretized optimally by the IFE method regardless of the location of the interface in a chosen mesh. We derive the formulas for the gradients of the objective function in the optimization problem which can be implemented efficiently in the IFE framework through a discrete adjoint method. We demonstrate the properties of the proposed algorithm by applying it to three representative applications.

Design, Analysis, and Application of Immersed Finite Element Methods

Ruchi Guo

(GENERAL AUDIENCE ABSTRACT)

Interface problems arise from many science and engineering applications modeling the transmission of some physical quantities between multiple materials. Mathematically, these multiple materials in general are modeled by partial differential equations (PDEs) with discontinuous parameters, which poses challenges to developing efficient and reliable numerical methods and the related theoretical error analysis.

The main contributions of this dissertation is on the development of a special finite element method, the so called immersed finite element (IFE) method, to solve the interface problems on a mesh independent of the interface geometry which can be advantageous especially when the interface is moving.

Specifically, this dissertation consists of three projects of IFE methods: elasticity interface problems, higher-order IFE methods and interface inverse problems, including their design, analysis, and application.

Dedication

To my parents, Tao Guo and Xiaowei Zhou.

Acknowledgments

First of all, I am grateful to the Math Department at Virginia Tech for the continuous support on my research in the past five years. The Math Department at Virginia Tech is a very nice community that provides a platform for me to learn from and communicate with many other graduate students, faculty members and visiting scholars.

I would like to express my sincere gratitude to my advisor Dr. Tao Lin for the inspiring guidance of my Ph.D. study and research. He leads me into this fantastic world of computational mathematics, and his patience, motivation, enthusiasm, and immense knowledge inspire me to become better as a scholar. I would not have gotten this far without the help and support from my advisor. I could not have imagined having a better advisor and mentor for my Ph.D. study.

I would like to thank the rest of my thesis committee Dr. Slimane Adjerid, Dr. Timothy Warburton and Dr. Pengtao Yue, for their insightful comments and encouragement. I have learned a lot from each of them which widen my research from various perspectives. Special thanks to Dr. Slimane Adjerid for his help in my research on high-order immersed finite element methods.

Special thanks to Dr. Yanping Lin for offering me a wonderful summer research experience at Department of Applied Mathematics, Hong Kong Polytechnic University, and for his help and collaboration in the research projects on elasticity interface problems and interface inverse problems.

I would also like to thank Dr. Xiaoming He and Dr. Xu Zhang for their help and suggestions in my graduate study.

Contents

List of Figures

List of Tables

Chapter 1

Introduction

Interface problems appear in many applications in science and engineering. In general, an interface problem is imposed in a domain consisting of multiple materials separated from each other such that each subdomain is occupied by one material distinguished from the surroundings, and the related physical parameters usually are discontinuous across the interface separating these materials. When partial differential equations (PDEs) are employed to model the pertinent physics, their coefficients are often discontinuous across the material interface, and this leads to the consideration of interface problems for these PDEs. For example, the heat transmission problem in a domain $\Omega \subseteq \mathbb{R}^2$ can be modeled by the following elliptic interface problem

$$-\nabla \cdot (\beta \nabla u) = f, \text{ in } \Omega^- \cup \Omega^+, \tag{1.1}$$

$$u = g, \text{ on } \partial\Omega, \tag{1.2}$$

where Ω^- and Ω^+ are the subdomains of Ω separated by an interface curve Γ, see an illustration in Figure 1.1, the coefficient β represents the heat conductivity which is assumed to be a piecewise constant, i.e.,

$$\beta(X) = \begin{cases} \beta^-, & \text{if } X \in \Omega^-, \\ \beta^+, & \text{if } X \in \Omega^+. \end{cases} \tag{1.3}$$

Because of this discontinuity in β, jump conditions need to be imposed on the interface Γ:

$$[u]_\Gamma := u^+|_\Gamma - u^-|_\Gamma = 0, \tag{1.4a}$$

$$[\beta \nabla u \cdot \mathbf{n}]_\Gamma := \beta^+ \nabla u^+ \cdot \mathbf{n}|_\Gamma - \beta^- \nabla u^- \cdot \mathbf{n}|_\Gamma = 0, \tag{1.4b}$$

where $\mathbf{n}$ is the normal vector to Γ. The elliptic interface problem such as the one described in (1.1) has wide applications in other fields too, for example, fluid dynamics [134, 140], biomolecular electrostatics [68, 201], plasma simulation [31, 108], to name just a few.

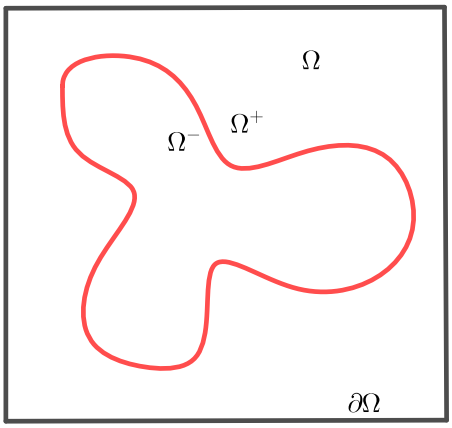

Figure 1.1: The physical domain of an interface problem

Another example is the planar linear elasticity system modeling an elastic body Ω consisting of two materials:

$$-\text{div } \sigma(\mathbf{u}) = \mathbf{f} \quad \text{in } \Omega^- \cup \Omega^+, \tag{1.5}$$

$$\mathbf{u} = \mathbf{g} \quad \text{on } \partial\Omega, \tag{1.6}$$

where $\mathbf{f} = (f_1, f_2)^T$ is the body force, $\mathbf{g} = (g_1, g_2)^T$ represents the displacement on the boundary, $\mathbf{u} = (u_1, u_2)^T$ is the unknown displacement field, and $\sigma(\mathbf{u}) = (\sigma_{ij}(\mathbf{u}))_{1\leqslant i,j\leqslant 2}$ is the stress tensor given by

$$\sigma_{ij}(\mathbf{u}) = \lambda(\nabla \cdot \mathbf{u})\delta_{i,j} + 2\mu\epsilon_{ij}(\mathbf{u}), \tag{1.7}$$

with the strain tensor $\epsilon(\mathbf{u}) = (\epsilon_{ij}(\mathbf{u}))_{1\leqslant i,j\leqslant 2}$ given by

$$\epsilon_{ij}(\mathbf{u}) = \frac{1}{2}\left(\frac{\partial u_i}{\partial x_j} + \frac{\partial u_j}{\partial x_i}\right). \tag{1.8}$$

Because of different elastic material properties in subdomains, the Lamé parameters of Ω are assumed to be piecewise constant functions in the following forms:

$$\lambda = \begin{cases} \lambda^- & \text{if } X \in \Omega^-, \\ \lambda^+ & \text{if } X \in \Omega^+, \end{cases} \qquad \mu = \begin{cases} \mu^- & \text{if } X \in \Omega^-, \\ \mu^+ & \text{if } X \in \Omega^+. \end{cases} \tag{1.9}$$

We recall that λ and μ can be calculated from the Young's modulus E and Poisson's ratio ν by the following formulas:

$$\lambda = \frac{E\nu}{(1+\nu)(1-2\nu)}, \quad \text{and} \quad \mu = \frac{E}{2(1+\nu)}. \tag{1.10}$$

The discontinuity in the Lamé parameters requires the displacement field $\mathbf{u} = (u_1, u_2)^T$ to satisfy the following jump conditions across the material interface Γ:

$$[\mathbf{u}]_\Gamma := \mathbf{u}^+|_\Gamma - \mathbf{u}^-|_\Gamma = \mathbf{0}, \tag{1.11a}$$

$$[\sigma(\mathbf{u})\cdot\mathbf{n}]_\Gamma := \sigma^+(\mathbf{u}^+)\cdot\mathbf{n}|_\Gamma - \sigma^-(\mathbf{u}^-)\cdot\mathbf{n}|_\Gamma = \mathbf{0}, \tag{1.11b}$$

where, again, $\mathbf{n}$ is the normal vector to Γ. Elasticity interface problems also have a wide range of applications, such as the detection of cracks, cavities or inclusions buried in elastic bodies [1, 14, 15], and structure compliance optimization [122, 132], to name just a few.

This dissertation is about immersed finite element (IFE) methods for solving these two types of interface problems and the applications to a group of interface inverse problems. A distinct feature of IFE methods is their capability to solve interface problems with unfitted meshes, i.e., meshes independent of the interface; hence, a highly structured mesh such as a Cartesian mesh can be used by an IFE method for solving an interface problem that has a material interface with a nontrivial geometry.

In the next section of this chapter, we will first provide a survey of the related numerical methods for interface problems, and address our motivation to study the IFE methods. Then, in Section 1.2, we will review the IFE methods in the literature for the elliptic interface problem (1.1)-(1.4). In Section 1.3, we will review the pertinent interface inverse problems and the shape optimization methods. In the last section of this chapter, based on these survey, we will outline the motivation and contributions of this dissertation. In particular, we will discuss the challenges for extending the current IFE methods in the literature, i.e., the one reviewed in Section 1.2, to interface problems of the linear elasticity systems and to the higher-degree IFE methods for the elliptic interface problem ubiquitously appearing in many applications, and for applying IFE methods to interface inverse problems through the shape optimization techniques. These challenges will guide us to present our original research in this dissertation.

1.1 Numerical Methods for Interface Problems

Traditional finite element methods or discontinuous Galerkin (DG) finite element methods require interface-fitted meshes to solve the interface problems; otherwise, they might perform unsatisfactorily, see [20, 22, 47] for discussions about interface-fitted meshes related to elliptic interface problems. However, when the interface has complex geometry, for example the material interface in biomedical images [16, 193] and geophysical images [60], it is a time-consuming and non-trivial process to generate a high-quality interface-fitted mesh to resolve the interface geometry. And this mesh generation issue will be more severe if the interface changes its shape or moves in computation, for example, the numerical interface is adjusted by a shape optimization method for an interface inverse problem or optimal design problem. A little more detailed discussions for related issues in inverse problems will be presented in Section 1.3 and Section 4.1. These applications can benefit from numerical methods based on unfitted meshes, i.e., interface-independent meshes, and this consideration is a major motivation for us to study the immersed finite element (IFE) methods specifically developed for taking advantages of unfitted meshes.

Many studies have been carried out about developing numerical methods for solving interface problems on unfitted meshes. Among related literatures, two types of techniques are considered in the finite element formulation around the interface to enforce the jump conditions. The first approach constructs suitable shape functions on elements around the interface according to the behaviors of the exact solutions so that they can produce good approximation, for example, the multiscale finite element method [54, 65], the extended finite element method [63, 186], and the partition of unity method [157, 187], as well as the IFE method to be discussed in this dissertation. The other approach employs the standard polynomials as the shape functions but uses suitable penalties in the finite element scheme near the interface, such as the CutFEM [25, 91, 92]. Also, we refer readers to [75, 76, 133, 138, 139, 202, 203] for immersed interface method (IIM) and [200, 206, 207, 211, 212, 213] for matched interface and boundary (MIB) method in the context of finite difference scheme based a Cartesian mesh. Recently, a new finite element method based on a semi-structured mesh was proposed in [46] where the interface geometry is fitted by a local Delaunay triangulation on interface elements of a pre-generated background Cartesian mesh.

Among those methods based on unfitted meshes, the IFE method and the CutFEM are related to each other somewhat more closer than to other methods in the sense that a finite element solution generated by either of these two methods is a standard polynomial when restricted on each non-interface element, but a macro polynomial, i.e., a piecewise polynomial, on each interface element defined according to the subelements partitioned by the interface curve. However, the IFE method and the CutFEM use essentially different ways to patch two polynomials together to form the macro polynomial on each interface element. The CutFEM uses two sets of polynomial shape functions on each interface element and uses a Nitsche's type penalty in the finite element scheme to glue them together according to the jump conditions. The IFE method employs one set of Hsieh-Clough-Tocher type [33, 56] macro shape functions on each interface element constructed to satisfy the jump conditions in a certain weak sense. This essential difference leads to different degrees of freedom around the interface for these two methods. Both the total number and location of degrees of freedom of the IFE space can be fixed and independent of the interface [99, 136, 148], and an IFE space can be constructed to be isomorphic to the standard H^1-conforming finite element space defined on the same mesh. This feature of IFE methods can be advantageous in some applications, for example, the method of lines [172] can be readily adopted for using an IFE method to solve problems with a moving interface [105, 147], and the shape optimization methodology can naturally work together with IFE methods to solve some interface inverse problems so that the numerical interface can be adjusted in the optimization procedure on a fixed mesh, see Section 1.3 and Section 4.1 for more discussions.

1.2 Previous Works for IFE Methods

We note that IFE methods have been applied in various applications related to interface problems, for example, the Particle-In-Cell method for plasma particle simulations [90, 123, 124, 151], the moving interface problems [6, 105, 147], the electroencephalography forward problem [193], fluid dynamics [6, 7], beam equations [143, 144], acoustic wave propagation [158], and elasticity systems [111, 142, 149, 203]. In this section, we specifically use the scalar elliptic interface problem in (1.1)-(1.4) as the example to review the current construction and analysis approaches in the IFE literature. Then, we will give explanations about the difficulties and challenges to extend these current approaches to a PDE system with a vector unknown, such as the elasticity interface problems (1.5)-(1.11), or the IFE methods with higher-degree polynomials.

The development and analysis of IFE methods for the scalar elliptic interface problems has been extensively studied in the literature, see [76, 129, 136, 141] for the linear IFE methods, [99, 100, 145] for the bilinear IFE methods, and [150, 209] for the rotated-Q_1 IFE methods. The basic idea in these works is to "explicitly" impose the approximate jump conditions on a linear approximation of the interface, for example, see Figure 1.2 below, the line connecting the intersection points of the interface and element boundary, such that the IFE shape functions can be uniquely determined and constructed with the Lagrange type degrees of freedom imposed at the vertices of an interface element (the linear or bilinear case) or midpoints of the element edges (the rotated-Q_1 case). As for the analysis of the approximation capabilities for these IFE spaces, a fundamental theoretical tool used in these works is the so called multipoint Taylor expansion. This technique was introduced to analyze the linear IFE space [136], and then the bilinear IFE space [99, 103] and the rotated-Q_1 IFE space [209].

We note that the construction procedure developed in those works mentioned above and the resulted format of IFE functions all rely on the related mesh type, the related polynomial spaces, and the related interface element configuration. Besides, the multipoint Taylor expansions require careful and lengthy calculus according to the involved polynomials and element shapes. These technical issues hinder the extension of the current approaches to more demanding IFE methods, such as the IFE methods for elasticity interface problems.

The state of disunity in the research for IFE methods motivated the authors in [78, 79] to develop a unified framework for constructing and analyzing IFE spaces using lower degree (linear, bilinear, or the rotated-Q_1) polynomials for solving elliptic interface problems.

For the IFE spaces based on the lower degree polynomials, the authors of [78, 79] showed that the construction of an IFE shape function could be accomplished by solving a linear system with a coefficient matrix in the Sherman-Morrison format; hence, the unisolvence of IFE shape functions, i.e., their existence and uniqueness, follows from the invertibility of the Sherman-Morrison matrix. This construction procedure is universally applicable to all the low-degree IFE functions and any interface element configurations. It simplifies the tedious

construction procedures presented in previous works.

Since the work in [78, 79] actually shed light on how to extend IFE methods to more demanding cases, we herein provide a review about this unified construction procedure. Given each element T in a mesh, define an index set $\mathcal{I} = \{1, 2, 3\}$ when T is triangular or $\mathcal{I} = \{1, 2, 3, 4\}$ when T is rectangular. We denote the local finite element space by (T, Π_T, Σ_T), with $\Pi_T = \text{Span}\{1, x, y\}$, or $\Pi_T = \text{Span}\{1, x, y, xy\}$, or $\Pi_T = \text{Span}\{1, x, y, x^2 - y^2\}$ for the linear, bilinear, or rotated-Q_1 polynomial space, respectively, and the local degrees of freedom $\Sigma_T = \{\psi_T(A_i) : i \in \mathcal{I},\ \psi_T \in \Pi_T\}$, where A_is are the vertices of T for the linear and bilinear polynomials, or A_is are the midpoints of edges of T for the Crouzeix-Raviart (CR elements) and the rotated-Q_1 polynomials [58]. For these finite element spaces, according to [35, 55, 58, 171], there exist shape functions $\psi_{i,T} \in \Pi_T$, $i = 1, 2, \cdots, |\mathcal{I}|$ such that $\Pi_T = \text{Span}\{\psi_{i,T}, 1 \le i \le |\mathcal{I}|\}$ with

$$\psi_{i,T}(A_j) = \delta_{i,j}, \quad i, j \in \mathcal{I}, \tag{1.12}$$

where $\delta_{i,j}$ is the Kronecker delta function. Then, the local IFE space on each non-interface element T is defined as

$$S_h(T) = \text{Span}\{\psi_{i,T} : i \in \mathcal{I}\}. \tag{1.13}$$

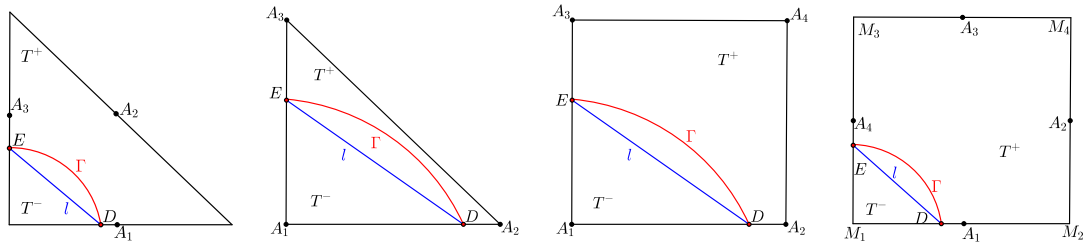

(a) CR elements (b) Linear elements (c) Bilinear elements (d) Rotated Q_1 elements

Figure 1.2: Examples of interface elements

For an interface element T, the interface Γ partitions T naturally into two subelements $T^- = \Omega^- \cap T$ and $T^+ = \Omega^+ \cap T$. Let l be the line connecting the intersection points of ∂T and Γ. As proposed in [79], we consider IFE functions in the following format:

$$\phi_T(X) = \begin{cases} \phi_T^-(X) \in \Pi_T, & \text{if} \quad X \in T^-, \\ \phi_T^+(X) \in \Pi_T, & \text{if} \quad X \in T^+, \end{cases} \tag{1.14}$$

with $\phi_T^+(X)$ and $\phi_T^-(X)$ satisfying that

$$\begin{cases} \phi_T^-|_l = \phi_T^+|_l, & \text{(for the linear polynomials)}, \\ \phi_T^-|_l = \phi_T^+|_l, \quad d(\phi_T^-) = d(\phi_T^+), & \text{(for the bilinear/rotated-}Q_1\text{ polynomials)}, \end{cases} \tag{1.15}$$

$$\beta^+ \nabla \phi_T^+(F) \cdot \mathbf{n}(F) = \beta^- \phi_T^-(F) \cdot \mathbf{n}(F), \tag{1.16}$$

where F is an arbitrary point on Γ, $\mathbf{n}(F)$ is the normal vector to Γ at F, and $d(\psi)$ is the coefficients of the second degree term of $\psi \in \Pi_T$, i.e., the coefficient of xy for a bilinear polynomial or the coefficient of $x^2 - y^2$ for a rotated-Q_1 polynomial. Given a set of nodal values v_i, $i \in \mathcal{I}$, regardless of interface location, by Theorem 5.1 in [79], we know that there exists a unique function ϕ_T satisfying (1.14)-(1.16) such that $\phi_T(A_i) = v_i$. In fact, it has been shown in [79] that this IFE function has the following explicit expression: let $\mu = \beta^+/\beta^- - 1$,

$$\phi_T(X) = \begin{cases} \phi_T^-(X) = \phi_T^+(X) + c_0 L(X) & \text{if } X \in T^-, \\ \phi_T^+(X) = \sum_{i \in \mathcal{I}^-} c_i \psi_{i,T}(X) + \sum_{i \in \mathcal{I}^+} v_i \psi_{i,T}(X) & \text{if } X \in T^+. \end{cases} \tag{1.17}$$

Denote the following vectors

$$\boldsymbol{\gamma} = (\nabla \psi_{i,T} \cdot \mathbf{n}(F)))_{i \in \mathcal{I}^-}, \quad \boldsymbol{\delta} = (L(A_i))_{i \in \mathcal{I}^-}, \tag{1.18a}$$

$$\mathbf{b} = \left(v_i - \mu L(A_i) \sum_{j \in \mathcal{I}^+} \nabla \psi_{j,T} \cdot \mathbf{n}(F)\ v_j \right)_{i \in \mathcal{I}^-}. \tag{1.18b}$$

Then, the coefficients $\mathbf{c} = (c_i)_{i \in \mathcal{I}^-}$ in (1.17) satisfy the following Sherman-Morrison system

$$(1 + \mu \boldsymbol{\delta} \boldsymbol{\gamma}^T)\mathbf{c} = \mathbf{b}. \tag{1.19}$$

By the Sherman-Morrison formula, we can express $\mathbf{c}$ as

$$\mathbf{c} = \mathbf{b} - \mu \frac{(\boldsymbol{\gamma}^T \mathbf{b})\boldsymbol{\delta}}{1 + \mu \boldsymbol{\gamma}^T \boldsymbol{\delta}}, \tag{1.20a}$$

$$\text{and then } \ c_0 = \mu \left(\sum_{i \in \mathcal{I}^-} c_i \nabla \psi_{i,T} \cdot \mathbf{n}(F) + \sum_{i \in \mathcal{I}^+} v_i \nabla \psi_{i,T} \cdot \mathbf{n}(F) \right). \tag{1.20b}$$

Consequently, there exist IFE shape functions satisfying

$$\phi_{i,T}(A_j) = \delta_{ij}, \quad i, j \in \mathcal{I}, \tag{1.21}$$

which are used to define the local IFE space on the interface element T:

$$S_h(T) = \text{Span}\{\phi_{i,T} \ : \ i \in \mathcal{I}\}. \tag{1.22}$$

We emphasize that the formulas in (1.17)-(1.20b) do not rely on the polynomial spaces involved, element shape, and interface element configuration. This feature makes it advantageous in both analysis and implementation.

In addition, according to [78, 79], a group of fundamental identities for the IFE shape functions have been established for all of these IFE spaces. These intrinsic identities reveal

the fact that the two polynomial components of an IFE function in the format of (1.14) are highly related to each other such that, in many situations, each IFE shape function essentially behaves like one polynomial instead of a macro polynomial with two polynomial components. Furthermore, these identities greatly help us to simplify and unify the error analysis techniques based on the multipoint Taylor expansion in the literature [9, 99, 100, 136, 209]. Specifically, given a function u, we consider its IFE interpolation $I_h u \in S_h(T)$:

$$I_{h,T} u = \sum_{i \in \mathcal{I}} u(A_i) \phi_{i,T}. \tag{1.23}$$

Then, this new and unified error analysis framework allows us to establish the following optimal error bound for the IFE interpolation on every element T in an interface-independent mesh:

$$|I_{h,T} u - u|_{H^j(T)} \leqslant C h^{2-j} \|u\|_{H^2(T)}, \quad j = 0, 1, \tag{1.24}$$

which states the optimal approximation capability of all of these IFE spaces, regardless of the involved polynomial types, element shapes, and interface element configurations, and the tedious derivation in those earlier works are avoided. We refer readers to Theorem 5.14 of [79] for the details of using this unified error analysis framework.

1.3 Interface Inverse Problems and Shape Optimization Methods

Since one of the contributions in this dissertation is to develop a shape optimization algorithm based on IFE methods for solving interface inverse problems, in this section we provide a survey on the related inverse problems and shape optimization methods.

Inverse problems related to the second order elliptic equations with discontinuous coefficients (1.1)-(1.4) can be found in many science and engineering applications. An important inverse problem is to identify the coefficient β where one needs to either identify the physical properties of materials, i.e., the values (the *parameter estimation problem*) and/or detect the location and shape of inclusions/interfaces (the *geometric inverse problem*) using the data measured for u on a subset of the domain or on a subset of the boundary $\partial\Omega$ [51, 106, 117]. This type of inverse problems arises from numerous applications, such as the electrical impedance tomography (EIT) [38, 110] where u and β represent the electrical potential and the conductivity, respectively, and groundwater or oil reservoir simulation [67, 205] where u and β are the piezometric head and transmissivity, respectively. Similar inverse problems related to other partial differential equations can be found in [109, 119] for medical imaging problems, [130, 180] for elastography, and so on. It is well known that these inverse problems are usually ill-posed, especially when the available data is rather limited. Numerical methods based on the output-least-squares formulation are commonly used to handle these types of inverse problems, see [43, 48, 51, 106, 116] and references therein.

In many applications, the values of material properties or parameters are known or chosen, such as the elastic properties of tissue and bone in medical problems [156, 169] and the electrical properties in EIT problems [12, 27] to mention just a couple of applications. Thus, to take advantages of IFE methods' capability for handling geometric changes of interface on fixed and unfitted meshes, we focus on the geometric inverse problems to recover the interface shape and location for the related forward problem (1.1)-(1.4).

The shape optimization method [97, 165] is widely used for various geometric inverse problems. By this method, we solve a geometric inverse problem by seeking for an interface Γ that can minimize a shape dependent functional constructed according to the available data. Applications of the shape optimization methods on geometric inverse problems have been studied by many researchers. For the internal measurements, the authors in [44, 49, 162, 190, 106] studied recovering both the interface location and coefficients with certain regularization techniques. A more challenging case is that only the boundary measurement is known a-priori, such as the well-known EIT problems [110], since the less data makes the problem severely ill-posed. Research has been carried out for overcoming difficulties caused by the limited data. The authors of [185] employed the regularized Gauss-Newton method to the geometric inverse problems in the electrical resistance and capacitance tomography (ERT and ECT). In [53], the authors investigated the affect of multiple boundary measurements (Neumann-to-Dirichlet pairs) on reconstruction through an output-least-squares type objective functional imposed on the boundary. According to their results, as naturally expected, the more Neumann-to-Dirichlet pairs of data are used, the better reconstruction is. A Kohn-Vogelius type functional for the shape optimization through topological derivatives in stead of the shape derivatives was investigated in [42]. And a comparison between the Kohn-Vogelius formulation and output-least-squares formulation as well as the derivation of their shape sensitivities in the continuous level is given in [10]. Recently, the authors of [11] proposed a method that uses multiple Neumann-to-Dirichlet data and an output-least-squares objective functional to solve the optical tomography problem in which there is an additional absorption term, and their method can simultaneously identify the piecewise constant diffusion and absorption coefficients including both the values and interface location.

It is important to note that shape optimization methods inevitably involve the movement of the structure, boundary or interface, which is actually a critical issue in implementation challenging a solver chosen for the related forward problems. The shape optimization methods based on standard finite element methods with interface-fitted meshes are referred as the Lagrangian approach [50]. This approach has been applied to deal with quite a few inverse problems, for example, the EIT and the related electrical capacitance tomography (ECT), electrical resistance tomography (ERT) [23, 30, 185], the reconstruction of elastic properties and material interface in elasticity systems [180], and optimal designing problems [13, 62, 167], including heat dissipation minimization, elasticity compliance minimization and so on. However, this approach has a few major drawbacks, and perhaps, the most obvious one is its computational cost to resolve the interface by the mesh again and again in the optimization iterations, especially when the interface becomes complicated. Other issues for

the Lagrangian approach are related to the sensitivity computations which will be discussed in Chapter 4 in more details.

1.4 An Outline of This Dissertation

Motivated by the survey of IFE methods above, in this dissertation, we focus on three topics related to IFE methods including the extension of the unified framework in [79] reviewed in Section 1.2 to elasticity system, invention of a framework for arbitrary p-th degree IFE methods, and the application of IFE methods to interface inverse problems.

We note that the framework reviewed in Section 1.2 provides us a powerful tool to develop and analyze various lower-degree IFE functions with Lagrange type degrees of freedom which avoid many tedious discussions in the earlier works. So we believe it is possible to employ this framework to handle more complicated interface jump conditions such as those in elasticity systems (1.11). Therefore in Chapter 2, we will extend this framework to the interface problems in elasticity systems (1.5)-(1.11). However, we also note that there are still many challenges in this extension, and the fundamental reason is that the two components in the unknown displacement vector are coupled together through the jump conditions in (1.11) which can not be simply decoupled into two functions satisfying the jump conditions independently. Therefore, in this project, following the framework in Section 1.2, we will study how to use the Sherman-Morrison idea to construct vector IFE functions and how to employ the multipoint Taylor expansions to estimate the Lagrange-type interpolation errors of these IFE spaces. In addition, we will also derive a suitable scheme to employ these vector IFE functions to solve the elasticity interface problems and prove its optimal convergence. All these results will be presented in Chapter 2.

Even though the current framework reviewed in Section 1.2 is useful for constructing and analyzing lower-degree IFE spaces, we note that it has some essential difficulties being extended to the higher-degree IFE methods. The most critical one is the linear approximation for both the interface curve and jump conditions involved in the formulation (1.15) and (1.16) due to the intrinsic $\mathcal{O}(h^2)$ limitation. Therefore, even if IFE functions as piecewise higher-degree polynomials can be constructed to satisfy these weak jump conditions on the line, the resulted IFE spaces still do not have the desired optimal approximation capabilities to the exact solutions. There are some works attempting to develop higher-degree IFE spaces within this direction, but limited to the linear interface [3]. Moreover, the approximation capabilities of the lower-degree IFE spaces are gauged by the Lagrange type interpolation errors as in (1.23) and (1.24) which are estimated through the multipoint Taylor expansion. This technique is restrictive since its derivation relies on that the jump conditions are exactly satisfied on a line approximating the interface, and this is not suitable for higher-degree IFE functions. We believe the multipoint Taylor expansion is difficult, if not impossible, to apply in the higher-degree IFE methods.

These issues motivate us to seek for new construction approaches and analysis tools for higher-degree IFE methods. For this topic, in Chapter 3, we present a new perspective on the construction of IFE functions which are actually related to Cauchy problems locally posed on each interface element where the jump conditions are considered as boundary conditions. In this approach, the existence of IFE functions is completely addressed and the proof totally avoids the tedious discussions based on interface element configuration. Besides, we design a new interpolation operator to gauge the approximation capabilities based on projections to the associated polynomial spaces, and it overcomes the limitation of the multipoint Taylor expansions used in the analysis of IFE methods in the literature. Moreover, we also employ these higher-degree IFE functions in a discontinuous Galerkin IFE method and prove its optimal convergence. To our best knowledge, the IFE method presented in Chapter 3 is the first one ever including both construction and analysis.

In addition to those fundamental works about development and analysis of IFE methods mentioned above, in this dissertation we will also apply and implement IFE methods for one moving interface problem and show the advantages. In particular, as described in Section 1.3, the shape optimization method and its applications in inverse problems strongly motivate us to study how to apply IFE methods to solve interface inverse problems on a fixed mesh independent of the changes of shape and location of the interface curve in computation. In Chapter 4, we will develop an IFE-based shape optimization algorithm to reconstruct interface curves in a spectrum of inverse problems and optimal designing problems. In this algorithm, both the shape objective functional and the underlying forward problem are discretized by IFE methods optimally. And a group of formulas are derived for efficiently and accurately computing the shape sensitivities on a fixed mesh which can be applied in a standard optimization algorithm such as the quasi-Newton method to minimize the shape functional in order to find the target interface.

Chapter 2

IFE Methods for Elasticity Interface Problems

In this chapter, we construct and analyze a group of vector IFE spaces formed by linear, bilinear, and rotated Q_1 polynomials for solving interface problems of linear planar elasticity systems. The IFE shape functions are constructed through certain weak jump conditions imposed on a linear approximation of the interface curve such that the unisolvence can be guaranteed regardless of the Lamé parameters and the interface location. Multipoint Taylor expansions are utilized to show the optimal approximation capabilities of the proposed IFE spaces through the Lagrange type interpolation operator. We employ these IFE spaces in a partially penalized immersed finite element (PPIFE) method to solve the elasticity interface problems which contains penalties on interface edges for dealing with the discontinuity in the IFE functions. We show that this PPIFE method converges optimally in both an energy norm and the usual L^2 norm under the standard piecewise H^2-regularity assumption for the exact solution. Features of the proposed PPIFE method are demonstrated with numerical examples. The works of this chapter are also reported in [81, 82].

2.1 Introduction

Finite element methods based on the so called fitted or unstructured meshes have been developed to solve the elasticity interface problems [57, 93, 199]. In many applications, such as those inverse/design problems mentioned in Section 1.3, the change of the interface shape and/or location in computation can challenge the traditional finite element methods based on fitted meshes, and this motivates us to study how to solve the elasticity interface problems on unfitted or structured meshes. Within this direction, there have been some publications on developing the finite element methods or the finite difference methods to solve elasticity interface problems. For example, the CutFEM using the Nitsche's penalty along the interface

to enforce the jump conditions is presented in [25, 92], and some immersed interface methods (IIM) based on finite difference formulation are presented in [202, 203] which handle the jump conditions through a local coordinate transformation across the interface.

In the literature of IFE methods, a non-conforming linear IFE space on a triangular mesh is discussed in in [75, 77, 202]. A conforming IFE space is developed in [142, 202] by extending the IFE shape functions in [75, 77, 202] to the neighborhood interface elements. A bilinear IFE space on a rectangular Cartesian mesh is discussed in [153]. A non-conforming IFE space using the rotated Q_1 polynomials is presented in [149] which leads to a locking-free IFE method. Most of the IFE methods for the planar-elasticity interface problems are Gelerkin type, i.e., the test and trial functions used in these methods are from the same IFE space. The Petrov-Galerkin formulation can also be used, for example, the IFE method presented in [111] uses standard polynomials as the test functions but the IFE functions in macro polynomial format as the trial functions.

The task of this chapter is to extend the unified framework [79] reviewed in Section 1.2 from the scalar case to the interface problem of the system of partial differential equations for the linear elasticity. We note that this is a non-trivial extension because the unknown in this inverse problem is a vector whose two components in the displacement are coupled through the jump conditions. Because of this coupling, a vector IFE function for the elasticity interface problem can not be constructed component by component though the procedure developed for the scalar interface problems in [79], i.e., the construction of a vector IFE function can not be decoupled for its two scalar components independently. Due to the same reason, the multipoint Taylor expansion in the literature for scalar functions can not be used directly in the analysis of the approximation capability of the proposed vector IFE spaces. In addition, many properties such as the trace inequalities have not been established for these vector IFE functions.

In this chapter, we will address three issues in the development of IFE methods on elasticity interface problems. Firstly, we construct the pertinent vector IFE spaces formed by piecewise linear, bilinear, and rotated Q_1 polynomials to satisfy the jump conditions (1.11) in a certain weak sense. In particular, we extend the construction approach in [79] to the vector case in which the coefficients in a vector IFE shape function satisfy a generalized *Sherman-Morrison* linear system and the unisolvence of the IFE shape functions is guaranteed regardless of the interface location and Lamé parameters. This construction method is superior to the one developed in [153] where the unisolvence of IFE shape functions can only hold conditionally.

Secondly, we establish the optimal approximation capabilities of the proposed vector IFE spaces to functions satisfying the jump conditions in (1.11). This result is achieved by estimating the Lagrange type interpolation errors through multipoint Taylor expansions. And for this purpose, we develop a group of essential identities for transferring the quantities of a vector function from one side of the interface to the other according to the jump conditions, and these identities are nontrivial extensions of their scalar counterparts in [79].

Thirdly, we derive a partially penalized IFE (PPIFE) method to employ the proposed vector

IFE space to solve the elasticity interface problems. To reduce the adverse effects from the discontinuity of IFE functions across interface edges, we apply interior penalties at all interface edges in this PPIFE method, which, in a certain sense, can be considered as an extension of the one in [85, 148] for scalar elliptic interface problems to interface problems of elasticity systems. To analyze these penalty terms, we develop a special trace inequality on interface edges for the stress of the elasticity IFE functions in which the constant in the bound is independent of the interface location. In addition, in the error analysis, we employ a patch idea to estimate IFE interpolation errors in these penalty terms with the standard piecewise H^2 regularity assumption for the exact solution. A similar idea was also used in [85] to circumvent the extra H^3 regularity assumption for the exact solution to show the optimal convergence of IFE solutions.

2.2 Preliminaries and Notations

In this section, we describe terms and facts to be used in the discussions of this chapter. For a measurable subset $\widetilde{\Omega} \subseteq \Omega$, we denote the vector Sobolev space by $\mathbf{W}^{k,q}(\widetilde{\Omega}) = \left[W^{k,q}(\widetilde{\Omega})\right]^2$ where $W^{k,q}(\widetilde{\Omega})$ is the standard Sobolev space, and the associated norm and semi-norm of $\mathbf{W}^{k,q}(\widetilde{\Omega})$ are such that for every $\mathbf{u} = (u_1, u_2)^T \in \mathbf{W}^{k,q}(\widetilde{\Omega})$,

$$\|\mathbf{u}\|_{W^{k,q}(\widetilde{\Omega})} = \|u_1\|_{W^{k,q}(\widetilde{\Omega})} + \|u_2\|_{W^{k,q}(\widetilde{\Omega})}, \quad |\mathbf{u}|_{W^{k,q}(\widetilde{\Omega})} = |u_1|_{W^{k,q}(\widetilde{\Omega})} + |u_2|_{W^{k,q}(\widetilde{\Omega})},$$
$$\|\mathbf{u}\|_{W^{k,\infty}(\widetilde{\Omega})} = \max\{\|u_1\|_{W^{k,\infty}(\widetilde{\Omega})}, \|u_2\|_{W^{k,\infty}(\widetilde{\Omega})}\}, \quad |\mathbf{u}|_{W^{k,\infty}(\widetilde{\Omega})} = \max\{|u_1|_{W^{k,\infty}(\widetilde{\Omega})}, |u_2|_{W^{k,q}(\widetilde{\Omega})}\}.$$

The related vector Hilbert space is denoted by $\mathbf{H}^k(\widetilde{\Omega}) = \mathbf{W}^{k,2}(\widetilde{\Omega})$. Let $\mathbf{C}^k(\widetilde{\Omega})$ be the collection of k-th differentiable smooth vector functions. When $\widetilde{\Omega}^s := \widetilde{\Omega} \cap \Omega^s \neq \emptyset, s = \pm$, we define

$$\mathbf{PW}^{k,q}(\widetilde{\Omega}) = \{\mathbf{u} : \mathbf{u} \in \mathbf{W}^{k,q}(\widetilde{\Omega}^s),\ s = \pm;\ [\mathbf{u}]_\Gamma = \mathbf{0},\ \text{and}\ [\sigma(\mathbf{u})\mathbf{n}]_\Gamma = \mathbf{0}\}, \tag{2.1}$$

$$\mathbf{PC}^k(\widetilde{\Omega}) = \{\mathbf{u} : \mathbf{u} \in \mathbf{C}^k(\widetilde{\Omega}^s),\ s = \pm;\ [\mathbf{u}]_\Gamma = \mathbf{0},\ \text{and}\ [\sigma(\mathbf{u})\mathbf{n}]_\Gamma = \mathbf{0}\}, \tag{2.2}$$

where the definition implicitly implies that $[\mathbf{u}]_\Gamma$ and $[\sigma(\mathbf{u})\mathbf{n}]_\Gamma$ are well-defined, with the following norms and semi-norms:

$$\|\mathbf{u}\|_{W^{k,q}(\widetilde{\Omega})} = \sum_{i=1}^{2} \left(\|u_i\|_{W^{k,q}(\widetilde{\Omega}^-)} + \|u_i\|_{W^{k,q}(\widetilde{\Omega}^+)} \right),$$
$$|\mathbf{u}|_{W^{k,q}(\widetilde{\Omega})} = \sum_{i=1}^{2} \left(|u_i|_{W^{k,q}(\widetilde{\Omega}^-)} + |u_i|_{W^{k,q}(\widetilde{\Omega}^+)} \right),$$
$$\|\mathbf{u}\|_{W^{k,\infty}(\widetilde{\Omega})} = \max_{i=1,2}\{\max\{\|u_i\|_{W^{k,\infty}(\widetilde{\Omega}^-)}, \|u_i\|_{W^{k,\infty}(\widetilde{\Omega}^+)}\}\},$$
$$|\mathbf{u}|_{W^{k,\infty}(\widetilde{\Omega})} = \max_{i=1,2}\{\max\{|u_i|_{W^{k,\infty}(\widetilde{\Omega}^-)}, |u_i|_{W^{k,\infty}(\widetilde{\Omega}^+)})\}\}.$$

Also we denote the corresponding Hilbert space by $\mathbf{PH}^k(\widetilde{\Omega}) = \mathbf{PW}^{k,2}(\widetilde{\Omega})$ with the norm $\|\cdot\|_{H^k(\widetilde{\Omega})} = \|\cdot\|_{W^{k,2}(\widetilde{\Omega})}$ and the semi-norm $|\cdot|_{H^k(\widetilde{\Omega})} = |\cdot|_{W^{k,2}(\widetilde{\Omega})}$. Furthermore, for any vector function $\mathbf{v} = (v_1, v_2)^T \in \mathbf{H}^1(\widetilde{\Omega})$, let $\nabla\mathbf{v}$ be its 2-by-2 Jacobian matrix where the i-th row is the row vector ∇v_i, $i = 1, 2$.

Without loss of generality, we assume that the solution domain Ω is the union of several rectangles. Let $\mathcal{T}_h$ be a Cartesian rectangular or Cartesian triangular mesh of the domain Ω with a mesh size $h > 0$. An element $T \in \mathcal{T}_h$ is called an interface element provided that the interface Γ intersects T with a non-empty intersection; otherwise, it is called a non-interface element. Let $\mathcal{T}_h^i$ and $\mathcal{T}_h^n$ be the collection of interface elements and non-interface elements, respectively. Similarly, let $\mathcal{E}_h^i(\mathring{\mathcal{E}}_h^i)$ and $\mathcal{E}_h^n(\mathring{\mathcal{E}}_h^n)$ be the collection of (interior) interface edges and non-interface edges, respectively. These notations will be used throughout this dissertation.

In addition, as in [84, 101], we assume that $\mathcal{T}_h$ satisfies the following hypotheses when the mesh size h is small enough:

(H1) The interface Γ cannot intersect an edge of any element at more than two points unless the edge is part of Γ.

(H2) If Γ intersects the boundary of an element at two points, these intersection points must be on different edges of this element.

(H3) The interface Γ is smooth enough so that $\mathbf{PC}^2(T)$ is dense in $\mathbf{PH}^2(T)$ for every interface element $T \in \mathcal{T}_h^i$.

In this chapter, we will discuss IFE spaces formed by vectors of linear polynomials (including the Crouzeix-Raviart elements) on triangular meshes and bilinear or rotated Q_1 polynomials on rectangular meshes. For each element T in a mesh $\mathcal{T}_h$, we introduce an index set $\mathcal{I} = \{1, 2, 3\}$ when T is triangular or $\mathcal{I} = \{1, 2, 3, 4\}$ when T is rectangular. Then, the local finite element space is denoted by $(T, \mathbf{\Pi}_T, \mathbf{\Sigma}_T)$, with $\mathbf{\Pi}_T = [\text{Span}\{1, x, y\}]^2$, or $[\text{Span}\{1, x, y, xy\}]^2$, or $[\text{Span}\{1, x, y, x^2 - y^2\}]^2$ for the linear, or bilinear, or rotated Q_1 polynomial space, respectively, and the local degrees of freedom $\mathbf{\Sigma}_T = \{\boldsymbol{\psi}_T(A_i) : i \in \mathcal{I},\ \boldsymbol{\psi}_T \in \mathbf{\Pi}_T\}$, where A_is are vertices of T for the linear and bilinear elements, or midpoints of edges of T for the rotated Q_1 elements and the Crouzeix-Raviart (CR) elements. For these local finite element spaces, according to [35, 55, 58, 171], there exist vector shape functions $\boldsymbol{\psi}_{i,T} \in \mathbf{\Pi}_T$, $i = 1, 2, \cdots, 2|\mathcal{I}|$ such that $\mathbf{\Pi}_T = \text{Span}\{\boldsymbol{\psi}_{i,T}, 1 \le i \le 2|\mathcal{I}|\}$ with

$$\boldsymbol{\psi}_{i,T}(A_j) = \begin{cases} \delta_{i,j}, \\ 0, \end{cases} \quad i = 1, \cdots, |\mathcal{I}|, \text{ and } \boldsymbol{\psi}_{i,T}(A_j) = \begin{cases} 0, \\ \delta_{i-|\mathcal{I}|,j}, \end{cases} \quad i = |\mathcal{I}| + 1, \cdots, 2|\mathcal{I}|, \tag{2.3}$$

$$|\boldsymbol{\psi}_{i,T}|_{W^{k,\infty}(T)} \leqslant Ch^{-k}, \quad k = 0, 1, 2. \tag{2.4}$$

Furthermore, we denote a vectorization map $\mathrm{Vec}:\mathbb{R}^{m\times n}\to\mathbb{R}^{mn\times 1}$ such that for any $A=(a_{ij})_{i=1,j=1}^{m,n}$,

$$\mathrm{Vec}(A):=(a_{11},\cdots,a_{m1},a_{12},\cdots,a_{m2},\cdots,a_{1n},\cdots,a_{mn})^T,$$

and a Kronecker product $\otimes:\mathbb{R}^{m\times n}\times\mathbb{R}^{p\times q}\to\mathbb{R}^{mp\times nq}$ such that for any $A=(a_{ij})_{i=1,j=1}^{m,n}\in\mathbb{R}^{m\times n}$ and $B\in\mathbb{R}^{p\times q}$, there holds

$$A\otimes B=\begin{bmatrix} a_{11}B & \cdots & a_{1n}B \\ \vdots & \ddots & \vdots \\ a_{m1}B & \cdots & a_{mn}B \end{bmatrix}. \tag{2.5}$$

There is a well-known formula about the Kronecker product and the vectorization operation for three matrices P,Q,R:

$$\mathrm{Vec}(PQR)=(R^T\otimes P)\mathrm{Vec}(Q). \tag{2.6}$$

Throughout this chapter, we use I_n to denote the n-by-n identity matrix and $0_{m\times n}$ to denote the m-by-n zero matrix for any positive integers m and n.

In this chapter, we shall adopt the generic constant C which only depends on the Lamé parameters $\lambda^{\pm}$, $\mu^{\pm}$, but independent of the relative interface location with respect to the mesh or the mesh size h.

2.3 Geometric Properties of the Interface

In this section, we discuss geometric properties on interface elements that are useful for developing and analyzing IFE spaces. We emphasize that these properties will be used in both this chapter and Chapter 3, because they are fundamental results describing how well the interface is resolved by interface elements. We also believe they can be used in the future for other IFE methods and other unfitted mesh methods.

Let T be an interface element partitioned by Γ into T^- and T^+. As illustrated in Figure 2.1, we let l be the line passing through the points D and E where ∂T and Γ intersect. For a point $\widetilde{X}$ on $\Gamma\cap T$, we let $\mathbf{n}(\widetilde{X})=(\tilde{n}_x(\widetilde{X}),\tilde{n}_y(\widetilde{X}))$ be the normal of Γ at $\widetilde{X}$, and we let $\widetilde{X}_\perp\in l$ be the orthogonal projection of $\widetilde{X}\in\Gamma\cap T$ onto the line l. Also, we let $\bar{\mathbf{n}}=(\bar{n}_x,\bar{n}_y)$ be the unit normal vector and let $\bar{\mathbf{t}}=(\bar{n}_y,-\bar{n}_x)$ be the vector tangential to l. Without loss of generality, we can assume the orientation of all the normal vectors are from T^- to T^+. In addition, we let κ be the maximum curvature of the curve Γ.

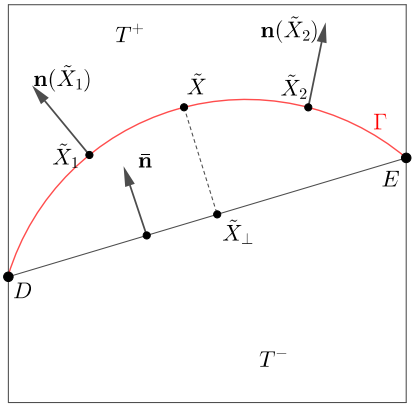

Figure 2.1: Quantities related to interface elements

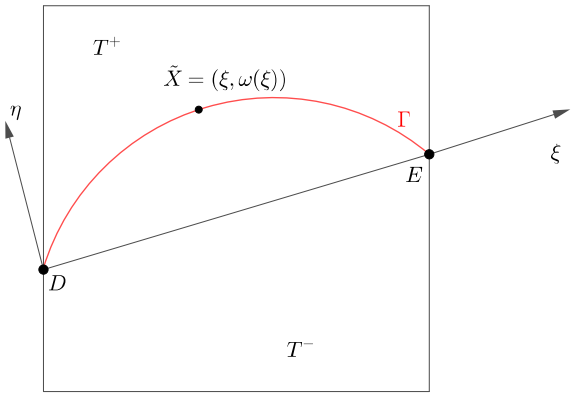

Figure 2.2: The local coordinate system

For each interface element $T \in \mathcal{T}_h^i$, without loss of generality, we can introduce a local coordinate system $(\xi, \eta) = (\xi, w(\xi))$ for a suitable function w such that, in this local system, D is the origin and its horizontal axis is aligned with l, as shown in Figure 2.2. We start from the following lemma which extends similar results in [136]:

Lemma 2.1. *Assume $h\kappa \leqslant \epsilon$ for an $\epsilon \in (0, \frac{\sqrt{2}}{2})$, then for any interface element $T \in \mathcal{T}_h^i$, the following estimates hold*

$$|w(\xi)| \leqslant 2(1-2\epsilon^2)^{-3/2}\kappa h^2, \tag{2.7}$$
$$|w'(\xi)| \leqslant \sqrt{2}(1-2\epsilon^2)^{-3/2}\kappa h. \tag{2.8}$$

Proof. In the local system, let ξ_E be the coordinate of the point E. And by the Mean Value Theorem, there is some $\xi_0 \in [0, \xi_E]$ such that $w'(\xi_0) = 0$. Consider a function g as well as its derivative

$$g(\xi) = \frac{w'(\xi)}{\sqrt{1+(w'(\xi))^2}}, \quad \text{and,} \quad g'(\xi) = \frac{w''(\xi)}{(1+(w'(\xi))^2)^{3/2}}.$$

Note that $g'(\xi)$ is the curvature of Γ at ξ; hence, we have $|g'(\xi)| \leq \kappa$. Then, by $g(\xi_0) = 0$, we have $|g(\xi)| = \left|\int_{\xi_0}^{\xi} g'(s)ds\right| \leqslant \int_{\xi_0}^{\xi} |g'(s)|ds \leqslant \sqrt{2}\kappa h = \sqrt{2}\epsilon$, which implies $|\omega'(\xi)| \leqslant \frac{\sqrt{2}\epsilon}{\sqrt{1-2\epsilon^2}}$. By the definition of κ, we have $|\omega''(\xi)| \leqslant (1-2\epsilon^2)^{-3/2}\kappa$.

Now using the Taylor expansion for w around D leads to $w(\xi) = w'(0)\xi + \frac{1}{2}w''(\bar{\xi})\xi^2$ for some $\bar{\xi} \in [0, \xi_E]$. Note that $w(\xi_E) = 0$ shows $w'(0) = -\frac{1}{2}w''(\bar{\xi}_E))\xi_E$. Thus we have $w(\xi) = -\frac{1}{2}w''(\bar{\xi}_E))\xi_E\xi + \frac{1}{2}w''(\bar{\xi})\xi^2$ and therefore, $|w(\xi)| \leqslant 2\|w''\|_\infty h^2 \leqslant 2(1-2\epsilon^2)^{-3/2}\kappa h^2$, which yields (2.7). And using Taylor expansion again for w' around ξ_0, we have $w'(\xi) = w''(\tilde{\xi})(\xi - \xi_0)$ for some $\tilde{\xi}$ between ξ_0 and ξ. Finally we obtain $|w'(\xi)| \leqslant \sqrt{2}\|w''\|h \leqslant \sqrt{2}(1-2\epsilon^2)^{-3/2}h$. □

We note that the argument for Lemma 2.1 is similar to Assumption 3.14 in [52] in which a local polar coordinate system is used on the interface element, but an essential difference is that we explicitly specify the dependence of constants on the curvature in the estimates given in Lemma 2.1. The following lemmas provide estimates about various geometric quantities defined at points on $\Gamma \cap T$.

Lemma 2.2. *Assume $h\kappa \leqslant \epsilon$ for an $\epsilon \in (0, \frac{\sqrt{2}}{2})$, then for any interface element $T \in \mathcal{T}_h^i$ and any point $\widetilde{X} \in \Gamma \cap T$, the following estimates hold:*

$$\|\widetilde{X} - \widetilde{X}_\perp\| \leqslant 2(1-2\epsilon^2)^{-3/2}\kappa h^2, \tag{2.9}$$

and

$$\|\mathbf{n}(\widetilde{X}_1) - \mathbf{n}(\widetilde{X}_2)\| \leqslant \sqrt{2}(1+(1-2\epsilon^2)^{-3/2})\kappa h, \quad \forall\ \widetilde{X}_1, \widetilde{X}_2 \in \Gamma \cap T, \tag{2.10a}$$

$$\mathbf{n}(\widetilde{X}_1) \cdot \mathbf{n}(\widetilde{X}_2) \geqslant 1 - 2(1+(1-2\epsilon^2)^{-3/2})^2\kappa^2 h^2, \quad \forall\ \widetilde{X}_1, \widetilde{X}_2 \in \Gamma \cap T. \tag{2.10b}$$

Proof. The estimate (2.9) directly follows from (2.7). For (2.10a), we assume $\widetilde{X}_1 = (\xi_1, w(\xi_2))$ and $\widetilde{X}_2 = (\xi_2, w(\xi_2))$ in the local system, respectively. Then we have

$$\mathbf{n}(\widetilde{X}_1) = \frac{1}{\sqrt{1+(w'(\xi_1))^2}} \begin{pmatrix} -w'(\xi_1) \\ 1 \end{pmatrix}, \quad \mathbf{n}(\widetilde{X}_2) = \frac{1}{\sqrt{1+(w'(\xi_2))^2}} \begin{pmatrix} -w'(\xi_2) \\ 1 \end{pmatrix}.$$

By the calculation in Lemma 2.1 and Mean Value Theorem, there is some $\bar{\xi} \in [0, \xi_E]$ such that

$$\left| \frac{w'(\xi_1)}{\sqrt{1+(w'(\xi_1))^2}} - \frac{w'(\xi_2)}{\sqrt{1+(w'(\xi_2))^2}} \right| = \frac{|w''(\bar{\xi})|}{(1+(w'(\bar{\xi}))^2)^{3/2}} |\xi_1 - \xi_2| \leqslant \sqrt{2}\kappa h$$

and $\tilde{\xi} \in [0, \xi_E]$ such that

$$\left| \frac{1}{\sqrt{1+(w'(\xi_1))^2}} - \frac{1}{\sqrt{1+(w'(\xi_2))^2}} \right| = \frac{|w'(\tilde{\xi})||w''(\tilde{\xi})|}{(1+(w'(\tilde{\xi}))^2)^{3/2}} |\xi_1 - \xi_2| \leqslant 2(1-2\epsilon^2)^{-3/2}\epsilon\kappa h$$

Then (2.10a) follows by applying these estimates in the local coordinate forms of $\mathbf{n}(\widetilde{X}_1)$ and $\mathbf{n}(\widetilde{X}_2)$. Furthermore, by (2.10a) and

$$\|\mathbf{n}(\widetilde{X}_1) - \mathbf{n}(\widetilde{X}_2)\|^2 = \|\mathbf{n}(\widetilde{X}_1)\|^2 + \|\mathbf{n}(\widetilde{X}_2)\|^2 - 2\mathbf{n}(\widetilde{X}_1) \cdot \mathbf{n}(\widetilde{X}_2) = 2 - 2\mathbf{n}(\widetilde{X}_1) \cdot \mathbf{n}(\widetilde{X}_2),$$

we have (2.10b). □

Remark 2.1. *Note that there exists a point $\widetilde{X}_1 = (\xi_1, w(\xi_1)) \in \Gamma \cap T$ such that $w'(\xi_1) = 0$ which means $\mathbf{n}(\widetilde{X}_1) = \bar{\mathbf{n}}$. Hence, by Lemma 2.2, we have the following estimates for an arbitrary point $\widetilde{X} \in \Gamma \cap T$:*

$$\|\mathbf{n}(\widetilde{X}) - \bar{\mathbf{n}}\| \leqslant \sqrt{2}(1+(1-2\epsilon^2)^{-3/2})\kappa h, \tag{2.11a}$$

$$\mathbf{n}(\widetilde{X}) \cdot \bar{\mathbf{n}} \geqslant 1 - 2(1+(1-2\epsilon^2)^{-3/2})^2\kappa^2 h^2. \tag{2.11b}$$

The two lemmas above have suggested a criteria about how small h should be according to the curvature κ so that the related analysis is valid. Therefore, for all discussions from now on, we further assume that

- h is sufficiently small such that for some fixed parameter $\epsilon \in (0, \sqrt{2}/2)$ and $\bar{\kappa} \in (0, 1]$ of one's own choice, there holds

$$h < \min\left\{ \frac{\sqrt{\bar{\kappa}}}{\sqrt{2}(1 + (1 - 2\epsilon^2)^{-3/2})\kappa}, \ \frac{\epsilon}{\kappa} \right\}. \tag{2.12}$$

Obviously ϵ is the proportion by which we should choose the mesh size h according to the interface curvature κ. Also, by (2.12) and (2.11b), we have

$$\mathbf{n}(\widetilde{X}) \cdot \bar{\mathbf{n}} \geq 1 - \bar{\kappa}, \quad \forall \widetilde{X} \in \Gamma \cap T \tag{2.13}$$

which shows how much the angle between the normal of $\Gamma \cap T$ and $\bar{\mathbf{n}}$ can vary in an interface element $T \in \mathcal{T}_h^i$, a larger value of $\bar{\kappa} \in (0, 1]$ allows $\mathbf{n}(\widetilde{X})$ to vary more from $\bar{\mathbf{n}}$ up to, but not equal to, 90 degree. Therefore, we will call $\bar{\kappa}$ the angle allowance. In this dissertation, we let the angle allowance $\bar{\kappa}$ and the parameter ϵ be small enough but fixed, i.e., the mesh size h is sufficiently small, such that all the estimates discussed in this section hold.

Now, we generalize the geometric estimates above to the so called patch of each interface element [87]. Specifically, for each interface element $T \in \mathcal{T}_h^i$, its patch or macro-element is the following set:

$$\omega_T = \bigcup \Big\{ T' \in \mathcal{T}_h : T' \cap T \neq \emptyset \Big\}. \tag{2.14}$$

Similarly, for any $\widetilde{X} \in \Gamma \cap \omega_T$, we let $\mathbf{n}(\widetilde{X})$ be its normal vector to Γ and let $\widetilde{X}_\perp$ be the projection of $\widetilde{X}$ onto l. Then, we can establish similar geometric estimates in the following lemma.

Lemma 2.3. *Given each interface element $T \in \mathcal{T}_h^i$ and its associated patch ω_T, assume the element size h is small enough, then for any point $\widetilde{X} \in \Gamma \cap \omega_T$, the following estimates hold:*

$$\|\widetilde{X} - \widetilde{X}^\perp\| \leqslant Ch^2, \tag{2.15a}$$

$$\|\mathbf{n}(\widetilde{X}) - \bar{\mathbf{n}}\| \leqslant Ch, \tag{2.15b}$$

$$\mathbf{n}(\widetilde{X}) \cdot \bar{\mathbf{n}} \geqslant 1 - Ch^2. \tag{2.15c}$$

Proof. The arguments for these estimates are the same as those used for Lemma 2.2 and Remark 2.1. □

For each interface element T and its associated patch ω_T, recalling that l with the normal vector $\bar{\mathbf{n}} = (\bar{n}_1, \bar{n}_2)$ is the line connecting the intersection points of Γ and ∂T , we let the

interface Γ and the line l partition the patch ω_T into sub-patches $\omega_T^s, s = \pm$ and $\hat{\omega}_T^s, s = \pm$, respectively. Let $\widetilde{\omega}_T^s = \omega_T^s \cap \hat{\omega}_T^s$, $s = \pm$, and then $\widetilde{\omega}_T = (\widetilde{\omega}_T^+ \cap \omega_T^-) \cup (\widetilde{\omega}_T^- \cap \omega_T^+)$ is the sub-patch sandwiched between l and Γ. In addition, following the idea in [81, 84], we consider the following set

$$\omega_T^{int} = \bigcup \{ l_t \cap \omega_T : l_t \text{ is a tangent line to } \omega_T \cap \Gamma \}. \tag{2.16}$$

We further define $\omega_T^{*,s} = \hat{\omega}_T^s \cap (\omega_T^s \backslash \omega_T^{int})$, $s = \pm$, and $\omega_T^* = \omega_T \backslash (\omega_T^{*,-} \cup \omega_T^{*,+})$. We can show that ω_T^* is actually a small subset of the patch ω_T in the following lemma.

Lemma 2.4. *Assume h is small enough, then there exists a constant C such that $|\omega_T^*| \leqslant Ch^3$ holds for every interface element T.*

Proof. By the definition, $\omega_T^* = \omega_T^{int} \cup \tilde{\omega}_T$. By (2.15a), it is easy to see that $|\tilde{\omega}_T| \leqslant Ch^3$. Besides, let X be one point in ω_T^{int}. According to the definition (2.16), there exists a point $Y \in \Gamma$ such that $\overline{XY}$ is tangential to Γ. Denote $X_\perp$ and $Y_\perp$ as the projection of X and Y onto l, respectively. Let $\theta \in [0, \pi/2]$ be the angle between $\overline{XY}$ and l. According to (2.15a), we have $|\overline{YY_\perp}| \leqslant Ch^2$. Using the fact $|\overline{XY}| \leqslant Ch$, we obtain $|\overline{XX_\perp}| = |\overline{YY_\perp}| + |\overline{XY}| \sin(\theta) \leqslant Ch^2 + Ch \sin(\theta)$. In addition, using (2.15c), there holds

$$\sin(\theta) = (1 - (\bar{\mathbf{n}} \cdot \mathbf{n}(Y))^2)^{1/2} \leqslant Ch. \tag{2.17}$$

It shows that $|\overline{XX_\perp}| \leqslant Ch^2$, i.e., the distance between X and $\overline{DE}$ is bounded by Ch^2. Since $|\overline{DE}| \leqslant Ch$, we have $|\omega_T^*| \leqslant Ch^3$, which finishes the proof. □

Finally, we end up this section by introducing a Patch Assumption:

Patch Assumption: For every interface element T, let e be one of the interface edges of T. Then for $s = \pm$, there exists a triangle $T_e^s \subset \Omega^s \cap \omega_T$ and two constants C_1, C_2 independent of the interface location such that $e \cap T^s$ is one edge of T_e^s and

$$C_1 |e \cap T^s| h \leqslant |T_e^s| \leqslant C_2 |e \cap T^s| h. \tag{2.18}$$

In fact, (2.18) can be guaranteed if the height of the auxiliary triangle T_e^s corresponding to the edge $e \cap T^s$ has the length $\mathcal{O}(h)$, and we note that this Patch Assumption can be easily satisfied when the mesh size h is sufficient small such that the interface is locally flat enough. Figure 2.3 provides illustrations for how $T_e^s, s = \pm$ are identified for an interface edge $e = A_1A_2$ in the patch ω_T of an interface element $T = \triangle A_1A_2A_3$ with $A_1 \in \Omega^-$ and $A_2 \in \Omega^+$, where $T_e^- = \triangle A_1PD$, $T_e^+ = \triangle A_2QD$ in Case 1, and $T_e^- = \triangle A_1DQ$, $T_e^+ = A_2DP$ in Case 2, respectively. The auxiliary triangles $T_e^s, s = \pm$ do not have to be formed by nodes in the mesh $\mathcal{T}_h$. For example, the point P in Case 1 in Figure 2.3 can be a point in $\overline{\omega_T} \cap \Omega^-$ so long as its perpendicular distance to the line passing e is $\mathcal{O}(h)$.

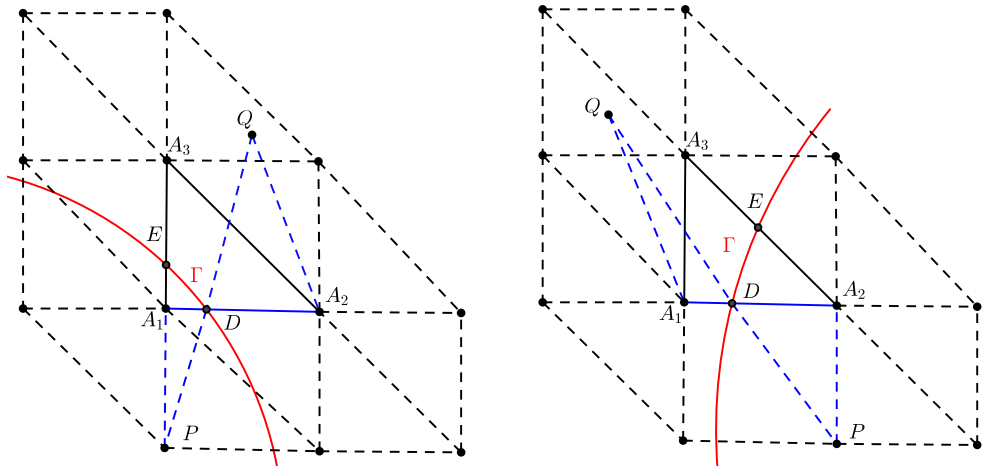

(a) Case 1 (b) Case 2

Figure 2.3: The patch for a triangular interface element

2.4 Vector IFE Functions For Elasticity Interface Problems

In this section, we construct local IFE spaces corresponding to the underlying finite element spaces $(T, \mathbf{\Pi}_T, \mathbf{\Sigma}_T)$ described in Section 2.3. As usual the local IFE space on every non-interface element T is the standard vector polynomial space, i.e.,

$$\mathbf{S}_h(T) = \text{Span}\{\boldsymbol{\psi}_{i,T},\, \boldsymbol{\psi}_{i+|\mathcal{I}|,T} : \, i \in \mathcal{I}\}, \tag{2.19}$$

where $\boldsymbol{\psi}_{i,T}$ are the standard vector linear, bilinear or rotated Q_1 Lagrange shape functions depending on whether T is triangular or rectangular, given by (2.3). Following the unified framework reviewed in Section 1.2, we now propose a procedure to construct vector IFE functions on interface elements for the jump conditions in (1.11).

2.4.1 Local Vector IFE Spaces

As in [79, 84, 209], without loss of generality, we focus on a typical interface element T with vertices $M_i, 1 \le i \le |\mathcal{I}|$ where $M_1 = (0,0)^T, M_2 = (h,0)^T, M_3 = (0,h)^T$ for discussions about a triangular interface element, but $M_1 = (0,0)^T, M_2 = (h,0)^T, M_3 = (0,h)^T, M_4 = (h,h)^T$ for discussions about a rectangular interface element. On this typical element T, the pertinent degrees of freedom will be imposed at the nodes $A_i, 1 \le i \le |\mathcal{I}|$. When linear and bilinear polynomials are considered on T, $A_i = M_i, 1 \le i \le |\mathcal{I}|$. When the non-conforming linear polynomials (Crouzeix-Raviart elements) on a triangular T are considered, $A_1 = (h/2, 0)^T$,

$A_2 = (h/2, h/2)^T$, $A_3 = (0, h/2)^T$. When the rotated Q_1 polynomials are discussed on a rectangular T, $A_1 = (h/2, 0)^T$, $A_2 = (h, h/2)^T$, $A_3 = (h/2, h)^T$, $A_4 = (0, h/2)^T$.

According to [79, 101, 136], by considering rotations, there are six possible vertices-nodes configurations for a non-conforming linear element, two possible configurations for a conforming linear and bilinear element, and 5 possible configurations for a rotated Q_1 element as illustrated in Figures 2.4-2.7.

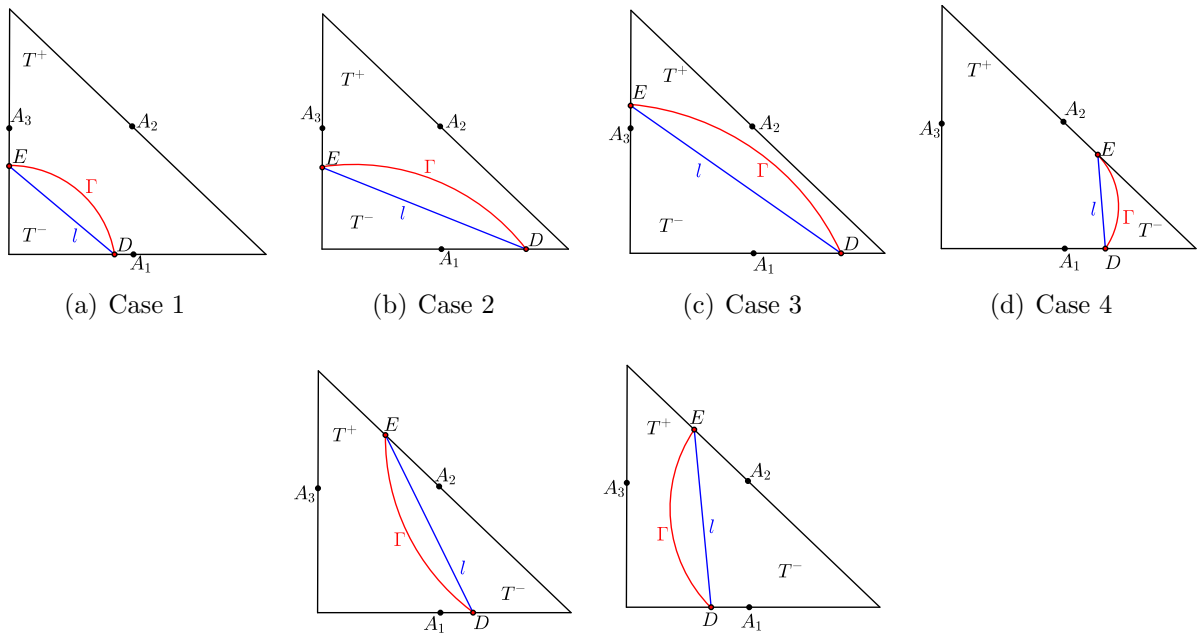

(a) Case 1 (b) Case 2 (c) Case 3 (d) Case 4

(e) Case 5 (f) Case 6

Figure 2.4: Typical non-conforming linear elements

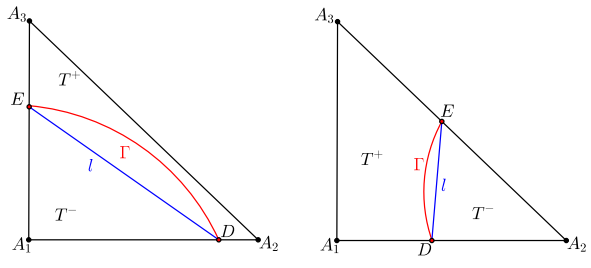

(a) Case 1 (b) Case 2

Figure 2.5: Typical conforming linear elements

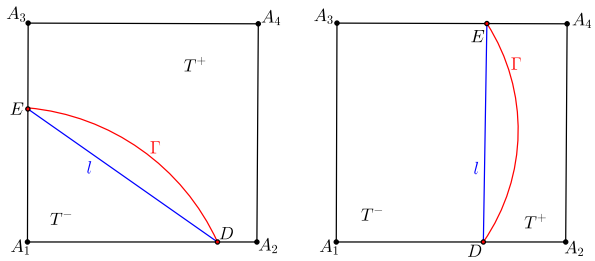

(a) Case 1 (b) Case 2

Figure 2.6: Typical bilinear elements

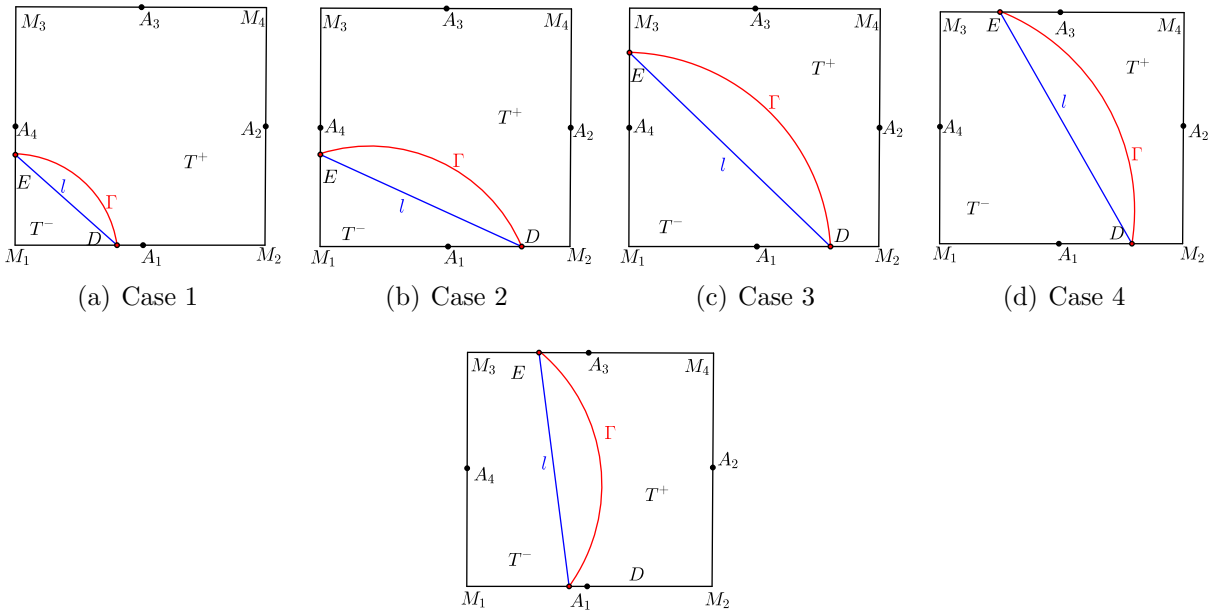

(a) Case 1 (b) Case 2 (c) Case 3 (d) Case 4

(e) Case 5

Figure 2.7: Typical rotated Q_1 elements

On an interface element T, let the line l partition T into subelements $\hat{T}^-$ and $\hat{T}^+$, then we consider the elasticity IFE functions as piecewise vector polynomials in the following format:

$$\boldsymbol{\phi}_T(X) = \begin{cases} \boldsymbol{\phi}_T^-(X) \in \mathbf{\Pi}_T, & \text{if} \quad X \in \hat{T}^-, \\ \boldsymbol{\phi}_T^+(X) \in \mathbf{\Pi}_T, & \text{if} \quad X \in \hat{T}^+, \end{cases} \tag{2.20}$$

with $\boldsymbol{\phi}_T^+(X)$ and $\boldsymbol{\phi}_T^-(X)$ satisfying that

$$\begin{cases} \boldsymbol{\phi}_T^-|_l = \boldsymbol{\phi}_T^+|_l, & \text{(for the linear polynomials)}, \\ \boldsymbol{\phi}_T^-|_l = \boldsymbol{\phi}_T^+|_l, \quad d(\boldsymbol{\phi}_T^-) = d(\boldsymbol{\phi}_T^+), & \text{(for the bilinear/rotated } Q_1 \text{ polynomials)}, \end{cases} \tag{2.21}$$

$$\sigma^+(\boldsymbol{\phi}_T^+)(F)\ \bar{\mathbf{n}} = \sigma^-(\boldsymbol{\phi}_T^-)(F)\ \bar{\mathbf{n}}, \tag{2.22}$$

where F is a point on l to be specified later and $d(\boldsymbol{\psi})$ is a vector formed by the coefficients of the second degree term of $\boldsymbol{\psi} \in \mathbf{\Pi}_T$, i.e., the coefficient of xy for a bilinear polynomial or the coefficient of $x^2 - y^2$ for a rotated Q_1 polynomial. Given a set of nodal-value vectors $\mathbf{v}_i$, $i \in \mathcal{I}$, we further impose the nodal value condition:

$$\boldsymbol{\phi}_T(A_i) = \mathbf{v}_i. \tag{2.23}$$

Let $\Psi_{i,T} = [\boldsymbol{\psi}_{i,T}, \boldsymbol{\psi}_{i+|\mathcal{I}|,T}]$, $i \in \mathcal{I}$ be 2-by-2 matrix basis functions and let $L(X) = 0$ be the equation of the line l with $L(X) = \bar{\mathbf{n}} \cdot (X - D)$. It is easy to see that $\Psi_{i,T}(A_j) = \delta_{i,j} I_2$,

$i, j \in \mathcal{I}$. Then by (2.23) and (2.21), we can express (2.20) as

$$\boldsymbol{\phi}_T(X) = \begin{cases} \boldsymbol{\phi}_T^-(X) = \boldsymbol{\phi}_T^+(X) + L(X)\mathbf{c}_0 & \text{if} \quad X \in \hat{T}^-, \\ \boldsymbol{\phi}_T^+(X) = \displaystyle\sum_{i\in\mathcal{I}^+} \Psi_{i,T}(X)\mathbf{v}_i + \sum_{i\in\mathcal{I}^-} \Psi_{i,T}(X)\mathbf{c}_i & \text{if} \quad X \in \hat{T}^+, \end{cases} \tag{2.24}$$

where $\mathbf{c}_0 = (c_0^1, c_0^2)^T$ and $\mathbf{c}_i = (c_i^1, c_i^2)^T$, $i \in \mathcal{I}^-$ are to be determined. Applying the jump condition for the stress tensor (2.22) to (2.24), we obtain

$$\sigma^- \left(L\mathbf{c}_0\right)(F)\bar{\mathbf{n}} = \hat{\sigma}(\boldsymbol{\phi}_T^+)(F)\bar{\mathbf{n}}, \tag{2.25}$$

where $\hat{\sigma}(\mathbf{v})(X)$ for a vector function $\mathbf{v}$ is defined as follows:

$$\begin{aligned} &\hat{\sigma}(\mathbf{v}) = (\hat{\sigma}_{ij}(\mathbf{v}))_{1\leqslant i,j\leqslant 2}, \quad \hat{\sigma}_{ij}(\mathbf{v}) = \hat{\lambda}(\nabla\cdot\mathbf{v})\delta_{i,j} + 2\hat{\mu}\epsilon_{ij}(\mathbf{v}), \\ &\text{with} \quad \hat{\lambda} = \lambda^+ - \lambda^-, \ \hat{\mu} = \mu^+ - \mu^-. \end{aligned} \tag{2.26}$$

Also, in $\hat{\sigma}(\boldsymbol{\phi}_T^+)(X)$, the function $\boldsymbol{\phi}_T^+$ is a polynomial so that it can be evaluated for any X, and this meaning applies to similar situations from now on. By direct calculations, we have

$$\sigma^-(L\mathbf{c}_0)(F) = \begin{bmatrix} \bar{n}_1^2(\lambda^- + \mu^-) + \mu^- & \bar{n}_1\bar{n}_2(\lambda^- + \mu^-) \\ \bar{n}_1\bar{n}_2(\lambda^- + \mu^-) & \bar{n}_2^2(\lambda^- + \mu^-) + \mu^- \end{bmatrix} \begin{bmatrix} c_0^1 \\ c_0^2 \end{bmatrix} := K\mathbf{c}_0. \tag{2.27}$$

Then we note that

$$K = Q\mathcal{P}^-Q^T, \quad \text{with} \ \ \mathcal{P}^- = \begin{bmatrix} (\lambda^- + 2\mu^-) & 0 \\ 0 & \mu^- \end{bmatrix}, \ \ Q = [\bar{\mathbf{n}}, \bar{\mathbf{t}}], \tag{2.28}$$

which is obviously non-singular. Hence, by (2.25), $\mathbf{c}_0$ is determined by

$$\mathbf{c}_0 = K^{-1}\hat{\sigma}(\boldsymbol{\phi}_T^+)(F)\bar{\mathbf{n}}. \tag{2.29}$$

Next we apply the nodal value condition (2.23) for $j \in \mathcal{I}^-$ and (2.29) to (2.24) to obtain

$$K\mathbf{c}_j + L(A_j)\sum_{i\in\mathcal{I}^-} \hat{\sigma}(\Psi_{i,T}\mathbf{c}_i)(F)\bar{\mathbf{n}} = K\mathbf{v}_j - L(A_j)\sum_{i\in\mathcal{I}^+} \hat{\sigma}(\Psi_{i,T}\mathbf{v}_i)(F)\bar{\mathbf{n}}, \quad j \in \mathcal{I}^-. \tag{2.30}$$

We now put equations in (2.30) into a matrix form. We let $(j_1, j_2, \cdots, j_{|\mathcal{I}|})$ be a permutation of $(1, 2, \cdots, |\mathcal{I}|)$ such that $j_k \in \mathcal{I}^-$ for $1 \leq k \leq |\mathcal{I}^-|$ but $j_k \in \mathcal{I}^+$ for $|\mathcal{I}^-| + 1 \leq k \leq |\mathcal{I}|$. Consider three vectors $\mathbf{c}$, $\mathbf{v}^-$ and $\mathbf{v}^+$ such that

$$\mathbf{c} = \left[\mathbf{c}_{j_k}\right]_{k=1}^{|\mathcal{I}^-|} \in \mathbb{R}^{2|\mathcal{I}^-|}, \quad \mathbf{v}^- = \left[\mathbf{v}_{j_k}\right]_{k=1}^{|\mathcal{I}^-|} \in \mathbb{R}^{2|\mathcal{I}^-|}, \quad \mathbf{v}^+ = \left[\mathbf{v}_{j_k}\right]_{k=|\mathcal{I}^-|+1}^{|\mathcal{I}|} \in \mathbb{R}^{2|\mathcal{I}^+|}.$$

We adopt the following notations:

$$\overline{K} = I_{|\mathcal{I}^-|} \otimes K \in \mathbb{R}^{2|\mathcal{I}^-|\times 2|\mathcal{I}^-|}, \quad \overline{L} = \left[L(A_{j_k})I_2\right]_{k=1}^{|\mathcal{I}^-|} \in \mathbb{R}^{2|\mathcal{I}^-|\times 2}, \tag{2.31a}$$

$$\overline{\Psi}^{-} = \left[\overline{\Psi}_{j_k}\right]_{k=1}^{|\mathcal{I}^-|} \in \mathbb{R}^{2|\mathcal{I}^-|\times 2}, \quad \overline{\Psi}^{+} = \left[\overline{\Psi}_{j_k}\right]_{k=|\mathcal{I}^-|+1}^{|\mathcal{I}|} \in \mathbb{R}^{2|\mathcal{I}^+|\times 2}, \tag{2.31b}$$

$$\text{with } \overline{\Psi}_j = \left[\begin{array}{cc} \hat{\sigma}(\boldsymbol{\psi}_{j,T})(F)\bar{\mathbf{n}} & \hat{\sigma}(\boldsymbol{\psi}_{j+|\mathcal{I}|,T})(F)\bar{\mathbf{n}} \end{array}\right]^T \in \mathbb{R}^{2\times 2}\ , \quad 1 \le j \le |\mathcal{I}|\,. \tag{2.31c}$$

For any vector $\mathbf{r} \in \mathbb{R}^{2\times 1}$, we note the identity $\hat{\sigma}(\Psi_{i,T}\mathbf{r})(F)\bar{\mathbf{n}} = \overline{\Psi}_i^T\mathbf{r}$. Hence by using the matrices defined in (2.31a)-(2.31c), we can represent equations in (2.30) as follows:

$$(\overline{K} + \overline{L}\ \overline{\Psi}^{-T})\mathbf{c} = \mathbf{b}, \tag{2.32}$$

$$\text{with} \qquad \mathbf{b} = \overline{K}\mathbf{v}^- - \overline{L}\ \overline{\Psi}^{+T}\mathbf{v}^+. \tag{2.33}$$

We emphasize that the weak jump conditions in (2.21) and (2.22) are similar to their counterparts given in (1.15) and (1.16), but the differences are the choice for the point F and defining the IFE function on two subelements of T determined by the line l instead of the interface curve. See Remark 2.6 for the reason and consideration behind these choices. We also note that the coefficient matrix of the linear system in (2.32) is a generalized *Sherman-Morrison* matrix formed by matrices $\overline{K}, \overline{L}$ and $\overline{\Psi}$ which can be considered a generalization of the one in (1.19).

Now we proceed to discuss the unisolvance for the bilinear and the rotated Q_1 IFE functions, i.e., the invertibility of the matrix in (2.32), which can always be guaranteed with a suitable choice for F through this proposed new construction procedure. The discussion for unisolvance of the linear IFE functions will be left to Remark 2.4 below.

First, for the rotated Q_1 IFE functions in Case 1 as illustrated in Figure 2.7(a), we note that there is no $\mathbf{c}_i,\ i \in \mathcal{I}^-$ coefficients in the formulation (2.24) and $\mathbf{c}_0$ is uniquely determined by (2.29), and this means that the unisolvence for this case is always guaranteed. To discuss other cases, we define two parameters d and e for describing the interface-element intersection points D and E for those typical rectangular interface elements illustrated in Figures 2.6-2.7:

- We let $d = \|D - A_1\|/h,\ e = \|E - A_1\|/h$ for **Case 1** in Figure 2.6 and $d = \|D - M_1\|/h,\ e = \|E - M_1\|/h$ for **Case 2** and **Case 3** in Figure 2.7.
- We let $d = \|D - A_1\|/h,\ e = \|E - A_3\|/h$ for **Case 2** in Figure 2.6 and $d = \|D - M_1\|/h,\ e = \|E - M_3\|/h$ for **Case 4** and **Case 5** in Figure 2.7.

We start from some estimates for the following two auxiliary functions:

$$g_n(X) = \sum_{i\in\mathcal{I}^-} L(A_i)\nabla\psi_{i,T}(X)\cdot\bar{\mathbf{n}}, \qquad g_t(X) = \sum_{i\in\mathcal{I}^-} L(A_i)\nabla\psi_{i,T}(X)\cdot\bar{\mathbf{t}}, \tag{2.34}$$

where $\psi_{i,T}$ are standard bilinear or rotate Q_1 scalar Lagrange type shape functions.

Lemma 2.5. *On each rectangular interface element $T \in \mathcal{T}_h^i$, let $F_0 = t_0 D + (1-t_0)E$ such that*

- *when it is a bilinear element in* ***Case 1*** *illustrated in Figure 2.6, assume* $t_0 = e/(d+e)$,
- *when it is a bilinear element in* ***Case 2*** *illustrated in Figure 2.6, assume* $t_0 = 1 - e$ *if* $d \geqslant e$, $t_0 = 1 - d$ *if* $e > d$,
- *when it is a rotated* Q_1 *element in* ***Case 2*** *or* ***Case 3*** *illustrated in Figure 2.7, assume* $t_0 = 1$ *when* $d \geqslant e$ *or* $t_0 = 0$ *when* $e > d$,
- *when it is a rotated* Q_1 *element in* ***Case 4*** *or* ***Case 5*** *illustrated in Figure 2.7, assume* $t_0 = 1/2$.

Then

$$(1 - g_n(F_0))^2 - g_t^2(F_0) \geqslant 0, \quad g_n^2(F_0) - g_t^2(F_0) \geqslant 0, \tag{2.35a}$$
$$g_n(F_0) \in [0, 1], \quad g_t(F_0) \in [-1, 1]. \tag{2.35b}$$

Proof. **Bilinear elements**:
Case 1. By direct calculation, we have

$$g_n^2(F_0) - g_t^2(F_0) = \frac{4d^3e^3(d + e - de)^2}{(d^2 + e^2)^2(d + e)^2} \geqslant 0;$$
$$(1 - g_n(F_0))^2 - g_t^2(F_0) = \frac{-d^2e^2(e^2(1 - d) - d^2(1 - e))^2 + (e^2(1 - d) + d^2(1 - e + e^2))^2(d + e)^2}{(d^2 + e^2)^2(d + e)^2} \geqslant 0.$$

Case 2. Because of the symmetry, we assume $d \geqslant e$ and take $t_0 = 1 - e$.

$$\begin{aligned} & g_n^2(F_0) - g_t^2(F_0) \\ =& \frac{1}{(1 + d^2 - 2de + e^2)^2}(-(2d^2(-1 + e) + d(1 + 2e - 4e^2) + e(-1 + 2e^2))^2 \\ & + (d^3(-1 + e) + d^2(1 + 2e - 3e^2) - e^2(-2 + e^2) + d(1 - 3e - e^2 + 3e^3))^2) \geqslant 0; \\ & (1 - g_n(F_0))^2 - g_t^2(F_0) \\ =& \frac{1}{(1 + d^2 - 2de + e^2)^2}(-(2d^2(-1 + e) + d(1 + 2e - 4e^2) + e(-1 + 2e^2))^2 \\ & + (-1 + d^3(-1 + e) + d^2(2 - 3e)e + e^2 - e^4 + d(1 - e - e^2 + 3e^3))^2) \geqslant 0. \end{aligned}$$

Rotated Q_1 elements:

Case 1. As shown by Figure 2.7, this case is trivial since there are no unknown coefficients involved.

Case 2. Note that $1 \geqslant d \geqslant 1/2 \geqslant e \geqslant 0$. Then

$$\begin{aligned}
g_n^2(F_0) - g_t^2(F_0) =& \frac{(e-2de)^2(4d^3-4d^4-3e^2-4de(2+e)+d^2(3+16e+4e^2))}{4(d^2+e^2)^2} \geqslant 0;\\
(1-g_n(F_0))^2 - g_t^2(F_0) =& \frac{1}{4(d^2+e^2)^2}(32d^5e^2-16d^6e^2-3e^4+24de^4+d^2e^2(7+32e-8e^2)\\
&+8d^3e(1+e-12e^2-4e^3)+4d^4(1-4e-6e^2+16e^3+4e^4)) \geqslant \frac{1}{4}.
\end{aligned}$$

Case 3. Note that $1 \geqslant d \geqslant e \geqslant 1/2$. Then

$$\begin{aligned}
g_n^2(F_0) - g_t^2(F_0) =& \frac{1}{4(d^2+e^2)^2}(8d^5-4d^6+8d(-1+e)e^3-3e^4-8d^3e(1+6e)\\
&+2d^2e^2(13+4e-2e^2)+d^4(-3+8e+24e^2)) \geqslant 0;\\
(1-g_n(F_0))^2 - g_t^2(F_0) =& \frac{1}{4(d^2+e^2)^2}(8d^5-4d^6+8d^3(1-6e)e-3e^4+8de^3(1+e)\\
&-2d^2e^2(-13+4e+2e^2)+d^4(-3-8e+24e^2)) \geqslant \frac{1}{4}.
\end{aligned}$$

Case 4. Note that $1 \geqslant d \geqslant 1/2 \geqslant e \geqslant 0$. Then

$$\begin{aligned}
g_n^2(F_0) - g_t^2(F_0) =& \frac{1}{4(1+d^2-2de+e^2)^2}(-d^6+2d^5(1+e)+d^4(10-6e+e^2)\\
&-4d^3(4+2e-e^2+e^3)+d^2(11+24e-12e^2+4e^3+e^4)\\
&+e(6+3e-8e^2+2e^3+2e^4-e^5)\\
&+2d(-1-9e+4e^3-3e^4+e^5)) \geqslant \frac{1}{16};\\
(1-g_n(F_0))^2 - g_t^2(F_0) =& \frac{1}{4(1+d^2-2de+e^2)^2}(-d^6+2d^5(1+e)+d^4(2-6e+e^2)\\
&-4d^3(2-2e-e^2+e^3)+d^2(3-12e^2+4e^3+e^4)\\
&+2d(3-9e+12e^2-4e^3-3e^4+e^5)\\
&-e(2-11e+16e^2-10e^3-2e^4+e^5)) \geqslant \frac{1}{16}.
\end{aligned}$$

Case 5. Note that $1/2 \geqslant d \geqslant 0$ and $1/2 \geqslant e \geqslant 0$. Then

$$\begin{aligned}
g_n^2(F_0) - g_t^2(F_0) =& \frac{(d^2+2d(-1+e)+(-2+e)e)^2(1-(d-e)^2)}{4(1+d^2-2de+e^2)^2} \geqslant 0;\\
(1-g_n(F_0))^2 - g_t^2(F_0) =& \frac{1}{4(1+d^2-2de+e^2)^2}(-(d^3+d^2(-2+e)-de^2-(-2+e)e^2)^2\\
&+(2+3d^2-2e+3e^2-2d(1+e))^2) \geqslant \frac{1}{4}.
\end{aligned}$$

These estimates lead to (2.35a). For (2.35b), the first inequality is just a special case of Lemma 5.1 in [79] and the second inequality is a consequence of (2.35a). □

Lemma 2.6. *The matrix in the linear system* (2.32) *is non-singular if and only if the follwoing matrix is non-singular:*

$$\Xi(F) = \mathcal{P}^- + \begin{bmatrix} (\hat{\lambda}+2\hat{\mu})g_n(F) & \hat{\lambda}g_t(F) \\ \hat{\mu}g_t(F) & \hat{\mu}g_n(F) \end{bmatrix}. \tag{2.36}$$

Proof. Note that the matrix in (2.32) is in a generalized *Sherman-Morrison* format. Since $\overline{K}$ is invertible, the linear system (2.32) is non-singular if and only if the matrix

$$I_2 + \overline{\Psi}^{-T}\overline{K}^{-1}\overline{L} = I_2 + \sum_{j\in\mathcal{I}^-} L(A_j)\overline{\Psi}_j^T K^{-1} = (K + \sum_{j\in\mathcal{I}^-} L(A_j)\overline{\Psi}_j)K^{-1} \tag{2.37}$$

is invertible. Then by using (2.28), we can directly verify that

$$Q(K + \sum_{j\in\mathcal{I}^-} L(A_j)\overline{\Psi}_j)Q^T = P^- + \begin{bmatrix} (\hat{\lambda}+2\hat{\mu})g_n(F) & \hat{\lambda}g_t(F) \\ \hat{\mu}g_t(F) & \hat{\mu}g_n(F) \end{bmatrix} \tag{2.38}$$

which leads to the conclusion of this lemma because Q is invertible. □

Lemma 2.7. *With the F_0 specified in Lemma 2.5, we have*

$$Det(\Xi(F_0)) > 2\left(\min\{\mu^+,\mu^-\}\right)^2. \tag{2.39}$$

Proof. By (2.36) and direct calculations, we have

$$\begin{aligned} \mathrm{Det}(\Xi(F_0)) =& \lambda^+\mu^+(g_n^2 - g_t^2) + \lambda^-\mu^-((1-g_n)^2 - g_t^2) \\ &+ \lambda^-\mu^+((1-g_n)g_n + g_t^2) + \lambda^+\mu^-(g_n(1-g_n) + g_t^2) \\ &+ 2(\mu^+)^2 g_n^2 + 2(\mu^-)^2(1-g_n)^2 + 4\mu^+\mu^-(1-g_n)g_n, \end{aligned}$$

in which $g_n = g_n(F_0)$ and $g_t = g_t(F_0)$. Then, applying estimates in Lemma 2.5 to the above, we have $\mathrm{Det}(\Xi(F_0)) \geqslant 2(\mu^+)^2 g_n^2 + 2(\mu^-)^2(1-g_n)^2 > 2\left(\min\{\mu^+,\mu^-\}\right)^2$. □

Finally we can prove the main theorem in this section.

Theorem 2.1 (Unisolvence)**.** *Let $T \in \mathcal{T}_h^i$ be a rectangular interface element with $F = F_0$ specified in Lemma 2.5. Then given any vector $\mathbf{v} \in \mathbb{R}^{2|\mathcal{I}^-|\times 1}$, for the bilinear and rotated Q_1 elements, there exists one and only one IFE shape function satisfying* (2.20)-(2.23)*.*

Proof. The proof directly follows from Lemma 2.6 and Lemma 2.7. □

Remark 2.2. *According to the generalized Sherman-Morrison formula and* (2.37), (2.38)*, we can give an analytical formula for the coefficients* $\mathbf{c}$ *in* (2.32) *as*

$$\begin{aligned} \mathbf{c} =& \overline{K}^{-1}\mathbf{b} - \overline{K}^{-1}\overline{L}(I_2 + \overline{\Psi}^{-T}\overline{K}^{-1}\overline{L})^{-1}\overline{\Psi}^{-T}\overline{K}^{-1}\mathbf{b} \\ =& \overline{K}^{-1}\mathbf{b} - \overline{K}^{-1}\overline{L}KQ^T\Xi^{-1}Q\overline{\Psi}^{-T}\overline{K}^{-1}\mathbf{b}. \end{aligned} \tag{2.40}$$

Here it is important to note that $\overline{K}$ is a diagonal block matrix formed only by the 2-by-2 matrix K and Ξ is also a 2-by-2 matrix so that their inverses are easy to calculate analytically. Hence, if preferred, there is no need to solve any algebraic systems for $\mathbf{c}$ numerically because of (2.40).

Remark 2.3. *When $F = (D + E)/2$, the linear and bilinear IFE shape functions given by* (2.24) *with the coefficients determined by* (2.29) *and* (2.32) *coincide with those in [153]. In this case, the unisolvence can be only conditionally guaranteed and an example of interface element configuration is given in [153] to demonstrate this.*

Remark 2.4. *For the linear IFE functions, because each side in* (2.22) *is a constant vector which is therefore independent of the location of F, the new construction procedure proposed above is the same as the one considered in [77, 153], i.e., the one in Remark 2.3, regardless of the choice of F_0. In this case, the authors in [153] constructed a specific interface element configuration such that the conforming linear IFE shape functions can not be uniquely determined by the Lagrange type degrees of freedom, i.e., the nodal values. They also showed that the unisolvance can be conditionally guaranteed by some assumptions on the Lamé parameters (Theorem 4.7 in [153]). The immersed nonconforming linear elements, i.e., the linear Crouzeix-Raviart IFE elements, also have a conditional unisolvence, which can be discussed similarly as Theorem 4.7 in [153].*

Remark 2.5. *For the bilinear and rotated Q_1 elements, the unisolvence of the IFE shape functions depends on suitable choices of the point F_0 stated in Lemma 2.5. It is easy to see that a small perturbation of a suitable choice of $F = F_0$ given in Lemma 2.5 can also yield $\det(\Xi(F)) > 0$ since the $\Xi(F)$ in* (2.36) *is a continuous function of F for a fixed interface location in an element. This means that the choice of F_0 is not unique and Lemma 2.5 only provides sufficient conditions for the unisolvence. We also note that, because of the continuous dependence of $\mathbf{c}$ given in* (2.40) *and $\mathbf{c}_0$ given in* (2.29) *on F, a small perturbation of $F = F_0$ should lead to a small change of the coefficients, and thus the corresponding IFE shape functions will not change much.*

Remark 2.6. *We note that the construction approach above and the resulted formulas are similar to the one reviewed in Section 1.2 for the scalar elliptic interface problems. We also emphasize that here the two polynomial components in an IFE function are partitioned by the line connecting the intersection points of the interface and element boundary instead of the interface itself in Section 1.2. This is to maintain the continuity of IFE functions on interface elements which can be considered as one advantage of lower-degree IFE methods. We also note that this property is difficult, if not impossible, to obtain for higher-degree IFE methods.*

By taking the nodal value vector $\mathbf{v}$ to be unit vectors, we construct the IFE shape functions satisfying the weak jump conditions (2.21)-(2.22) and the following nodal value constraints:

$$\boldsymbol{\phi}_{i,T}(A_j) = \begin{cases} \delta_{i,j}, \\ 0, \end{cases} \quad i = 1, \cdots, |\mathcal{I}|, \text{ and } \boldsymbol{\phi}_{i,T}(A_j) = \begin{cases} 0, \\ \delta_{i-|\mathcal{I}|,j}, \end{cases} \quad i = |\mathcal{I}| + 1, \cdots, 2|\mathcal{I}|. \tag{2.41}$$

The local IFE spaces on interface elements $T \in \mathcal{T}_h^i$ are then defined as

$$\mathbf{S}_h(T) = \text{Span}\{\boldsymbol{\phi}_{i,T},\ \boldsymbol{\phi}_{i+|\mathcal{I}|,T} : i \in \mathcal{I}\}. \tag{2.42}$$

The local IFE spaces defined by (2.19) and (2.42) can be used to construct an IFE space over the whole domain Ω according to the need of a finite element scheme. For example, in this chapter, by enforcing the continuity at the mesh nodes, we can consider the following global IFE space:

$$\begin{aligned}\mathbf{S}_h(\Omega) =& \big\{\mathbf{v} \in [L^2(\Omega)]^2 : \mathbf{v}|_T \in \mathbf{S}_h(T) \ \ \forall T \in \mathcal{T}_h; \\ & \mathbf{v}|_{T_1}(N) = \mathbf{v}|_{T_2}(N)\ \forall N \in \mathcal{N}_h,\ \forall T_1, T_2 \in \mathcal{T}_h \text{ such that } N \in \partial T_1 \cap \partial T_2\big\}.\end{aligned} \tag{2.43}$$

2.4.2 Properties of IFE Shape Functions

In this subsection, we present some fundamental properties of the proposed IFE shape functions. We tacitly assume that, on each interface element $T \in \mathcal{T}_h^i$, $\boldsymbol{\phi}_{i,T}, 1 \le i \le 2|\mathcal{I}|$ are the bilinear or the rotated Q_1 IFE shape functions constructed according to Theorem 2.1 or they are the conforming/non-conforming linear IFE shape functions which uniquely exist according to their degrees of freedom under some conditions on the Lamé parameters, see Remark 2.4.

Theorem 2.2 (Boundedness)**.** *There exists a constant C such that the following estimates are valid for IFE shape functions on each interface element T:*

$$|\boldsymbol{\phi}_{i,T}|_{W^{k,\infty}(T)} \leqslant Ch^{-k}, \quad k = 0, 1, 2, \quad 1 \le i \le 2|\mathcal{I}|, \quad \forall T \in \mathcal{T}_h^i. \tag{2.44}$$

Proof. For the bilinear or the rotated Q_1 IFE shape functions, we note that (2.28) yields $\|\overline{K}\| \leqslant C$. And (2.31a) shows $\|\overline{L}\| \leqslant Ch$ because $|L|_{0,\infty,T} \leqslant Ch$, and $\|\overline{\Psi}^s\| \leqslant Ch^{-1}$. So we have $\|\mathbf{b}\| \leqslant C$, of which the constants C only depend on Lamé parameters. Next (2.35b) and (2.39) suggest $\|\Xi^{-1}\| \leqslant C$. So by the formula (2.40), we have $\|\mathbf{c}\| \leqslant C$ and then use (2.29) to show $\|\mathbf{c}_0\| \leqslant Ch^{-1}$. Therefore $\|\mathbf{c}_0 L\|_{0,\infty,T} \leqslant C$ and $|\mathbf{c}_0 L|_{1,\infty,T} \leqslant Ch^{-1}$ because $|L|_{0,\infty,T} \leqslant Ch$ and $|L|_{1,\infty,T} \leqslant C$. In addition, it is easy to see $|\mathbf{c}_0 L|_{2,\infty,T} = 0$, since L is a linear function. Finally, applying these estimates and (2.4) to (2.24) leads to (2.44). Similar arguments can be used for the linear IFE shape functions. □

Remark 2.7. *Because the estimates in* (2.4) *also hold on each patch ω_T associated with an interface element T, we can extend* (2.44) *to the patch:*

$$|\boldsymbol{\phi}_{i,T}|_{W^{k,\infty}(\omega_T)} \leqslant Ch^{-k}, \quad k = 0, 1, 2, \quad 1 \le i \le 2|\mathcal{I}|. \tag{2.45}$$

For simplicity of presentation, we will use the following matrix shape functions:

$$\Phi_{i,T}(X) = \left[\boldsymbol{\phi}_{i,T}(X),\ \boldsymbol{\phi}_{i+|\mathcal{I}|,T}(X)\right], \quad i \in \mathcal{I}. \tag{2.46}$$

Theorem 2.3 (Partition of Unity)**.** *On each interface element $T \in \mathcal{T}_h^i$, we have*

$$\sum_{i\in\mathcal{I}} \Phi_{i,T}(X) = I_2, \quad \sum_{i\in\mathcal{I}} \partial_{x_j}\Phi_{i,T}(X) = \mathbf{0}_{2\times 2}, \quad \sum_{i\in\mathcal{I}} \partial_{x_jx_k}\Phi_{i,T}(X) = \mathbf{0}_{2\times 2}, \quad j,k = 1,2. \tag{2.47}$$

Proof. By direct verifications, we can see that vector functions $\boldsymbol{\phi}^1 = (1,0)^T$ and $\boldsymbol{\phi}^2 = (0,1)^T$ satisfy the weak jump conditions (2.21) and (2.22) exactly; hence, they are in the IFE space $\mathbf{S}_h(T)$. Then the unisolvence of the IFE function leads to the first identity in (2.47). And the second and third identity in (2.47) are just the derivatives of the first one. □

Remark 2.8. *The first identity in* (2.47) *was proved in [153] for the linear and bilinear IFE shape functions by direct verifications.*

Recall that $\bar{\mathbf{n}} = (\bar{n}_1, \bar{n}_2)^T$ and $\bar{\mathbf{t}} = (\bar{n}_2, -\bar{n}_1)^T$ are normal and tangential vectors to the line l. We introduce the following matrices:

$$\overline{N}^s = \begin{bmatrix} (\lambda^s + 2\mu^s)\bar{n}_1 & \mu^s\bar{n}_2 & \mu^s\bar{n}_2 & \lambda^s\bar{n}_1 \\ \lambda^s\bar{n}_2 & \mu^s\bar{n}_1 & \mu^s\bar{n}_1 & (\lambda^s + 2\mu^s)\bar{n}_2 \\ -\bar{n}_2 & 0 & \bar{n}_1 & 0 \\ 0 & -\bar{n}_2 & 0 & \bar{n}_1 \end{bmatrix}, \quad s = \pm. \tag{2.48}$$

It can be directly verified that

$$\mathrm{Det}(\overline{N}^s) = \mu^s(\lambda^s + 2\mu^s), \quad s = \pm, \tag{2.49}$$

which shows the matrices $\overline{N}^s$ are non-singular. We can use these matrices to define

$$\overline{M}^- = \left(\overline{N}^+\right)^{-1}\overline{N}^-, \qquad \overline{M}^+ = \left(\overline{N}^-\right)^{-1}\overline{N}^+. \tag{2.50}$$

The motivation for us to introduce/construct these matrices is that they can be used to connect the two polynomial components in an IFE function in the following sense.

Lemma 2.8. *For IFE functions satisfying* (2.21)-(2.22)*, there hold*

$$\mathrm{Vec}(\nabla\boldsymbol{\phi}_T^+(F)) = \overline{M}^-\mathrm{Vec}(\nabla\boldsymbol{\phi}_T^-(F)), \qquad \mathrm{Vec}(\nabla\boldsymbol{\phi}_T^-(F)) = \overline{M}^+\mathrm{Vec}(\nabla\boldsymbol{\phi}_T^+(F)). \tag{2.51}$$

Proof. Let $\boldsymbol{\phi}_T = (\phi_T^1, \phi_T^2)^T$. By direction calculations, for $s = \pm$, we have

$$\sigma^s(\boldsymbol{\phi}_T(F))\,\bar{\mathbf{n}} = \begin{bmatrix} (\lambda^s + 2\mu^s)\bar{n}_1\partial_{x_1}\phi_T^{1,s} + \mu^s\bar{n}_2\partial_{x_2}\phi_T^{1,s} + \mu^s\bar{n}_2\partial_{x_1}\phi_T^{2,s} + \lambda^s\bar{n}_1\partial_{x_2}\phi_T^{2,s} \\ \lambda^s\bar{n}_2\partial_{x_1}\phi_T^{1,s} + \mu^s\bar{n}_1\partial_{x_2}\phi_T^{1,s} + \mu^s\bar{n}_1\partial_{x_1}\phi_T^{2,s} + (\lambda^s + 2\mu^s)\bar{n}_2\partial_{x_1}\phi_T^{2,s} \end{bmatrix}. \tag{2.52}$$

From the continuity jump condition, we have $\nabla\phi_T^{i,+}\,\bar{\mathbf{t}} = \nabla\phi_T^{i,-}\,\bar{\mathbf{t}}$, $i = 1,2$. Combining this with the stress jump condition (2.52) leads to

$$\overline{N}^-\mathrm{Vec}(\nabla\boldsymbol{\phi}_T^-(F)) = \overline{N}^+\mathrm{Vec}(\nabla\boldsymbol{\phi}_T^+(F))$$

from which we have (2.51) because of (2.50). □

Now, using these matrices, we consider the following 2-by-4 matrix functions:

$$\Lambda_-(X) = \sum_{i\in\mathcal{I}} \left((A_i - X)^T \otimes (\Phi^-_{i,T}(X))\right) + \sum_{i\in\mathcal{I}^+} \left((A_i - \overline{X}_i)^T \otimes (\Phi^-_{i,T}(X))\right)(\overline{M}^- - I_4), \quad (2.53a)$$

$$\Lambda_+(X) = \sum_{i\in\mathcal{I}} \left((A_i - X)^T \otimes (\Phi^+_{i,T}(X))\right) + \sum_{i\in\mathcal{I}^-} \left((A_i - \overline{X}_i)^T \otimes (\Phi^+_{i,T}(X))\right)(\overline{M}^+ - I_4), \quad (2.53b)$$

where $\overline{X}_i$, $i \in \mathcal{I}$ are arbitrary points on l, and we further use them to define

$$\Lambda^+(X) = \Lambda_+(X), \quad \Lambda^-(X) = \Lambda_-(X)\overline{M}^+. \quad (2.54)$$

First we show that both $\Lambda^-(X)$ and $\Lambda^+(X)$ are well defined, i.e., they are independent of $\overline{X}_i \in l$, $i \in \mathcal{I}$.

Lemma 2.9. *The matrix functions $\Lambda^-(X)$ and $\Lambda^+(X)$ are independent of the points $\overline{X}_i \in l$, $i \in \mathcal{I}$.*

Proof. Denote the vectors $\alpha_1 = [-\bar{n}_2, 0, \bar{n}_1, 0]^T$ and $\alpha_2 = [0, -\bar{n}_2, 0, \bar{n}_1]^T$. It can be directly verified that they are eigenvectors of $\left(\overline{M}^s\right)^T$, $s = +$, or $-$, i.e.,

$$\left(\overline{M}^s\right)^T \alpha_i = \alpha_i, \quad i = 1, 2. \quad (2.55)$$

Let $\overline{X}_i$ and $\overline{X}'_i$ be two points on l. Then, by (2.55), we have

$$\begin{aligned} &\left((A_i - \overline{X}_i)^T \otimes (\Phi^s_i(X))\right)(\overline{M}^s - I_4) - \left((A_i - \overline{X}'_i)^T \otimes (\Phi^s_i(X))\right)(\overline{M}^s - I_4) \\ =&\|\overline{X}_i - \overline{X}'_i\| \left[\Phi^s_i, \Phi^s_i\right] \ [\alpha_1, \alpha_2]\,(\overline{M}^s - I_4) = \mathbf{0}, \quad s = \pm, \end{aligned} \quad (2.56)$$

Hence, by (2.53)-(2.54), functions $\Lambda^-(X)$ and $\Lambda^+(X)$ are independent of $\overline{X}_i$, $i \in \mathcal{I}$. □

Lemma 2.9 allows us to consolidate $\overline{X}_i$, $i \in \mathcal{I}$ in $\Lambda^-(X)$ and $\Lambda^+(X)$ into a single point $\overline{X} \in l$. So, by using (2.47), we rewrite these two functions as follows:

$$\Lambda^-(X) = \sum_{i\in\mathcal{I}^-} (A_i - \overline{X})^T \otimes \Phi^-_i(X)\overline{M}^+ + \sum_{i\in\mathcal{I}^+} (A_i - \overline{X})^T \otimes \Phi^-_i(X) - \left((X - \overline{X})^T \otimes I_2\right)\overline{M}^+. \quad (2.57a)$$

$$\Lambda^+(X) = \sum_{i\in\mathcal{I}^-} (A_i - \overline{X})^T \otimes \Phi^+_i(X)\overline{M}^+ + \sum_{i\in\mathcal{I}^+} (A_i - \overline{X})^T \otimes \Phi^+_i(X) - (X - \overline{X})^T \otimes I_2. \quad (2.57b)$$

For every fixed $\overline{X}$, we consider the following piecewise 2-by-4 matrix function:

$$V(X) = \begin{cases} (X - \overline{X})^T \otimes I_2 & \text{if } X \in \hat{T}^+, \\ \left((X - \overline{X})^T \otimes I_2\right)\overline{M}^+ & \text{if } X \in \hat{T}^-. \end{cases} \quad (2.58)$$

To simplify the presentation, in the following discussions, we adopt the notations $\partial_{x_k} = \frac{\partial}{\partial_{x_k}}$, $k = 1, 2$, for partial derivatives with respect to $x_1 = x,\ x_2 = y$.

Lemma 2.10. *On every interface element $T \in \mathcal{T}_h^i$, each column of $V(X)$ is in the local IFE space $\mathbf{S}_h(T)$.*

Proof. Clearly, each column of $V(X)$ restricted on either $\hat{T}^+$ or $\hat{T}^-$ is in the corresponding polynomial space $\mathbf{\Pi}_T$. Furthermore, we note that $V^-(\overline{X}) = V^+(\overline{X})$ and

$$\begin{bmatrix} \partial_{x_1} V^+ \\ \partial_{x_2} V^+ \end{bmatrix} = I_4 = \overline{M}^+ \overline{M}^- = \begin{bmatrix} \partial_{x_1} V^- \\ \partial_{x_2} V^- \end{bmatrix} \overline{M}^-,$$

which, together with the fact $d(V) = 0_{2\times 4}$, shows each column of V satisfies (2.21) and (2.22) simultaneously; thus, it is in the corresponding IFE space. □

Theorem 2.4. *For every interface element $T \in \mathcal{T}_h$, we have the identities $\Lambda_+ = 0_{2\times 4}$ and $\Lambda_- = 0_{2\times 4}$. And let $I^1 = [I_2, 0_{2\times 2}]$, $I^2 = [0_{2\times 2}, I_2]$, for $j, k = 1, 2$, $s = \pm$, we also have*

$$\sum_{i\in\mathcal{I}} \left((A_i - X)^T \otimes (\partial_{x_j} \Phi_i^s(X))\right) + \sum_{i\in\mathcal{I}^{s'}} \left((A_i - \overline{X}_i)^T \otimes (\partial_{x_j} \Phi_i^s(X))\right) (\overline{M}^s - I_4) = I^j, \quad (2.59a)$$

$$\sum_{i\in\mathcal{I}} \left((A_i - X)^T \otimes (\partial_{x_j x_k} \Phi_i^s(X))\right) + \sum_{i\in\mathcal{I}^{s'}} \left((A_i - \overline{X}_i)^T \otimes (\partial_{x_j x_k} \Phi_i^s(X))\right) (\overline{M}^s - I_4) = 0_{2\times 4}. \quad (2.59b)$$

Proof. We construct a piecewise 2-by-4 matrix function:

$$\Lambda(X) = \begin{cases} \Lambda^-(X) & \text{if } X \in \hat{T}^-, \\ \Lambda^+(X) & \text{if } X \in \hat{T}^+. \end{cases} \quad (2.60)$$

According to (2.57b) and (2.57a), the first two terms in $\Lambda^-(X)$ and $\Lambda^+(X)$ are the linear combination of the IFE shape functions with the same coefficients. Lemma 2.10 shows that their last terms together form a function in the local IFE space. So each column of the piecewise matrix function (2.60) belongs to $\mathbf{S}_h(T)$ for every interface element T. In addition, by (2.53b) and (2.53a), we can see that $\Lambda(A_i) = 0_{2\times 4}$, $i \in \mathcal{I}$. Hence, by the unisolvence of IFE functions, we know that each column of $\Lambda(X)$ must be $0_{2\times 1}$ which leads to $\Lambda_\pm(X) = 0_{2\times 4}$ because $\overline{M}^+$ is non-singular. Furthermore, (2.59a) and (2.59b) can be obtained by differentiating (2.53b) and (2.53a). □

2.5 Approximation Capabilities

In this section, we show optimal approximation capabilities of the proposed IFE spaces by estimating the errors of the Lagrange type interpolation. Again, we assume the conditions for the unisolvence of IFE shape functions are satisfied, i.e., $F = F_0$ given in Lemma 2.5 in

the construction of the bilinear and rotated Q_1 IFE shape functions and the conditions on Lamé parameters are satisfied, see Remark 2.4, in the construction of the conforming/non-confomring linear IFE shape functions.

The local Lagrange type interpolation operator on each element T: $I_{h,T} : \mathbf{C}^0(T) \to \mathbf{S}_h(T)$ is defined as

$$I_{h,T}\mathbf{u}(X) = \begin{cases} \sum_{i\in\mathcal{I}} \Psi_{i,T}(X)\mathbf{u}(A_i), & \text{if } T \in \mathcal{T}_h^n, \\ \sum_{i\in\mathcal{I}} \Phi_{i,T}(X)\mathbf{u}(A_i), & \text{if } T \in \mathcal{T}_h^i, \end{cases} \quad \forall \mathbf{u} \in \mathbf{C}^0(T). \tag{2.61}$$

The global interpolation operator I_h on $\mathbf{C}^0(\Omega)$ can be defined by a usual piecewise mannar such that

$$(I_h\mathbf{u})|_T = I_{h,T}\mathbf{u}, \quad \forall T \in \mathcal{T}_h, \quad \forall \mathbf{u} \in \mathbf{C}^0(\Omega). \tag{2.62}$$

Applying the standard scaling argument [35, 55, 171] to each component of the vector function $\mathbf{u} = (u_1, u_2)^T \in \mathbf{H}^2(T)$, we can show that

$$\begin{aligned} \|I_{h,T}\mathbf{u} - \mathbf{u}\|_{L^2(T)} + h|I_{h,T}\mathbf{u} - \mathbf{u}|_{H^1(T)} + h^2|I_{h,T}\mathbf{u} - \mathbf{u}|_{H^2(T)} \\ \leqslant Ch^2|\mathbf{u}|_{H^2(T)}, \qquad i = 1, 2, \quad \forall\ T \in \mathcal{T}_h^n. \end{aligned} \tag{2.63}$$

However, on interface elements $T \in \mathcal{T}_h^i$, because of the jump conditions (1.11a) and (1.11b), the two components of $\mathbf{u}$ have to be treated together. To estimate the errors in $I_{h,T}\mathbf{u}$, we will use the technique of the multipoint Taylor expansions. In particular, we extend the approach in [79] to the proposed IFE spaces of vector functions.

2.5.1 Multipoint Taylor Expansions

We start by introducing the following quantities related to the interface curve and giving some useful estimates for them. These quantities and estimates are extensions of those developed in [79] for scalar functions. Let T be an interface element with its associated patch ω_T. Let $\mathbf{n}(\widetilde{X}) = (\tilde{n}_1(\widetilde{X}), \tilde{n}_2(\widetilde{X}))^T$ and $\mathbf{t}(\widetilde{X}) = (\tilde{n}_2(\widetilde{X}), -\tilde{n}_1(\widetilde{X}))^T$ be the normal and tangential vectors of Γ at a point $\widetilde{X} \in \Gamma \cap \omega_T$, respectively. For $s = \pm$, consider the following matrices which are the continuous counterparts of the (2.48) defined on the curve:

$$N^s(\widetilde{X}) = \begin{bmatrix} (\lambda^s + 2\mu^s)\tilde{n}_1(\widetilde{X}) & \mu^s\tilde{n}_2(\widetilde{X}) & \mu^s\tilde{n}_2(\widetilde{X}) & \lambda^s\tilde{n}_1(\widetilde{X}) \\ \lambda^s\tilde{n}_2(\widetilde{X}) & \mu^s\tilde{n}_1(\widetilde{X}) & \mu^s\tilde{n}_1(\widetilde{X}) & (\lambda^s + 2\mu^s)\tilde{n}_2(\widetilde{X}) \\ -\tilde{n}_2(\widetilde{X}) & 0 & \tilde{n}_1(\widetilde{X}) & 0 \\ 0 & -\tilde{n}_2(\widetilde{X}) & 0 & \tilde{n}_1(\widetilde{X}) \end{bmatrix}. \tag{2.64}$$

Similar to (2.49), by straightforward calculations, we have

$$\mathrm{Det}(N^s(\widetilde{X})) = \mu^s(\lambda^s + 2\mu^s), \quad s = \pm. \tag{2.65}$$

Hence the matrices $N^s(\widetilde{X})$, $s=\pm$, are non-singular, and we can define

$$M^-(\widetilde{X}) = \left(N^+(\widetilde{X})\right)^{-1} N^-(\widetilde{X}), \qquad M^+(\widetilde{X}) = \left(N^-(\widetilde{X})\right)^{-1} N^+(\widetilde{X}). \tag{2.66}$$

These matrices can be used to transfer the exact solutions across the interface curve in the following sense.

Lemma 2.11. *For every $\mathbf{u} \in \mathbf{PC}^2(\omega_T)$ and $\widetilde{X} \in \Gamma \cap \omega_T$, there hold*

$$\mathrm{Vec}(\nabla \mathbf{u}^+(\widetilde{X})) = M^-(\widetilde{X})\mathrm{Vec}(\nabla \mathbf{u}^-(\widetilde{X})), \quad \mathrm{Vec}(\nabla \mathbf{u}^-(\widetilde{X})) = M^+(\widetilde{X})\mathrm{Vec}(\nabla \mathbf{u}^+(\widetilde{X})). \tag{2.67}$$

Proof. The derivation is the same as Lemma 2.8. □

Next, as proved in the following lemma, the matrices $\overline{M}^s$ constructed on l can be used to approximate the matrices M^s constructed on the interface $\Gamma \cap \omega_T$, $s = +$ or $-$.

Lemma 2.12. *There exists a constant C such that for every interface element $T \in \mathcal{T}_h^i$ and every point $\widetilde{X} \in \Gamma \cap \omega_T$, we have*

$$\|M^s(\widetilde{X})\| \leqslant C, \qquad \|\overline{M}^s\| \leqslant C, \quad s=\pm, \tag{2.68}$$

and

$$\|M^s(\widetilde{X}) - \overline{M}^s\| \leqslant Ch, \quad s=\pm. \tag{2.69}$$

Proof. We only prove the case for $s=-$, and the argument for $s=+$ is similar. Since $\|\bar{\mathbf{n}}\| = 1$ and $\|\mathbf{n}(\widetilde{X})\| = 1$, we have $\|\overline{N}^-\| \leqslant C$ and $\|N^-(\widetilde{X})\| \leqslant C$. Besides, we note that

$$\| \left(N^+(\widetilde{X})\right)^{-1} \| = \frac{1}{\mathrm{Det}(N^+(\widetilde{X}))} \|\mathrm{adj}(N^+(\widetilde{X}))\| \leqslant C,$$

$$\| \left(\overline{N}^+\right)^{-1} \| = \frac{1}{\mathrm{Det}(\overline{N}^+)} \|\mathrm{adj}(\overline{N}^+)\| \leqslant C,$$

because $\mathrm{Det}(N^-(\widetilde{X})) = \mathrm{Det}(\overline{N}^-) = \mu^-(\lambda^- + 2\mu^-)$ and each term of the adjugate matrices is bounded by some constants C. Then, (2.68) follows from applying these estimates in the inequalities below:

$$\|M^-(\widetilde{X})\| \leqslant \| \left(N^+(\widetilde{X})\right)^{-1} \| \, \|N^-(\widetilde{X})\| \quad \text{and} \quad \|\overline{M}^-\| \leqslant \| \left(\overline{N}^+\right)^{-1} \| \, \|\overline{N}^-\|.$$

For (2.69), we note that

$$\begin{aligned}
\|M^-(\widetilde{X}) - \overline{M}^-\| &= \| \left(N^+(\widetilde{X})\right)^{-1} N^-(\widetilde{X}) - \left(\overline{N}^+\right)^{-1} \overline{N}^- \| \\
&= \| \left(N^+(\widetilde{X})\right)^{-1} \left(N^-(\widetilde{X}) - \overline{N}^-\right) + \left(N^+(\widetilde{X})\right)^{-1} \left(\overline{N}^+ - N^+(\widetilde{X})\right) \left(\overline{N}^+\right)^{-1} \overline{N}^- \| \\
&\leqslant C\|N^-(\widetilde{X}) - \overline{N}^-\| + C\|\overline{N}^+ - N^+(\widetilde{X})\| \\
&\leqslant Ch
\end{aligned}$$

in which we have used the geometric estimate (2.15b). □

Now, we utilize the matrices in (2.64) to describe multipoint Taylor expansions for the piecewise smooth vector functions satisfying (1.11a)-(1.11b) on the patch of each interface element. Then we derive the estimates of the remainders in these expansions.

In the discussions from now on, we let $s = \pm$ and $s' = \mp$, which means s and s' always take opposite signs when they appear in the same formula. Note that, for every node A_i of T and each point $X \in \omega_T \backslash \omega_T^{int}$, the line segment A_iX intersects $\Gamma \cap \omega_T$ either with no point or only one point. In the former case, A_i and X must be on the same side of $\Gamma \cap \omega_T$, while in the latter case, they are on different sides. Therefore, by the notations introduced in Section 2.3, we present expansions for $\mathbf{u}(X)$ around each node $A_i \in T^s$ for $X \in \omega_T^{*,s}$, $X \in \omega_T^{*,s'}$ and $X \in \omega_T^*$, respectively.

For every $X \in \omega_T^{*,s}$, $s = \pm$, we let $Y_i(t, X) = tA_i + (1-t)X$, $t \in [0,1]$, $i \in \mathcal{I}$. Let $\tilde{t}_i = \tilde{t}_i(X) \in [0,1]$ be such that $\widetilde{Y}_i = Y_i(\tilde{t}_i, X)$ is on the curve $\Gamma \cap T$ if X and A_i are on different sides of ω_T. We start from the following theorem that gives the expansion of $\mathbf{u}(A_i)$ around X if A_i and X are the same side of ω_T, i.e., $A_i \in T^s$ and $X \in \omega_T^{*,s}$, $s = \pm$.

Theorem 2.5. *For every interface element $T \in \mathcal{T}_h^i$ and its associated patch ω_T, let $\mathbf{u} \in \mathbf{PC}^2(\omega_T)$, then for $A_i \in T^s$, $s = \pm$, we have*

$$\mathbf{u}^s(A_i) = \mathbf{u}^s(X) + \left((A_i - X)^T \otimes I_2\right) \mathrm{Vec}(\nabla \mathbf{u}^s(X)) + \mathbf{R}_i^s(X), \ i \in \mathcal{I}^s, \ \forall X \in \omega_T^{*,s}, \tag{2.70}$$

$$\text{where } \ \mathbf{R}_i^s(X) = \int_0^1 (1-t) \frac{d^2}{dt^2} \mathbf{u}^s(Y_i(t, X)) dt, \ i \in \mathcal{I}^s. \tag{2.71}$$

Proof. Since $A_i \in T^s$ and $X \in \omega_T^{*,s}$, we know that $Y_i(t, X) \in \omega_T^{*,s}$, $\forall t \in [0,1]$. Applying the standard Taylor expansion with integral remainder to the components of $\mathbf{u}(X) = (u_1(X), u_2(X))^T$, we have

$$\mathbf{u}^s(A_i) = \mathbf{u}^s(X) + \nabla \mathbf{u}^s(X)(A_i - X) + \mathbf{R}_i^s(X), \ i \in \mathcal{I}^s, \ \forall X \in \omega_T^{*,s}, s = \pm. \tag{2.72}$$

Then, we obtain (2.70) by applying the vectorization on each side of (2.72) and using the formula (2.6) with $P = I_2$, $Q = \nabla \mathbf{u}^s(X)$, and $R = A_i - X$. □

In the following theorem, we describe how to expand $\mathbf{u}(A_i)$ about X if A_i and X are on different sides of Γ, i.e., $A_i \in T^{s'}$ but $X \in \omega_T^{*,s}$.

Theorem 2.6. *On every interface element $T \in \mathcal{T}_h^i$ and the associated patch ω_T, let $\mathbf{u} \in \mathbf{PC}^2(\omega_T)$, then for $A_i \in T^{s'}$, we have*

$$\begin{aligned} \mathbf{u}^{s'}(A_i) = \mathbf{u}^s(X) &+ ((A_i - X)^T \otimes I_2) \mathrm{Vec}\left(\nabla \mathbf{u}^s(X)\right) \\ &+ ((A_i - \widetilde{Y}_i)^T \otimes I_2)(M^s - I_4) \mathrm{Vec}\left(\nabla \mathbf{u}^s(X)\right) + \mathbf{R}_i^s(X), \end{aligned} \quad i \in \mathcal{I}^{s'}, \ \forall X \in \omega_T^{*,s}, \ s = \pm, \tag{2.73}$$

where $\mathbf{R}_i^s = \mathbf{R}_{i1}^s + \mathbf{R}_{i2}^s + \mathbf{R}_{i3}^s$, *with*

$$\begin{cases} \mathbf{R}_{i1}^s(X) = \int_0^{\tilde{t}_i}(1-t)\frac{d^2}{dt^2}\mathbf{u}^s(Y_i(t,X))dt, \\ \mathbf{R}_{i2}^s(X) = \int_{\tilde{t}_i}^1(1-t)\frac{d^2}{dt^2}\mathbf{u}^{s'}(Y_i(t,X))dt, \\ \mathbf{R}_{i3}^s(X) = (1-\tilde{t}_i)((A_i-X)^T\otimes I_2)(M^s(\widetilde{Y}_i)-I_4)\int_0^{\tilde{t}_i}\frac{d}{dt}\mathrm{Vec}\left(\nabla\mathbf{u}^s(Y_i(t,X))\right)dt. \end{cases} \tag{2.74}$$

Proof. Without loss of generality, we only discuss the case $A_i \in T^+$ and $X \in \omega_T^{*,-}$. Following a procedure similar to that used in [136], we have

$$\begin{aligned} \mathbf{u}^+(A_i) =& \mathbf{u}^-(X) + \int_0^{\tilde{t}_i}\frac{d}{dt}\mathbf{u}^-(Y_i(t,X))dt + \int_{\tilde{t}_i}^1\frac{d}{dt}\mathbf{u}^+(Y_i(t,X))dt \\ =& \mathbf{u}^-(X) + \nabla\mathbf{u}^-(X)(A_i-X) - \nabla\mathbf{u}^-(\widetilde{Y}_i)(A_i-\widetilde{Y}_i) + \nabla\mathbf{u}^+(\widetilde{Y}_i)(A_i-\widetilde{Y}_i) \\ &+ \int_0^{\tilde{t}_i}(1-t)\frac{d^2}{dt^2}\mathbf{u}^-(Y_i(t,X))dt + \int_{\tilde{t}_i}^1(1-t)\frac{d^2}{dt^2}\mathbf{u}^+(Y_i(t,X))dt, \end{aligned} \tag{2.75}$$

where the last two terms are actually $\mathbf{R}_{i1}^-$ and $\mathbf{R}_{i2}^-$. For the second and the third term on the right hand side of (2.75), by applying (2.6), we have

$$\begin{aligned} \nabla\mathbf{u}^-(X)(A_i-X) &= ((A_i-X)^T\otimes I_2)\mathrm{Vec}(\nabla\mathbf{u}^-(X)), \\ \nabla\mathbf{u}^-(\widetilde{Y}_i)(A_i-\widetilde{Y}_i) &= ((A_i-\widetilde{Y}_i)^T\otimes I_2)\mathrm{Vec}(\nabla\mathbf{u}^-(\widetilde{Y}_i)). \end{aligned} \tag{2.76}$$

For the forth term on the right of (2.75), by applying (2.6) and Lemma 2.11, we have

$$\begin{aligned} \nabla\mathbf{u}^+(\widetilde{Y}_i)(A_i-\widetilde{Y}_i) &= ((A_i-\widetilde{Y}_i)^T\otimes I_2)\mathrm{Vec}(\nabla\mathbf{u}^+(\widetilde{Y}_i)) \\ &= (1-\tilde{t}_i)((A_i-X)^T\otimes I_2)M^-(\widetilde{Y}_i)\mathrm{Vec}(\nabla\mathbf{u}^-(\widetilde{Y}_i)). \end{aligned} \tag{2.77}$$

Moreover we note that

$$\nabla\mathbf{u}^-(\widetilde{Y}_i) = \int_0^{\tilde{t}_i}\frac{d}{dt}\nabla\mathbf{u}^-(Y_i(t,x))dt + \nabla\mathbf{u}^-(X). \tag{2.78}$$

Finally, expansion (2.73) follows from substituting (2.78), (2.77) and (2.76) into (2.75). □

For $X \in \omega_T^*$, we consider another group of expansions which only involve the first derivative of $\mathbf{u}$.

Theorem 2.7. *On every interface element $T \in \mathcal{T}_h^i$ and the associated patch ω_T, let $\mathbf{u} \in \mathbf{PC}^2(\omega_T)$, then for each $X \in \omega_T^*$, we have*

$$\mathbf{u}(A_i) = \mathbf{u}(X) + \widetilde{\mathbf{R}}_i(X), \quad \text{with } \widetilde{\mathbf{R}}_i(X) = \int_0^1\frac{d}{dt}\mathbf{u}(Y_i(t,X))dt. \tag{2.79}$$

Proof. The proof follows from a straightforward derivation by using the continuity of $\mathbf{u}$. □

We proceed to estimate the remainders in (2.71) and (2.74) in terms of the Hilbert norms associated with $\mathbf{PH}^2$ spaces. For every scalar function u, let $\nabla^2 u$ be its Hessian matrix. Then we note that

$$\frac{d^2}{dt^2}\mathbf{u}(Y_i(t,X)) = \begin{bmatrix} (A_i-X)^T\nabla^2 u_1\ (A_i-X) \\ (A_i-X)^T\nabla^2 u_2\ (A_i-X) \end{bmatrix}, \tag{2.80}$$

$$\frac{d}{dt}\left(\nabla\mathbf{u}(Y_i(t,X))\right) = \begin{bmatrix} (A_i-X)^T\nabla^2 u_1 \\ (A_i-X)^T\nabla^2 u_2 \end{bmatrix}. \tag{2.81}$$

Lemma 2.13. *There exist constants $C>0$ such that for every $\mathbf{u}\in\mathbf{PC}^2(\omega_T)$ we have*

$$\begin{aligned} &\|\mathbf{R}_i^s\|_{L^2(\omega_T^{*,s})} \leqslant Ch^2|\mathbf{u}|_{H^2(\omega_T)}, \quad i\in\mathcal{I}^s,\ s=\pm, \\ &\|\mathbf{R}_{i1}^s\|_{L^2(\omega_T^{*,s})} \leqslant Ch^2|\mathbf{u}|_{H^2(\omega_T)}, \quad \|\mathbf{R}_{i2}^s\|_{L^2(\omega_T^{*,s})} \leqslant Ch^2|\mathbf{u}|_{H^2(\omega_T)}, \quad i\in\mathcal{I}^{s'},\ s=\pm. \end{aligned} \tag{2.82}$$

Proof. Let $\mathbf{R}_i^s = (R_i^{1s}, R_i^{2s})^T$, then according to (2.80), using Minkowski inequality and the fact $\|A_i - X\| \leqslant h$, we have

$$\begin{aligned} R_i^{js}(X) &= \left(\int_{\omega_T^{*,s}}\left(\int_0^1 (1-t)(A_i-X)^T\nabla^2 u_j^s(Y_i(t,X))(A_i-X)dt\right)^2 dX\right)^{\frac{1}{2}} \\ &\leqslant Ch^2\int_0^1\left(\int_{\omega_T^{*,s}}(1-t)^2\sum_{k,l=1}^2|\partial_{x_kx_l}u_j^s|^2\right)^{\frac{1}{2}}dt \leqslant Ch^2|u_j|_{H^2(\omega_T)}, \quad j=1,2, \end{aligned}$$

where we have used arguments similar to those used in the Lemma 4.1 in [79], and these estimates lead to the first estimate in (2.82). The derivations for the estimates of $\mathbf{R}_{i1}^s$ and $\mathbf{R}_{i2}^s$ are similar. □

Lemma 2.14. *There exist constants $C>0$ such that for every $\mathbf{u}\in\mathbf{PC}^2(\omega_T)$ we have*

$$\|\mathbf{R}_{i3}^s\|_{L^2(\omega_T^{*,s})} \leqslant Ch^2|\mathbf{u}|_{H^2(\omega_T)},\ i\in\mathcal{I}^{s'}, s=\pm. \tag{2.83}$$

Proof. Let $\mathbf{R}_{i3}^s = (R_{i3}^{1s}, R_{i3}^{2s})^T$. Using (2.81), (2.68), the fact $\|A_i - X\| \leqslant h$ and $0 \leqslant 1-\tilde{t}_i(X) \leqslant 1-t$, we have

$$\|R_{i3}^{js}\|_{L^2(\omega_T^{*,s})} \leqslant Ch^2\left(\int_{\omega_T^{*,s}}\left(\int_0^{\tilde{t}_i}(1-t)\sum_{k,l=1}^2\sum_{j=1}^2|\partial_{x_kx_l}u_j|dt\right)^2 dX\right)^{\frac{1}{2}}.$$

Then, applying the Minkowski inequality and Lemma 4.1 in [79] to the inequality above yields

$$\|R_{i3}^{js}\|_{L^2(\omega_T^{*,s})} \leqslant Ch^2\int_0^{\tilde{t}_i}\left(\sum_{k,l=1}^2\sum_{j=1}^2\int_{\omega_T^{*,s}}(1-t)^2|\partial_{x_kx_l}u_j|^2dX\right)^{\frac{1}{2}}dt \leqslant Ch^2(|u_1|_{H^2(\omega_T)}+|u_2|_{H^2(\omega_T)}),$$

from which (2.83) readily follows. □

In addition, since $\mathbf{u} \in [H^2(\omega_T^s)]^2$, the Sobolev embedding theorem indicates $\mathbf{u} \in [W^{1,6}(\omega_T^s)]^2$, $s = \pm$. Therefore we can bound the remainder $\widetilde{\mathbf{R}}_i$ in (2.79) in terms of the $W^{1,6}$-norm.

Lemma 2.15. *There exist constants $C > 0$ such that for every $\mathbf{u} \in \mathbf{PC}^2(\omega_T)$ we have*

$$\|\widetilde{\mathbf{R}}_i\|_{L^2(\omega_T^{*,s})} \leqslant Ch^2 \|\mathbf{u}\|_{W^{1,6}(\omega_T)}, \quad i \in \mathcal{I}. \tag{2.84}$$

Proof. We note that $\omega_T^* = \widetilde{\omega}_T \cup \omega_T^{int}$ is a small set by Lemma 2.4. So denote $\widetilde{\mathbf{R}}_i = (\widetilde{R}_i^1, \widetilde{R}_i^2)^T$, and by using (2.81), we have

$$\widetilde{R}_i^j(X) = \int_0^1 \nabla u_j(Y_i(t, X)) \, (A_i - X) dt, \quad j = 1, 2.$$

Then, applying arguments similar to those used for Lemma 3.2 in [84] and using the fact $|\omega_T^*| \leqslant Ch^3$, we have $\|\widetilde{R}_i^j\|_{L^2(\omega_T^*)} \leqslant Ch^2 \|u_j\|_{W^{1,6}(T)}$ for $j = 1, 2$ from which (2.84) follows. □

2.5.2 Interpolation Error Analysis

In this subsection, we use the results above to estimate the errors of the IFE interpolation defined in (2.61) on the patch of each interface element. For this purpose, we give the following two theorems on the expansions of the interpolation operator in which the key idea is to use the 2nd order expansion on $\omega_T^{*,s}$ (a major part of ω_T) and the first order expansion on ω_T^* (a small subset of ω_T). Denote the matrix functions $\Phi_{i,T} = [\boldsymbol{\phi}_{i,T}, \boldsymbol{\phi}_{i+|\mathcal{I}|,T}]$ as in (2.46).

Theorem 2.8. *On each interface element $T \in \mathcal{T}_h^i$ and its associated patch ω_T, assume $\mathbf{u} \in \mathbf{PC}^2(\omega_T)$, then, for any $\overline{X}_i \in l$, the following expansions hold for every $X \in \omega_T^{*,s}$:*

$$I_{h,T}\mathbf{u}(X) - \mathbf{u}(X) = \sum_{i \in \mathcal{I}^{s'}} \Phi_{i,T}(X)(\mathbf{E}_i^s(X) + \mathbf{F}_i^s(X)) + \sum_{i \in \mathcal{I}} \Phi_{i,T}(X)\mathbf{R}_i^s(X), \ s = \pm, \tag{2.85a}$$

$$\partial_{x_j}(I_{h,T}\mathbf{u}(X) - \mathbf{u}(X)) = \sum_{i \in \mathcal{I}^{s'}} \partial_{x_j}\Phi_{i,T}(X)(\mathbf{E}_i^s(X) + \mathbf{F}_i^s(X)) + \sum_{i \in \mathcal{I}} \partial_{x_j}\Phi_{i,T}(X)\mathbf{R}_i^s(X), \ s = \pm, \tag{2.85b}$$

$$\partial_{x_j x_k} I_{h,T}\mathbf{u}(X) = \sum_{i \in \mathcal{I}^{s'}} \partial_{x_j x_k}\Phi_{i,T}(X)(\mathbf{E}_i^s(X) + \mathbf{F}_i^s(X)) + \sum_{i \in \mathcal{I}} \partial_{x_j x_k}\Phi_{i,T}(X)\mathbf{R}_i^s(X), \ s = \pm, \tag{2.85c}$$

where $j, k = 1, 2$, $\mathbf{R}_i^s(X)$ are given in (2.71), (2.74), *and*

$$\begin{aligned} \mathbf{E}_i^s(X) &= \left((A_i - \widetilde{Y}_i)^T \otimes I_2\right) \left(M^s(\widetilde{Y}_i) - \overline{M}^s\right) \mathrm{Vec}(\nabla \mathbf{u}^s(X)), \\ \mathbf{F}_i^s(X) &= -\left((\widetilde{Y}_i - \overline{X}_i)^T \otimes I_2\right) \left(\overline{M}^s - I_4\right) \mathrm{Vec}(\nabla \mathbf{u}^s(X)). \end{aligned} \tag{2.86}$$

Proof. The argument is similar to the one used in [79], i.e., we apply the fundamental identities in Theorem 2.4 to the interpolation operator (2.61). Expanding the nodal values $\mathbf{u}(A_i)$, $i \in \mathcal{I}$, about $X \in \omega_T^{*,s}$ in the interpolation operator (2.61) by (2.70) and (2.73), we obtain

$$\begin{aligned} I_{h,T}\mathbf{u}(X) = &\sum_{i\in\mathcal{I}} \Phi_{i,T}(X)\mathbf{u}(X) + \left(\sum_{i\in\mathcal{I}} \Phi_{i,T}(X)\left((A_i - X)^T \otimes I_2\right)\right) \mathrm{Vec}(\nabla \mathbf{u}^s(X)) \\ &+ \left(\sum_{i\in\mathcal{I}^{s'}} \Phi_{i,T}(X)\left((A_i - \widetilde{Y}_i)^T \otimes I_2\right)(M^s - I_4)\right) \mathrm{Vec}(\nabla \mathbf{u}^s(X)) + \sum_{i\in\mathcal{I}} \Phi_{i,T}(X)\mathbf{R}_i^s. \end{aligned} \tag{2.87}$$

Note that for any vector $\mathbf{r} \in \mathbb{R}^{2\times 1}$, there holds

$$\Phi_{i,T}(X)\left(\mathbf{r}^T \otimes I_2\right) = \mathbf{r}^T \otimes \Phi_{i,T}(X). \tag{2.88}$$

Then we apply Theorem 2.4 onto the second term in (2.87) to have

$$\begin{aligned} I_{h,T}\mathbf{u}(X) = &\sum_{i\in\mathcal{I}} \Phi_{i,T}(X)\mathbf{u}(X) - \left(\sum_{i\in\mathcal{I}^{s'}} \left((A_i - \overline{X}_i)^T \otimes \Phi_{i,T}(X)\right)(\overline{M}^s - I_4)\right) \mathrm{Vec}(\nabla \mathbf{u}^s(X)) \\ &+ \left(\sum_{i\in\mathcal{I}^{s'}} \left((A_i - \widetilde{Y}_i)^T \otimes \Phi_{i,T}(X)\right)(M^s - I_4)\right) \mathrm{Vec}(\nabla \mathbf{u}^s(X)) + \sum_{i\in\mathcal{I}} \Phi_{i,T}(X)\mathbf{R}_i^s. \end{aligned} \tag{2.89}$$

Then, (2.85a) follows by applying partition of unity, the fact $A_i - \overline{X}_i = (A_i - \widetilde{Y}_i) + (\widetilde{Y}_i - \overline{X}_i)$, and the identity (2.88) to (2.89). For (2.85b), we apply (2.70) and (2.73) to $\partial_{x_j} I_{h,T}\mathbf{u}(X) = \sum_{i\in\mathcal{I}} \partial_{x_j}\Phi_{i,T}(X)\mathbf{u}(A_i)$ to obtain

$$\begin{aligned} \partial_{x_j} I_{h,T}\mathbf{u}(X) = &\sum_{i\in\mathcal{I}} \partial_{x_j}\Phi_{i,T}(X)\mathbf{u}(X) + \left(\sum_{i\in\mathcal{I}} \partial_{x_j}\Phi_{i,T}(X)\left((A_i - X)^T \otimes I_2\right)\right) \mathrm{Vec}(\nabla \mathbf{u}^s(X)) \\ &+ \left(\sum_{i\in\mathcal{I}^{s'}} \partial_{x_j}\Phi_{i,T}(X)\left((A_i - \widetilde{Y}_i)^T \otimes I_2\right)(M^s - I_4)\right) \mathrm{Vec}(\nabla \mathbf{u}^s(X)) + \sum_{i\in\mathcal{I}} \partial_{x_j}\Phi_{i,T}(X)\mathbf{R}_i^s. \end{aligned}$$

By using (2.47), (2.59a) and (2.88) in the above, we have

$$\begin{aligned} \partial_{x_j} I_{h,T}\mathbf{u}(X) = &I^j \mathrm{Vec}(\nabla \mathbf{u}^s(X)) \\ &- \left(\sum_{i\in\mathcal{I}^{s'}} \left((A_i - \overline{X}_i)^T \otimes \partial_{x_j}\Phi_{i,T}(X)\right)(\overline{M}^s - I_4)\right) \mathrm{Vec}(\nabla \mathbf{u}^s(X)) \\ &+ \left(\sum_{i\in\mathcal{I}^{s'}} \left((A_i - \widetilde{Y}_i)^T \otimes \partial_{x_j}\Phi_{i,T}(X)\right)(M^s - I_4)\right) \mathrm{Vec}(\nabla \mathbf{u}^s(X)) + \sum_{i\in\mathcal{I}} \partial_{x_j}\Phi_{i,T}(X)\mathbf{R}_i^s, \end{aligned}$$

which is in the same format as (2.89) because $I^j\text{Vec}(\nabla \mathbf{u}^s(X) = \partial_{x_j}\mathbf{u}(X)$. Therefore, (2.85b) follows from arguments used to derive (2.85a) from (2.89). Finally, (2.85c) can be derived very similarly by applying (2.70) and (2.73) in $\partial_{x_jx_k} I_{h,T}\mathbf{u}(X) = \sum_{i\in\mathcal{I}} \partial_{x_jx_k}\Phi_{i,T}(X)\mathbf{u}(A_i)$ and then using (2.47), (2.59b) and (2.88). □

Remark 2.9. *We note that* (2.85c) *is trivial for the linear IFE shape functions* $\Phi_{i,T}, i \in \mathcal{I}$ *since each side is simply a zero vector. And the non-trivial one is the bilinear case with* $j = 1$, $k = 2$ *and the rotated-*Q_1 *case with* $j = k = 1$ *or* $j = k = 2$.

For $X \in \omega_T^*$, we have simpler expansions as the follows.

Theorem 2.9. *On each interface element* $T \in \mathcal{T}_h^i$ *and the associated patch* ω_T, *let* $\mathbf{u} \in \mathbf{PC}^2(\omega_T)$, *then the following expansions hold for every* $X \in \omega_T^*$:

$$I_{h,T}\mathbf{u}(X) - \mathbf{u}(X) = \sum_{i\in\mathcal{I}} \Phi_{i,T}(X)\widetilde{\mathbf{R}}_i(X), \tag{2.90a}$$

$$\partial_{x_j}(I_{h,T}\mathbf{u}(X) - \mathbf{u}(X)) = -\partial_{x_j}\mathbf{u}(X) + \sum_{i\in\mathcal{I}} \partial_{x_j}\Phi_{i,T}(X)\widetilde{\mathbf{R}}_i(X), \tag{2.90b}$$

$$\partial_{x_jx_k}(I_{h,T}\mathbf{u}(X) - \mathbf{u}(X)) = -\partial_{x_jx_k}\mathbf{u}(X) + \sum_{i\in\mathcal{I}} \partial_{x_jx_k}\Phi_{i,T}(X)\widetilde{\mathbf{R}}_i(X), \tag{2.90c}$$

where $j, k = 1, 2$ *and* $\widetilde{\mathbf{R}}_i$ *is given in* (2.79).

Proof. They can be directly verified by applying (2.79) to the IFE interpolation (2.61) □

Now we are ready to estimate the interpolation errors.

Theorem 2.10. *There exists a constant* C *such that the following estimate holds for every* $\mathbf{u} \in \mathbf{PH}^2(\omega_T)$ *on the patch* ω_T *associated with each interface element* $T \in \mathcal{T}_h^i$:

$$\begin{aligned} &\|I_{h,T}\mathbf{u} - \mathbf{u}\|_{L^2(\omega_T^{*,s})} + h|I_{h,T}\mathbf{u} - \mathbf{u}|_{H^1(\omega_T^{*,s})} + h^2|I_{h,T}\mathbf{u} - \mathbf{u}|_{H^2(\omega_T^{*,s})} \\ \leqslant &Ch^2(|\mathbf{u}|_{H^1(\omega_T)} + |\mathbf{u}|_{H^2(\omega_T)}) \end{aligned} \qquad s = \pm. \tag{2.91}$$

Proof. First by (2.69) and $\|A_i - \widetilde{Y}_i\| \leqslant Ch$, we have $\|\mathbf{E}_i^s\|_{L^2(\omega_T^{*,s})} \leqslant Ch^2|\mathbf{u}|_{H^1(\omega_T)}$, $i \in \mathcal{I}$, $s = \pm$. Noticing $\|\widetilde{Y}_i - \overline{X}_i\| \leqslant Ch^2$ from (2.15a) by taking $\overline{X}_i = \widetilde{Y}_{i\perp}$ because of Lemma 2.9, and then using (2.68), we have $\|\mathbf{F}_i^s\|_{L^2(\omega_T^{*,s})} \leqslant Ch^2|\mathbf{u}|_{H^1(\omega_T)}$, $i \in \mathcal{I}$, $s = \pm$. Now putting these estimates, Lemmas 2.13, 2.14 and Theorem 2.2 into (2.85a), (2.85b) and (2.85c), for $s = \pm$, $j, k = 1, 2$, we have

$$\begin{aligned} \|I_{h,T}\mathbf{u} - \mathbf{u}\|_{L^2(\omega_T^{*,s})} &\leqslant \sum_{i\in\mathcal{I}^{s'}} C(\|\mathbf{E}_i^s\|_{L^2(\omega_T^{*,s})} + \|\mathbf{F}_i^s\|_{L^2(\omega_T^{*,s})}) + \sum_{i\in\mathcal{I}} C\|\mathbf{R}_i^s\|_{L^2(\omega_T^{*,s})} \\ &\leqslant Ch^2(|\mathbf{u}|_{H^1(\omega_T)} + |\mathbf{u}|_{H^2(\omega_T)}), \end{aligned}$$

$$\begin{aligned}\|\partial_{x_j} I_{h,T}\mathbf{u} - \partial_{x_j}\mathbf{u}\|_{L^2(\omega_T^{*,s})} &\leqslant \sum_{i\in\mathcal{I}^{s'}} Ch^{-1}(\|\mathbf{E}_i^s\|_{L^2(\omega_T^{*,s})} + \|\mathbf{F}_i^s\|_{L^2(\omega_T^{*,s})}) + \sum_{i\in\mathcal{I}} Ch^{-1}\|\mathbf{R}_i^s\|_{L^2(\omega_T^{*,s})}\\ &\leqslant Ch(|\mathbf{u}|_{H^1(\omega_T)} + |\mathbf{u}|_{H^2(\omega_T)}).\end{aligned}$$

$$\begin{aligned}\|\partial_{x_jx_k} I_{h,T}\mathbf{u} - \partial_{x_jx_k}\mathbf{u}\|_{L^2(\omega_T^{*,s})} &\leqslant \|\partial_{x_jx_k}\mathbf{u}\|_{L^2(\omega_T^{*,s})}\\ &\quad + \sum_{i\in\mathcal{I}^{s'}} Ch^{-2}(\|\mathbf{E}_i^s\|_{L^2(\omega_T^{*,s})} + \|\mathbf{F}_i^s\|_{L^2(\omega_T^{*,s})}) + \sum_{i\in\mathcal{I}} Ch^{-2}\|\mathbf{R}_i^s\|_{L^2(\omega_T^{*,s})}\\ &\leqslant C(|\mathbf{u}|_{H^1(\omega_T)} + |\mathbf{u}|_{H^2(\omega_T)}).\end{aligned}$$

These estimates lead to the desired result for $\mathbf{u} \in \mathbf{PC}^2(\omega_T)$. Then the estimate for $\mathbf{u} \in \mathbf{PH}^2(\omega_T)$ can be obtained from the density Hypothesis **(H3)**. □

Theorem 2.11. *There exists a constant C such that the following estimate holds for every $\mathbf{u} \in \mathbf{PH}^2(\omega_T)$ on each patch ω_T associated with each interface element $T \in \mathcal{T}_h^i$:*

$$\begin{aligned}&\|I_{h,T}\mathbf{u} - \mathbf{u}\|_{L^2(\omega_T^*)} + h|I_{h,T}\mathbf{u} - \mathbf{u}|_{H^1(\omega_T^*)} + h^2|I_{h,T}\mathbf{u} - \mathbf{u}|_{H^2(\omega_T^*)}\\ \leqslant& Ch^2(\|\mathbf{u}\|_{W^{1,6}(\omega_T)} + \|\mathbf{u}\|_{H^2(\omega_T)}).\end{aligned} \tag{2.92}$$

Proof. According to (2.45), Lemma 2.15 and Theorem 2.9, for $j,k = 1,2$, we have

$$\begin{aligned}&\|\Phi_{i,T}\widetilde{\mathbf{R}}_i\|_{L^2(\omega_T^*)} \leqslant Ch^2\|\mathbf{u}\|_{W^{1,6}(\omega_T)},\\ &\|\partial_{x_j}\Phi_{i,T}\widetilde{\mathbf{R}}_i\|_{L^2(\omega_T^*)} \leqslant Ch\|\mathbf{u}\|_{W^{1,6}(\omega_T)},\\ &\|\partial_{x_jx_k}\Phi_{i,T}\widetilde{\mathbf{R}}_i\|_{L^2(\omega_T^*)} \leqslant C\|\mathbf{u}\|_{W^{1,6}(\omega_T)}.\end{aligned}$$

Besides, for $\mathbf{u} = (u_1, u_2)^T$, the Hölder's inequality implies

$$\left(\int_{\omega_T^*}(\partial_{x_j}u_m)^2dX\right)^{\frac{1}{2}} \leqslant \left(\int_{\omega_T^*}1^{\frac{3}{2}}dX\right)^{\frac{1}{3}}\left(\int_{\omega_T^*}(\partial_{x_j}u_m)^6dX\right)^{\frac{1}{6}} \leqslant Ch\|u_m\|_{W^{1,6}(\omega_T)},\ m=1,2,$$

where we have used the fact $|\omega_T^*| \leqslant Ch^3$. For the second term above, it is easy to see that

$$\left(\int_{\omega_T^*}(\partial_{x_jx_k}u_m)^2dX\right)^{\frac{1}{2}} \leqslant C\|u_m\|_{H^2(\omega_T)},\quad m=1,2.$$

Applying the estimates above to (2.90a), (2.90b) and (2.90c), we have (2.92) for all $\mathbf{u} \in \mathbf{PC}^2(\omega_T)$. Again the result for $\mathbf{u} \in \mathbf{PH}^2(\omega_T)$ follows from the density Hypothesis **(H3)**. □

Finally, by combing the results above, we can prove the optimal approximation capabilities for the proposed IFE space through the following error estimation for the global IFE interpolation.

Theorem 2.12. *There exists a constant C such that the following estimate holds for every $\mathbf{u} \in \mathbf{PH}^2(\Omega)$:*

$$\|I_h\mathbf{u} - \mathbf{u}\|_{L^2(\Omega)} + h|I_h\mathbf{u} - \mathbf{u}|_{H^1(\Omega)} + h^2|I_h\mathbf{u} - \mathbf{u}|_{H^2(\Omega)} \leqslant Ch^2\|\mathbf{u}\|_{H^2(\Omega)}. \tag{2.93}$$

Proof. By applying (2.63) to all the non-interface elements and applying (2.91) and (2.92) to all the interface elements, then summing all the estimates over all the elements in the mesh, we have

$$\|I_h\mathbf{u} - \mathbf{u}\|_{L^2(\Omega)} + h|I_h\mathbf{u} - \mathbf{u}|_{H^1(\Omega)} + h^2|I_h\mathbf{u} - \mathbf{u}|_{H^2(\Omega)} \leqslant Ch^2(\|\mathbf{u}\|_{H^2(\Omega)} + \|\mathbf{u}\|_{W^{1,6}(\Omega)}).$$

Then using the inequality $\|w\|^2_{W^{1,p}(\Omega)} \leqslant C\|w\|^2_{H^2(\Omega)}$ for any $w \in W^{1,p}(\Omega), p \geq 6$ [173], we have (2.93). □

2.5.3 Numerical Examples

In this subsection, we numerically demonstrate the optimal approximation capabilities of the proposed IFE spaces. We use an example similar to that given in [153] in which the domain is $\Omega = [-1, 1] \times [-1, 1]$ and the function $\mathbf{u}$ is

$$\mathbf{u}(x_1, x_2) = \begin{cases} \begin{bmatrix} u_1^-(x_1, x_2) \\ u_2^-(x_1, x_2) \end{bmatrix} = \begin{bmatrix} \frac{a^2b^2}{\lambda^-} r^{\alpha_1} \\ \frac{a^2b^2}{\lambda^-} r^{\alpha_2} \end{bmatrix} & \text{if } X \in \Omega^-, \\ \begin{bmatrix} u_1^+(x_1, x_2) \\ u_2^+(x_1, x_2) \end{bmatrix} = \begin{bmatrix} \frac{a^2b^2}{\lambda^+} r^{\alpha_1} + \left(\frac{1}{\lambda^-} - \frac{1}{\lambda^+}\right) a^2b^2 \\ \frac{a^2b^2}{\lambda^+} r^{\alpha_2} + \left(\frac{1}{\lambda^-} - \frac{1}{\lambda^+}\right) a^2b^2 \end{bmatrix} & \text{if } X \in \Omega^+, \end{cases} \tag{2.94}$$

where $\lambda^- = 1$, $\lambda^+ = 5$, $\mu^- = 2$ and $\mu^+ = 10$, $a = b = \pi/6.28$, $\alpha_1 = 5$, $\alpha_2 = 7$ and $r(x_1, x_2) = (x_1^2/a^2 + x_2^2/b^2)^{1/2}$, the interface Γ is a circle defined by the zero level set $r(x_1, x_2) - 1 = 0$ and $\Omega^- = \{(x_1, x_2)^T \ : \ r(x_1, x_2) < 1\}$, $\Omega^+ = \{(x_1, x_2)^T \ : \ r(x_1, x_2) > 1\}$. We note that the function in (2.94) is simply a constant multiplier of the one used in [153], and here we use a circle with different radius as the interface. All the numerical results presented below are generated by the proposed bilinear IFE space on Cartesian meshes. The errors are measured in both the L^2 and semi-H^1 norms over a sequence a meshes with the size specified by h.

We present the numerical results for the interpolation operator $I_h\mathbf{u}$ defined by (2.61) and (2.62) in Table 2.1 where the convergence rates are estimated from the errors computed on two consecutive meshes. As predicted by Theorem 2.12, numerical results presented in this table clearly show that the IFE interpolation converges optimally.

h	$\|\mathbf{u}-I_h\mathbf{u}\|_{L^2(\Omega)}$	rate	$\|\mathbf{u}-I_h\mathbf{u}\|_{H^1(\Omega)}$	rate
1/10	5.6990E-1		6.8680E+0	
1/20	1.4528E-1	1.9719	3.4933E+0	0.9753
1/40	3.6502E-2	1.9928	1.7544E+0	0.9936
1/80	9.1372E-3	1.9981	8.7822E-1	0.9984
1/160	2.2851E-3	1.9995	4.3924E-1	0.9996
1/320	5.7132E-4	1.9999	2.1964E-1	0.9999
1/640	1.4283E-4	2.0000	1.0982E-1	1.0000
1/1280	3.5709E-5	2.0000	5.4911E-2	1.0000

Table 2.1: IFE Interpolation errors and rates for the bilinear IFE functions

2.6 A PPIFE Scheme and Its Error Analysis

In this section, we propose a partially penalized IFE (PPIFE) method that employs the vector IFE space $\mathbf{S}_h(\Omega)$ described in (2.43) to solve the elasticity interface problem (1.5)-(1.11) on an interface-independent mesh. As usual, we assume $\mathbf{g}=\mathbf{0}$ in (1.5) to simplify the discussions, the method and the related analysis can be extended to the case in which $\mathbf{g}\neq\mathbf{0}$ via the standard homogenization procedure.

To describe this PPIFE method, we consider the following underlying space

$$\begin{aligned}\mathbf{V}_h=\Big\{\mathbf{v}:\mathbf{v}|_T\in\left[H^1(T)\right]^2,\ \forall T\in\mathcal{T}_h,\ \nabla\mathbf{v}\cdot\mathbf{n}_e|_e \text{ is well defined for each } e\in\mathcal{E}_h,\\ \mathbf{v} \text{ is continuous across each } e\in\mathring{\mathcal{E}}_h^n,\ \mathbf{v}|_{\partial\Omega}=\mathbf{0}\Big\}.\end{aligned} \tag{2.95}$$

Let $\mathbf{S}_h^0(\Omega)$ be the subspace of $\mathbf{S}_h(\Omega)$ whose functions have zero traces on $\partial\Omega$. Clearly, we have $\mathbf{S}_h^0(\Omega)\subset\mathbf{V}_h$. We emphasize that the global IFE basis functions of $\mathbf{S}_h(\Omega)$ are discontinuous across each interface edges $e\in\mathring{\mathcal{E}}_h^i$ which imposes challenges to the error analysis of the IFE method.

Now, for every $e\in\mathring{\mathcal{E}}_h^i$ shared by the two elements denoted by T_e^1 and T_e^2, and for every $\mathbf{g}\in\mathbf{V}_h$, we adopt the following notations for its average and jump over e:

$$\{\mathbf{g}\}_e=\frac{(\mathbf{g}|_{T_e^1})|_e+(\mathbf{g}|_{T_e^2})|_e}{2}\quad\text{and}\quad[\mathbf{g}]_e=(\mathbf{g}|_{T_e^1})|_e-(\mathbf{g}|_{T_e^2})|_e. \tag{2.96}$$

To derive the PPIFE scheme for the elasticity interface problem, we formally multiply (1.5) by a test function $\mathbf{v}\in\mathbf{V}_h$ as usual, then by the Green's formula, we have

$$-\int_T(\text{div }\sigma(\mathbf{u}))\cdot\mathbf{v}dX=\int_T\nabla\mathbf{v}:\sigma(\mathbf{u})dX-\int_{\partial T}(\sigma(\mathbf{u})\mathbf{n})\cdot\mathbf{v}ds,\quad\forall\mathbf{v}\in\mathbf{V}_h,\ \forall T\in\mathcal{T}_h, \tag{2.97}$$

where $\nabla = (\partial_{x_1}, \partial_{x_2})$ is the gradient operator as a row vector. Then, summing (2.97) over all the elements and using the continuity of $\mathbf{v} \in \mathbf{V}_h$ on all the non-interface edges $e \in \mathring{\mathcal{E}}_h^n$, we have

$$\sum_{T\in\mathcal{T}_h} \int_T \nabla \mathbf{v} : \sigma(\mathbf{u}) dX - \sum_{e\in\mathring{\mathcal{E}}_h^i} \int_e \{\sigma(\mathbf{u})\mathbf{n}_e\} \cdot [\mathbf{v}] ds = \int_\Omega \mathbf{f} \cdot \mathbf{v} dX, \tag{2.98}$$

where $\mathbf{n}_e$ is from T_e^1 to T_e^2. The assumption that $\mathbf{u}$ satisfies the jump conditions (1.11) implies

$$\int_e \{\sigma(\mathbf{v})\mathbf{n}_e\} \cdot [\mathbf{u}] ds = 0, \quad \text{and} \quad \int_e [\mathbf{u}] \cdot [\mathbf{v}] ds = 0, \quad \forall e \in \mathring{\mathcal{E}}_h^i. \tag{2.99}$$

Adding these vanishing terms in (2.99) to (2.98) leads to the following weak form for the elasticity interface problem (1.5)-(1.11):

$$a_h(\mathbf{u}, \mathbf{v}) = L_f(\mathbf{v}), \quad \forall \mathbf{v} \in \mathbf{V}_h, \tag{2.100}$$

where

$$\begin{aligned} a_h(\mathbf{u}, \mathbf{v}) = & \sum_{T\in\mathcal{T}_h} \int_T 2\mu\epsilon(\mathbf{u}) : \epsilon(\mathbf{v}) dX + \sum_{T\in\mathcal{T}_h} \int_T \lambda(\nabla \cdot \mathbf{u})(\nabla \cdot \mathbf{v}) dX \\ & - \sum_{e\in\mathring{\mathcal{E}}_h^i} \int_e \{\sigma(\mathbf{u})\mathbf{n}_e\} \cdot [\mathbf{v}] ds + \theta \sum_{e\in\mathring{\mathcal{E}}_h^i} \int_e \{\sigma(\mathbf{v})\mathbf{n}_e\} \cdot [\mathbf{u}] ds + \sum_{e\in\mathring{\mathcal{E}}_h^i} \frac{\rho}{h} \int_e [\mathbf{u}] \cdot [\mathbf{v}] ds, \end{aligned} \tag{2.101}$$

$$L_f(\mathbf{v}) = \sum_{T\in\mathcal{T}_h} \int_T \mathbf{f} \cdot \mathbf{v} dX, \tag{2.102}$$

and ρ is a stabilizing parameter for the scheme. According to the weak form (2.100) and the fact that the IFE space $\mathbf{S}_h^0(\Omega)$ has the optimal approximation capabilities for functions in $\mathbf{PH}^2(\Omega)$ as stated in Theorem 2.12, we propose the PPIFE method for the planar-elasticity interface problems (1.5)-(1.11) as finding $\mathbf{u}_h \in \mathbf{S}_h^0(\Omega)$ such that

$$a_h(\mathbf{u}_h, \mathbf{v}_h) = L_f(\mathbf{v}_h), \quad \forall \mathbf{v}_h \in \mathbf{S}_h^0. \tag{2.103}$$

In this chapter, we consider three PPIFE schemes corresponding to three popular choices for the parameter: $\theta = -1, 0, 1$, and following the convention [148, 174], we call them the symmetric, incomplete, and non-symmetric PPIFE (SPPIFE, IPPIFE and NPPIFE) methods.

We note that the weak formulation described by (2.100)-(2.102) is similar to the interior penalty DG (IPDG) methods [57] in the sense that the interior penalties are used to penalize the discontinuities. But in our proposed PPIFE method, the penalties are used only on interface edges because of the H^1 regularity of IFE functions in the subdomain formed by all the non-interface elements. Moreover, both the location and number of the global degrees of freedom of the IFE space (2.43) are the same as the those for standard continuous finite element space defined on the same mesh. This feature makes the proposed PPIFE method advantageous in moving interface problems.

2.6.1 A Trace Inequality for Vector IFE Functions

In this subsection, we derive a trace inequality for the elasticity IFE functions in (2.42) on each $T \in \mathcal{T}_h^i$. Again, by considering geometries, we can classify the interface element configurations in Figures 2.4-2.7 into two typical configurations for both the rectangular and triangular interface elements, see Figures 2.8 and 2.9. Without loss of generality, the rest of our discussions in this subsection are all based on the interface element configurations shown in Figures 2.8 and 2.9.

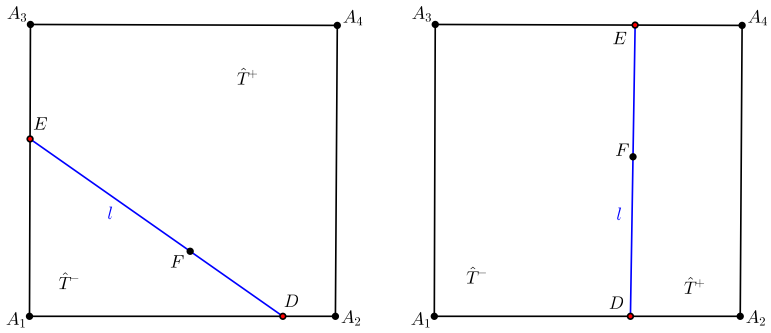

(a) Case 1 (b) Case 2

Figure 2.8: Rectangular elements for trace inequalities of vector IFE functions

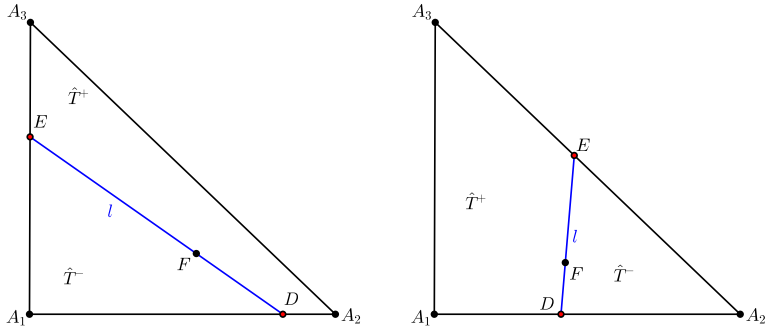

(a) Case 1 (b) Case 2

Figure 2.9: Triangular elements for trace inequalities of vector IFE functions

On every interface element $T \in \mathcal{T}_h^i$, recall that l is the line connecting the intersection points D, E of the interface and ∂T that partitions T into $\hat{T}^-$ and $\hat{T}^+$, see Figures 2.8 and 2.9 for illustrations, $\bar{\mathbf{n}} = (\bar{n}_1, \bar{n}_2)^T$ and $\bar{\mathbf{t}} = (\bar{n}_2, -\bar{n}_1)^T$ are the normal vector and tangential vector to l, and $L(X) = 0$ with $L(X) = (X - D) \cdot \bar{\mathbf{n}}$ being the equation of the line l. By

(2.20)-(2.29), we have the following formula for IFE functions on T:

$$\boldsymbol{\phi}_T(X) = \begin{cases} \boldsymbol{\phi}_T^-(X) \in \boldsymbol{\Pi}_T, & X \in \hat{T}^-, \\ \boldsymbol{\phi}_T^+(X) \in \boldsymbol{\Pi}_T, & X \in \hat{T}^+, \end{cases} \quad \text{with} \quad \boldsymbol{\phi}_T^- - \boldsymbol{\phi}_T^+ = \mathbf{c}_0 L(X), \tag{2.104}$$

in which the coefficient vector $\mathbf{c}_0$ can be expressed as

$$\mathbf{c}_0 = \left(K^-\right)^{-1} \hat{\sigma}(\boldsymbol{\phi}_T^+)(F)\bar{\mathbf{n}}, \tag{2.105a}$$

$$\text{with} \quad K^s = Q\mathcal{P}^s Q^T \ \text{ and } \ Q = [\bar{\mathbf{n}}, \bar{\mathbf{t}}], \ \ \mathcal{P}^s = \begin{bmatrix} \lambda^s + 2\mu^s & 0 \\ 0 & \mu^s \end{bmatrix}, \ \ s = \pm, \tag{2.105b}$$

where F is a point on l specified in Lemma 2.5.

Because of the lack of regularity, the first order trace inequality commonly used in error estimation of finite element methods can not be applied to IFE functions on the whole element directly, and this motivates us to develop a trace inequality for IFE functions that is useful for proving the coercivity of the bilinear form used in the PPIFE method. We start from recalling the following trace inequalities for polynomials [197]:

$$\forall v \in \mathbb{P}_k(m), \ \ \forall t \in \partial m, \ \ |v(t)| \leqslant \frac{k+1}{\sqrt{|m|}} \|v\|_{L^2(m)}, \ \ \text{for a 1-d segment } m; \tag{2.106}$$

$$\forall v \in \mathbb{P}_k(T), \ \ \forall e \text{ be an edge of } T, \ \ \|v\|_{L^2(e)} \leqslant \sqrt{\frac{(k+1)(k+2)}{2}\frac{|e|}{|T|}} \|v\|_{L^2(T)},$$
$$\text{for a 2-d triangle } T. \tag{2.107}$$

By (2.104), the function $\mathbf{c}_0 L(X)$ relates the two polynomial components $\boldsymbol{\phi}_T^-(X)$ and $\boldsymbol{\phi}_T^+(X)$ of an IFE function $\boldsymbol{\phi}_T(X)$, and we derive a few estimates for it first. We note that $\sigma^-(\mathbf{c}_0 L)$ is a matrix independent of spatial variable X.

Lemma 2.16. *There exists a constant C independent of the Lamé parameters such that*

$$\|\sigma^-(\mathbf{c}_0 L)\| \leqslant \frac{C}{|l|^{1/2}} \|\hat{\sigma}(\boldsymbol{\phi}_T^+)\bar{\mathbf{n}}\|_{L^2(l)}, \ \ \forall T \in \mathcal{T}_h^i. \tag{2.108}$$

Proof. Let $\mathbf{c}_0 = (c_0^1, c_0^2)^T$. Using the formula $L(X) = \bar{\mathbf{n}} \cdot (X - D)$ with $\bar{\mathbf{n}} = (\bar{n}_1, \bar{n}_2)^T$, we have

$$\sigma^-(\mathbf{c}_0 L) = \begin{bmatrix} (\lambda^- + 2\mu^-)c_0^1\bar{n}_1 + \lambda^- c_0^2 \bar{n}_2 & \mu^-(c_0^1\bar{n}_2 + c_0^2\bar{n}_1) \\ \mu^-(c_0^1\bar{n}_2 + c_0^2\bar{n}_1) & (\lambda^- + 2\mu^-)c_0^2\bar{n}_2 + \lambda^- c_0^1\bar{n}_1 \end{bmatrix}. \tag{2.109}$$

Given any unit vector $\mathbf{r} = (r_1, r_2)^T$, using (2.105a) and (2.109), we obtain

$$\sigma^-(\mathbf{c}_0 L)\mathbf{r} = \begin{bmatrix} \lambda^- r_1 + 2\mu^- \bar{n}_1 \mathbf{r}\cdot\bar{\mathbf{n}} & \mu^-(2\bar{n}_1\bar{n}_2 r_1 + \bar{n}_2^2 r_2 - \bar{n}_1^2 r_2) \\ \lambda^- r_2 + 2\mu^- \bar{n}_2 \mathbf{r}\cdot\bar{\mathbf{n}} & -\mu^-(2\bar{n}_1\bar{n}_2 r_2 + \bar{n}_1^2 r_1 - \bar{n}_2^2 r_1) \end{bmatrix} (\mathcal{P}^-)^{-1} Q^T \hat{\sigma}(\boldsymbol{\phi}_T^+)(F)\bar{\mathbf{n}}. \tag{2.110}$$

Rewrite (2.110) as $\sigma^-(\mathbf{c}_0 L)\mathbf{r} = \Lambda(\mathbf{r})\hat{\sigma}(\boldsymbol{\phi}_T^+)(F)\bar{\mathbf{n}}$. Then, taking $\mathbf{r} = \bar{\mathbf{n}}$, $\bar{\mathbf{t}}$, we have

$$\Lambda(\bar{\mathbf{n}}) = I_2, \quad \text{and} \quad \Lambda(\bar{\mathbf{t}}) = \begin{bmatrix} \frac{\lambda^-}{\lambda^-+2\mu^-}\bar{n}_2 & \bar{n}_1 \\ \frac{-\lambda^-}{\lambda^-+2\mu^-}\bar{n}_1 & \bar{n}_2 \end{bmatrix} Q^T, \tag{2.111}$$

where I_2 is the 2-by-2 identity matrix. Hence, we have $\|\sigma^-(\mathbf{c}_0 L)\bar{\mathbf{n}}\| = \|\hat{\sigma}(\boldsymbol{\phi}_T^+)(F)\bar{\mathbf{n}}\|$, and a direct computation yields

$$\begin{aligned} \|\sigma^-(\mathbf{c}_0 L)\bar{\mathbf{t}}\| &\leqslant \|\Lambda(\bar{\mathbf{t}})\|_F \|\hat{\sigma}(\boldsymbol{\phi}_T^+)(F)\bar{\mathbf{n}}\| \\ &= \sqrt{\left(1 + \frac{(\lambda^-)^2}{(\lambda^- + 2\mu^-)^2}\right)(1 + 2\bar{n}_1^2\bar{n}_2^2)}\|\hat{\sigma}(\boldsymbol{\phi}_T^+)(F)\bar{\mathbf{n}}\| \\ &\leqslant \sqrt{3}\|\hat{\sigma}(\boldsymbol{\phi}_T^+)(F)\bar{\mathbf{n}}\|, \end{aligned} \tag{2.112}$$

where $\|\cdot\|_F$ denotes the Frobenius norm. Therefore, for every unit vector $\mathbf{r}$, we have

$$\|\sigma^-(\mathbf{c}_0 L)\mathbf{r}\| \leqslant \left(\|\sigma^-(\mathbf{c}_0 L)\bar{\mathbf{n}}\|^2 + \|\sigma^-(\mathbf{c}_0 L)\bar{\mathbf{t}}\|^2\right)^{1/2} \leqslant 2\|\hat{\sigma}(\boldsymbol{\phi}_T^+)(F)\bar{\mathbf{n}}\|. \tag{2.113}$$

Using (2.113) with $\mathbf{r} = \mathbf{e}_1$ and $\mathbf{e}_2$ where $\mathbf{e}_i$ is the i-th unit vector in $\mathbb{R}^2$, we obtain

$$\|\sigma^-(\mathbf{c}_0 L)\| \leqslant \|\sigma^-(\mathbf{c}_0 L)\mathbf{e}_1\| + \|\sigma^-(\mathbf{c}_0 L)\mathbf{e}_2\| \leqslant 4\|\hat{\sigma}(\boldsymbol{\phi}_T^+)(F)\bar{\mathbf{n}}\|. \tag{2.114}$$

In addition, on the line l, without loss of generality, we can assume $\left|\overline{DF}\right| \geqslant |l|/2$. Then, applying the standard 1-D trace inequality (2.106) to (2.114) with $m = DF$, we obtain (2.108). □

The estimate in the previous lemma can be refined so that its bound is expressed in terms of the IFE function $\boldsymbol{\phi}_T(X)$ and the ratios of the Lamé parameters in the two subelements of $T \in \mathcal{T}_h^i$. In particular, we discuss this estimate in the following two lemmas for some tricky cases in which the standard trace inequality (2.107) can not be applied directly. We denote $\lambda_M = \max\{\lambda^+, \lambda^-\}$, $\lambda_m = \min\{\lambda^+, \lambda^-\}$ and similarly define μ_M and μ_m.

Lemma 2.17. *There exists a constant C independent of the Lamé parameters such that for every IFE function $\boldsymbol{\phi}_T$*

$$\|\sigma^-(\mathbf{c}_0 L)\| \leqslant \frac{C}{h^{1/2}|l|^{1/2}}\left(\frac{\mu_M}{\sqrt{\mu_m}}\|\sqrt{2\mu}\epsilon(\boldsymbol{\phi}_T)\|_{L^2(T)} + \frac{\lambda_M}{\sqrt{\lambda_m}}\|\sqrt{\lambda}\nabla\cdot\boldsymbol{\phi}_T\|_{L^2(T)}\right) \tag{2.115}$$

on the interface element T satisfying one of the following conditions:

(a): T is a Case 1 rectangular interface element illustrated in Figure 2.8.

(b): T is a Case 1 triangular interface element illustrated in Figure 2.9 such that $|A_1 D| \leqslant h/2$ or $|A_1 E| \leqslant h/2$.

(c): T is a Case 2 triangular interface element illustrated in Figure 2.9 such that $|A_2D| \leqslant h/2$ or $|A_2E| \leqslant h/2$.

Proof. Assume T is an interface element satisfying the condition (a), we note that $|\triangle A_4ED| \geqslant \sqrt{2}h|l|/4$ because the distance from A_4 to l is greater than $\sqrt{2}h/2$. Then we apply the standard trace inequality (2.107) to the right hand side of (2.108) on the triangle $\triangle A_4ED$ to obtain

$$\begin{aligned}\|\sigma^-(\mathbf{c}_0 L)\| &\leqslant \frac{C|l|^{1/2}}{|l|^{1/2}\ |\triangle A_4ED|^{1/2}}\|\hat{\sigma}(\boldsymbol{\phi}_T^+)\|_{L^2(\triangle A_4ED)} \\ &\leqslant \frac{C}{|l|^{1/2}h^{1/2}}\left(\|(\mu^+-\mu^-)\epsilon(\boldsymbol{\phi}_T^+)\|_{L^2(\hat{T}^+)} + \|(\lambda^+-\lambda^-)\nabla\cdot\boldsymbol{\phi}_T^+\|_{L^2(\hat{T}^+)}\right) \quad (2.116)\\ &\leqslant \frac{C}{|l|^{1/2}h^{1/2}}\left(\frac{\mu_M}{\sqrt{\mu_m}}\|\sqrt{2\mu}\epsilon(\boldsymbol{\phi}_T)\|_{L^2(T)} + \frac{\lambda_M}{\sqrt{\lambda_m}}\|\sqrt{\lambda}\nabla\cdot\boldsymbol{\phi}_T\|_{L^2(T)}\right),\end{aligned}$$

which implies (2.115).

For an interface element T satisfying the condition (b) such that $|A_1E| \leqslant h/2$, i.e., $|A_3E| \geqslant h/2$. In such a case, we note that $|\triangle A_3ED| \geqslant \sqrt{2}h|l|/8$. Then, following similar arguments used for T satisfying the condition (a), we can obtain (2.115) by applying the standard trace inequality (2.107) to the right hand side of (2.108) on the triangle $\triangle A_3ED$. Similar arguments apply when $|A_1D| \leqslant h/2$.

Estimate (2.115) can be proved similarly when T is an interface element satisfying condition (c). □

By Lemma 2.17, we can develop a stress trace inequality for IFE functions in the following theorem.

Theorem 2.13. *On every interface element T and its interface edge e whose normal is $\mathbf{n}_e$, the following inequality holds for every IFE function $\boldsymbol{\phi}_T$:*

$$\|h^{1/2}\sigma(\boldsymbol{\phi}_T)\mathbf{n}_e\|_{L^2(e)} \leqslant C_t\left(\|\sqrt{2\mu}\epsilon(\boldsymbol{\phi}_T)\|_{L^2(T)} + \|\sqrt{\lambda}\nabla\cdot\boldsymbol{\phi}_T\|_{L^2(T)}\right), \quad (2.117)$$

where $C_t \leqslant \max\left\{\frac{\mu_M}{\sqrt{\mu_m}}, \frac{\lambda_M}{\sqrt{\lambda_m}}\right\}\widetilde{C}_t$ with $\widetilde{C}_t$ independent of the interface location, mesh size h and Lamé parameters.

Proof. We present our arguments for the rectangular and triangular elements separately.

Rectangular interface elements: Assuming that T is a Case 1 rectangular interface element illustrated in Figure 2.8, without loss of generality, we only consider the interface edge $e = A_1A_2 = A_1D \cup DA_2$ with $A_1D \subset \hat{T}^-$ and $DA_2 \subset \hat{T}^+$. On the first piece A_1D of

e, applying the trace inequality (2.107) on $\triangle A_1DA_3$ to the polynomial component $\boldsymbol{\phi}_T^-$, we have

$$\begin{aligned}\|h^{1/2}\sigma(\boldsymbol{\phi}_T)\mathbf{n}_e\|_{L^2(A_1D)} &= \|h^{1/2}\sigma^-(\boldsymbol{\phi}_T^-)\mathbf{n}_e\|_{L^2(A_1D)} \leqslant C\|\sigma^-(\boldsymbol{\phi}_T^-)\|_{L^2(\triangle A_1DA_3)}\\ &\leqslant C(\|\sigma^-(\boldsymbol{\phi}_T^-)\|_{L^2(\triangle A_1DE)} + \|\sigma^-(\boldsymbol{\phi}_T^-)\|_{L^2(\triangle A_3ED)})\\ &\leqslant C(\|\sigma^-(\boldsymbol{\phi}_T^-)\|_{L^2(\hat{T}^-)} + \|\sigma^-(\boldsymbol{\phi}_T^+)\|_{L^2(\triangle A_3ED)} + \|\sigma^-(\mathbf{c}_0L)\|_{L^2(\triangle A_3ED)}),\end{aligned} \tag{2.118}$$

where we have used the relation (2.104) between $\boldsymbol{\phi}_T^-$ and $\boldsymbol{\phi}_T^+$ in the last inequality. The second term in the last inequality of (2.118) can be bounded by

$$\begin{aligned}\|\sigma^-(\boldsymbol{\phi}_T^+)\|_{L^2(\triangle A_3ED)} &\leqslant C\left(\|\mu^-\epsilon(\boldsymbol{\phi}_T^+)\|_{L^2(\triangle A_3ED)} + \|\lambda^-\nabla\cdot\boldsymbol{\phi}_T^+\|_{L^2(\triangle A_3ED)}\right)\\ &\leqslant C\left(\frac{\mu_M}{\sqrt{\mu_m}}\|\sqrt{2\mu^+}\epsilon(\boldsymbol{\phi}_T^+)\|_{L^2(\hat{T}^+)} + \frac{\lambda_M}{\sqrt{\lambda_m}}\|\sqrt{\lambda^+}\nabla\cdot\boldsymbol{\phi}_T^+\|_{L^2(\hat{T}^+)}\right).\end{aligned} \tag{2.119}$$

For the third term in the last inequality of (2.118), we note that $\sigma^-(\mathbf{c}_0L)$ is a constant tensor and $|\triangle A_3ED| \leqslant Ch|l|$. Then, Lemma 2.17 implies

$$\begin{aligned}\|\sigma^-(\mathbf{c}_0L)\|_{L^2(\triangle A_3ED)} &= |\triangle A_3ED|^{1/2}\|\sigma^-(\mathbf{c}_0L)\|\\ &\leqslant C\left(\frac{\mu_M}{\sqrt{\mu_m}}\|\sqrt{2\mu}\epsilon(\boldsymbol{\phi}_T)\|_{L^2(T)} + \frac{\lambda_M}{\sqrt{\lambda_m}}\|\sqrt{\lambda}\nabla\cdot\boldsymbol{\phi}_T\|_{L^2(T)}\right).\end{aligned} \tag{2.120}$$

On the second piece DA_2 of e, applying the standard trace inequality (2.107) to the polynomial component $\boldsymbol{\phi}_T^+$ on $\triangle DA_2A_3$, we have

$$\begin{aligned}\|h^{1/2}\sigma(\boldsymbol{\phi}_T)\mathbf{n}_e\|_{L^2(DA_2)} &= \|h^{1/2}\sigma^+(\boldsymbol{\phi}_T^+)\mathbf{n}_e\|_{L^2(DA_2)} \leqslant C\|\sigma^+(\boldsymbol{\phi}_T^+)\|_{L^2(\triangle DA_2A_3)}\\ &\leqslant C\left(\frac{\mu_M}{\sqrt{\mu_m}}\|\sqrt{2\mu^+}\epsilon(\boldsymbol{\phi}_T^+)\|_{L^2(\hat{T}^+)} + \frac{\lambda_M}{\sqrt{\lambda_m}}\|\sqrt{\lambda^+}\nabla\cdot\boldsymbol{\phi}_T^+\|_{L^2(\hat{T}^+)}\right).\end{aligned} \tag{2.121}$$

Therefore, estimate (2.117) for the Case 1 rectangular interface element follows from (2.118)-(2.121) through the triangular inequality.

When T is a Case 2 rectangular interface element illustrated in Figure 2.8, we can simply apply the trace inequality (2.107) on $\triangle A_1DE$ and $\triangle DA_2E$:

$$\begin{aligned}\|h^{1/2}\sigma(\boldsymbol{\phi}_T)\mathbf{n}_e\|_{L^2(A_1D)} &= \|h^{1/2}\sigma^-(\boldsymbol{\phi}_T^-)\mathbf{n}_e\|_{L^2(A_1D)} \leqslant C\|\sigma^-(\boldsymbol{\phi}_T^-)\|_{L^2(\triangle A_1DE)}\\ &\leqslant C\left(\|\sqrt{2\mu^-}\epsilon(\boldsymbol{\phi}_T^-)\|_{L^2(\hat{T}^-)} + \|\sqrt{\lambda^-}\nabla\cdot\boldsymbol{\phi}_T^-\|_{L^2(\hat{T}^-)}\right),\end{aligned} \tag{2.122}$$

$$\begin{aligned}\|h^{1/2}\sigma(\boldsymbol{\phi}_T)\mathbf{n}_e\|_{L^2(DA_2)} &= \|h^{1/2}\sigma^+(\boldsymbol{\phi}_T^+)\mathbf{n}_e\|_{L^2(DA_2)} \leqslant C\|\sigma^+(\boldsymbol{\phi}_T^+)\|_{L^2(\triangle DA_2E)}\\ &\leqslant C\left(\|\sqrt{2\mu^+}\epsilon(\boldsymbol{\phi}_T^+)\|_{L^2(\hat{T}^+)} + \|\sqrt{\lambda^+}\nabla\cdot\boldsymbol{\phi}_T^+\|_{L^2(\hat{T}^+)}\right),\end{aligned} \tag{2.123}$$

from which estimate (2.117) follows through the triangular inequality.

Triangular interface elements: Assuming T is a Case 1 triangular interface element illustrated in Figure 2.9, without loss of generality, we also only need to consider the interface edge A_1A_2. If $|A_1E| \leqslant h/2$, by Lemma 2.17, estimate (2.115) holds. Then (2.117) follows from arguments similar to those for (2.118)-(2.121). If $|A_1E| \geqslant h/2$, the proof reduces to the application of the standard trace inequality (2.107) on $\triangle A_1DE$ and $\triangle DA_2E$, and (2.117) follows from arguments similar to those for (2.122) and (2.123). The result for a Case 2 triangular interface element illustrated in Figure 2.9 can be proven similarly. □

Remark 2.10. *We highlight that the relation* (2.104) *together with the estimate* (2.115) *suggests the connection of the two component polynomials in an IFE function, i.e., the difference of the two polynomial components of an IFE function is always bounded by the energy norm of the IFE function itself. On each interface element, although an IFE function is a piecewise polynomial, by this connection, its two component polynomials behave collectively like a standard polynomial, which, we believe, is the foundation that the stress trace inequality given in* (2.117) *can hold and is also the fundamental spirit in its proof.*

2.6.2 Error Estimation of the PPIFE Method

Now, we are ready to estimate errors in the PPIFE solution described by (2.103). We begin with discussing the following two quantities:

$$\|\mathbf{v}\|_h^2 = \sum_{T\in\mathcal{T}_h}\int_T 2\mu\|\epsilon(\mathbf{v})\|^2 dX + \sum_{T\in\mathcal{T}_h}\int_T \lambda\|\nabla\cdot\mathbf{v}\|^2 dX + \sum_{e\in\mathring{\mathcal{E}}_h^i}\rho\int_e \|h^{-1/2}[\mathbf{v}]\|^2 ds, \tag{2.124a}$$

$$|||\mathbf{v}|||_h^2 = \|\mathbf{v}\|_h^2 + \sum_{e\in\mathring{\mathcal{E}}_h^i}\rho^{-1}\int_e \|h^{1/2}\{\sigma(\mathbf{v})\mathbf{n}_e\}\|^2 ds. \tag{2.124b}$$

It is clear that

$$\|\mathbf{v}\|_h \leqslant |||\mathbf{v}|||_h, \quad \forall \mathbf{v}\in\mathbf{V}_h. \tag{2.125}$$

Indeed, in the spirit of [94], we can show that they are norms on the space $\mathbf{V}_h$.

Lemma 2.18. $|||\cdot|||_h$ *and* $\|\cdot\|_h$ *both are norms of* $\mathbf{V}_h$.

Proof. We present arguments only for $|||\cdot|||_h$ because the arguments for $\|\cdot\|_h$ are similar. It is obvious that we only need to show that $|||\mathbf{v}|||_h \neq 0$ for every nonzero $\mathbf{v}\in\mathbf{V}_h$. Suppose $|||\mathbf{v}|||_h = 0$ for some $\mathbf{v}\in\mathbf{V}_h(\Omega)$, then $\|\epsilon(\mathbf{v})\|_{L^2(T)} = 0$ for every $T\in\mathcal{T}_h$. Thus, by direct application of calculus, $\mathbf{v} = \mathbf{p}_T + q_T(-x_2, x_1)^T$ on each non-interface element $T\in\mathcal{T}_h^n$, and $\mathbf{v} = \mathbf{p}_T^s + q_T^s(-x_2, x_1)^T$ on T^s, $s = \pm$ on each interface element $T\in\mathcal{T}_h^i$, where q_T, q_T^s and $\mathbf{p}_T = (p_T^1, p_T^2)^T$, $\mathbf{p}_T^s = (p_T^{s,1}, p_T^{s,2})^T$ are some constants (vectors) defined on each element. The continuity on interior non-interface edges and $\|h^{-1/2}[\mathbf{v}]\| = 0$ on every $e\in\mathring{\mathcal{E}}_h^i$ yield that $\mathbf{p}_T = \mathbf{p}_T^s = \mathbf{p}$ and $q_T = q_T^s = q$ for all the elements $T\in\mathcal{T}_h$ for some constant q and vector $\mathbf{p}$. In addition, since $\mathbf{v}|_{\partial\Omega_D} = \mathbf{0}$, we have $\mathbf{p} = \mathbf{0}$, $q = 0$ and thus $\mathbf{v} = \mathbf{0}$ on Ω. □

We can establish another relationship for these two norms.

Lemma 2.19. *For sufficient large ρ, there holds $|||\mathbf{v}|||_h \leqslant \sqrt{2}\|\mathbf{v}\|_h$, $\forall \mathbf{v} \in \mathbf{S}_h(\Omega)$.*

Proof. For each $e \in \mathring{\mathcal{E}}_h^i$, let T_e^1 and T_e^2 be the two elements sharing e. By the trace inequality in Theorem 2.13 we have

$$\rho^{-1}\|h^{1/2}\{\sigma(\mathbf{v})\mathbf{n}_e\}\|_{L^2(e)}^2 \leqslant \frac{C_t^2}{2\rho}\sum_{i=1,2}\left(\|\sqrt{2\mu}\epsilon(\mathbf{v})\|_{L^2(T_e^i)}^2 + \|\sqrt{\lambda}\nabla\cdot\mathbf{v}\|_{L^2(T_e^i)}^2\right). \tag{2.126}$$

Then by adding and subtracting the term $\sum_{e\in\mathring{\mathcal{E}}_h^i}\rho^{-1}\int_e\|h^{1/2}\{\sigma(\mathbf{v})\mathbf{n}_e\}\|^2 ds$ in the norm $\|\cdot\|_h$ defined by (2.124a) and using (2.126), we have

$$\begin{aligned}\|\mathbf{v}\|_h^2 \geqslant& \left(1-\frac{C_t^2}{\rho}\right)\left(\sum_{T\in\mathcal{T}_h}\|\sqrt{2\mu}\epsilon(\mathbf{v})\|_{L^2(T)}^2 + \sum_{T\in\mathcal{T}_h}\|\sqrt{\lambda}\nabla\cdot\mathbf{v}_h\|_{L^2(T)}^2\right)\\ &+\sum_{e\in\mathring{\mathcal{E}}_h^i}\rho^{-1}\|h^{1/2}\{\sigma(\mathbf{v})\mathbf{n}_e\}\|_{L^2(e)}^2 + \sum_{e\in\mathring{\mathcal{E}}_h^i}\rho\|h^{-1/2}[\mathbf{v}]\|_{L^2(e)}^2,\end{aligned} \tag{2.127}$$

which yields $\|\mathbf{v}\|_h^2 \geqslant \frac{1}{2}|||\mathbf{v}|||_h^2$ by taking $\rho = 2C_t^2$. □

Remark 2.11. *Lemma 2.19 together with* (2.125) *imply that the two energy norms given by* (2.124a) *and* (2.124b) *are equivalent in the IFE space $\mathbf{S}_h(\Omega)$ when ρ is large enough, which, according to Theorem 2.13, can be sufficiently satisfied by choosing its value such that*

$$\rho \geqslant 2\max\left\{\frac{\mu_M^2}{\mu_m}, \frac{\lambda_M^2}{\lambda_m}\right\}\widetilde{C}_t^2. \tag{2.128}$$

We need to gauge the interpolation errors in terms of the energy norms (2.124) for which we shall estimate the errors on interface edges. Similar edge estimation is obtained in [148] for elliptic interface problems by assuming a $H^3(\Omega^{\pm})$ regularity for the exact solutions. Here, inspired by ideas presented in [87], we circumvent the excessive H^3 assumption by carrying out related analysis on a patch or macro-element around each interface element so that an error bound in the optimal order can be derived under the usual H^2 regularity assumption. Using the Patch Assumption and the estimates (2.91) and (2.92), we can apply the standard trace inequality to estimate the interpolation errors on interface edges.

Theorem 2.14. *Assume the mesh $\mathcal{T}_h$ is sufficiently fine and satisfies the Patch Assumption. Then, there exists a constant C such that the following estimate holds:*

$$\sum_{e\in\mathring{\mathcal{E}}_h^i}\|\{\sigma(\mathbf{u}-I_h\mathbf{u})\}\mathbf{n}_e\|_{L^2(e)} \leqslant Ch^{1/2}\|\mathbf{u}\|_{H^2(\Omega)}, \quad \forall \mathbf{u}\in\mathbf{PH}^2(\Omega). \tag{2.129}$$

Proof. For each $T \in \mathcal{T}_h^i$, we consider its patch ω_T. Let $e \in \mathcal{E}_h^i$ be one edge of T and denote the subedges in each subdomain by $e^s = e \cap \Omega^s$, $s = \pm$. According to the Patch Assumption, there exist triangles $T_e^s \in \omega_T$ with e^s as one of its edge such that $T_e^s \subset \Omega^s$ and $C_1 h \leqslant |T_e^s|/|e^s|$. Then we apply the standard trace inequality on T_e^s and use the estimate (2.92) to obtain

$$\begin{aligned}\|\nabla(I_{h,T}\mathbf{u} - \mathbf{u})\|_{L^2(e^s)} &\leqslant C|e^s|^{1/2}/|T_e^s|^{1/2}\left(\|\nabla(I_{h,T}\mathbf{u} - \mathbf{u})\|_{L^2(T_e^s)} + h\|\nabla^2(I_{h,T}\mathbf{u} - \mathbf{u})\|_{L^2(T_e^s)}\right)\\ &\leqslant Ch^{1/2}(\|\mathbf{u}\|_{H^2(\omega_T)} + \|\mathbf{u}\|_{W^{1,6}(\omega_T)}).\end{aligned} \tag{2.130}$$

For each $e \in \mathcal{E}_h^i$, let T_e^1 and T_e^2 be the two interface elements sharing e, then (2.130) implies

$$\begin{aligned}\sum_{e\in\mathring{\mathcal{E}}_h^i}\|\{\sigma(\mathbf{u} - I_h\mathbf{u})\}\mathbf{n}_e\|_{L^2(e)} &\leqslant C\sum_{e\in\mathring{\mathcal{E}}_h^i}\left(\|\nabla(I_{h,T_e^1}\mathbf{u} - \mathbf{u})\|_{L^2(e)} + \|\nabla(I_{h,T_e^2}\mathbf{u} - \mathbf{u})\|_{L^2(e)}\right)\\ &\leqslant Ch^{1/2}\sum_{e\in\mathring{\mathcal{E}}_h^i}\sum_{j=1,2}\left(\|\mathbf{u}\|_{H^2(\omega_{T_e^j})} + \|\mathbf{u}\|_{W^{1,6}(\omega_{T_e^j})}\right)\\ &\leqslant Ch^{1/2}(\|\mathbf{u}\|_{H^2(\Omega)} + \|\mathbf{u}\|_{W^{1,6}(\Omega)}),\end{aligned} \tag{2.131}$$

where we have used the finite overlapping property of ω_T, $T \in \mathcal{T}_h^i$. Finally, we obtain (2.129) by applying the standard imbedding inequality $\|w\|_{W^{1,6}(\Omega^s)} \leqslant C\|w\|_{H^2(\Omega^s)}$ [173], $\forall w \in W^{1,6}(\Omega^s)$, $s = \pm$ to (2.131) with $w = u_1$ and u_2. □

Now we can estimate the interpolation error $I_h\mathbf{u} - \mathbf{u}$ in terms of the energy norms.

Theorem 2.15. *Assume the mesh $\mathcal{T}_h$ is sufficiently fine and satisfies the Patch Assumption. Then there exists a constant C such that the following estimates hold for every $\mathbf{u} \in \mathbf{PH}^2(\Omega)$:*

$$\|I_h\mathbf{u} - \mathbf{u}\|_h \leqslant Ch\|\mathbf{u}\|_{H^2(\Omega)}, \tag{2.132a}$$

$$|||I_h\mathbf{u} - \mathbf{u}|||_h \leqslant Ch\|\mathbf{u}\|_{H^2(\Omega)}. \tag{2.132b}$$

Proof. Since (2.132a) directly follows from (2.132b) because of (2.125), we only need to prove (2.132b). According to the interpolation error estimation in terms of H^1 norm given by Theorem 5.9 in [81], we directly have

$$\sum_{T\in\mathcal{T}_h}\int_T 2\mu\|\epsilon(I_h\mathbf{u} - \mathbf{u})\|^2 dX + \sum_{T\in\mathcal{T}_h}\int_T \lambda\|\nabla\cdot(I_h\mathbf{u} - \mathbf{u})\|^2 dX \leqslant Ch^2\|\mathbf{u}\|^2_{H^2(\Omega)}. \tag{2.133}$$

In addition, since $I_h\mathbf{u} - \mathbf{u} \in [H^1(T)]^2$ for each interface element $T \in \mathcal{T}_h^i$, we apply the trace

inequality and the approximation capability of Theorem 5.9 in [81] to obtain

$$\begin{aligned}\sum_{e\in\mathring{\mathcal{E}}_h^i}\int_e \|h^{-1/2}[I_h\mathbf{u}-\mathbf{u}]\|^2 ds &\leqslant Ch^{-1}\sum_{e\in\mathring{\mathcal{E}}_h^i}\sum_{j=1,2}\|(I_h\mathbf{u}-\mathbf{u})|_{T_e^j}\|^2_{L^2(e)}\\ &\leqslant Ch^{-2}\sum_{e\in\mathring{\mathcal{E}}_h^i}\sum_{j=1,2}\left(\|I_h\mathbf{u}-\mathbf{u}\|^2_{L^2(T_e^j)}+h^2\|\nabla(I_h\mathbf{u}-\mathbf{u})\|^2_{L^2(T_e^j)}\right)\\ &\leqslant Ch^{-2}\left(\|I_h\mathbf{u}-\mathbf{u}\|^2_{L^2(\Omega)}+h^2\|\nabla(I_h\mathbf{u}-\mathbf{u})\|^2_{L^2(\Omega)}\right)\\ &\leqslant Ch^2\|\mathbf{u}\|^2_{H^2(\Omega)},\end{aligned} \tag{2.134}$$

where T_e^1 and T_e^2 are two elements sharing the interface edge e. Finally applying (2.134), (2.133) and Theorem 2.14 to $\|\!|I_h\mathbf{u}-\mathbf{u}|\!\|_h$ according to its definition given in (2.124b) leads the desired estimation (2.132b). □

With the energy norms $\|\!|\cdot|\!\|_h$ and $\|\cdot\|_h$, we can prove the coercivity and continuity for the bilinear form $a_h(\cdot,\cdot)$ defined by (2.101).

Theorem 2.16. *The bilinear form $a_h(\cdot,\cdot)$ has the coercivity as follows:*

- *For SPPIFE and IPPIFE, the following inequality holds for ρ sufficiently large:*

$$a_h(\mathbf{v},\mathbf{v})\geqslant\frac{1}{2}\|\!|\mathbf{v}|\!\|_h^2,\quad\forall\mathbf{v}\in\mathbf{S}_h(\Omega). \tag{2.135}$$

- *For NPPIFE, the following inequality holds for $\rho>0$:*

$$a_h(\mathbf{v},\mathbf{v})\geqslant\|\mathbf{v}\|_h^2,\quad\forall\mathbf{v}\in\mathbf{V}_h. \tag{2.136}$$

Proof. For the NPPIFE, i.e., $\theta=1$, we note that the coercivity (2.136) directly follows from the definitions for $a_h(\cdot,\cdot)$ and $\|\cdot\|_h$ given in (2.101) and (2.124a), respectively. For the SPPIFE or IPPIFE, i.e., $\theta=0$ or -1, letting $\mathbf{u}=\mathbf{v}$ in (2.101), we have

$$\begin{aligned}a_h(\mathbf{v},\mathbf{v}) &= \sum_{T\in\mathcal{T}_h}\int_T\|\sqrt{2\mu}\epsilon(\mathbf{v})\|^2dX+\sum_{T\in\mathcal{T}_h}\int_T\|\sqrt{\lambda}\nabla\cdot\mathbf{v}\|^2dX\\ &\quad+(\theta-1)\sum_{e\in\mathring{\mathcal{E}}_h^i}\int_e\{\sigma(\mathbf{v})\mathbf{n}_e\}\cdot[\mathbf{v}]ds+\sum_{e\in\mathring{\mathcal{E}}_h^i}\rho\int_e\|h^{-1/2}[\mathbf{v}]\|^2ds.\end{aligned} \tag{2.137}$$

We only need to bound the third term in (2.137). For each interface edge $e\in\mathring{\mathcal{E}}_h^i$, let T_e^1 and T_e^2 be its two adjacent interface elements under the notation of (2.96). Then, by the

trace inequality for IFE functions given by Theorem 2.13, Hölder's inequality, and Young's inequality, we have

$$\begin{aligned}\int_e \{\sigma(\mathbf{v})\mathbf{n}_e\}\cdot[\mathbf{v}]ds &= \int_e \frac{1}{2}\left(\sigma(\mathbf{v}|_{T_e^1})\mathbf{n}_e+\sigma(\mathbf{v}|_{T_e^2})\mathbf{n}_e\right)\cdot[\mathbf{v}]ds\\ &\leqslant \frac{1}{2}\left(\|h^{1/2}\sigma(\mathbf{v}|_{T_e^1})\mathbf{n}_e\|_{L^2(e)}+\|h^{1/2}\sigma(\mathbf{v}|_{T_e^2})\mathbf{n}_e\|_{L^2(e)}\right)\|h^{-1/2}[\mathbf{v}]\|_{L^2(e)}\\ &\leqslant \frac{C_t}{2}\left(\sum_{i=1,2}\|\sqrt{2\mu}\epsilon(\mathbf{v})\|_{L^2(T_e^i)}+\|\sqrt{\lambda}\nabla\cdot\mathbf{v}\|_{L^2(T_e^i)}\right)\|h^{-1/2}[\mathbf{v}_h]\|_{L^2(e)}\\ &\leqslant \frac{\alpha}{2}\left(\sum_{i=1,2}\|\sqrt{2\mu}\epsilon(\mathbf{v})\|^2_{L^2(T_e^i)}+\|\sqrt{\lambda}\nabla\cdot\mathbf{v}\|^2_{L^2(T_e^i)}\right)+\frac{C_t^2}{2\alpha}\|h^{-1/2}[\mathbf{v}_h]\|^2_{L^2(e)},\end{aligned} \tag{2.138}$$

where $\alpha>0$ and the constant C_t is from the the trace inequality in Theorem 2.13. Since $|\theta-1|\leq 2$, substituting (2.138) into (2.137) leads to

$$\begin{aligned}a_h(\mathbf{v},\mathbf{v}) \geqslant (1-\alpha)&\left(\sum_{T\in\mathcal{T}}\|\sqrt{2\mu}\epsilon(\mathbf{v})\|^2_{L^2(T)}+\sum_{T\in\mathcal{T}_h}\|\sqrt{\lambda}\nabla\cdot\mathbf{v}\|^2_{L^2(T)}\right)\\ &+\sum_{e\in\mathring{\mathcal{E}}_h^i}\left(\rho-\frac{C_t^2}{\alpha}\right)\|h^{-1/2}[\mathbf{v}]\|^2_{L^2(e)}.\end{aligned} \tag{2.139}$$

Then, by adding and subtracting $\sum_{e\in\mathring{\mathcal{E}}_h^i}\rho^{-1}\|\{\sigma(\mathbf{v})\mathbf{n}_e\}\|^2_{L^2(e)}$ in (2.139), and applying the inequality (2.126), we have

$$\begin{aligned}a_h(\mathbf{v},\mathbf{v}) \geqslant \left(1-\alpha-\frac{C_t^2}{\rho}\right)&\left(\sum_{T\in\mathcal{T}}\|\sqrt{2\mu}\epsilon(\mathbf{v})\|^2_{L^2(T)}+\sum_{T\in\mathcal{T}_h}\|\sqrt{\lambda}\nabla\cdot\mathbf{v}_h\|^2_{L^2(T)}\right)\\ &+\sum_{e\in\mathring{\mathcal{E}}_h^i}\rho^{-1}\|h^{1/2}\{\sigma(\mathbf{v})\mathbf{n}_e\}\|^2_{L^2(e)}+\sum_{e\in\mathring{\mathcal{E}}_h^i}\left(\rho-\frac{C_t^2}{\alpha}\right)\|h^{-1/2}[\mathbf{v}]\|^2_{L^2(e)}.\end{aligned} \tag{2.140}$$

Finally, by letting $\alpha=1/4$ and $\rho=4C_t^2+1/2$ in (2.140), we have the coercivity (2.135). □

Remark 2.12. *According to Theorem 2.13 and the proof above, for $a_h(\cdot,\cdot)$ in the SPPIFE and IPPIFE methods to be coercive, it is sufficient to choose ρ such that*

$$\rho \geqslant 4\max\left\{\frac{\mu_M^2}{\mu_m},\frac{\lambda_M^2}{\lambda_m}\right\}\widetilde{C}_t^2+\frac{1}{2}, \tag{2.141}$$

where $\widetilde{C}_t$ is independent of the interface location and Lamé parameters. Here we choose stability parameters large enough to enforce and prove the stability, and this technique is widely used in the interior penalty discontinuous Galerkin (IPDG) methods, for example [66, 183].

Theorem 2.17. *For every $\mathbf{w}, \mathbf{v} \in \mathbf{V}_h$, there holds*

$$a_h(\mathbf{w}, \mathbf{v}) \leqslant C_b |||\mathbf{w}|||_h |||\mathbf{v}|||_h, \tag{2.142}$$

where $C_b \leq 5$.

Proof. According to the definition (2.101), we have

$$\begin{aligned} a_h(\mathbf{w}, \mathbf{v}) = & \sum_{T \in \mathcal{T}_h} \int_T 2\mu \epsilon(\mathbf{w}) : \epsilon(\mathbf{v}) dX + \sum_{T \in \mathcal{T}_h} \int_T \lambda (\nabla \cdot \mathbf{w})(\nabla \cdot \mathbf{v}) dX \\ & + \theta \sum_{e \in \mathring{\mathcal{E}}_h^i} \int_e \{\sigma(\mathbf{v}) \mathbf{n}_e\} \cdot [\mathbf{w}] ds - \sum_{e \in \mathring{\mathcal{E}}_h^i} \int_e \{\sigma(\mathbf{w}) \mathbf{n}_e\} \cdot [\mathbf{v}] ds + \sum_{e \in \mathring{\mathcal{E}}_h^i} \frac{\rho}{h} \int_e [\mathbf{w}] \cdot [\mathbf{v}] ds. \end{aligned} \tag{2.143}$$

Denote each term on the right in (2.143) by Q_i, $i = 1, 2, \cdots, 5$. For Q_1, Q_2, the Hölder's inequality directly yields

$$|Q_1| \leqslant \sum_{T \in \mathcal{T}_h} \| \sqrt{2\mu} \epsilon(\mathbf{w}) \|_{L^2(T)} \| \sqrt{2\mu} \epsilon(\mathbf{v}) \|_{L^2(T)} \leqslant |||\mathbf{w}|||_h \, |||\mathbf{v}|||_h, \tag{2.144}$$

$$|Q_2| \leqslant \sum_{T \in \mathcal{T}_h} \| \sqrt{\lambda} (\nabla \cdot \mathbf{w}) \|_{L^2(T)} \| \sqrt{\lambda} (\nabla \cdot \mathbf{v}) \|_{L^2(T)} \leqslant |||\mathbf{w}|||_h \, |||\mathbf{v}|||_h. \tag{2.145}$$

For Q_3, Q_4 and Q_5, a similar argument yields

$$\begin{aligned} |Q_3| & \leqslant \sum_{e \in \mathring{\mathcal{E}}_h^i} \| \{\sigma(\mathbf{v}) \mathbf{n}_e\} \|_{L^2(e)} \, \| [\mathbf{w}] \|_{L^2(e)} \\ & \leqslant \left(\sum_{e \in \mathring{\mathcal{E}}_h^i} \rho^{-1} \| h^{1/2} \{\sigma(\mathbf{v}) \mathbf{n}_e\} \|_{L^2(e)}^2 \right)^{1/2} \left(\sum_{e \in \mathring{\mathcal{E}}_h^i} \rho \| h^{-1/2} [\mathbf{w}] \|_{L^2(e)}^2 \right)^{1/2} \\ & \leqslant |||\mathbf{w}|||_h |||\mathbf{v}|||_h, \end{aligned} \tag{2.146}$$

$$\begin{aligned} |Q_4| & \leqslant \sum_{e \in \mathring{\mathcal{E}}_h^i} \| \{\sigma(\mathbf{w}) \mathbf{n}_e\} \|_{L^2(e)} \, \| [\mathbf{v}] \|_{L^2(e)} \\ & \leqslant \left(\sum_{e \in \mathring{\mathcal{E}}_h^i} \rho^{-1} \| h^{1/2} \{\sigma(\mathbf{w}) \mathbf{n}_e\} \|_{L^2(e)}^2 \right)^{1/2} \left(\sum_{e \in \mathring{\mathcal{E}}_h^i} \rho \| h^{-1/2} [\mathbf{v}] \|_{L^2(e)}^2 \right)^{1/2} \\ & \leqslant |||\mathbf{w}|||_h |||\mathbf{v}|||_h, \end{aligned} \tag{2.147}$$

$$\begin{aligned} |Q_5| & \leqslant \sum_{e \in \mathring{\mathcal{E}}_h^i} \rho^{1/2} \| h^{-1/2} [\mathbf{v}] \|_{L^2(e)} \, \rho^{1/2} \| h^{-1/2} [\mathbf{w}] \|_{L^2(e)} \\ & \leqslant \left(\sum_{e \in \mathring{\mathcal{E}}_h^i} \rho \| h^{-1/2} [\mathbf{v}] \|_{L^2(e)}^2 \right)^{1/2} \left(\sum_{e \in \mathring{\mathcal{E}}_h^i} \rho \| h^{1/2} [\mathbf{w}] \|_{L^2(e)}^2 \right)^{1/2} \\ & \leqslant |||\mathbf{v}|||_h \, |||\mathbf{w}|||_h. \end{aligned} \tag{2.148}$$

Combining (2.144)-(2.148), we obtain the boundedness (2.142). □

The coercivity guarantees the existence and uniqueness of the solution $\mathbf{u}_h$ determined by the PPIFE scheme (2.103). Now we are ready to analyze the error with the energy norm $|||\cdot|||_h$.

Theorem 2.18. *Assume $\mathbf{u} \in \mathbf{PH}^2(\Omega)$ is the exact solution to the elasticity interface problem (1.5)-(1.11), and let $\mathbf{u}_h$ be the corresponding PPIFE solution defined by (2.103) with ρ sufficiently large according to (2.141) for SPPIFE and IPPIFE methods or (2.128) for NPPIFE methods on a Cartesian triangular or Cartesian rectangular mesh $\mathcal{T}_h$ whose mesh size is sufficiently small. Then there exists a constant C such that*

$$|||\mathbf{u} - \mathbf{u}_h|||_h \leqslant Ch\|\mathbf{u}\|_{H^2(\Omega)}. \tag{2.149}$$

Proof. By (2.100) and (2.103), we have

$$a_h(\mathbf{u}_h - I_h\mathbf{u}, \mathbf{v}) = a_h(\mathbf{u} - I_h\mathbf{u}, \mathbf{v}), \quad \forall \mathbf{v} \in \mathbf{S}_h(T). \tag{2.150}$$

For the SPPIFE and IPPIFE methods, let ρ be large enough such that (2.141) is satisfied. Then, letting $\mathbf{v} = \mathbf{u}_h - I_h\mathbf{u}$ in (2.150), applying the coercivity (2.135) in Theorem 2.16 and boundedness in Theorem 2.17, we have

$$\begin{aligned} \frac{1}{2}|||\mathbf{u}_h - I_h\mathbf{u}|||_h^2 &\leqslant a_h(\mathbf{u}_h - I_h\mathbf{u}, \mathbf{u}_h - I_h\mathbf{u}) = a_h(\mathbf{u} - I_h\mathbf{u}, \mathbf{u}_h - I_h\mathbf{u}) \\ &\leqslant C_b|||\mathbf{u} - I_h\mathbf{u}|||_h \, |||\mathbf{u}_h - I_h\mathbf{u}|||_h, \end{aligned} \tag{2.151}$$

which leads to $|||\mathbf{u}_h - I_h\mathbf{u}|||_h \leqslant 2C_b|||\mathbf{u} - I_h\mathbf{u}|||_h$. For the NPPIFE method, let ρ be large enough such that (2.128) is satisfied. Then, applying Lemma 2.19, the coercivity (2.136) in Theorem 2.16, and the boundedness in Theorem 2.17, we have

$$\begin{aligned} \frac{1}{2}|||\mathbf{u}_h - I_h\mathbf{u}|||_h^2 &\leqslant \|\mathbf{u}_h - I_h\mathbf{u}\|_h^2 \leqslant a_h(\mathbf{u}_h - I_h\mathbf{u}, \mathbf{u}_h - I_h\mathbf{u}) = a_h(\mathbf{u} - I_h\mathbf{u}, \mathbf{u}_h - I_h\mathbf{u}) \\ &\leqslant C_b|||\mathbf{u} - I_h\mathbf{u}|||_h \, |||\mathbf{u}_h - I_h\mathbf{u}|||_h, \end{aligned} \tag{2.152}$$

which also leads to $|||\mathbf{u}_h - I_h\mathbf{u}||| \leqslant 2C_b|||\mathbf{u} - I_h\mathbf{u}|||_h$. Hence, for the PPIFE solution $\mathbf{u}_h$ generated by all the PPIFE schemes considered, by the triangle inequality and (2.132b) in Theorem 2.15, we have

$$|||\mathbf{u} - \mathbf{u}_h||| \leqslant |||\mathbf{u} - I_h\mathbf{u}|||_h + |||\mathbf{u}_h - I_h\mathbf{u}|||_h \leqslant (1 + 2C_b)|||\mathbf{u} - I_h\mathbf{u}|||_h \leqslant Ch\|\mathbf{u}\|_{H^2(\Omega)}. \tag{2.153}$$

□

At last, we use the duality argument to derive an error bound in L^2 norm.

Theorem 2.19. *Under the condition of Theorem 2.18, there exists a constant C such that*

$$\|\mathbf{u} - \mathbf{u}_h\|_{L^2(\Omega)} \leqslant Ch^2\|\mathbf{u}\|_{H^2(\Omega)}. \tag{2.154}$$

Proof. According to the regularity of elasticity interface problem in [131], we can define an auxiliary function $\boldsymbol{\omega} = (\omega_1, \omega_2)^T \in \mathbf{PH}^2(\Omega)$ which is the solution to (1.5)-(1.11) with the right hand side $\mathbf{f}$ replaced by the error $\mathbf{u} - \mathbf{u}_h$. Since $\mathbf{u} - \mathbf{u}_h \in \mathbf{V}_h$, a similar derivation to (2.97) and (2.98) yields

$$\|\mathbf{u} - \mathbf{u}_h\|^2_{L^2(\Omega)} = \int_\Omega (\text{div } \sigma(\boldsymbol{\omega})) \cdot (\mathbf{u} - \mathbf{u}_h) dX = a_h(\boldsymbol{\omega}, \mathbf{u} - \mathbf{u}_h). \tag{2.155}$$

Let $I_h\boldsymbol{\omega}$ be the interpolant of $\boldsymbol{\omega}$ in the IFE space. Since $I_h\boldsymbol{\omega} \in \mathbf{S}_h(\Omega)$ and $a_h(I_h\boldsymbol{\omega}, \mathbf{u}-\mathbf{u}_h) = 0$, we have $a_h(\boldsymbol{\omega}, \mathbf{u}-\mathbf{u}_h) = a_h(\boldsymbol{\omega} - I_h\boldsymbol{\omega}, \mathbf{u}-\mathbf{u}_h)$. Then the boundedness in Theorem 2.17 yields

$$\|\mathbf{u} - \mathbf{u}_h\|^2_{L^2(\Omega)} = a_h(\boldsymbol{\omega}, \mathbf{u}-\mathbf{u}_h) = a_h(\boldsymbol{\omega} - I_h\boldsymbol{\omega}, \mathbf{u}-\mathbf{u}_h) \leqslant C_b |\!|\!|\boldsymbol{\omega} - I_h\boldsymbol{\omega}|\!|\!|_h \, |\!|\!|\mathbf{u} - \mathbf{u}_h|\!|\!|_h. \tag{2.156}$$

In addition, the regularity [131] and (2.132b) in Theorem 2.15 lead to

$$|\!|\!|\boldsymbol{\omega} - I_h\boldsymbol{\omega}|\!|\!|_h \leqslant Ch\|\boldsymbol{\omega}\|_{H^2(\Omega)} \leqslant Ch\|\mathbf{u} - \mathbf{u}_h\|_{L^2(\Omega)}. \tag{2.157}$$

Finally, by combining (2.156), (2.157) and Theorem 2.18, we have

$$\|\mathbf{u} - \mathbf{u}_h\|^2_{L^2(\Omega)} \leqslant Ch^2\|\mathbf{u} - \mathbf{u}_h\|_{L^2(\Omega)}\|\mathbf{u}\|_{H^2(\Omega)}, \tag{2.158}$$

which leads to the estimate in (2.154). □

2.6.3 Numerical Examples

In this section, we compare the proposed PPIFE method and the classic IFE method [81, 153] for solving the linear elasticity interface problems through a group of numerical examples. Recall from [81, 153], the classic IFE solution $\mathbf{u}_h$ is defined by the following discretized variational form:

$$\sum_{T\in\mathcal{T}_h} \left(\int_T 2\mu\epsilon(\mathbf{u}_h) : \epsilon(\mathbf{v}_h) dX + \lambda(\nabla \cdot \mathbf{u}_h)(\nabla \cdot \mathbf{v}_h) dX \right) = \sum_{T\in\mathcal{T}_h} \int_T \mathbf{f} \cdot \mathbf{v}_h dX, \quad \forall \mathbf{v}_h \in \mathbf{S}_h^0(\Omega). \tag{2.159}$$

We note that the major difference between the proposed PPIFE method (2.101)-(2.103) and the classic IFE method (2.159) is those terms involving line integrals on interface edges added in (2.101) for dealing with the discontinuity of IFE functions.

In the numerical experiments, a Cartesian mesh for the domain $\Omega = (-1, 1) \times (-1, 1)$ is generated by partitioning Ω into $N \times N$ squares with the mesh size $h = 2/N$. For each example, we generate the numerical results with the bilinear SPPIFE ($\theta = -1$) with $\rho = 30 \max_{s=\pm}\{\lambda^s, \mu^s\}$ and the classic IFE method on a sequence of meshes, and estimate the convergence rates of the errors in $W^{k,p}$-norms (semi norms), $k = 0, 1$, $p = 2, \infty$, computed on every two consecutive meshes.

Example 1: We consider a simple interface problem whose interface is a line $\Gamma : x + y - 2\pi/3 = 0$ cutting Ω into two sub-domains $\Omega^- : x+y-1.5/\pi < 0$ and $\Omega^+ : x+y-1.5/\pi > 0$. The exact solution is also a linear vector function given by

$$\mathbf{u}^s(X) = \begin{cases} (x + y - 1.5/\pi)/\lambda^s, \\ (x + y - 1.5/\pi)/\lambda^s, \end{cases} \quad \text{on } \Omega^s,\ s = \pm, \tag{2.160}$$

with $\lambda^- = \mu^- = 1$ and $\lambda^+ = \mu^+ = 10$, by which the boundary condition and body force of the interface problem are determined. We note that the function (2.160) is in the corresponding elasticity IFE space. Compared to the obvious errors of the classic IFE method, the SPPIFE method can produce accurate results, i.e., the SPPIFE solution is exactly the function (2.160), see the results in Tables 2.2 and 2.3. We believe this is the consequence of the consistence of the PPIFE methods, i.e., if the exact solution $\mathbf{u}$ to the interface problem is such that $\mathbf{u} \in \mathbf{PH}^2(\Omega)$, then $a_h(\mathbf{u} - \mathbf{u}_h, \mathbf{v}_h) = 0$, $\forall \mathbf{v}_h \in \mathbf{S}_h^0(\Omega)$.

h	$\|\mathbf{u} - \mathbf{u}_h\|_{L^\infty(\Omega)}$	$\|\mathbf{u} - \mathbf{u}_h\|_{L^2(\Omega)}$	$\|\mathbf{u} - \mathbf{u}_h\|_{H^1(\Omega)}$
1/2	8.0840e-02	7.7812e-02	2.2946e-01
1/4	1.8265e-03	1.1554e-03	6.3312e-03
1/8	1.6146e-03	8.8800e-04	8.2845e-03

Table 2.2: Errors of classic IFE solutions for $\lambda^- = \mu^- = 1$, $\lambda^+ = \mu^+ = 10$.

h	$\|\mathbf{u} - \mathbf{u}_h\|_{L^\infty(\Omega)}$	$\|\mathbf{u} - \mathbf{u}_h\|_{L^2(\Omega)}$	$\|\mathbf{u} - \mathbf{u}_h\|_{H^1(\Omega)}$
1/2	4.4409e-16	4.5269e-16	8.8509e-16
1/4	3.9968e-15	3.1617e-15	1.0767e-14
1/8	1.7208e-15	1.1623e-15	5.4891e-15

Table 2.3: Errors of SPPIFE solutions for $\lambda^- = \mu^- = 1$, $\lambda^+ = \mu^+ = 10$.

Example 2: This is a benchmark example from [186] which has been used in other articles such as [25, 92]. This example has a cicular interface described by the zero level set: $x^2+y^2 = a^2$ that separates Ω into two sub-domains $\Omega^- : x^2 + y^2 < a^2$ and $\Omega^+ : x^2 + y^2 > a^2$. On Ω, the displacement is defined in the polar coordinates i.e., $\mathbf{u} = (u^r, u^\theta)^T$, where u^r and u^θ represent the radial component and circumferential component, respectively. Then the exact solution is given by $u^\theta = 0$ and

$$u^r(r) = \begin{cases} \left(\left(1 - \frac{b^2}{a^2}\right)c + \frac{b^2}{a^2}\right), & \text{on } \Omega^-, \\ \left(r - \frac{b^2}{r}\right)c + \frac{b^2}{r}, & \text{on } \Omega^+, \end{cases} \tag{2.161}$$

with

$$c = \frac{(\lambda^- + \mu^- + \mu^+)b^2}{(\lambda^+ + \mu^+)a^2 + (\lambda^- + \mu^-)(b^2 - a^2) + \mu^+ b^2}. \tag{2.162}$$

Also, the body force in Ω and the boundary displacement on $\partial\Omega$ are generated according to (2.161). We choose $a = \pi/8$ and $b = 2$ in (2.161) and (2.162), and employ the same Lamé parameters used by [25, 92, 186] in our computation: $\lambda^- = \mu^- = 0.4$ in Ω^- and $\lambda^+ = 5.7692$, $\mu^+ = 3.8461$ in Ω^+, which correspond to the Young's modules $E^- = 1$, $\nu^- = 0.25$ and $E^+ = 10$, $\nu^+ = 0.3$. The numerical results in Table 2.4 indicate a slow convergence of the classic IFE method. Nevertheless, according to Table 2.5, the PPIFE method converges optimally in both the L^2 norm and semi-H^1 norm. The data in Table 2.5 indicates the convergence of the PPIFE method in the L^∞ norm seems to be sub-optimal, but it is much better than the classic IFE method.

In summary, because those edge integral terms contribute favorably to the accuracy of the numerical solution and the related error estimation, the proposed PPIFE method is superior to the classic IFE method discussed in the literature [81, 153].

h	$\|\mathbf{u} - \mathbf{u}_h\|_{L^\infty(\Omega)}$	rate	$\|\mathbf{u} - \mathbf{u}_h\|_{L^2(\Omega)}$	rate	$\|\mathbf{u} - \mathbf{u}_h\|_{\mathbf{PH}^1(\Omega)}$	rate
1/10	8.0609E-2		4.6267E-2		6.5199E-1	
1/20	6.7026E-2	0.2662	2.0816E-2	1.1523	5.7409E-1	0.1836
1/40	5.3065E-2	0.3369	7.9983E-3	1.3799	3.9965E-1	0.5225
1/80	3.7741E-2	0.4917	3.5784E-3	1.1604	3.5914E-1	0.1542
1/160	1.7209E-2	1.1329	1.4183E-3	1.3352	2.5530E-1	0.4923
1/320	9.3939E-3	0.8734	5.5905E-4	1.3431	1.7710E-1	0.5277
1/640	5.0778E-3	0.8875	2.5381E-4	1.1393	1.3084E-1	0.4367

Table 2.4: Errors of the classic IFE solutions for $\lambda^- = \mu^- = 0.4$, $\lambda^+ = 5.7692$ and $\mu^+ = 3.8461$.

h	$\|\mathbf{u} - \mathbf{u}_h\|_{L^\infty(\Omega)}$	rate	$\|\mathbf{u} - \mathbf{u}_h\|_{L^2(\Omega)}$	rate	$\|\mathbf{u} - \mathbf{u}_h\|_{\mathbf{PH}^1(\Omega)}$	rate
1/10	6.9597E-2		3.5335E-2		4.6843E-1	
1/20	2.1967E-2	1.6637	8.2012E-3	2.1072	2.1572E-1	1.1187
1/40	4.9360E-3	2.1539	2.1165E-3	1.9542	1.0506E-1	1.0379
1/80	1.7577E-3	1.4897	5.1717E-4	2.0329	5.0728E-2	1.0504
1/160	4.9811E-4	1.8191	1.1584E-4	2.1585	2.3756E-2	1.0945
1/320	1.3869E-4	1.8446	2.7700E-5	2.0642	1.1531E-2	1.0428
1/640	3.8867E-5	1.8353	6.9254E-6	1.9999	5.7069E-3	1.0147

Table 2.5: Errors of SPPIFE solutions for $\lambda^- = \mu^- = 0.4$, $\lambda^+ = 5.7692$ and $\mu^+ = 3.8461$.

Chapter 3

Higher-Degree IFE Methods Based on A Cauchy Extension

In this chapter, we develop a new framework to construct and analyze arbitrary p-th degree IFE functions as well as the a related discontinuous Galerkin IFE (DGIFE) method. In this framework, the proposed p-th degree IFE functions are constructed by the discrete solutions of local Cauchy problems imposed on each interface element where the jump conditions are employed as the boundary conditions. Penalties on both the edges of interface elements and the interface itself are employed in the proposed DGIFE scheme to reduce the adverse effects from the discontinuities in IFE functions. Analysis is carried to show that the proposed p-th degree IFE space has the optimal approximation capability and to establish a group of trace inequalities for these IFE functions. These results are then used to prove that the proposed p-th degree DGIFE method has optimal convergence rates in both the L^2 and H^1 norms. The results of this chapter are also reported in [80].

3.1 Introduction

To facilitate discussions in this chapter, we herein recall the second order elliptic interface problem:

$$-\nabla \cdot (\beta \nabla u) = f, \quad \text{in } \Omega = \Omega^- \cup \Omega^+, \tag{3.1a}$$

$$u = 0, \quad \text{on } \partial\Omega, \tag{3.1b}$$

where Ω^- and Ω^+ are the subdomains of $\Omega \subseteq \mathbb{R}^2$ partitioned by a C^{p+1} simple curve Γ which does not intersect $\partial\Omega$, β is assumed to be a piecewise constant function defined as in (1.3) such that, without loss of generality, $\beta^- \geqslant \beta^+$ for the discussions in this chapter. Also, we have assumed the zero boundary condition in (3.1b) for simplifying the discussions,

all the results in this chapter can be readily extended to interface problems with a non-homogeneous boundary condition through the standard procedure. Besides, we employ the following functionals to denote the required jump conditions on the interface curve Γ:

$$\mathcal{J}_0(u) = [u]_\Gamma := u^+|_\Gamma - u^-|_\Gamma = 0, \tag{3.1c}$$

$$\mathcal{J}_1(u) = \left[\beta \nabla u \cdot \mathbf{n}\right]_\Gamma := \beta^+ \nabla u^+ \cdot \mathbf{n}|_\Gamma - \beta^- \nabla u^- \cdot \mathbf{n}|_\Gamma = 0, \tag{3.1d}$$

in which $\mathbf{n}$ is the unit normal vector to the interface Γ. When $p \geqslant 2$, following [5, 8, 9], in addition to the original jump conditions (3.1c) and (3.1d), we further impose the so called Laplacian extended jump conditions

$$\mathcal{J}_j(u) = \left[\beta \frac{\partial^{j-2} \triangle u}{\partial \mathbf{n}^{j-2}}\right]_\Gamma = 0, \quad j = 2, \cdots p. \tag{3.1e}$$

The jump conditions in (3.1e) are suggested by the smoothness of the body force term f across the interface curve which is in fact satisfied in many applications such as the the constant gravity [181], charge density in electrostatic [110], the source term in Helmholtz equations [118], and so on.

One dimensional IFE methods for arbitrary degree have already been investigated in the literature. The extended jump conditions (3.1e) were firstly employed in [9, 39, 146] for solving 1-D interface problems which led to unisolvence of the IFE shape functions and optimally convergent IFE spaces. Due to the trivial geometry of the interface (a point), these 1-D IFE functions can satisfy the all the jump conditions (3.1c)-(3.1e) exactly across the interface. Recently, the authors in [41] studied super convergence properties for these 1-D IFE spaces through the generalized orthogonal polynomials.

In two dimensions, compared with the lower-degree IFE methods in the literature [76, 79, 84, 100, 102, 136, 141, 145], there are two major issues in the development of higher-degree IFE methods. The first and a fundamental one concerns the construction. The current construction approaches for the lower-degree IFE spaces in the literature such as those reviewed in Section 1.2, all involve a certain linear approximation to the curved interface whose intrinsic $O(h^2)$ accuracy hinders the extension to IFE functions based on higher-degree polynomials from which a better than $O(h^2)$ accuracy is expected [4], see the discussions in Section 1.4. Since two polynomials in general can not satisfy the jump conditions exactly across a generic curved interface, it remains unknown in the literature how to enforce the jump conditions in a suitably weak sense such that the existence of IFE functions is guaranteed and the resulted IFE space has optimal approximation capabilities. The second issue concerns a suitable formulation in the related IFE schemes for solving the interface problems. Specifically, this is about the design of penalties to handle the discontinuities of IFE functions on edges and the interface.

There are more challenges for the error analysis of a higher-degree IFE method because of the lack of analysis tools in the literature handling macro polynomials. For example, the commonly used scaling argument is not applicable since piecewise polynomials do not

have the sufficient regularity and the related piecewise Sobolev spaces mapped from different interface elements to the reference element are not the same. In particular, it remains obscure how to show the approximation capabilities of higher-degree IFE spaces. The technique of multipoint Taylor expansions successfully used in the analysis for lower-degree IFE spaces is difficulty, if not impossible, to be utilized to analyze the approximation capabilities of higher-degree IFE spaces, see the discussions in Section 1.4. Besides, the penalties in the IFE scheme demand trace inequalities for IFE functions as piecewise polynomials on interface elements. Trace inequalities have been established for lower-degree IFE functions [148, 152] for which the proof highly relies on the constant gradients of the difference between two pieces of lower-degree polynomials; however, in general, this feature is not available for the higher-degree IFE functions. These issues motivate us to develop new tools in the development and analysis of higher-degree IFE methods.

There have been some exploratory works to address these issues for higher-degree IFE methods in two dimension. The authors in [3] introduced a correction function to construct the IFE shape functions for a linear interface, and this idea was also used in [86] to handle curved interface for a constant coefficient β. As for the interface problem with a curved interface and discontinuous coefficients, i.e., the one considered in this dissertation, the authors in [5] considered a L^2 inner product defined on the actual interface curve to penalize the jump conditions, but even the existence of the IFE shape functions has not been generally established in this approach. Later, the authors in [8, 214] developed a least squares method to construct the IFE shape functions for which the existence is a natural consequence of the least squares formulation. Specifically, in this approach, the IFE shape functions are constructed by minimizing a certain energy functional formed according to the jump conditions. However, the local linear system for constructing the IFE shape functions by this least squares approach can be ill-conditioned when the jump of $\beta^{\pm}$ is large or the size of subelements is too small.

In this chapter, we propose a new construction procedure for p-th degree IFE functions. By this procedure, an IFE function is the extension of a p-th degree polynomial from one subelement to the whole interface element by solving a local Cauchy problem on interface elements in which the original jump conditions across the interface are employed as the boundary conditions and all the extended jump conditions are reformulated into the Laplace's equation. We note that the extension idea from one piece to another in the construction of an IFE function was inspired by the one used in [88]. This approach completely addresses the existence issue of higher-degree IFE functions. The cumbersome case by case procedures [3, 79, 84, 100, 136, 176] for analyzing the existence of IFE functions based on different interface element configurations or different polynomial degrees are circumvented, see the related discussions in Section 1.4. The underlying idea in the proposed construction procedure can be traced back to the early works of Babuška, Caloz and Osborn [19, 21] which proposed special shape functions constructed by solving some local differential equations. This idea was further employed by Chu, Graham and Hou in [52] where the special shape functions were the piecewise linear finite element solutions of a local interface problem on a submesh in each interface element. In addition, Trefftz methods [137] also use exact solutions to

the related differential equations as parts in the approximation solution. As for the suitable formulation for the related p-th degree IFE methods, we propose to use penalties on interface edges like those used in the partially penalized IFE method in [85, 148] and on the interface itself like those used in CutFEM [155, 196].

The contributions made in thesis to higher-degree IFE methods are multifold. The core idea, i.e., constructing IFE functions by solving a Cauchy problem locally on each interface element, is invented in this chapter which leads to a so called Cauchy mapping to connect polynomial components in an IFE function. This mapping also plays a critical role in the related analysis such that major results including the existence of IFE functions, the approximation capabilities, and trace inequalities for the macro polynomials in the proposed IFE method can be traced back to properties of this mapping. The new analysis techniques developed in this thesis enable us to derive error bounds whose proportional constants are all independent of the interface location relative to the mesh. All of these together form a framework for us to establish the optimal convergence of a related DGIFE method. We believe the tools developed in this research overcome the limitations of current analysis techniques in the literature for macro polynomials and may be useful for other finite element methods based on unfitted meshes. To our best knowledge, the research presented here is the first systematic framework for both developing and analyzing p-th degree IFE methods for elliptic interface problems.

3.2 Notations and Assumptions

In this section, we introduce some basic notations and assumptions. Given a measurable subset $\widetilde{\Omega} \subseteq \Omega$, let $W^{k,q}(\widetilde{\Omega})$ be the standard Sobolev space with the norm $\|\cdot\|_{W^{k,q}(\widetilde{\Omega})}$ and semi-norm $|\cdot|_{W^{k,q}(\widetilde{\Omega})}$, $k \geqslant 0$, $1 \leqslant q \leqslant \infty$. In the case $\widetilde{\Omega}$ has a non-empty intersection with the interface Γ, we define $\widetilde{\Omega}^{\pm} = \widetilde{\Omega} \cap \Omega^{\pm}$, and further introduce the following the split space for $k \geq 1$ with the associated norm and semi-norm according to the jump conditions (3.1c)-(3.1e):

$$PW^{k,q}(\widetilde{\Omega}) = \Big\{ v \in W^{1,q}(\widetilde{\Omega}) \,:\, v|_{\tilde{\Omega}^{\pm}} \in W^{k,q}(\widetilde{\Omega}^{\pm});\ \mathcal{J}_i(u) = 0, i = 0, 1, \cdots, k-1 \Big\}, \tag{3.2a}$$

$$\|v\|_{W^{k,q}(\widetilde{\Omega})} = \|v\|_{W^{k,q}(\widetilde{\Omega}^-)} + \|v\|_{W^{k,q}(\widetilde{\Omega}^+)}, \quad |v|_{W^{k,q}(\widetilde{\Omega})} = |v|_{W^{k,q}(\widetilde{\Omega}^-)} + |v|_{W^{k,q}(\widetilde{\Omega}^+)}. \tag{3.2b}$$

In particular, when $q = 2$, we have the Hilbert spaces $H^k(\widetilde{\Omega})$ and $PH^k(\widetilde{\Omega})$ with norms $\|\cdot\|_{H^k(\widetilde{\Omega})}$, $\|\cdot\|_{PH^k(\widetilde{\Omega})}$ and semi-norms $|\cdot|_{H^k(\widetilde{\Omega})}$, $|\cdot|_{PH^k(\widetilde{\Omega})}$, respectively. Let $PW_0^{k,q}(\widetilde{\Omega})$ and $W_0^{k,q}(\widetilde{\Omega})$ be the related spaces with zero trace on $\partial\widetilde{\Omega}$. We note that the spaces in (3.2a) are different from those in (2.1) in the sense that the spaces in (3.2a) contain scalar functions and involve more jump conditions. Besides, we will use $\mathbb{P}_p$ to denote space of polynomials with degree not exceeding p.

We let $\mathcal{T}_h$ be a triangular mesh of Ω and let $h = \max_{T\in\mathcal{T}_h}\{h_T\}$ where h_T is the diameter of each element $T \in \mathcal{T}_h$. In the discussions of this chapter, we do not assume the mesh $\mathcal{T}_h$ is Cartesian, but we assume that it is shape-regular, i.e., there exists a constant σ such that

$$\frac{h_T}{\rho_T} \leqslant \sigma, \quad \forall T \in \mathcal{T}_h, \tag{3.3}$$

where ρ_T is the diameter of the largest inscribed circle of T. It is well known that the condition (3.3) yields the existence of constants $\theta_m, \theta_M \in (0, \pi)$ such that

$$\theta_m \leqslant \text{every angle of } T \leqslant \theta_M, \quad \forall T \in \mathcal{T}_h. \tag{3.4}$$

We still use $\mathcal{N}_h$ and $\mathcal{E}_h$ as the sets of nodes and edges of the mesh $\mathcal{T}_h$ and denote the sets of interface and non-interface elements in this mesh by $\mathcal{T}_h^i$ and $\mathcal{T}_h^n$. In this chapter, we specifically employ $\widetilde{\mathcal{E}}_h^i$ as the collection of all the edges of elements in $\mathcal{T}_h^i$ and $\widetilde{\mathcal{E}}_h^n = \mathcal{E}_h \backslash \widetilde{\mathcal{E}}_h^i$. Note that $\widetilde{\mathcal{E}}_h^i$ contains the non-interface edges of interface elements which are not in $\mathcal{E}_h^i$ used in Chapter 2.

As in [196], given each domain $K \subseteq \mathbb{R}^2$, we call $K' := \{X \in \mathbb{R}^2 : \exists Y \in K \text{ s.t. } \overrightarrow{OX} = \mu\overrightarrow{OY}\}$ the homothetic image of K with respect to the homothetic center O and the scaling constant μ. Hinted by [214], for each interface element $T \in \mathcal{T}_h^i$, we define its fictitious element T_λ as the homothetic image of T with the homothetic center being the incenter G of T and a scaling factor $\lambda \geqslant 1$ independent of mesh size h, and let $\Gamma_T^\lambda = \Gamma \cap T_\lambda$, see Figure 3.1 for an illustration. To facilitate a simple presentation of the main ideas, and without loss of generality, we assume that $T_\lambda \subset \Omega$ for every interface element T.

In addition, we employ $|\cdot|$ to denote the measure of a d-dimensional manifold such as edges for $d = 1$ and elements for $d = 2$. Also, the generic constants C appearing in estimates in this chapter are all assumed to be positive and independent of the mesh size h, the interface location relative to the mesh, and the coefficients $\beta^\pm$. Besides, following a convention in the literature, we employ the notation $q_1 \simeq q_2$ to denote the equivalence of two quantities q_1 and q_2, i.e., both $q_1 \leqslant Cq_2$ and $q_2 \leqslant Cq_1$ hold. We note that the generic constants C in Chapter 2 still depend on the discontinuous coefficients $\lambda^\pm$ and $\mu^\pm$ due to the limitation of the analysis method there; but in the analysis presented in this chapter, we are able to explicitly specify how the error bounds depend on the discontinuous coefficients in each estimate such that all the generic constants C are independent of the coefficients $\beta^\pm$.

Furthermore, we make two assumptions for the mesh $\mathcal{T}_h$ as follows:

(**A1**) The mesh is generated such that the interface Γ can intersect each interface element $T \in \mathcal{T}_h^i$ and its fictitious element T_λ at two distinct points which locate on two different edges of T and T_λ.

(**A2**) There exists a fixed integer N such that for each $K \in \mathcal{T}_h$, the number of elements in the set $\{T \in \mathcal{T}_h^i : K \cap T_\lambda \neq \emptyset\}$ is bounded by N.

We note that assumption (**A1**) can be satisfied when the mesh is fine enough, assumption (**A2**) can be satisfied if $\mathcal{T}_h$ is shape regular and $\lambda \geq 1$ is not too large.

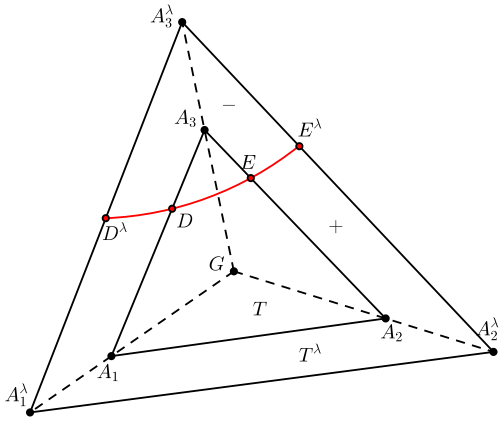

Figure 3.1: $T = \triangle A_1A_2A_3$ and its fictitious element $T_\lambda = \triangle A_1^\lambda A_2^\lambda A_3^\lambda$

To end this section, we describe the Sobolev extensions needed in discussions of this chapter. Given each $u \in PH_0^{p+1}(\Omega)$, we let $u_E^s \in H_0^{p+1}(\Omega)$ be the Sobolev extensions [72] of $u^s = u|_{\Omega^s}$ from $\Omega^s, s = -, +$ to Ω such that

$$\sum_{k=1}^{p+1} |u_E^s|_{H^k(\Omega)} \leqslant C_E \sum_{k=1}^{p+1} |u^s|_{H^k(\Omega^s)}, \quad s = -, +, \tag{3.5}$$

for some constant C_E depending only on $\Omega^\pm$, Ω and p. Estimate (3.5) follows from the boundedness for the Sobolev extensions (Theorem 7.25 in [72]) and the Poincaré inequality.

3.3 Some Basic Estimates

In this section, we first present some basic geometric estimates related to each interface element T and the associated fictitious element T_λ. These results enable us to establish a group of norm equivalences in the polynomial spaces to be used.

3.3.1 Geometric Estimates

Given an interface element $T = \triangle A_1A_2A_3 \in \mathcal{T}_h^i$ with its fictitious element $T_\lambda = A_1^\lambda A_2^\lambda A_3^\lambda$, $\lambda \geqslant 1$, without loss of generality, we only consider the interface element configuration where Γ cuts the edges $A_1^\lambda A_3^\lambda$ and $A_3^\lambda A_2^\lambda$ with the intersection points D^λ and E^λ, as shown by Figure 3.1. We note that the original element and the fictitious element may have different interface configuration; but for simplicity's sake, we also assume that Γ intersects the original element

T with the intersection points D and E on the edges A_1A_3 and A_2A_3. In this configuration, we let T_λ^- and T_λ^+ be the curved-edge triangle $D^\lambda E^\lambda A_3^\lambda$ and the curved-edge quadrilateral $A_1^\lambda A_2^\lambda E^\lambda D^\lambda$, respectively, as shown in Figure 3.1. First of all, due to the geometric relation between T_λ and T, we can follow the same arguments for Lemma 2.2 to prove the results in the following lemma.

Lemma 3.1. *On each T_λ, $\lambda \geqslant 1$, associated with an interface element $T \in \mathcal{T}_h^i$, assume h_T is small enough, then there exist constants δ_0 and δ_1 independent of the relative interface location inside T_λ and h_T such that for every two points $X_1, X_2 \in \Gamma \cap T_\lambda$ with their normal vectors $\mathbf{n}(X_1), \mathbf{n}(X_2)$ to Γ and every point $X \in \Gamma \cap T_\lambda$ with its orthogonal projection $X^\perp$ onto $D^\lambda E^\lambda$, the following estimates hold*

$$\|X - X^\perp\| \leqslant \delta_0 \lambda^2 h_T^2, \tag{3.6a}$$

$$\mathbf{n}(X_1) \cdot \mathbf{n}(X_2) \geqslant 1 - \delta_1 \lambda^2 h_T^2. \tag{3.6b}$$

Again, the estimates (3.6) describe the local flatness of the interface inside each interface element (the special case $\lambda = 1$) and the associated fictitious element. The constants δ_0, δ_1 depend only on the maximal curvature of Γ. Now we let θ_D and θ_E be the angles between the interface Γ and the ray $D^\lambda A_3^\lambda$, $E^\lambda A_3^\lambda$, see Figure 3.2 for an illustration. The following lemma describes the relative location of Γ inside T_λ.

Lemma 3.2. *For each T_λ, $\lambda > 1$, associated with an element $T \in \mathcal{T}_h^i$ as shown in Figure 3.2, assume h_T is small enough, then there exist positive constants θ^λ, l^λ and $r_\lambda^1 \leqslant r_\lambda^2 < 1$ independent of interface location and h_T such that*

$$\angle A_3^\lambda D^\lambda E^\lambda > \theta^\lambda, \quad \angle A_3^\lambda E^\lambda D^\lambda > \theta^\lambda \quad \theta_D > \theta^\lambda, \quad \theta_E > \theta^\lambda, \tag{3.7a}$$

$$r_\lambda^1 \leqslant \min\left\{ \frac{|A_3^\lambda D^\lambda|}{|A_3^\lambda A_1^\lambda|}, \frac{|A_3^\lambda E^\lambda|}{|A_3^\lambda A_2^\lambda|} \right\} \leqslant r_\lambda^2. \tag{3.7b}$$

$$|\Gamma_T^\lambda| > |D^\lambda E^\lambda| > l^\lambda h_T. \tag{3.7c}$$

Proof. First, in order to show (3.7a), we consider the auxiliary angle $\angle A_3^\lambda D^\lambda D$, as shown by Figure 3.2. Denote the normal vectors to $D^\lambda E^\lambda$ and $D^\lambda D$ by $\bar{\mathbf{n}}$ and $\bar{\mathbf{n}}_0$. By geometry and (3.6b), there holds

$$\cos(\angle A_3^\lambda D^\lambda E^\lambda - \angle A_3^\lambda D^\lambda D) = \bar{\mathbf{n}} \cdot \bar{\mathbf{n}}_0 \geqslant 1 - \delta_1 \lambda^2 h_T^2. \tag{3.8}$$

We note that the smallest case for $\angle A_3^\lambda D^\lambda D$ is $\angle A_3^\lambda A_1^\lambda A_3$ directly calculated by

$$\begin{aligned} \angle A_3^\lambda A_1^\lambda A_3 &= \tan^{-1}\left(\frac{\lambda - 1}{\lambda \cot(\angle A_3^\lambda A_1^\lambda A_1) + \cot(\angle A_3 A_3^\lambda A_1^\lambda)} \right) \\ &\geqslant \tan^{-1}\left(\frac{\lambda - 1}{\lambda + 1} \tan(\theta_m/2) \right) := \theta_0, \end{aligned} \tag{3.9}$$

which only depends on λ and the shape regularity (3.4). So (3.8) and (3.9) yield

$$\angle A_3^\lambda D^\lambda E^\lambda \geqslant \angle A_3^\lambda D^\lambda D - \cos^{-1}(1-\delta_1\lambda^2 h^2) \geqslant \theta_0 - 2\sqrt{\delta_1}\lambda h_T, \tag{3.10}$$

which can be lower bounded by a positive constant independent of the interface location for h_T small enough. The argument for the angles $\angle A_3^\lambda E^\lambda D^\lambda$, θ_D and θ_E is similar.

Next, for (3.7b), we consider the auxiliary line connecting D and E which intersects the lines $A_1^\lambda A_3^\lambda$ and $A_2^\lambda A_3^\lambda$ at D_0^λ and E_0^λ, respectively. See Figure 3.3 for an illustration. From (3.6a) and (3.6b), it can be directly verified that the distance from E_0^λ to the line $D^\lambda E^\lambda$ is bounded by $(\delta_0\lambda^2+\sqrt{2\delta_1}\lambda)h_T^2$. Then (3.7a) yields $|E^\lambda E_0^\lambda| \leqslant (\delta_0\lambda^2+\sqrt{2\delta_1}\lambda)h_T^2/\sin(\theta^\lambda) := d_M h_T^2$, and so does $|D^\lambda D_0^\lambda|$. In addition, we let D_1^λ and E_1^λ be the intersection points of the edges A_1A_3 with $A_1^\lambda A_2^\lambda$ and $A_3^\lambda A_2^\lambda$, respectively. Similarly, we define D_2^λ and E_2^λ, as shown by Figure 3.3. Without loss of generality, we assume $|A_3^\lambda E_0^\lambda|/|A_3^\lambda A_2^\lambda| \leqslant |A_3^\lambda D_0^\lambda|/|A_3^\lambda A_1^\lambda|$. Then E_0^λ must be between E_1^λ and E_2^λ. Hence, it can be verified that $\frac{|A_3^\lambda E_2^\lambda|}{|A_3^\lambda A_2^\lambda|} \leqslant \frac{\sigma\lambda+1}{\sigma\lambda+\lambda}$ and $\frac{|A_3^\lambda E_1^\lambda|}{|A_3^\lambda A_2^\lambda|} \geqslant \frac{\lambda-1}{\sigma\lambda+\lambda}$. Therefore, we have

$$\min\left\{\frac{|A_3^\lambda E^\lambda|}{|A_3^\lambda A_2^\lambda|}, \frac{|A_3^\lambda D^\lambda|}{|A_3^\lambda A_1^\lambda|}\right\} \leqslant \min\left\{\frac{|A_3^\lambda E_0^\lambda|}{|A_3^\lambda A_2^\lambda|}, \frac{|A_3^\lambda D_0^\lambda|}{|A_3^\lambda A_1^\lambda|}\right\} + \frac{d_M h_T^2}{\rho_T} \leqslant \frac{\sigma\lambda+1}{\sigma\lambda+\lambda} + d_M\sigma h_T, \tag{3.11}$$

$$\min\left\{\frac{|A_3^\lambda E^\lambda|}{|A_3^\lambda A_2^\lambda|}, \frac{|A_3^\lambda D^\lambda|}{|A_3^\lambda A_1^\lambda|}\right\} \geqslant \min\left\{\frac{|A_3^\lambda E_0^\lambda|}{|A_3^\lambda A_2^\lambda|}, \frac{|A_3^\lambda D_0^\lambda|}{|A_3^\lambda A_1^\lambda|}\right\} - \frac{d_M h_T^2}{\rho_T} \geqslant \frac{\lambda-1}{\sigma\lambda+\lambda} - d_M\sigma h_T, \tag{3.12}$$

which can be both upper bounded from 1 and lower bounded from 0 for h_T small enough.

At last, for (3.7c), let $D_0^\lambda E_0^\lambda$ be the segment parallel to $D^\lambda E^\lambda$ passing through D, as shown by Figure 3.4. It is easy to verify that the shortest length of $D_0^\lambda E_0^\lambda$ is achieved when it is orthogonal to $A_3A_3^\lambda$ and passing through A_3, i.e., it moves to $D_3^\lambda E_3^\lambda$, as illustrated by Figure 3.4. Therefore, using (3.6a), we have

$$\begin{aligned} |D^\lambda E^\lambda| &\geqslant 2\tan(\angle A_3A_3^\lambda A_1^\lambda)(|A_3A_3^\lambda| - \delta_0\lambda^2 h_T^2) \\ &\geqslant 2\tan(\theta_m/2)\left(\frac{(\lambda-1)}{\sigma} - \delta_0\lambda^2 h_T\right) h_T \geqslant l^\lambda h_T, \end{aligned} \tag{3.13}$$

for some $l^\lambda > 0$ independent of interface location for h_T small enough, where we have used (3.3) and (3.4). □

Remark 3.1. *Lemma 3.2 actually shows that given each interface element T, the triangular curved-edge subelement of its fictitious element T_λ, $\lambda > 1$, has the regular shape.*

In the following discussions, we always assume the mesh size h is small enough such that the results in Lemma 3.1 and Lemma 3.2 hold. Next, we present an estimation of the difference between the Laplacians of the Sobolev extensions $u_E^\pm$.

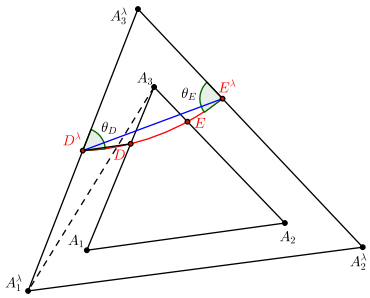

Figure 3.2: Angle estimation

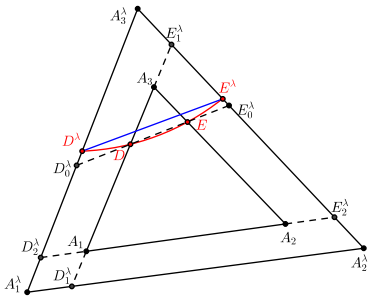

Figure 3.3: Ratio estimation

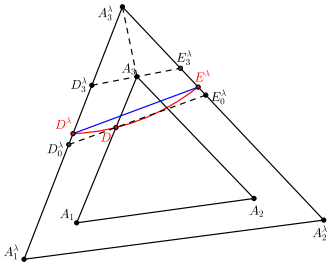

Figure 3.4: Length estimation

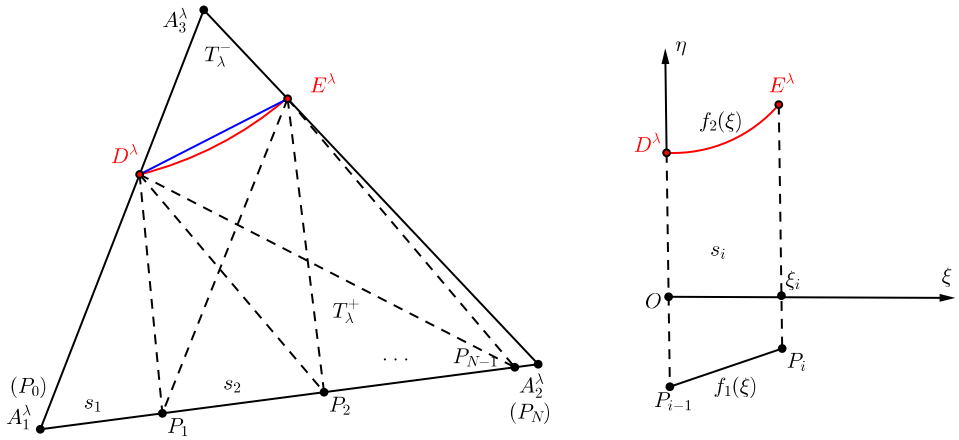

Figure 3.5: Interface elements and strips

Lemma 3.3. *Let $u \in PH^{p+1}(\Omega)$ with the integer $p \geqslant 1$ and the extensions $u_E^{\pm}$. Then, there exists a constant C such that on each interface element $T \in \mathcal{T}_h^i$ we have*

$$\|\beta^+ \triangle u_E^+ - \beta^- \triangle u_E^-\|_{L^2(T_\lambda)} \leqslant C h_T^{p-1} (\beta^+ |u_E^+|_{H^{p+1}(T_\lambda)} + \beta^- |u_E^-|_{H^{p+1}(T_\lambda)}), \quad \lambda > 1. \tag{3.14}$$

Proof. Let $w = \beta^+ \triangle u_E^+ - \beta^- \triangle u_E^- \in H^{p-1}(\Omega)$. Note that the case $p = 1$ is trivial, so we only discuss $p \geqslant 2$. Since $u_E^{\pm}|_{\Omega^{\pm}} = u^{\pm}$, by the definition (2.1), for $i = 0, 1, \cdots, p-2$, the i-th order trace of w on Γ_T^λ is zero.

First, for the curved-edge triangular subelement T_λ^-, according to (3.7a) and Remark 3.1, there exists an one-to-one mapping F [215] from the reference element $\hat{T} = \hat{A}_1\hat{A}_2\hat{A}_3$ with $\hat{A}_1 = (0,0)^T$, $\hat{A}_2 = (1,0)^T$ and $\hat{A}_3 = (0,1)^T$ on the $\hat{x}$-$\hat{y}$ plane to T_λ^- such that its Jacobian satisfies

$$C_1 h_T^2 \leqslant \left| \det \left(\frac{\partial F(\hat{x}, \hat{y})}{\partial (\hat{x}, \hat{y})} \right) \right| \leqslant C_2 h_T^2,$$

for some constants C_1, C_2 independent of the curved edge. Let $\hat{w} = w(F(\hat{x}, \hat{y}))$, then the scaling argument together with the Friedrichs' inequality for functions vanishing on part of the boundary [2] yields

$$\|w\|^2_{L^2(T_\lambda^-)} \leqslant Ch_T^2 \|\hat{w}\|^2_{L^2(\hat{T})} \leqslant Ch_T^2 |\hat{w}|^2_{H^{p-1}(\hat{T})} \leqslant Ch_T^{2(p-1)} |w|^2_{H^{p-1}(T_\lambda^-)}. \tag{3.15}$$

On the curved-edge quadrilateral T_λ^+, the scaling argument is not applicable directly. Instead, we employ a different approach by constructing a finite number of strips with bounded width to cover the whole quadrilateral T_λ^+ of which the number is bounded independent of the interface inside T_λ. Let P_0 be A_1^λ and P_1 be a point on the edge $A_1^\lambda A_2^\lambda$ such that $A_1^\lambda D^\lambda$ is parallel to $P_1 E^\lambda$, and the first strip s_1 is the curved-edge quadrilateral $A_1^\lambda P_1 E^\lambda D^\lambda$. Then we proceed by induction to find P_n on $A_1^\lambda A_2^\lambda$ such that $P_{n-1} D^\lambda$ is parallel to $P_n E^\lambda$, $n \geqslant 2$, and the n-th strip s_n is the curved-edge quadrilateral $P_{n-1} P_n E^\lambda D^\lambda$. The last P_N may locate outside of the edge $A_1^\lambda A_2^\lambda$ for which we simply let $P_N = A_2^\lambda$. This procedure constructs the total N strips $s_1, s_2, \cdots, s_N$, as shown by the left plot in Figure 3.5. Obviously, we have $T_\lambda^+ = \cup_{i=1}^N s_i$. Without loss of generality, we assume $\angle A_3^\lambda E^\lambda D^\lambda \geqslant \angle A_3^\lambda D^\lambda E^\lambda$ which implies

$$|P_{N-1} P_{N-2}| \geqslant |P_{N-2} P_{N-3}| \geqslant \cdots \geqslant |P_1 P_0| \geqslant l^\lambda \sin(\theta^\lambda) h_T, \tag{3.16}$$

where in the last inequality, we have used the estimates (3.7a) and (3.7c). Therefore, we have $N \leqslant \frac{1}{l^\lambda \sin(\theta^\lambda)} + 1$, and this bound is independent of the interface. On each strip s_i, $i = 1, \cdots, N-1$, i.e., the curved-edge quadrilateral $P_{i-1} P_i D^\lambda E^\lambda$, we consider a local system with the ξ-direction perpendicular to the parallel sides $P_{i-1} D^\lambda$ and $P_i E^\lambda$, and the η-direction perpendicular to the ξ-direction, as shown in the right plot in Figure 3.5. On this local system, let $f_1(\xi)$ and $f_2(\xi)$ be the functions of the line $P_{i-1} P_i$ and the curve $D^\lambda E^\lambda$, $\xi \in (0, \xi_i)$, respectively. Then the 1-d Friedrichs' inequality [2] yields

$$\|w\|^2_{L^2(s_i)} = \int_0^{\xi_i} \int_{f_1(\xi)}^{f_2(\xi)} w^2 d\eta d\xi \leqslant \int_0^{\xi_i} |f_2(\xi) - f_1(\xi)|^2 \int_{f_1(\xi)}^{f_2(\xi)} (\partial_\eta w)^2 d\eta d\xi \leqslant h_T^2 |w|^2_{H^1(s_i)}. \tag{3.17}$$

The estimation on the last strip s_N can be shown similarly. Then (3.17) together with the bound of N gives

$$\|w\|_{L^2(T_\lambda^+)} \leqslant \sum_{i=1}^N \|w\|_{L^2(s_i)} \leqslant h_T \sum_{i=1}^N |w|_{H^1(s_i)} \leqslant N h_T |w|_{H^1(T_\lambda^+)}. \tag{3.18}$$

Therefore, following the argument based on the mathematical induction [2], we have

$$\|w\|_{L^2(T_\lambda^+)} \leqslant CN^{p-1} h_T^{p-1} |w|_{H^{p-1}(T_\lambda^+)}, \tag{3.19}$$

where the constant C only depends on the order p. Finally (3.14) follows from (3.15) and (3.19). □

3.3.2 Norm Equivalence

Now we use Lemma 3.2 to establish a group of delicate norm equivalences on every interface element T and its associated fictitious element T_λ. These results are the fundamental components in the proposed analysis framework. We begin with recalling the following lemma from [196].

Lemma 3.4. *Given an integer $p \geqslant 0$ and $\mu \in (0,1)$. Let K be a closed convex domain in $\mathbb{R}^2$ with a (piecewise) smooth boundary. Assume K' contains a homothetic subset of K with the scaling factor μ. Then there exists a constant $C(\mu, p+1)$ only depending on p and μ such that*

$$\|v\|_{L^2(K)} \leqslant C(\mu, p+1)\|v\|_{L^2(K')}, \quad \forall v \in \mathbb{P}_p. \tag{3.20}$$

The following lemmas are about the equivalence of the L^2 norm on an interface element T and its associated fictitious element T_λ.

Lemma 3.5. *Given an interface element T and its fictitious element T_λ, for each degree p, there holds*

$$\|\cdot\|_{L^2(T)} \simeq \|\cdot\|_{L^2(T_\lambda)} \quad on \;\; \mathbb{P}_p. \tag{3.21}$$

Proof. By the definition, T is a homothetic subset of T_λ with the homothetic center being the incenter, hence (3.21) is a direct consequence of (3.20) by taking $\mu = 1/\lambda$. □

Now we define $\widetilde{T}_\lambda^{\pm}$ and $\widetilde{T}^{\pm}$ as the auxiliary straight-edge subelements partitioned by the line connecting the intersection points of the element boundary and the interface. In particular, on the interface element configuration shown by Figure 3.1, $\widetilde{T}_\lambda^{+}$ and $\widetilde{T}_\lambda^{-}$ are the straight-edge quadrilateral $A_1^\lambda A_2^\lambda E^\lambda D^\lambda$ and triangle $D^\lambda E^\lambda A_3^\lambda$, respectively, while $\widetilde{T}^{+}$ and $\widetilde{T}^{-}$ are the straight-edge quadrilateral A_1A_2ED and triangle DEA_3, respectively. Then, we have the following norm equivalence.

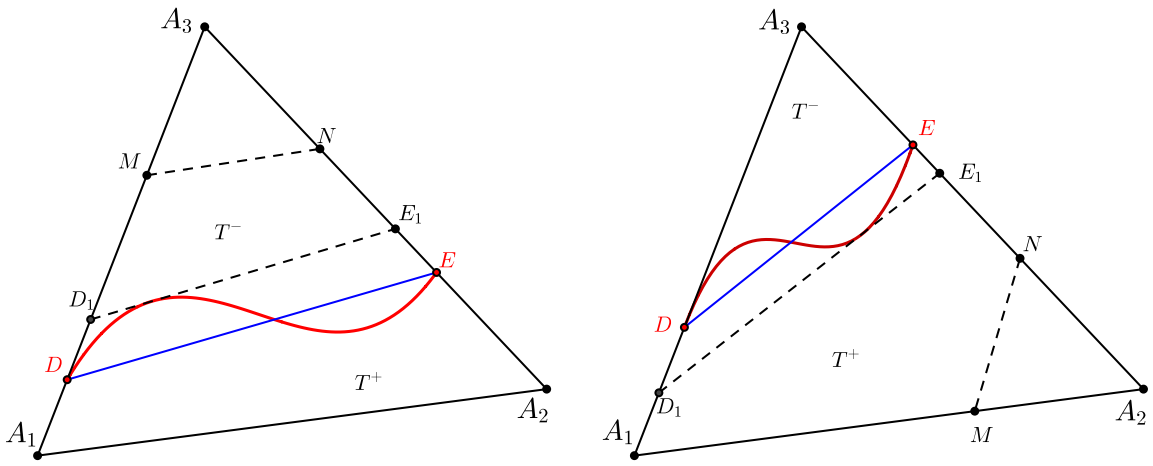

(a) Case 1 (b) Case 2

Figure 3.6: Equivalent norms on T

Lemma 3.6. *Given an interface element T as shown in Figure 3.6, for every degree p, if $|A_3D| \geqslant 1/2|A_3A_1|$ and $|A_3E| \geqslant 1/2|A_3A_2|$, there holds*

$$\|\cdot\|_{L^2(T^-)} \simeq \|\cdot\|_{L^2(\widetilde{T}^-)} \simeq \|\cdot\|_{L^2(T)} \quad \text{on } \mathbb{P}_p. \tag{3.22}$$

On the other hand, if $|A_3D| \leqslant 1/2|A_3A_1|$ or $|A_3E| \leqslant 1/2|A_3A_2|$, there holds

$$\|\cdot\|_{L^2(T^+)} \simeq \|\cdot\|_{L^2(\widetilde{T}^+)} \simeq \|\cdot\|_{L^2(T)} \quad \text{on } \mathbb{P}_p. \tag{3.23}$$

Proof. We first prove (3.22). Without of loss of generality, we consider the segment D_1E_1 which is parallel to the segment DE, tangent to Γ at a certain point and bounds Γ_T above, we further let M and N be the points on A_1A_3 and A_2A_3 such that $|A_3M|/|A_3A_1| = |A_3N|/|A_3A_2| = 1/3$, see the first plot in Figure 3.6 for an illustration. Then $\triangle A_3MN$ is a homothetic subset of T with A_3 being the homothetic center and the scaling factor $1/3$. Since $|A_3D| \geqslant 1/2|A_3A_1|$ and $|A_3E| \geqslant 1/2|A_3A_2|$, i.e., $\triangle A_3MN \subset \widetilde{T}^-$, given any $v \in \mathbb{P}_p$, Lemma 3.4 directly implies

$$\|v\|_{L^2(\widetilde{T}^-)} \leqslant \|v\|_{L^2(T)} \leqslant C(1/3, p+1)\|v\|_{L^2(\triangle A_3MN)} \leqslant C(1/3, p+1)\|v\|_{L^2(\widetilde{T}^-)}, \tag{3.24}$$

which suggests $\|\cdot\|_{L^2(\widetilde{T}^-)} \simeq \|\cdot\|_{L^2(T)}$ on $\mathbb{P}_p$, where the constant $C(1/3, p+1)$ inherits from (3.20) with $\mu = 1/3$. In addition, we let d_1 and d_2 be the distance from A_3 to the lines DE and D_1E_1, respectively. Then, (3.6a) implies $|d_1 - d_2| \leqslant \delta_0 h_T^2$; hence we have $\frac{d_2}{d_1} = 1 - \frac{d_1 - d_2}{d_1} \geqslant 1 - \frac{2\delta_0\sigma^2}{\pi} h_T \geqslant 2/3$ for h_T small enough, where we have also used $d_0 \geqslant \frac{|\triangle A_1A_2A_3|}{2|DE|} \geqslant \frac{\pi\rho_T^2}{2h_T}$ and (3.3). Therefore, we can obtain $\frac{|A_3E_1|}{|A_3A_2|} = \frac{|A_3E_1|}{|A_3E|}\frac{|A_3E|}{|A_3A_2|} \geqslant 1/3$, and similarly $\frac{|A_3D_1|}{|A_3A_1|} \geqslant 1/3$. This shows $\triangle A_3MN \subseteq \triangle A_3D_1E_1 \subseteq T^- \subseteq T$. So the same argument as (3.24) yields $\|\cdot\|_{L^2(T^-)} \simeq \|\cdot\|_{L^2(T)}$ on $\mathbb{P}_p$, which further implies (3.22) together with (3.24).

Next, for (3.23), without loss of generality, we assume $|A_3E| \leqslant 1/2|A_3A_2|$. Let the points M and N be at the edges A_1A_2 and A_3A_2 such that $|A_2M|/|A_1A_2| = |A_2N|/|A_2A_3| = 1/3$, see the second plot in Figure 3.6 for an illustration. Through similar arguments above, we can show $\triangle A_2NM \subseteq \widetilde{T}^+ \cap T^+$. Therefore, we have (3.23) by following the same arguments used for (3.24). □

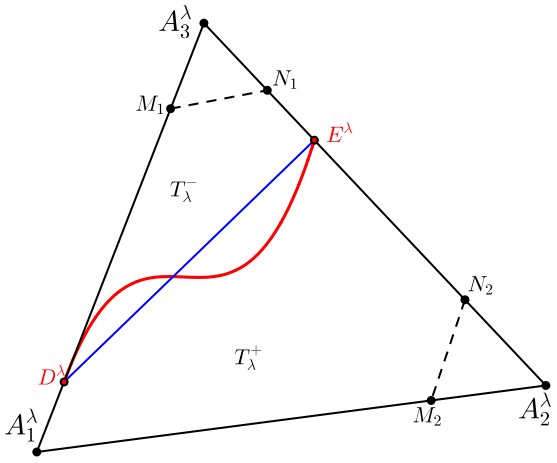

Figure 3.7: Equivalent norms on T^λ

Lemma 3.7. *Given a fictitious element T_λ, $\lambda > 1$, as shown in Figure 3.7, associated with an interface element T, then for each degree p, there holds*

$$\|\cdot\|_{L^2(T_\lambda^-)} \simeq \|\cdot\|_{L^2(\widetilde{T}_\lambda^-)} \simeq \|\cdot\|_{L^2(T_\lambda^+)} \simeq \|\cdot\|_{L^2(\widetilde{T}_\lambda^+)} \simeq \|\cdot\|_{L^2(T_\lambda)} \quad \text{on } \mathbb{P}_p. \tag{3.25}$$

Proof. Using (3.7b) and the arguments used in Lemma 3.6, we can show that there always exist two fixed triangles $\triangle A_3^\lambda M_1 N_1 \subseteq T_\lambda^- \cap \widetilde{T}_\lambda^-$ and $A_2^\lambda M_2 N_2 \subseteq T_\lambda^+ \cap \widetilde{T}_\lambda^+$ both homothetic to T_λ regardless of the interface location, as shown in Figure 3.7. Then, (3.25) follows from similar arguments used for (3.24). □

Finally, we present the trace and inverse inequalities related to curved-edge subelements.

Lemma 3.8. *There exist constants c_i and c_t such that for each interface element T, the following estimates hold on its associated fictitious element $T_\lambda, \lambda > 1$:*

$$\textit{the inverse inequality:} \quad \|\nabla v\|_{L^2(T_\lambda^\pm)} \leqslant c_i h_T^{-1} \|v\|_{L^2(T_\lambda^\pm)}, \quad \forall v \in \mathbb{P}_p, \tag{3.26a}$$

$$\textit{the trace inequality:} \quad \|v\|_{L^2(\Gamma_T^\lambda)} \leqslant c_t h_T^{-1/2} \|v\|_{L^2(T_\lambda^\pm)}, \quad \forall v \in \mathbb{P}_p. \tag{3.26b}$$

Proof. For (3.26a), we apply the Lemma 3.7 and the standard inverse inequality on T_λ to obtain

$$\|\nabla v\|_{L^2(T_\lambda^\pm)} \leqslant C\|\nabla v\|_{L^2(T_\lambda)} \leqslant Ch_T^{-1}\|v\|_{L^2(T_\lambda)} \leqslant Ch_T^{-1}\|v\|_{L^2(T_\lambda^\pm)}. \tag{3.27}$$

For (3.26b), the standard inverse inequality on T_λ, Lemma 3.2 in [196], and Lemma 3.7 together lead to

$$\begin{aligned}\|v\|_{L^2(\Gamma_T^\lambda)} &\leqslant Ch_T^{-1/2}\|v\|_{L^2(T_\lambda)} + Ch_T^{1/2}\|\nabla v\|_{L^2(T_\lambda)} \\ &\leqslant Ch_T^{-1/2}\|v\|_{L^2(T_\lambda)} \leqslant Ch_T^{-1/2}\|v\|_{L^2(T_\lambda^\pm)}.\end{aligned} \tag{3.28}$$

□

3.4 IFE Spaces Based on Cauchy Extension

In this section, we develop local IFE functions which can satisfy the jump conditions (3.1c)-(3.1e) in certain weak sense. On an interface element T, let's consider an IFE function consisting of two polynomial components v^- on T^- and v^+ on T^+ in $\mathbb{P}_p$. Ideally, we want these two components to satisfy the the jump conditions (3.1e) exactly along the portion of the interface curve $\Gamma \cap T$ and this consideration leads to $\beta^- \triangle v^- \equiv \beta^+ \triangle v^+$. We also want these two polynomial components to satisfy (3.1c) and (3.1d). These properties presumed for the two polynomial components suggest a way to construct an IFE function: choose one of its polynomial component v^+, for instance, then find the other polynomial component v^- of the IFE function by solving the following equations:

$$\beta^- \triangle v^- = \beta^+ \triangle v^+, \qquad \text{in } T_\lambda^-, \tag{3.29a}$$

$$v^- = v^+, \qquad \text{on } \Gamma_T^\lambda = T_\lambda \cap \Gamma, \tag{3.29b}$$

$$\beta^- \nabla v^- \cdot \mathbf{n} = \beta^+ \nabla v^+ \cdot \mathbf{n}, \qquad \text{on } \Gamma_T^\lambda = T_\lambda \cap \Gamma. \tag{3.29c}$$

Note that this is a Cauchy problem [89] about v^- posed on the subelement T_λ^- since two boundary conditions are given on part of its boundary $T_\lambda^- \cap \Gamma$. We note that it is in general impossible to find a polynomial solution v^- to this Cauchy problem. Alternatively, in the proposed framework, we consider solving this Cauchy problem in an approximation sense or a weak sense based on the least squares finite element idea [32, 112], and this procedure further allows us to introduce a mapping which is a crucial tool in both the construction and analysis for p-th degree IFE functions.

3.4.1 The Cauchy Mapping

In this subsection, we discuss how to solve the Cauchy problem (3.29) in a weakly approximate sense using the least squares finite element formulation [32, 112] on each interface element. The weakly approximate solution to this Cauchy problem allows us to introduce a discrete extension operator that is a crucial tool in our construction and analysis framework for IFE functions. We shall see that all the critical analysis components in the proposed method are related to certain properties of this extension operator.

On each fictitious element T_λ associated with an interface element $T \in \mathcal{T}_h^i$, we introduce the following bilinear forms and the associated semi-norms:

$$a_\lambda(v,w) = \int_{T_\lambda^-} \triangle v \triangle w dX + h_T^{-3} \int_{\Gamma_T^\lambda} vw ds + h_T^{-1} \int_{\Gamma_T^\lambda} \partial_{\mathbf{n}} v \, \partial_{\mathbf{n}} w ds, \ \forall v, w \in H^2(T_\lambda^-), \tag{3.30a}$$

$$b_\lambda(v,w) = \int_{T_\lambda^-} \frac{\beta^+}{\beta^-} \triangle v \triangle w dX + h_T^{-3} \int_{\Gamma_T^\lambda} vw ds + h_T^{-1} \int_{\Gamma_T^\lambda} \frac{\beta^+}{\beta^-} \partial_{\mathbf{n}} v \, \partial_{\mathbf{n}} w ds, \ \forall v, w \in H^2(T_\lambda^-), \tag{3.30b}$$

$$|||v|||_{a_\lambda}^2 = a_\lambda(v,v), \qquad |||v|||_{b_\lambda}^2 = b_\lambda(v,v), \quad \forall v \in H^2(T_\lambda^-), \tag{3.30c}$$

here and from now on, we employ the notation $\partial_{\boldsymbol{\xi}} v = \nabla v \cdot \boldsymbol{\xi}$ for any direction $\boldsymbol{\xi}$. Recall the assumption that $\beta^- \geqslant \beta^+$, it is easy to see that

$$\frac{\beta^+}{\beta^-} |||v|||_{a_\lambda}^2 \leqslant |||v|||_{b_\lambda}^2 \leqslant |||v|||_{a_\lambda}^2, \quad \forall v \in \mathbb{P}_p. \tag{3.31}$$

We note that similar bilinear forms also appear in the discussion of the least squares finite element method [32]. This idea was recently invented in [112] to solve a Cauchy problem on the whole domain. The next lemma shows the semi-norms (3.30c) actually become norms when restricted on polynomial spaces.

Lemma 3.9. *$|||\cdot|||_{a_\lambda}$ and $|||\cdot|||_{b_\lambda}$ are both norms on the polynomial space $\mathbb{P}_p$ for each degree $p \geq 1$.*

Proof. From (3.31), we only need to prove $|||\cdot|||_{a_\lambda}$ is a norm. The result for the linear case i.e., $p = 1$ is trivial. Now we proceed by the mathematical induction. Suppose the result is true for degree p. Then, given each $v \in \mathbb{P}_{p+1}$, $|||v|||_{a_\lambda} = 0$ is equivalent to $\triangle v \equiv 0$ and $v = 0$, $\partial_{\mathbf{n}} v = 0$ on Γ_T^λ. According to [86, 133], we actually have $\partial_{\mathbf{t}}^l v = 0$ for $l = 1, 2$, $\partial_{\mathbf{n}}^2 v = 0$ and $\partial_{\mathbf{n}} \partial_{\mathbf{t}} v = 0$ on Γ_T^λ where $\mathbf{t}$ is the tangential vector to Γ_T^λ. Consider the polynomial $\partial_x v \in \mathbb{P}_p$ and let $a\mathbf{n} + b\mathbf{t} = (1,0)^T$ on Γ_T^λ. Note that $\triangle v \equiv 0$ yields $\triangle \partial_x v \equiv 0$. Besides, since $\partial_{\mathbf{n}} v = \partial_{\mathbf{t}} v = 0$ on Γ_T^λ, we have $\partial_x v = a\partial_{\mathbf{n}} v + b\partial_{\mathbf{t}} v = 0$ on Γ_T^λ. In addition, there also holds $\partial_{\mathbf{n}} \partial_x v = a\partial_{\mathbf{n}}^2 v + b\partial_{\mathbf{n}} \partial_{\mathbf{t}} v = 0$ on Γ_T^λ. Therefore, by the hypothesis, we have $\partial_x v = 0$, and similarly $\partial_y v = 0$. Then v must be a constant. Now using $v = 0$ on Γ_T^λ, we have $v \equiv 0$. □

Based on Lemma 3.9, we can further prove an equivalence between the standard L^2 norm and $|||\cdot|||_{a_\lambda}$.

Lemma 3.10. *For every interface element $T \in \mathcal{T}_h^i$, we have*

$$h_T^2 |||v|||_{a_\lambda} \simeq \|v\|_{L^2(T_\lambda^-)}, \quad \forall v \in \mathbb{P}_p, \ \lambda > 1.$$

Proof. Firstly, we consider the case that T_λ^- is the curved-edge triangular subelement $A_3^\lambda D^\lambda E^\lambda$, as shown in the left plot in Figure 3.8. The first two estimates in (3.7a) enable us to construct an isosceles triangle $T_0 = \triangle P D^\lambda E^\lambda$ with $\angle P D^\lambda E^\lambda = \angle P E^\lambda D^\lambda = \theta^\lambda$ such that it is always contained in the straight-edge triangle $\triangle A_3^\lambda D^\lambda E^\lambda$. Then, we consider a special reference element $\hat{T}_0 = \triangle \hat{P}\hat{E}\hat{D}$ on the $\hat{x}$-$\hat{y}$ plane which is also isosceles with $\angle \hat{P}\hat{E}\hat{D} = \angle \hat{P}\hat{D}\hat{E} = \theta^\lambda$ and $|\hat{D}\hat{E}| = 1$ as shown in the second plot in Figure 3.8. Define an affine mapping F which is simply a scaling rotation transformation:

$$\begin{aligned} F(\hat{x},\hat{y}) &= |D^\lambda E^\lambda| \begin{bmatrix} \cos(\alpha) & -\sin(\alpha) \\ \sin(\alpha) & \cos(\alpha) \end{bmatrix} \begin{bmatrix} \hat{x} \\ \hat{y} \end{bmatrix} + D^\lambda, \\ \text{with } \ (l^\lambda)^2 h_T^2 &\leqslant \left| \frac{\partial F(\hat{x},\hat{y})}{\partial(\hat{x},\hat{y})} \right| \leqslant \lambda^2 h_T^2, \end{aligned} \tag{3.32}$$

where α is the angle between $D^\lambda E^\lambda$ and the x-axis, and the bound of Jacobian matrix follows from (3.7c).

Let F map a curve $\hat{\Gamma} : \hat{y} = f(\hat{x})$ to Γ_T^λ, and consider $\hat{v} = v(F(\hat{x},\hat{y})) \in \mathbb{P}_p$. (3.32) and (3.6a) yield $|f(\hat{x})| \leqslant \delta_0 (l^\lambda)^{-1} \lambda^2 h_T$, $\forall \hat{x} \in (0,1)$. So, we can construct a new triangle $\hat{T}_1 = \triangle \hat{P}\hat{D}_1\hat{E}_1$ homothetic to $\hat{T}_0$ according to the center $\hat{P}$ with the scaling factor $|\hat{P}\hat{D}|/|\hat{P}\hat{D}_1| = |\hat{P}\hat{E}|/|\hat{P}\hat{E}_1| = 2/3$ such that it always contains the curve $\hat{\Gamma}$ inside for h_T small enough, see the right plot in Figure 3.8 for an illustration. Then,

$$\begin{aligned} \|\hat{v}\|_{L^2(\hat{\Gamma})} &= \left(\int_0^1 \hat{v}^2(\hat{x}, f(\hat{x}))(1 + f'^2(\hat{x}))^{1/2} d\hat{x} \right)^{1/2} \\ &\geqslant \left(\int_0^1 \left(\hat{v}(\hat{x},0) + \int_0^{f(\hat{x})} \partial_{\hat{y}} v d\hat{y} \right)^2 d\hat{x} \right)^{1/2} \\ &\geqslant \left(\int_0^1 \hat{v}^2(\hat{x},0)\hat{x} \right)^{1/2} - \left(\int_0^1 \left(\int_0^{f(\hat{x})} \partial_{\hat{y}} v d\hat{y} \right)^2 d\hat{x} \right)^{1/2} \\ &\geqslant \|\hat{v}\|_{L^2(0,1)} - (\delta_0/l^\lambda)^{1/2} \lambda h_T^{1/2} |\hat{v}|_{H^1(\hat{T}_1)}, \end{aligned} \tag{3.33}$$

where we have used the Hölder's inequality and the bound for $|f(\hat{x})|$. From (3.6b), it is easy to verify that $|f'(\hat{x})| \leqslant 2\sqrt{2}\delta_1^{1/2}\lambda h_T$, $\forall \hat{x} \in (0,1)$, for h_T small enough, which shows

$$\begin{aligned} \|\partial_{\mathbf{n}} \hat{v}\|_{\hat{\Gamma}} &= \left(\int_0^1 \left(-f'(\hat{x}) \partial_{\hat{x}} \hat{v}(\hat{x}, f(\hat{x})) + \partial_{\hat{y}} \hat{v}(\hat{x}, f(\hat{x})) \right)^2 d\hat{x} \right)^{1/2} \\ &\geqslant \left(\int_0^1 (\partial_{\hat{y}} \hat{v}(\hat{x}, f(\hat{x})))^2 d\hat{x} \right)^{1/2} - 2\sqrt{2}\delta_1^{1/2} \lambda h_T \left(\int_0^1 (\partial_{\hat{x}} \hat{v}(\hat{x}, f(\hat{x})))^2 d\hat{x} \right)^{1/2}. \end{aligned} \tag{3.34}$$

Applying the similar arguments in (3.33) to each term in the right hand side of (3.34), we obtain

$$\left(\int_0^1 (\partial_{\hat{y}} \hat{v}(\hat{x}, f(\hat{x})))^2 d\hat{x} \right)^{1/2} \geqslant \|\partial_{\hat{y}} \hat{v}\|_{L^2(0,1)} - (\delta_0/l^\lambda)^{1/2} \lambda h_T^{1/2} |\hat{v}|_{H^2(\hat{T}_1)}, \tag{3.35}$$

$$\left(\int_0^1 (\partial_{\hat{x}}\hat{v}(\hat{x}, f(\hat{x})))^2 d\hat{x}\right)^{1/2} \leqslant \|\partial_{\hat{x}}\hat{v}\|_{L^2(0,1)} + (\delta_0/l^\lambda)^{1/2}\lambda h_T^{1/2}|\hat{v}|_{H^2(\hat{T}_1)}. \tag{3.36}$$

Substituting (3.35) and (3.36) into (3.34), and using the trace inequality (2.107) on $\|\partial_{\hat{x}}\hat{v}\|_{L^2(0,1)}$ in (3.36) together with the distance from $\hat{P}$ to $\hat{D}\hat{E}$ equaling $\tan(\theta^\lambda)/2$, we have

$$\|\partial_{\mathbf{n}}\hat{v}\|_{\hat{\Gamma}} \geqslant \|\partial_{\hat{y}}\hat{v}\|_{L^2(0,1)} - \left[C_1 h_T|\hat{v}|_{H^1(\hat{T}_0)} + (C_2 h_T^{1/2} + C_3 h_T^{3/2})|\hat{v}|_{H^2(\hat{T}_1)}\right], \tag{3.37}$$

where C_1, C_2, C_3 depend only on p, λ. δ_1, δ_2 and θ^λ. Combining (3.33) and (3.37), using Lemma 3.4 to bound $|\hat{v}|_{H^k(\hat{T}_1)}$ by $|\hat{v}|_{H^k(\hat{T}_0)}$, $k = 1, 2$, with $\mu = 2/3$, and applying the inverse inequality on $\hat{T}_0$, we have

$$\begin{aligned} &\|\triangle\hat{v}\|_{L^2(\hat{T}_0)} + \|\hat{v}\|_{L^2(\hat{\Gamma})} + \|\partial_{\mathbf{n}}\hat{v}\|_{L^2(\hat{\Gamma})} \\ \geqslant &\|\triangle\hat{v}\|_{L^2(\hat{T}_0)} + \|\hat{v}\|_{L^2(0,1)} + \|\partial_{\hat{y}}\hat{v}\|_{L^2(0,1)} - Ch_T^{1/2}\|\hat{v}\|_{L^2(\hat{T}_0)}, \end{aligned} \tag{3.38}$$

for h_T small enough, where the previous derivation shows this generic constant C also only depends on p, λ, δ_1, δ_2 and θ^λ. By the same argument in Lemma 3.9, $\|\triangle\hat{v}\|_{L^2(\hat{T}_0)} + \|\hat{v}\|_{L^2(0,1)} + \|\partial_{\hat{y}}\hat{v}\|_{L^2(0,1)}$ forms a norm on the polynomial space $\mathbb{P}_p$. Therefore, the norm equivalence on finite dimensional spaces yields

$$\begin{aligned} &\|\triangle\hat{v}\|_{L^2(\hat{T}_0)} + \|\hat{v}\|_{L^2(\hat{\Gamma})} + \|\partial_{\mathbf{n}}\hat{v}\|_{L^2(\hat{\Gamma})} \\ \geqslant &C\|\hat{v}\|_{L^2(\hat{T}_0)} - Ch_T^{1/2}\|\hat{v}\|_{L^2(\hat{T}_0)} \geqslant C\|\hat{v}\|_{L^2(\hat{T}_0)} \end{aligned} \tag{3.39}$$

for h_T small enough. Furthermore, Lemma 3.7 indicates $\|\triangle v\|_{L^2(T_\lambda^-)} \geqslant C\|\triangle v\|_{L^2(\widetilde{T}_\lambda^-)} \geqslant C\|\triangle v\|_{L^2(T_0)}$, where recall $\widetilde{T}_\lambda^- = \triangle A_3^\lambda D^\lambda E^\lambda$. Hence, using (3.39), (3.32) and the scaling argument, we arrive at

$$\begin{aligned} |||v|||_{a_\lambda}^2 &\geqslant C\|\triangle v\|_{L^2(T_0)}^2 + h_T^{-3}\|v\|_{L^2(\Gamma_T^\lambda)}^2 + h_T^{-1}\|\partial_{\mathbf{n}} v\|_{L^2(\Gamma_T^\lambda)}^2 \\ &\geqslant Ch_T^{-2}\left(\|\triangle\hat{v}\|_{L^2(\hat{T}_0)}^2 + \|\hat{v}\|_{L^2(\hat{\Gamma})}^2 + \|\partial_{\mathbf{n}}\hat{v}\|_{L^2(\hat{\Gamma})}^2\right) \geqslant Ch_T^{-2}\|\hat{v}\|_{L^2(\hat{T}_0)}^2 \geqslant Ch_T^{-4}\|v\|_{L^2(T_0)}^2. \end{aligned} \tag{3.40}$$

Next, on T_λ, we consider the intersection point Q of the lines $A_3^\lambda P$ and $D^\lambda E^\lambda$. By (3.7c), we have

$$\frac{|QP|}{|QA_3^\lambda|} = \frac{\sin(\theta^\lambda)|PE^\lambda|}{\sin(\angle A_3^\lambda E^\lambda D^\lambda)|A_3^\lambda E^\lambda|} = \frac{\sin(\theta^\lambda)|D^\lambda E^\lambda|}{2\cos(\theta^\lambda)\sin(\angle A_3^\lambda E^\lambda D^\lambda)|A_3^\lambda E^\lambda|} \geqslant \frac{\tan(\theta^\lambda) l^\lambda}{2\lambda}. \tag{3.41}$$

Therefore, we can construct a triangle $T_0' = \triangle P' D^{\lambda'} E^{\lambda'}$ which is homothetic to T_0 according to the chosen center Q such that $|QP|/|QP'| = \frac{\tan(\theta^\lambda) l^\lambda}{4\lambda}$, i.e., a fixed scaling factor. Then, the triangle $\widetilde{T}_\lambda^- = \triangle A_3^\lambda D^\lambda E^\lambda$ is always contained in T_0' regardless of the interface location inside T_λ, as shown in Figure 3.8. Hence, using Lemma 3.4 again, the norm equivalences in Lemma 3.7 and (3.40), for each $v \in \mathbb{P}_p$, we have

$$\|v\|_{L^2(T_\lambda^-)} \leqslant C\|v\|_{L^2(\widetilde{T}_\lambda^-)} \leqslant C\|v\|_{T_0'} \leqslant C\|v\|_{L^2(T_0)} \leqslant Ch_T^2|||v|||_{a_\lambda}. \tag{3.42}$$

Finally, the other direction $\|v\|_{L^2(T_\lambda^-)} \geqslant Ch_T^2 |||v|||_{a_\lambda}$ can be easily obtained by the trace inequality and inverse inequality in Lemma 3.8.

Secondly, we note that Lemma 3.7 implies $C_1\|\triangle v\|_{L^2(T_\lambda^+)} \leqslant \|\triangle v\|_{L^2(T_\lambda^-)} \leqslant C_2\|\triangle v\|_{L^2(T_\lambda^+)}$. Thus, when T_λ^- is the curved-edge quadrilateral subelement of T_λ, the result simply follows from what we have already shown for the curved-edge triangular subelement together with the norm equivalence in Lemma 3.7.

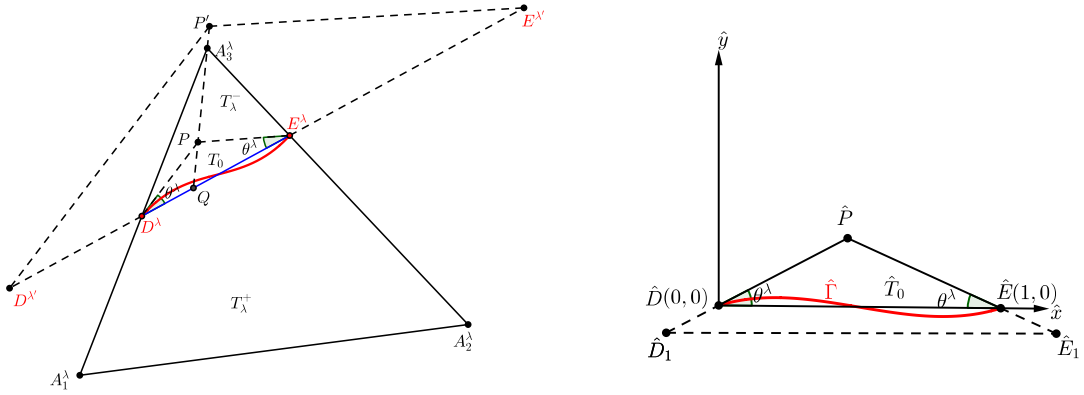

Figure 3.8: Illustration of the proof for Lemma 3.10

□

Following the ideas in [112], we then consider a weak problem in the least squares sense associated with the Cauchy problem (3.29): for each $v \in \mathbb{P}_p$, find $\tilde{v} \in \mathbb{P}_p$ such that $a_\lambda(\tilde{v}, w) = b_\lambda(v, w)$, $\forall w \in \mathbb{P}_p$. Since $|||\cdot|||_{a_\lambda}$ is indeed a norm, the coercivity and boundedness of the bilinear form $a_\lambda(v, w)$ (Lemma 4.2 in [112]) in this special norm together with the Lax-Milgram Theorem directly implies that the solution $\tilde{v} \in \mathbb{P}_p$ to the weak problem uniquely exists. Hence, we know that the Cauchy problem (3.29) has a unique solution in this weak sense that allows us to introduce a key tool for the framework presented in this chapter for higher-degree IFE methods.

Definition 3.1. *Define a mapping $\mathfrak{C} : \mathbb{P}_p \to \mathbb{P}_p$ such that for every $v \in \mathbb{P}_p$, $\mathfrak{C}(v) \in \mathbb{P}_p$ is determined by*

$$a_\lambda(\mathfrak{C}(v), w) = b_\lambda(v, w), \quad \forall w \in \mathbb{P}_p, \tag{3.43}$$

and we call $\mathfrak{C}$ the Cauchy Mapping.

Because of the uniqueness and the fact $\mathfrak{C}(0) = 0$, $\mathfrak{C}$ is an one-to-one linear mapping from the polynomial space $\mathbb{P}_p$ to itself. We let P_{T_λ} be the standard L^2 projection from $H^{p+1}(T_\lambda)$ onto the polynomial space $\mathbb{P}_p$ on T_λ. We present a few properties of the *Cauchy Mapping* $\mathfrak{C}$ that are the fundamental ingredients for us to analyze the local approximation capabilities and trace inequalities of IFE spaces later on.

Theorem 3.1. *For every $u \in PH^{p+1}(\Omega)$ with the extensions $u_E^{\pm}$, there exists a constant C such that for each interface element T there holds*

$$\left|\left|\left|\mathfrak{C}(P_{T_\lambda}u_E^+) - P_{T_\lambda}u_E^-\right|\right|\right|_{a_\lambda} \leqslant Ch_T^{p-1}\left(\frac{\beta^+}{\beta^-}|u_E^+|_{H^{p+1}(T_\lambda)} + |u_E^-|_{H^{p+1}(T_\lambda)}\right),\ \lambda > 1. \tag{3.44}$$

Proof. Let $w = \mathfrak{C}(P_{T_\lambda}u_E^+) - P_{T_\lambda}u_E^-$ and note that $w \in \mathbb{P}_p$, so the definition (3.43) directly yields

$$\begin{aligned}
|||w|||_{a_\lambda}^2 &= a_\lambda(\mathfrak{C}(P_{T_\lambda}u_E^+) - P_{T_\lambda}u_E^-, w) = b_\lambda(P_{T_\lambda}u_E^+, w) - a_\lambda(P_{T_\lambda}u_E^-, w)\\
&= \int_{T_\lambda^-}(\frac{\beta^+}{\beta^-}\triangle P_{T_\lambda}u_E^+ - \triangle P_{T_\lambda}u_E^-)\triangle w dX + h_T^{-3}\int_{\Gamma_T^\lambda}(P_{T_\lambda}u_E^+ - P_{T_\lambda}u_E^-)w ds\\
&+ h_T^{-1}\int_{\Gamma_T^\lambda}(\frac{\beta^+}{\beta^-}\partial_{\mathbf{n}}P_{T_\lambda}u_E^+ - \partial_{\mathbf{n}}P_{T_\lambda}u_E^-)\ \partial_{\mathbf{n}}w ds.
\end{aligned} \tag{3.45}$$

Then, applying the Hölder's inequality to each term on the right hand side of (3.45), we have

$$\begin{aligned}
|||w|||_{a_\lambda} \leqslant \|\frac{\beta^+}{\beta^-}\triangle P_{T_\lambda}u_E^+ - \triangle P_{T_\lambda}u_E^-\|_{L^2(T_\lambda^-)} + h_T^{-3/2}\|P_{T_\lambda}u_E^+ - P_{T_\lambda}u_E^-\|_{L^2(\Gamma_T^\lambda)}\\
+ h_T^{-1/2}\|\frac{\beta^+}{\beta^-}\partial_{\mathbf{n}}P_{T_\lambda}u_E^+ - \partial_{\mathbf{n}}P_{T_\lambda}u_E^-\|_{L^2(\Gamma_T^\lambda)}.
\end{aligned} \tag{3.46}$$

For the first term in (3.46), by the triangular inequality, the error estimation for the projection operator P_{T_λ}, and Lemma 3.3, we obtain

$$\begin{aligned}
&\|\frac{\beta^+}{\beta^-}\triangle P_{T_\lambda}u_E^+ - \triangle P_{T_\lambda}u_E^-\|_{L^2(T_\lambda^-)}\\
\leqslant&\|\frac{\beta^+}{\beta^-}\triangle P_{T_\lambda}u_E^+ - \frac{\beta^+}{\beta^-}\triangle u_E^+\|_{L^2(T_\lambda)} + \|\triangle P_{T_\lambda}u_E^- - \triangle u_E^-\|_{L^2(T_\lambda)} + \|\frac{\beta^+}{\beta^-}\triangle u_E^+ - \triangle u_E^-\|_{L^2(T_\lambda)}\\
\leqslant&C\frac{\beta^+}{\beta^-}h_T^{p-1}|u_E^+|_{H^{p+1}(T_\lambda)} + Ch_T^{p-1}|u_E^-|_{H^{p+1}(T_\lambda)} + Ch_T^{p-1}(\frac{\beta^+}{\beta^-}|u_E^+|_{H^{p+1}(T_\lambda)} + |u_E^-|_{H^{p+1}(T_\lambda)}).
\end{aligned} \tag{3.47}$$

To estimate the second term in (3.46), we first apply the special trace inequality given by Lemma 3.2 in [196] and the error estimation for the projection operator P_{T_λ} to obtain

$$\begin{aligned}
\|P_{T_\lambda}u_E^\pm - u_E^\pm\|_{L^2(\Gamma_T^\lambda)} &\leqslant Ch_T^{-\frac{1}{2}}\|P_{T_\lambda}u_E^\pm - u_E^\pm\|_{L^2(T_\lambda)} + Ch_T^{\frac{1}{2}}\|\nabla(P_{T_\lambda}u_E^\pm - u_E^\pm)\|_{L^2(T_\lambda)}\\
&\leqslant Ch_T^{p+\frac{1}{2}}|u_E^\pm|_{H^{p+1}(T_\lambda)}.
\end{aligned} \tag{3.48}$$

Then, we employ the jump condition (3.1c) for $u_E^\pm$ to obtain

$$\begin{aligned}
h_T^{-3/2}\|P_{T_\lambda}u_E^+ - P_{T_\lambda}u_E^-\|_{L^2(\Gamma_T^\lambda)} &\leqslant h_T^{-3/2}(\|P_{T_\lambda}u_E^+ - u_E^+\|_{L^2(\Gamma_T^\lambda)} + \|P_{T_\lambda}u_E^- - u_E^-\|_{L^2(\Gamma_T^\lambda)})\\
&\leqslant Ch_T^{p-1}(|u_E^+|_{H^{p+1}(T_\lambda)} + |u_E^-|_{H^{p+1}(T_\lambda)}).
\end{aligned} \tag{3.49}$$

By a similar argument to (3.48) and (3.49), we can also show that

$$h_T^{-1/2}\|\frac{\beta^+}{\beta^-}\partial_{\mathbf{n}}P_{T_\lambda}u_E^+ - \partial_{\mathbf{n}}P_{T_\lambda}u_E^-\|_{L^2(\Gamma_T^\lambda)} \leqslant C\frac{\beta^+}{\beta^-}h_T^{p-1}|u_E^+|_{H^{p+1}(T_\lambda)} + Ch_T^{p-1}|u_E^-|_{H^{p+1}(T_\lambda)}. \quad (3.50)$$

Substituting (3.47), (3.49) and (3.50) into (3.46) yields the desired result. □

Lemma 3.11. *There exists a constant C such that for each interface element T there hold*

$$|||\mathfrak{C}(v) - v|||_{a_\lambda} \leqslant Ch_T^{-1}|v|_{H^1(T_\lambda^-)}, \qquad \forall v \in \mathbb{P}_p,\ \lambda > 1, \quad (3.51a)$$

$$|||\mathfrak{C}(v) - v|||_{a_\lambda} \leqslant Ch_T^{-1}\frac{\beta^-}{\beta^+}|\mathfrak{C}(v)|_{H^1(T_\lambda^-)}, \quad \forall v \in \mathbb{P}_p,\ \lambda > 1. \quad (3.51b)$$

Proof. Let $w = \mathfrak{C}(v) - v$. The definition (3.43), the Hölder's inequality, and the assumption $\beta^- \geqslant \beta^+$ yield

$$\begin{aligned}
&|||w|||_{a_\lambda}^2 = a_\lambda(w,w) = b_\lambda(v,w) - a_\lambda(v,w)\\
=&\int_{T_\lambda^-}\left(\frac{\beta^+}{\beta^-} - 1\right)\triangle v\ \triangle w dX + h_T^{-1}\int_{\Gamma_T^\lambda}\left(\frac{\beta^+}{\beta^-} - 1\right)\partial_{\mathbf{n}}v\ \partial_{\mathbf{n}}w ds\\
\leqslant&\left(\|\triangle v\|_{L^2(T_\lambda^-)} + h_T^{-1/2}\|\partial_{\mathbf{n}}v\|_{L^2(\Gamma_T^\lambda)}\right)|||w|||_{a_\lambda}\\
\leqslant&Ch_T^{-1}|v|_{H^1(T_\lambda^-)}|||w|||_{a_\lambda},
\end{aligned} \quad (3.52)$$

which implies (3.51a), here in the last inequality above, we have used the inverse inequality (3.26a) and trace inequality (3.26b). For (3.51b), by (3.31), we have

$$|||w|||_{a_\lambda}^2 \leqslant \frac{\beta^-}{\beta^+}|||w|||_{b_\lambda}^2 = \frac{\beta^-}{\beta^+}(b_\lambda(\mathfrak{C}(v),w) - a_\lambda(\mathfrak{C}(v),w)), \quad (3.53)$$

and the rest of derivation is the same as (3.52). □

The following theorem is about the stability of the Cauchy mapping $\mathfrak{C}$ and its inverse $\mathfrak{C}^{-1}$.

Theorem 3.2. *The Cauchy mapping $\mathfrak{C}$ and its inverse $\mathfrak{C}^{-1}$ are bounded in terms of the semi-H^1 norm, i.e., there are some constants c_b and C_b such that for every interface element T there holds*

$$c_b\frac{\beta^+}{\beta^-}|v|_{H^1(T_\lambda^-)} \leqslant |\mathfrak{C}(v)|_{H^1(T_\lambda^-)} \leqslant C_b|v|_{H^1(T_\lambda^-)},\ \lambda > 1. \quad (3.54)$$

Proof. We only prove the inequality on the right side since the one on the left side can be proved by a similar argument. By the inverse inequality (3.26a), the norm equivalence in Lemma 3.10 and (3.51a), we have

$$|\mathfrak{C}(v) - v|_{H^1(T_\lambda^-)} \leqslant Ch_T^{-1}\|\mathfrak{C}(v) - v\|_{L^2(T_\lambda^-)} \leqslant Ch_T|||\mathfrak{C}(v) - v|||_{a_\lambda} \leqslant C|v|_{H^1(T_\lambda^-)},$$

which gives the right inequality in (3.54). □

3.4.2 A p-th Degree IFE Space

In this subsection, using the Cauchy mapping introduced in Subsection 3.4.1, we proceed to define a p-th degree IFE space and study its properties. Specifically, on each interface element $T \in \mathcal{T}_h^i$ with its fictitious element T_λ, $\lambda > 1$, the local p-th degree IFE space is defined as the following space of piecewise polynomials:

$$S_h^p(T) = \{v \in L^2(T) \ : \ \exists w \in \mathbb{P}_p \text{ s.t. } v|_{T^+} = w \text{ and } v|_{T^-} = \mathfrak{C}(w)\}. \tag{3.55}$$

By definition, every function in $S_h^p(T)$ is the extension of a polynomial from T^+ to T through the Cauchy mapping; hence, every function in this local p-th degree IFE space is called a *Cauchy Extension* of the related p-th degree polynomial. On every non-interface element $T \in \mathcal{T}_h^n$, we use the standard polynomial space as the local IFE space, i.e., $S_h^p(T) = \mathbb{P}_p$. As usual, these local IFE spaces can be put together to form a global IFE space in the way suitable for a finite element formulation. For example, for the IFE method to be introduced in the next section, we can form the following global IFE space:

$$S_h^p(\Omega) = \{v \in L^2(\Omega) \ : \ v|_T \in S_h^p(T), \ \forall T \in \mathcal{T}_h \text{ and } v \text{ is continuous on each } e \in \widetilde{\mathcal{E}}_h^n\}. \tag{3.56}$$

Now let $\{\zeta_i \ : \ i = 1, 2 \cdots, n\}$ be a set of basis functions with desirable features for the polynomial space $\mathbb{P}_p$ with $n = (p+1)(p+2)/2$. Clearly, since $\mathfrak{C}$ is bijective on $\mathbb{P}_p$, the following piecewise polynomials

$$v_i = \begin{cases} \zeta_i & X \in T^+, \\ \mathfrak{C}(\zeta_i) & X \in T^-, \end{cases} \quad i = 1, 2, \cdots, n, \ \ \forall T \in \mathcal{T}_h^i \tag{3.57}$$

form a set of basis functions of the local IFE space $S_h^p(T)$.

We note that, by the traditional construction approaches, for example the procedure for vector IFE functions described in Section 2.4 and scalar IFE functions reviewed in Section 1.2 (or see [79, 84, 100, 136]), the IFE functions all have the Lagrange type degrees of freedom, i.e., they are constructed according to their nodal values, and their existence involves tedious analysis and calculation of the determinant of matrix in the pertinent linear system according to how the interface cuts the interface element and partitions the Lagrange nodes which is cumbersome, if not impossible, to be extended to arbitrary degree p. In contrast, the existence of the proposed p-th degree IFE functions reduces to showing the Cauchy mapping $\mathfrak{C}$ has a trivial kernel which is actually easy to verify (because the resulted functional $|||\cdot|||_{a_\lambda}$ is a norm) for any degree p. The construction procedure for IFE functions proposed here is obvious advantageous over the traditional ones in the literature.

3.4.3 Approximation Capabilities

Now we show that the proposed IFE space (3.56) has the optimal approximation capabilities to the space $PH^{p+1}(\Omega)$ with respect to the degree of polynomial space used to construct this

IFE space. On non-interface elements $T \in \mathcal{T}_h^n$, we use the usual Lagrange type interpolation operator I_T [35] to describe the approximation capability, the optimal error bounds for the Lagrange interpolation are standard which can be obtained by the scaling argument. The challenge is on interface elements where IFE functions are discontinuous across the interface Γ because of the lack of readily available error analysis tools in the literature for macro polynomials. Inspired by [88], we construct a special operator to gauge the approximation capability by taking the advantages of the Cauchy mapping. Recalling that, for each interface element $T \in \mathcal{T}_h^i$, P_{T_λ} is the standard L^2 projection from $H^{p+1}(T_\lambda)$ to $\mathbb{P}_p$, we define the following interpolation operator

$$I_T u = \begin{cases} I_T^+ u := P_{T_\lambda} u_E^+ & \text{on } T^+, \\ I_T^- u := \mathfrak{C}(P_{T_\lambda} u_E^+) & \text{on } T^-, \end{cases} \quad \forall u \in H^{p+1}(T_\lambda). \tag{3.58}$$

Then, the global interpolation operator $I_h : PH^{p+1}(\Omega) \to S_h^p(\Omega)$ is defined piecewise as

$$I_h u|_T = I_T u, \quad \forall T \in \mathcal{T}_h. \tag{3.59}$$

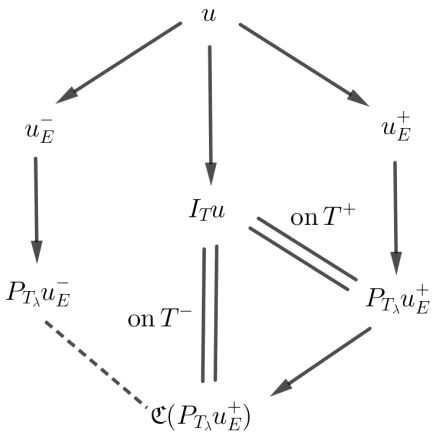

Figure 3.9: Diagram for analyzing approximation capabilities

The key idea for using this interpolation operator to analyze the approximation capability of the proposed p-th degree IFE space is a delicate decomposition of the interpolation errors illustrated by the diagram in Figure 3.9. As shown in this diagram, the error of the interpolation $I_T u$ can be decomposed into the errors between the Sobolev extensions $u_E^s, s = \pm$ of the components of u and their projections $P_{T_\lambda} u_E^s, s = \pm$, and the error between the projection $P_{T_\lambda} u_E^-$ and the Cauchy extension $\mathfrak{C}(P_{T_\lambda} u_E^+)$. We note that the errors between the Sobolev extensions and their projections are well understood; hence, a solid arrow is used to connect them in the diagram. However, the difference between the projection $P_{T_\lambda} u_E^-$ and the Cauchy extension $\mathfrak{C}(P_{T_\lambda} u_E^+)$, connected by a dashed line in the diagram, is unknown in the literature which motivates us to carry out preparations such as Theorem 3.1 in the previous sections.

Theorem 3.3. *Let $u \in PH^{p+1}(\Omega)$. There exist constants C such that, on every interface element $T \in \mathcal{T}_h^i$ with its associated fictitious element T_λ, $\lambda > 1$,*

$$\sum_{j=0}^{2} h_T^j |u_E^+ - I_T^+ u|_{H^j(T)} \leqslant C h_T^{p+1} |u_E^+|_{H^{p+1}(T_\lambda)}, \tag{3.60a}$$

$$\sum_{j=0}^{2} h_T^j |u_E^- - I_T^- u|_{H^j(T)} \leqslant C h_T^{p+1} (\frac{\beta^+}{\beta^-} |u_E^+|_{H^{p+1}(T_\lambda)} + |u_E^-|_{H^{p+1}(T_\lambda)}), \tag{3.60b}$$

where $I_T^+ u$ and $I_T^- u$ are understood as polynomials on the whole element T.

Proof. We note that (3.60a) is simply the optimal approximation capability for the projection operator P_{T_λ}. For (3.60b), note that $I_T^- u - P_{T_\lambda} u_E^- = \mathfrak{C}(P_{T_\lambda} u_E^+) - P_{T_\lambda} u_E^- \in \mathbb{P}_p$, then the norm equivalence given in Lemmas 3.5, 3.7, and 3.10 together with the estimate given in Theorem 3.1 imply

$$\begin{aligned} \|I_T^- u - P_{T_\lambda} u_E^-\|_{L^2(T)} &\leqslant C \|I_T^- u - P_{T_\lambda} u_E^-\|_{L^2(T_\lambda^-)} \leqslant C h_T^2 \left|\!\left|\!\left| \mathfrak{C}(P_{T_\lambda} u_E^+) - P_{T_\lambda} u_E^- \right|\!\right|\!\right|_{a_\lambda} \\ &\leqslant C h_T^{p+1} (\frac{\beta^+}{\beta^-} |u_E^+|_{H^{p+1}(T_\lambda)} + |u_E^-|_{H^{p+1}(T_\lambda)}). \end{aligned} \tag{3.61}$$

In addition, applying the standard inverse inequality to (3.61), we have

$$\begin{aligned} h_T^j |I_T^- u - P_{T_\lambda} u_E^-|_{H^j(T)} &\leqslant C \|I_T^- u - P_{T_\lambda} u_E^-\|_{L^2(T)} \\ &\leqslant C h_T^{p+1} (\frac{\beta^+}{\beta^-} |u_E^+|_{H^{p+1}(T_\lambda)} + |u_E^-|_{H^{p+1}(T_\lambda)}). \end{aligned} \tag{3.62}$$

Finally, the triangular inequality and the optimal approximation capability for the projection P_{T_λ} yield

$$\begin{aligned} h_T^j |u_E^- - I_T^- u|_{L^2(T)} &\leqslant C h_T^j |u_E^- - P_{T_\lambda} u_E^-|_{L^2(T)} + C h_T^j |P_{T_\lambda} u_E^- - I_T^- u|_{L^2(T)} \\ &\leqslant C h_T^{p+1} (\frac{\beta^+}{\beta^-} |u_E^+|_{H^{p+1}(T_\lambda)} + |u_E^-|_{H^{p+1}(T_\lambda)}). \end{aligned} \tag{3.63}$$

□

Remark 3.2. *Since $\beta^- \geqslant \beta^+$, from* (3.60)*, we have the following estimate which is independent of the jumps $\beta^\pm$*

$$\sum_{j=0}^{2} h_T^j |u - I_T u|_{H^j(T)} \leqslant C h_T^{p+1} (|u_E^+|_{H^{p+1}(T_\lambda)} + |u_E^-|_{H^{p+1}(T_\lambda)}). \tag{3.64}$$

This is also an advantage of the proposed IFE spaces and the related analysis.

3.5 A p-th Degree DGIFE Method for the Interface Problems

In this section, we develop and analyze a discontinuous Galerkin immersed finite element (DGIFE) method for solving the elliptic interface problem (3.1a)-(3.1e). First of all, on the unfitted mesh $\mathcal{T}_h$, inspired by [88], we consider a mesh-dependent space V_h defined as

$$\begin{aligned} V_h = \big\{ v \in L^2(\Omega) \ : \ & v|_T \in H^1(T) \text{ if } T \in \mathcal{T}_h^n, \ v|_{T^\pm} \in H^1(T^\pm) \text{ if } T \in \mathcal{T}_h^i, \\ & \text{and } v \text{ is continuous on each } e \in \widetilde{\mathcal{E}}_h^n, \ v|_{\partial\Omega} = 0 \big\}, \end{aligned} \tag{3.65}$$

and we note that the functions in V_h are in $H^1(\Omega \backslash (\overline{\cup_{T \in T_h^i} T}))$. Let $S_{h,0}^p(\Omega)$ be the subspace of $S_h^p(\Omega)$ with zero trace on $\partial\Omega$, and clearly, we have $S_{h,0}^p(\Omega) \subseteq V_h$. We emphasize that functions in V_h may not be continuous across non-interface edges of interface elements. We will use the following operators on V_h defined across the interface and across an interface edge $e \in \widetilde{\mathcal{E}}_h^i$ shared by two elements T_1 and T_2, respectively:

$$[v]_\Gamma = (v|_{\Omega^+})|_\Gamma - (v|_{\Omega^-})|_\Gamma \quad \text{and} \quad \{v\}_\Gamma = \frac{(v|_{\Omega^+})|_\Gamma + (v|_{\Omega^-})|_\Gamma}{2}, \ \ \forall v \in V_h, \tag{3.66a}$$

$$[v]_e = (v|_{T_1})|_e - (v|_{T_2})|_e \quad \text{and} \quad \{v\}_e = \frac{(v|_{T_1})|_e + (v|_{T_2})|_e}{2}, \ \ \forall v \in V_h. \tag{3.66b}$$

Then, testing (3.1a) by a function in $V_h(\Omega)$ and applying the integration by parts on each element, we obtain the following weak formulation:

$$a_h(u,v) = L_f(v), \ \ \forall v \in V_h(\Omega), \tag{3.67a}$$

$$\begin{aligned} a_h(u,v) = & \sum_{T \in \mathcal{T}_h} \int_T \beta \nabla u \cdot \nabla v dX \\ & - \sum_{e \in \widetilde{\mathcal{E}}_h^i} \int_e \{\beta \nabla u \cdot \mathbf{n}\}_e [v]_e ds + \epsilon_0 \sum_{e \in \widetilde{\mathcal{E}}_h^i} \int_e \{\beta \nabla v \cdot \mathbf{n}\}_e [u]_e ds + \sum_{e \in \widetilde{\mathcal{E}}_h^i} \frac{\rho_e^0 \gamma}{|e|} \int_e [u]_e \, [v]_e ds \\ & - \sum_{T \in \mathcal{T}_h^i} \int_{\Gamma_T} \{\beta \nabla u \cdot \mathbf{n}\}_\Gamma [v]_\Gamma ds + \epsilon_1 \sum_{T \in \mathcal{T}_h^i} \int_{\Gamma_T} \{\beta \nabla v \cdot \mathbf{n}\}_\Gamma [u]_\Gamma ds + \sum_{T \in \mathcal{T}_h^i} \frac{\rho_e^1 \gamma}{h_T} \int_{\Gamma_T} [u]_\Gamma \, [v]_\Gamma ds, \end{aligned} \tag{3.67b}$$

$$L_f(v) = \int_\Omega f v dX, \tag{3.67c}$$

where ρ_e^0 ,ρ_e^1 are some constants independent of the coefficients $\beta^\pm$, and

$$\gamma = (\max\{\beta^-, \beta^+\})^2 / \min\{\beta^-, \beta^+\}. \tag{3.68}$$

Based on the weak formulation in (3.67), we define the p-th degree DGIFE solution to the interface problem (3.1a)-(3.1d) as the $u_h \in S_{h,0}^p(\Omega)$ such that

$$a_h(u_h, v_h) = L_f(v_h), \quad \forall v_h \in S_{h,0}^p(\Omega). \tag{3.69}$$

Following the tradition, we also call (3.69) the symmetric, non-symmetric and incomplete p-th degree DGIFE method for $\epsilon_0 = \epsilon_1 = -1$, $\epsilon_0 = \epsilon_1 = 1$ and $\epsilon_0 = \epsilon_1 = 0$ in (3.67), respectively. Note that the bilinear form (3.67b) used in this method involves the penalties on edges in $\widetilde{\mathcal{E}}_h^i$ and the interface itself which set the proposed DGIFE method apart from the partially penalized IFE (PPIFE) method [85, 148] and the one in (2.101) in Chapter 2 where the penalties are only used on the interface edges, and from the CutFEM [91] where the penalties are only enforced on the interface. This p-th degree DGIFE method (3.69) is also related with the selective IFE method [104] and the IFE method in [88] sans the penalty on the interface.

3.5.1 Trace Inequalities for p-th Degree IFE Functions

In this subsection, we establish a group of trace inequalities for the p-th degree IFE functions on interface elements, which are critical for the error analysis of the proposed DGIFE scheme. We emphasize that the trace inequalities for IFE functions as well as their proofs are nontrivial since the underlying piecewise polynomials do not have sufficient regularity for standard trace inequalities to be applied and the usual scaling argument of finite element analysis is also inapplicable. We seek for new analysis techniques by taking advantages of the Cauchy extension, in particular its stability stated in Theorem 3.2 which suggests two polynomial components in an IFE function are connected together to behave collectively in a certain way close to a standard polynomial. Without loss of generality, we consider the two interface element configuration as shown in Figure 3.10 where T^- is either the triangular or quadrilateral curved-edge subelement.

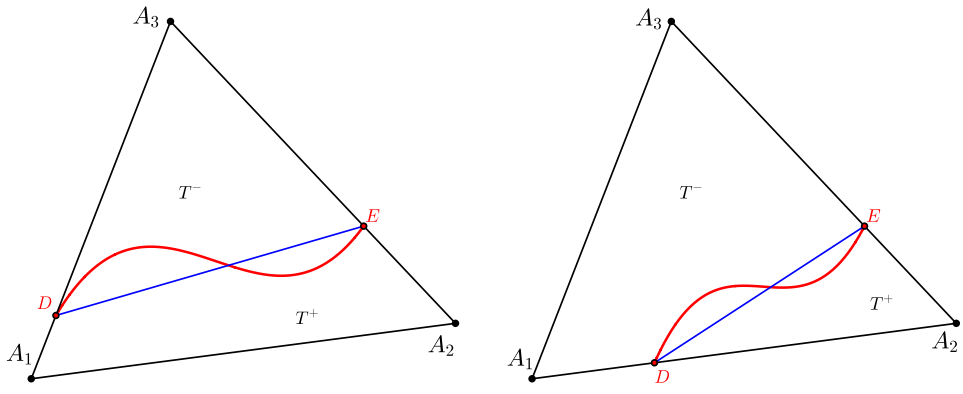

(a) Case 1 (b) Case 2

Figure 3.10: Trace inequalities for higher-degree IFE functions

Theorem 3.4. *Let e be an edge of an interface element T in the configuration of Case 1 in*

Figure 3.10. If $|A_3D| \geqslant 1/2|A_3A_1|$ *and* $|A_3E| \geqslant 1/2|A_3A_2|$*, then*

$$\|\beta\nabla\phi\|_{L^2(e)} \leqslant Ch_T^{-1/2}\|\beta\nabla\phi\|_{L^2(T)}, \quad \forall\phi \in S_h^p(T). \tag{3.70}$$

On the other hand, if $|A_3D| \leqslant 1/2|A_3A_1|$ *or* $|A_3E| \leqslant 1/2|A_3A_2|$*, then*

$$\|\nabla\phi\|_{L^2(e)} \leqslant Ch_T^{-1/2}\|\nabla\phi\|_{L^2(T)}, \quad \forall\phi \in S_h^p(T). \tag{3.71}$$

Proof. Without loss of generality, we consider the interface edge A_1A_3 and the non-interface edge A_1A_2. Recall $\widetilde{T}^-$ and $\widetilde{T}^+$ are the straight-edge triangle $\triangle A_3DE$ and quadrilateral A_1A_2ED. Firstly, if $|A_3E| \geqslant 1/2|A_3A_2|$ and $|A_3D| \geqslant 1/2|A_3A_1|$, the trace inequality (2.107) and the norm equivalence in (3.22) lead to

$$\|\beta^-\nabla\phi^-\|_{L^2(A_3D)} \leqslant Ch_T^{-1/2}\|\beta^-\nabla\phi^-\|_{L^2(\widetilde{T}^-)} \leqslant Ch_T^{-1/2}\|\beta^-\nabla\phi^-\|_{L^2(T^-)}. \tag{3.72}$$

For the estimation on the sub-edge DA_1, we apply the trace inequality (2.107) to obtain

$$\begin{aligned}\|\beta^+\nabla\phi^+\|_{L^2(DA_1)} &\leqslant Ch_T^{-1/2}\|\beta^+\nabla\phi^+\|_{L^2(T)} \\ &\leqslant Ch_T^{-1/2}(\|\beta^+\nabla\phi^+\|_{L^2(T^+)} + \|\beta^+\nabla\phi^+\|_{L^2(T^-)}).\end{aligned} \tag{3.73}$$

Now using the fictitious element T_λ, we proceed to bound the second term on the right hand side of (3.73). The triangular inequality and the norm equivalence in (3.22), (3.25) and the lower bound in Theorem 3.2 yield

$$\begin{aligned}\|\beta^+\nabla\phi^+\|_{L^2(T^-)} &\leqslant C\|\beta^+\nabla\phi^+\|_{L^2(T_\lambda^-)} \leqslant C|\beta^+\mathfrak{C}^{-1}(\phi^-)|_{H^1(T_\lambda^-)} \\ &\leqslant C|\beta^-\phi^-|_{H^1(T_\lambda^-)} \leqslant C\|\beta^-\nabla\phi^-\|_{L^2(T^-)},\end{aligned} \tag{3.74}$$

where we have also used the definition $\phi^- = \mathfrak{C}(\phi^+)$. Thus, combining (3.72)-(3.74), we have the desired trace inequality (3.70) on the interface edge $e = A_1A_3$. The estimation on the non-interface edge $e = A_1A_2$ follows from a similar derivation to (3.73)-(3.74).

Secondly, if $|A_3E| \leqslant 1/2|A_3A_2|$ or $|A_3D| \leqslant 1/2|A_3A_1|$, without loss of generality, we assume $|A_3D| \leqslant 1/2|A_3A_1|$. Then, the estimation on the sub-edge A_1D directly follows from the trace inequality (2.107) and the norm equivalence in (3.23). For the sub-edge A_3D, a similar argument to (3.73) yields

$$\begin{aligned}\|\nabla\phi^-\|_{L^2(A_3D)} &\leqslant Ch_T^{-1/2}\|\nabla\phi^-\|_{L^2(T)} \\ &\leqslant Ch_T^{-1/2}(\|\nabla\phi^-\|_{L^2(T^-)} + \|\nabla\phi^-\|_{L^2(T^+)}).\end{aligned} \tag{3.75}$$

Then, similar to (3.74), using the norm equivalence in (3.23) and (3.25), but the upper bound in Theorem 3.2, we have

$$\begin{aligned}\|\nabla\phi^-\|_{L^2(T^+)} &\leqslant C\|\nabla\phi^-\|_{L^2(T_\lambda^+)} \leqslant C|\phi^-|_{H^1(T_\lambda^-)} \leqslant C|\phi^+|_{H^1(T_\lambda^-)} \\ &\leqslant C\|\nabla\phi^+\|_{L^2(T_\lambda^+)} \leqslant C\|\nabla\phi^+\|_{L^2(T^+)}.\end{aligned} \tag{3.76}$$

Therefore, (3.71) on the interface edge A_1A_2 follows from (3.75)-(3.76). The result for the non-interface edge follows directly from the standard trace inequality (2.107) together with the norm equivalence (3.23). □

The next theorem concerns the trace inequalities on the interface.

Theorem 3.5. *Let T be an interface element in the configuration of Case 1 in Figure 3.10. If $|A_3D| \geqslant 1/2|A_3A_1|$ and $|A_3E| \geqslant 1/2|A_3A_2|$, then for $\forall \phi \in S_h^p(T)$,*

$$\|\nabla\phi^-\|_{L^2(\Gamma_T)} \leqslant Ch_T^{-1/2}\|\nabla\phi^-\|_{L^2(T^-)}, \quad \|\beta^+\nabla\phi^+\|_{L^2(\Gamma_T)} \leqslant Ch_T^{-1/2}\|\beta\nabla\phi\|_{L^2(T)}. \tag{3.77}$$

On the other hand, if $|A_3D| \leqslant 1/2|A_3A_1|$ or $|A_3E| \leqslant 1/2|A_3A_2|$, then for $\forall \phi \in S_h^p(T)$,

$$\|\nabla\phi^-\|_{L^2(\Gamma_T)} \leqslant Ch_T^{-1/2}\|\nabla\phi\|_{L^2(T)}, \quad \|\nabla\phi^+\|_{L^2(\Gamma_T)} \leqslant Ch_T^{-1/2}\|\nabla\phi^+\|_{L^2(T^+)}. \tag{3.78}$$

Proof. The proof is basically as the same as the one of Theorem 3.4. Here, for simplicity, we only discuss the case that $|A_3D| \geqslant 1/2|A_3A_1|$ and $|A_3E| \geqslant 1/2|A_3A_2|$, and the other case can be discussed similarly. The trace inequality (3.26b) and the norm equivalence in (3.21), (3.22) and (3.25) yield

$$\|\nabla\phi^-\|_{L^2(\Gamma_T)} \leqslant Ch_T^{-1/2}\|\nabla\phi^-\|_{L^2(T_\lambda^-)} \leqslant Ch_T^{-1/2}\|\nabla\phi^-\|_{L^2(T^-)}. \tag{3.79}$$

$$\begin{aligned}\|\beta^+\nabla\phi^+\|_{L^2(\Gamma_T)} &\leqslant Ch_T^{-1/2}\|\beta^+\nabla\phi^+\|_{L^2(T_\lambda)} \\ &\leqslant Ch_T^{-1/2}(\|\beta^+\nabla\phi^+\|_{L^2(T^+)} + \|\beta^+\nabla\phi^+\|_{L^2(T^-)}).\end{aligned} \tag{3.80}$$

Note that (3.79) already gives the first inequality in (3.77). Applying the results in (3.74) to the second term on the right of (3.80), we arrive at the second inequality in (3.77). □

To avoid redundancy, we now present the trace inequalities for an interface element T in the configuration of Case 2 in Figure 3.10 without giving the detailed proof because the arguments are basically as same as those for Theorems 3.4 and 3.5.

Theorem 3.6. *Let e be an edge of an interface element T in the configuration of Case 2 in Figure 3.10. If $|A_2D| \geqslant 1/2|A_2A_1|$ and $|A_2E| \geqslant 1/2|A_3A_2|$, then*

$$\|\nabla\phi\|_{L^2(e)} \leqslant Ch_T^{-1/2}\|\nabla\phi\|_{L^2(T)}, \quad \forall \phi \in S_h^p(T). \tag{3.81}$$

On the other hand, if $|A_2D| \leqslant 1/2|A_2A_1|$ or $|A_2E| \leqslant 1/2|A_3A_2|$, then

$$\|\beta\nabla\phi\|_{L^2(e)} \leqslant Ch_T^{-1/2}\|\beta\nabla\phi\|_{L^2(T)}, \quad \forall \phi \in S_h^p(T). \tag{3.82}$$

Theorem 3.7. *Let T be an interface element in the configuration of Case 2 in Figure 3.10. If $|A_2D| \geqslant 1/2|A_2A_1|$ and $|A_2E| \geqslant 1/2|A_3A_2|$, then for $\forall \phi \in S_h^p(T)$,*

$$\|\nabla\phi^-\|_{L^2(\Gamma_T)} \leqslant Ch_T^{-1/2}\|\nabla\phi\|_{L^2(T)}, \quad \|\nabla\phi^+\|_{L^2(\Gamma_T)} \leqslant Ch_T^{-1/2}\|\nabla\phi^+\|_{L^2(T^+)}. \tag{3.83}$$

On the other hand, if $|A_2D| \leqslant 1/2|A_2A_1|$ or $|A_2E| \leqslant 1/2|A_3A_2|$, then for $\forall \phi \in S_h^p(T)$

$$\|\nabla\phi^-\|_{L^2(\Gamma_T)} \leqslant Ch_T^{-1/2}\|\nabla\phi^-\|_{L^2(T^-)}, \quad \|\beta^+\nabla\phi^+\|_{L^2(\Gamma_T)} \leqslant Ch_T^{-1/2}\|\beta\nabla\phi\|_{L^2(T)}. \tag{3.84}$$

Remark 3.3. *We can summarize estimates given in Theorems 3.4-3.7 as follows so that they can be directly used later on:*

$$\begin{aligned} |e|^{1/2}\|\beta\nabla\phi\|_{L^2(e)} &\leqslant C_t\frac{\beta^-}{\sqrt{\beta^+}}\|\sqrt{\beta}\nabla\phi\|_{L^2(T)}, \quad \forall\phi\in S_h^p(T),\\ h_T^{1/2}\|\beta\nabla\phi\|_{L^2(\Gamma_T)} &\leqslant C_t\frac{\beta^-}{\sqrt{\beta^+}}\|\sqrt{\beta}\nabla\phi\|_{L^2(T)}, \quad \forall\phi\in S_h^p(T), \end{aligned} \tag{3.85}$$

where C_t is a constant independent of interface location and $\beta^{\pm}$.

Remark 3.4. *We highlight that the stability in Theorem 3.2 reveals the connection of the two polynomials components in an IFE function for arbitrary degree which is also the fundamental spirit in the proofs for Theorems 3.4-3.7.*

3.5.2 Error Estimation of the DGIFE Method

In this subsection, we employ the results established above to estimate errors in the solution of the DGIFE scheme. According to (3.67b), we consider the following quantities on the space V_h:

$$\|v\|_h^2 = \sum_{T\in\mathcal{T}_h}\int_T \|\sqrt{\beta}\nabla v\|^2 dX + \sum_{e\in\widetilde{\mathcal{E}}_h^i}\frac{\rho_e^0\gamma}{|e|}\int_e [v]_e^2 ds + \sum_{T\in\mathcal{T}_h^i}\frac{\rho_e^1\gamma}{h_T}\int_{\Gamma_T}[v]_\Gamma^2 ds, \tag{3.86a}$$

$$|||v|||_h^2 = \|v\|_h^2 + \frac{|e|}{\rho_e^0\gamma}\sum_{e\in\widetilde{\mathcal{E}}_h^i}\int_e(\{\beta\nabla v\cdot\mathbf{n}\}_e)^2 ds + \frac{h_T}{\rho_e^1\gamma}\sum_{T\in\mathcal{T}_h^i}\int_{\Gamma_T}(\{\beta\nabla v\cdot\mathbf{n}\}_\Gamma)^2 ds, \tag{3.86b}$$

and it is easy to verify that

$$\|v\|_h \leqslant |||v|||_h, \quad \forall v\in V_h. \tag{3.87}$$

In addition, we show that they are indeed norms in the space V_h.

Lemma 3.12. *$\|\cdot\|_h$ and $|||\cdot|||_h$ are both norms on the space V_h.*

Proof. Because of (3.87), we only need to discuss $\|\cdot\|_h$. Given each $v\in V_h$, $\|\cdot\|_h = 0$ yields $v|_T\in\mathbb{P}_0$ for every $T\in\mathcal{T}_h^n$, $v|_{T^\pm}\in\mathbb{P}_0$ for every $T\in\mathcal{T}_h^i$ and v is continuous on all the edges and the interface. Furthermore, due to that $v|_{\partial\Omega}=0$, we have $v=0$ on the whole domain Ω. □

Furthermore, in addition to (3.87), we can prove the following relation between these two norms.

Lemma 3.13. *For sufficiently large ρ_e^0 and ρ_e^1, there holds $\sqrt{2}\|v\|_h \geqslant |||v|||_h$, $\forall v\in S_h^p(\Omega)$.*

Proof. Given each $e \in \widetilde{\mathcal{E}}_h^i$, let T^1 and T^2 be the two elements sharing e. Then the Hölder's inequality and the trace inequality (3.85) yield

$$\frac{|e|}{\rho_e^0\gamma}\int_e(\{\beta\nabla v\cdot\mathbf{n}_e\}_e)^2ds \leqslant \frac{C_t^2}{2\rho_e^0}(\|\sqrt{\beta}\nabla\phi\|^2_{L^2(T^1)}+\|\sqrt{\beta}\nabla\phi\|^2_{L^2(T^2)}), \tag{3.88}$$

$$\frac{h_T}{\rho_e^1\gamma}\int_{\Gamma_T}(\{\beta\nabla v\cdot\mathbf{n}_\Gamma\}_\Gamma)^2ds \leqslant \frac{C_t^2}{\rho_e^1}\|\sqrt{\beta}\nabla\phi\|^2_{L^2(T)}, \tag{3.89}$$

Hence, we have $|||v|||_h^2 \leqslant 2\|v\|_h^2$, $\forall v \in S_h^p(\Omega)$ for any $\rho_e^0 \geq 3C_t^2/2$ and any $\rho_e^1 \geq 3C_t^2/2$. □

The following theorem provides an estimate for the global approximation capability in terms of the energy norms defined in (3.86b).

Theorem 3.8. *Given each $u \in PH^{p+1}(\Omega)$, there exists a constant C such that*

$$|||u-I_hu|||_h \leqslant Ch^p\frac{\beta^-}{\sqrt{\beta^+}}\sum_{k=1}^{p+1}(|u^-|_{H^k(\Omega^-)}+|u^+|_{H^k(\Omega^+)}). \tag{3.90}$$

Proof. Firstly, using the estimate for the Lagrange interpolation [35] on non-interface elements, we have

$$\sum_{T\in\mathcal{T}_h^n}\int_T\beta\|\nabla(u-I_Tu)\|^2dX \leqslant Ch^{2p}\beta^-\sum_{T\in\mathcal{T}_h^n}|u|^2_{H^{p+1}(T)}. \tag{3.91}$$

Over all the interface elements, Theorem 3.3 directly yields

$$\sum_{T\in\mathcal{T}_h^i}\int_T\beta\|\nabla(u-I_Tu)\|^2dX \leqslant Ch^{2p}\beta^-\sum_{T\in\mathcal{T}_h^i}(|u_E^+|^2_{H^{p+1}(T_\lambda)}+|u_E^-|^2_{H^{p+1}(T_\lambda)}), \tag{3.92}$$

In addition, given each interface edge $e \in \widetilde{\mathcal{E}}_h^i$ with the two neighbor elements T^1 and T^2, let $e^\pm = e\cap\Omega^\pm$ and $\tilde{h} = \max\{h_{T^1}, h_{T^2}\}$. Using Theorem 3.3 and the standard trace inequality, we have

$$\begin{aligned}
\sum_{r=\pm}\frac{\rho_e^0\gamma}{|e|}\int_{e^r}[u^r-I_h^ru]_e^2ds &\leqslant C\sum_{r=\pm}\tilde{h}^{-1}\gamma\int_e[u_E^r-I_h^ru]_e^2ds\\
&\leqslant C\sum_{r=\pm}\sum_{j=1,2}\tilde{h}^{-1}\gamma\int_e((u_E^r-I_h^ru)|_{T^j})^2ds\\
&\leqslant C\sum_{r=\pm}\sum_{j=1,2}\gamma(\tilde{h}^{-2}\|u_E^r-I_{T^j}^ru\|^2_{L^2(T^j)}+|u_E^r-I_{T^j}^ru|^2_{H^1(T^j)})\\
&\leqslant C\tilde{h}^{2p}\gamma(|u_E^+|^2_{H^{p+1}(T_\lambda^1\cup T_\lambda^2)}+|u_E^-|^2_{H^{p+1}(T_\lambda^1\cup T_\lambda^2)}).
\end{aligned} \tag{3.93}$$

The estimations on non-interface edges in $\widetilde{\mathcal{E}}_h^i$ can be proven similarly. Thus, we have

$$\sum_{e\in\widetilde{\mathcal{E}}_h^i}\frac{\rho_e^0\gamma}{|e|}\int_e[u-I_hu]_e^2ds\leqslant Ch^{2p}\gamma\sum_{T\in\mathcal{T}_h^i}(|u_E^+|^2_{H^{p+1}(T_\lambda)}+|u_E^-|^2_{H^{p+1}(T_\lambda)}). \tag{3.94}$$

Next, using Lemma 3.2 in [196], Theorem 3.3 and the standard trace inequality, we have

$$\begin{aligned}\sum_{T\in\mathcal{T}_h^i}\frac{\rho_e^1\gamma}{h_T}\int_{\Gamma_T}[u-I_hu]_\Gamma^2ds&\leqslant C\sum_{T\in\mathcal{T}_h^i}\sum_{r=\pm}h_T^{-1}\gamma\int_{\Gamma_T}(u_E^r-I_T^ru)^2ds\\&\leqslant C\sum_{T\in\mathcal{T}_h^i}\sum_{r=\pm}h_T^{-1}\gamma\left(h_T^{-1}\|u_E^r-I_T^ru\|^2_{L^2(T)}+h_T\|\nabla(u_E^r-I_T^ru)\|^2_{L^2(T)}\right)\\&\leqslant Ch_T^{2p}\gamma\sum_{T\in\mathcal{T}_h^i}(|u_E^+|^2_{H^{p+1}(T_\lambda)}+|u_E^-|^2_{H^{p+1}(T_\lambda)}).\end{aligned} \tag{3.95}$$

By similar arguments, we can also show that

$$\begin{aligned}&\sum_{e\in\widetilde{\mathcal{E}}_h^i}\frac{|e|}{\rho_e^0\gamma}\int_e(\{\beta\nabla(I_hu-u)\cdot\mathbf{n}_e\}_e)^2ds\\\leqslant&Ch^{2p}\gamma\sum_{T\in\mathcal{T}_h^i}(|u_E^+|^2_{H^{p+1}(T_\lambda^1\cup T_\lambda^2)}+|u_E^-|^2_{H^{p+1}(T_\lambda^1\cup T_\lambda^2)}),\end{aligned} \tag{3.96}$$

$$\begin{aligned}&\sum_{T\in\mathcal{T}_h^i}\frac{h_T}{\rho_e^1\gamma}\int_{\Gamma_T}(\{\beta\nabla(I_hu-u)\cdot\mathbf{n}_\Gamma\}_\Gamma)^2ds\\\leqslant&Ch^{2p}\gamma\sum_{T\in\mathcal{T}_h^i}(|u_E^+|^2_{H^{p+1}(T_\lambda)}+|u_E^-|^2_{H^{p+1}(T_\lambda)}).\end{aligned} \tag{3.97}$$

Now recall $\gamma=(\beta^-)^2/\beta^+$ because of the assumption that $\beta^-\geq\beta^+$, then combining the estimations above and using the finite overlapping Assumption (**A2**), we arrive at

$$|||u-I_hu|||_h\leqslant Ch^p\sqrt{\gamma}\left(|u_E^-|_{H^{p+1}(\Omega)}+|u_E^+|_{H^{p+1}(\Omega)}\right), \tag{3.98}$$

which yields the desired result by the boundedness of Sobolev extension in (3.5). □

Remark 3.5. *Let $m\geqslant 1$ and $p\geqslant 1$ be two integers with $m\leqslant p$, $u\in PH^{m+1}(\Omega)$ and let I_h be p-th degree interpolation operator defined in* (3.58)*. Using the more general approximation capability for the Lagrange interpolation operator and standard L^2 projection operator, we can actually prove a more general result:*

$$|||u-I_hu|||_h\leqslant Ch^m\frac{\beta^-}{\sqrt{\beta^+}}\sum_{k=1}^{m+1}(|u^-|_{H^k(\Omega^-)}+|u^+|_{H^k(\Omega^+)}). \tag{3.99}$$

The following two theorems establish the coercivity and continuity of the bilinear form $a_h(\cdot,\cdot)$.

Theorem 3.9. *Assume the constants ρ_e^0 and ρ_e^1 are large enough for the symmetric and incomplete p-th degree IFE method or they are just positive for non-symmetric p-th degree IFE method, then there holds*

$$a_h(v,v) \geqslant \frac{1}{2}\|v\|_h^2, \quad \forall v \in S_h^p(\Omega). \tag{3.100}$$

Proof. We note that

$$\begin{aligned} a_h(v,v) = &\sum_{T\in\mathcal{T}_h}\int_T \beta\nabla v\cdot\nabla v dX + (\epsilon_0-1)\sum_{e\in\widetilde{\mathcal{E}}_h^i}\int_e \{\beta\nabla v\cdot\mathbf{n}_e\}_e[v]_e ds + \sum_{e\in\widetilde{\mathcal{E}}_h^i}\frac{\rho_e^0\gamma}{|e|}\int_e [v]_e^2 ds \\ &(\epsilon_1-1)\sum_{T\in\mathcal{T}_h^i}\int_{\Gamma_T}\{\beta\nabla v\cdot\mathbf{n}_\Gamma\}_\Gamma[v]_\Gamma ds + \sum_{T\in\mathcal{T}_h^i}\frac{\rho_e^1\gamma}{h_T}\int_{\Gamma_T}[v]_\Gamma^2 ds. \end{aligned} \tag{3.101}$$

Thus, the result (3.100) is trivial for the non-symmetric case because $\epsilon_1=\epsilon_0=1$. For the other two, given each $e\in\widetilde{\mathcal{E}}_h^i$, let T^1 and T^2 be the two elements sharing e, then the derivation in (3.88) and (3.89) gives

$$\left|(\epsilon_0-1)\int_e\{\beta\nabla v\cdot\mathbf{n}_e\}_e[v]_e ds\right| \leqslant \alpha(\|\sqrt{\beta}\nabla\phi\|_{L^2(T^1)}^2 + \|\sqrt{\beta}\nabla\phi\|_{L^2(T^2)}^2) + \frac{C_t^2\gamma}{2\alpha|e|}\|[v]_e\|_{L^2(e)}^2, \tag{3.102}$$

$$\left|(\epsilon_1-1)\int_{\Gamma_T}\{\beta\nabla v\cdot\mathbf{n}_\Gamma\}_\Gamma[v]_\Gamma ds\right| \leqslant 2\alpha\|\sqrt{\beta}\nabla\phi\|_{L^2(T)}^2 + \frac{C_t^2\gamma}{2\alpha h_T}\|[v]_\Gamma\|_{L^2(\Gamma_T)}^2, \tag{3.103}$$

for $\alpha>0$, where we have used the Young's inequality. Substituting (3.102) and (3.103) into (3.101) yields

$$a_h(v,v) \geqslant \sum_{T\in\mathcal{T}_h}(1-5\alpha)\|\sqrt{\beta}\nabla\phi\|_{L^2(T)}^2 + (\rho_e^0-\frac{C_t^2}{2\alpha})\frac{\gamma}{|e|}\|[v]_e\|_{L^2(e)}^2 + (\rho_e^1-\frac{C_t^2}{2\alpha})\frac{\gamma}{h_T}\|[v]_\Gamma\|_{L^2(\Gamma_T)}^2. \tag{3.104}$$

Then, letting $\alpha=1/10$, $\rho_e^0\geq 5C_t^2+1/2$, and $\rho_e^1\geq 5C_t^2+1/2$ in (3.104) leads to the desired (3.100). □

Again, we note that the technique of choosing stability parameters ρ_e^0 and ρ_e^1 large enough to prove the coercivity of the related bilinear form is widely used in the interior penalty DG methods such as those in [66, 183].

Theorem 3.10. *For every $v,w\in V_h$, there holds*

$$a_h(v,w) \leqslant 7|||v|||_h|||w|||_h. \tag{3.105}$$

Proof. The result follows from applying the Hölder's inequality on each term in the bilinear form (3.67b). □

The coercivity in term of the energy norm $\|\cdot\|_h$ guarantees the existence and uniqueness of IFE solution u_h to the p-th degree IFE method (3.69). Now we show the fundamental error estimation for the p-th degree IFE solution u_h.

Theorem 3.11. *Let $u \in PH^{p+1}(\Omega)$ with the integer $p \geqslant 1$ be the exact solution to the interface problem* (3.1a)-(3.1d)*. Assume that the mesh $\mathcal{T}_h$ is fine enough such that all the previous results hold and assume that ρ_e^0 and ρ_e^1 large enough such that Lemma 3.13-Theorem 3.9 hold. Then the p-degree IFE solution u_h has the following optimal error bound:*

$$|||u - u_h|||_h \leqslant C\frac{\beta^-}{\sqrt{\beta^+}}h^p \sum_{k=1}^{p+1}(|u^-|_{H^k(\Omega^-)} + |u^+|_{H^k(\Omega^+)}). \tag{3.106}$$

Proof. Note that the exact solution u satisfies the weak formulation (3.67) for every $v \in V_h$. Then

$$a_h(u_h - I_h u, v) = a_h(u - I_h u, v), \quad \forall v \in S_{h,0}^p(\Omega). \tag{3.107}$$

where $I_h u \in S_h^p(\Omega)$ is given by (3.59). Since $u_h - I_h u \in S_{h,0}^p(\Omega)$, Lemma 3.13 and Theorems 3.9, 3.10 give

$$\begin{aligned} \frac{1}{4}|||u_h - I_h u|||_h^2 \leqslant \frac{1}{2}\|u_h - I_h u\|_h^2 &\leqslant a_h(u_h - I_h u, u_h - I_h u) \\ &= a_h(u - I_h u, u_h - I_h u) \leqslant 7|||u - I_h u|||_h |||u_h - I_h u|||_h, \end{aligned} \tag{3.108}$$

which yields $|||u_h - I_h u|||_h \leqslant C|||u - I_h u|||_h$. Then, (3.108), the triangular inequality, and Theorem 3.8 together lead to

$$|||u - u_h|||_h \leqslant |||u - I_h u|||_h + |||I_h u - u_h|||_h \leqslant Ch^p \frac{\beta^-}{\sqrt{\beta^+}} \sum_{k=1}^{p+1}(|u^-|_{H^k(\Omega^-)} + |u^+|_{H^k(\Omega^+)}). \tag{3.109}$$

□

Remark 3.6. *The regularity result from [52, 88, 113] implies that the exact solution u to the interface problem satisfies*

$$\beta^- \sum_{k=1}^{p+1} |u^-|_{H^k(\Omega^-)} + \beta^+ \sum_{k=1}^{p+1} |u^+|_{H^k(\Omega^+)} \leqslant C\|f\|_{H^{p-1}(\Omega)}. \tag{3.110}$$

Therefore (3.106) *implies*

$$|||u - u_h|||_h \leqslant C\frac{\beta^-}{(\beta^+)^{3/2}}h^p\|f\|_{H^{p-1}(\Omega)}. \tag{3.111}$$

Finally, we follow the standard duality argument to estimate the error in L^2 norm.

Theorem 3.12. *Under the conditions of Theorem 3.11, there exists a constant C such that*

$$\|u-u_h\|_{L^2(\Omega)} \leqslant C\left(\frac{\beta^-}{\beta^+}\right)^2 h^{p+1}\sum_{k=1}^{p+1}(|u^-|_{H^k(\Omega^-)}+|u^+|_{H^k(\Omega^+)}). \tag{3.112}$$

Proof. Define an auxiliary function $z \in PH^2(\Omega)$ as the solution to the interface problem (3.1a)-(3.1d) with the right hand side f replaced by the solution error $u-u_h \in L^2(\Omega)$. In particular, we let I_h be the p-th degree interpolation defined in (3.59). Because $u-u_h \in V_h$ and $I_h z \in S^p_{h,0}(\Omega)$, we have $a_h(I_h z, u-u_h)=0$. By the continuity in Theorem 3.10, we have

$$\begin{aligned}\|u-u_h\|^2_{L^2(\Omega)} &= \int_\Omega \beta\nabla z\cdot\nabla(u-u_h)dX = a_h(z,u-u_h)\\ &= a_h(z-I_hz,u-u_h) \leqslant C|||z-I_hz|||_h|||u-u_h|||_h.\end{aligned} \tag{3.113}$$

Besides, Remark 3.5 and the regularity (3.110) yield

$$|||z-I_hz|||_h \leqslant Ch\frac{\beta^-}{\sqrt{\beta^+}}\sum_{k=1}^{2}(|z^-|_{H^k(\Omega^-)}+|z^+|_{H^k(\Omega^+)}) \leqslant C\frac{\beta^-}{(\beta^+)^{3/2}}h\|u-u_h\|_{L^2(\Omega)}. \tag{3.114}$$

Finally, combining (3.113), (3.114) and (3.111), we arrive at (3.112). □

Remark 3.7. *Following Remark 3.6, we also have*

$$\|u-u_h\|_{L^2(\Omega)} \leqslant C\frac{(\beta^-)^2}{(\beta^+)^3}h^{p+1}\|f\|_{H^{p-1}(\Omega)}. \tag{3.115}$$

Remark 3.8. *Let $m \geqslant 1$ and $p \geqslant 1$ be two integers with $m \leqslant p$, and further let the exact solution $u \in PH^{m+1}(\Omega)$. Based on Remark 3.5, we can derive the following estimates corresponding to* (3.106) *and* (3.112)*, respectively, for u with a lower regularity:*

$$|||u-u_h|||_h \leqslant C\frac{\beta^-}{\sqrt{\beta^+}}h^m\sum_{k=1}^{m+1}(|u^-|_{H^k(\Omega^-)}+|u^+|_{H^k(\Omega^+)}), \tag{3.116a}$$

$$\|u-u_h\|_{L^2(\Omega)} \leqslant C\left(\frac{\beta^-}{\beta^+}\right)^2 h^{m+1}\sum_{k=1}^{m+1}(|u^-|_{H^k(\Omega^-)}+|u^+|_{H^k(\Omega^+)}). \tag{3.116b}$$

Their proof are standard and similar to those in Theorems 3.11 and 3.12 but with the estimate in (3.99)*. Therefore, for solving problems whose exact solutions do not have the optimal regularities, the proposed higher-degree IFE method behaves in the same way as standard higher-degree finite element methods in the sense that the order of convergence of the finite element solution decreases as the regularity of the exact solution deteriorates.*

3.5.3 Numerical Examples

Now, we present some numerical examples to demonstrate features of the proposed DGIFE method. To avoid redundancy, we only consider the SDGIFE method and similar results have been observed for other choices of penalty parameters. All the computations for the presented numerical results are carried in the domain $\Omega = (-1, 1) \times (-1, 1)$ in which the interface curve Γ is a circle with radius $r_0 = \pi/6.28$ which divides Ω into two subdomains Ω^- and Ω^+ with

$$\Omega^- = \{(x, y) : x^2 + y^2 < r_0^2\}.$$

The exact solution to be tested is

$$u(x, y) = \begin{cases} \dfrac{1}{\beta^-} r^\alpha, & (x, y) \in \Omega^-, \\ \dfrac{1}{\beta^+} r^\alpha + \left(\dfrac{1}{\beta^-} - \dfrac{1}{\beta^+} \right) r_0^\alpha, & (x, y) \in \Omega^+, \end{cases} \tag{3.117}$$

where $r = \sqrt{x^2 + y^2}$ and $\alpha = 7$. It is easy to verify that u satisfies the interface jump conditions. We note that similar numerical examples have been used in [8, 79, 88, 148]. An implementation issue is the numerical quadrature on interface elements due to the cut of interface. Since the proposed IFE shape functions are piecewise polynomials partitioned by the exact interface curve, given the parametric equation of the interface, we perform the quadrature by building an iso-parametric mapping between the reference straight edge triangle/square and the physical curved edge triangles/quadrilaterals. We refer readers to [182] for the details of this quadrature technique as well as other quadrature rules on curved-edge domains.

Let e_h^0, e_h^1, e_h^∞ and $e_h^{1,\infty}$ be the solution errors measured in L^2, H^1, L^∞ and $W^{1,\infty}$ norms, respectively. In addition, we choose $\lambda = 1.4$ for constructing the fictitious elements and IFE spaces. To avoid redundancy, we only present numerical results generated by the cubic IFE methods for a small ratio of $\beta^- = 1$, $\beta^+ = 10$ and a large ratio $\beta^- = 1$, $\beta^+ = 1000$ in Tables 3.1 and 3.2, respectively. For the example with the small ratio, Table 3.1 clearly shows an optimal convergence rate in all the L^2, H^1, L^∞ and $W^{1,\infty}$ norms. In contrast, in the large ratio case, the convergence in L^∞ and $W^{1,\infty}$ norms has a little wiggle while the convergence in L^2 and H^1 norms clearly behaves optimally. These numerical results corroborate the error analysis presented in the previous section.

	e_h^∞	order	$e_h^{1,\infty}$	order	e_h^0	order	e_h^1	order
20	1.95E-4	NA	3.15E-2	NA	4.24E-5	NA	5.01E-3	NA
30	4.09E-5	3.85	5.65E-3	4.24	8.20E-6	4.05	1.48E-3	3.01
40	1.36E-5	3.83	2.84E-3	2.40	2.57E-6	4.03	6.26E-4	2.99
50	5.73E-6	3.87	1.28E-3	3.56	1.04E-6	4.04	3.20E-4	3.01
60	2.82E-6	3.89	7.59E-4	2.87	5.02E-7	4.02	1.85E-4	2.99
70	1.54E-6	3.91	4.76E-4	3.03	2.70E-7	4.03	1.17E-4	3.00
80	9.13E-7	3.92	3.21E-4	2.95	1.58E-7	4.02	7.82E-5	3.00

Table 3.1: Solution errors for $p = 3$, $\beta^- = 1$, $\beta^+ = 10$

	e_h^∞	order	$e_h^{1,\infty}$	order	e_h^0	order	e_h^1	order
20	8.34E-5	NA	1.90E-2	NA	1.19E-5	NA	1.33E-3	NA
30	1.56E-5	4.13	4.64E-3	3.48	2.36E-6	3.98	4.03E-4	2.94
40	6.68E-6	2.95	3.24E-3	1.25	7.91E-7	3.80	1.81E-4	2.78
50	2.68E-6	4.09	1.35E-3	3.91	3.21E-7	4.03	9.34E-5	2.97
60	1.39E-6	3.60	9.69E-4	1.83	1.57E-7	3.91	5.50E-5	2.91
70	7.21E-7	4.26	6.15E-4	2.95	8.49E-8	4.01	3.45E-5	3.02
80	5.21E-7	2.43	3.64E-4	3.93	4.98E-8	3.98	2.33E-5	2.93

Table 3.2: Solution errors for $p = 3$, $\beta^- = 1$, $\beta^+ = 1000$

Chapter 4

Applications of IFE Methods to Inverse Problems

In this chapter, we develop an IFE-based shape optimization algorithm for solving a class of interface inverse problems related to scalar elliptic equations on unfitted meshes. In the proposed method, both the governing PDEs and the objective functionals in the shape optimization are discretized accurately by an IFE method regardless of the interface location in a chosen unfitted mesh. Explicit formulas for both the velocity fields and the shape derivatives of IFE shape functions are derived on the unfitted mesh and they are employed in the material derivative formula together with the discretized adjoint method for accurately and efficiently computing the gradients of objective functionals with respect to the parameters of the interface curve. The shape optimization problem is therefore accurately reduced to a constrained optimization that can be implemented efficiently within the IFE framework together with a standard optimization algorithm. As demonstrated by three representative applications, the proposed IFE-based shape optimization algorithm can be employed to solve a spectrum of interface inverse problems efficiently and satisfactorily. The results in this chapter were also reported in [83].

4.1 Introduction

In this chapter, we focus on the inverse problems governed by the scalar elliptic interface (forward) problems described in (1.1)-(1.4). Here, in order to describe a general algorithm for inverse problems, we consider a group of K interface forward problems:

$$\begin{aligned} &-\nabla\cdot(\beta\nabla u^k) = f^k, && \text{in } \Omega^-\cup\Omega^+,\\ &u^k = g_D^k, && \text{on } \partial\Omega_D^k\subseteq\partial\Omega,\\ &\frac{\partial u^k}{\partial \mathbf{n}} = g_N^k, && \text{on } \partial\Omega_N^k\subseteq\partial\Omega, \end{aligned} \tag{4.1}$$

where $\overline{\partial\Omega_N^k} \cup \overline{\partial\Omega_D^k} = \partial\Omega$ and $\mathbf{n}$ is the outward normal vector of $\partial\Omega$, together with the jump conditions on the interface Γ:

$$\begin{aligned} &[u^k]|_\Gamma := u^{k,+}|_\Gamma - u^{k,-}|_\Gamma = 0, \\ &[\beta\nabla u^k \cdot \mathbf{n}]|_\Gamma := \beta^+\nabla u^{k,+}|_\Gamma \cdot \mathbf{n} - \beta^-\nabla u^{k,-}|_\Gamma \cdot \mathbf{n} = 0, \end{aligned} \tag{4.2}$$

in which $\mathbf{n}$ is the normal vector of Γ, $u^{k,s} = u^k|_{\Omega^s}$, and $\beta(X) = \beta^s$ for $X \in \Omega^s$, $s = \pm$, and $k = 1, 2\cdots, K$. We note that all these forward problems share the same interface and coefficient β, and the difference is on the boundary data g_D^k, g_N^k and the load force data f^k which represent multiple measurements in practice.

As discussed in Section 1.3, the focus of this chapter is to develop an efficient shape optimization method based on an unfitted mesh for solving geometric inverse problems related to the interface forward problems described by (4.1) and (4.2) in which we assume that the material values $\beta^s = \beta|_{\Omega^s}, s = -, +$ are known a-prior. In particular, we need to use the given measurements about u^k, $1 \le k \le K$ to recover the location and shape of the material interface Γ. By the shape optimization method [97, 165], we seek for the interface Γ^* from an optimization problem:

$$\Gamma^* = \text{argmin}\, \mathcal{J}(\Gamma), \tag{4.3}$$

where

$$\mathcal{J}(\Gamma) = \int_{\Omega_0} J(u^1(\Gamma), u^2(\Gamma), \cdots, u^K(\Gamma); X, \Gamma) dX, \tag{4.4}$$

and $u^k(\Gamma)$s, $k = 1, 2, \cdots, K$, are the solutions to the interface forward problems (4.1) and (4.2), but $\Omega_0 \subseteq \Omega$ and $J(u^1(\Gamma), u^2(\Gamma), \cdots, u^K(\Gamma); X, \Gamma)$ are application dependent. Some specific formulations of J are given in Section 4.6 for a group of representative applications. A survey of shape optimization methods applied to geometric inverse problems can be found in Section 1.3.

Due to the movement of interface, the shape optimization methods based on fitted meshes, referred as the Lagrangian approach [50], have a few drawbacks. The first concerns the mesh updating process from one iteration to the next in the optimization. As the geometry changes, to guarantee the accuracy, the mesh used by the chosen solver for the forward problems needs to be updated to fit the new interface [28, 188], which not only consumes time but also generates unsatisfactory meshes in many situations, see the illustrations in Figure 4.1 where the two plots on the left demonstrate an inappropriate mesh movement strategy leading to a mesh with less desirable qualities, especially near the right boundary. Various approaches were proposed to overcome this issue [29, 34, 191], but these approaches are challenged by complicated geometries and large shape changes in shape optimization [29, 204] which can cause excessive mesh distortion and consequently inaccurate finite element solutions. We refer readers to a survey of works about the application of the Lagrange approaches to geometric inverse problems in Section 1.3.

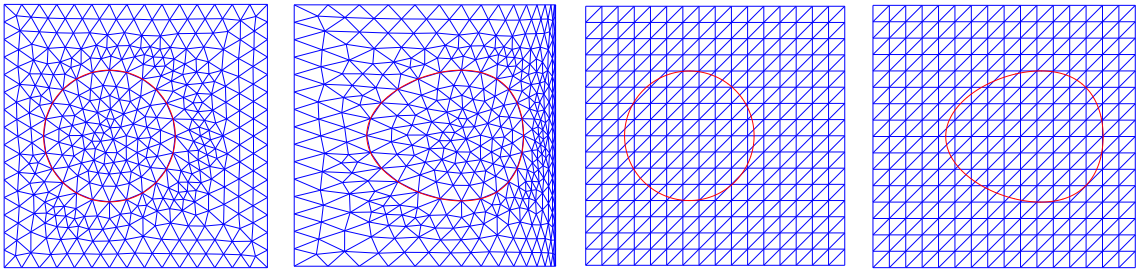

(a) The initial fitted mesh (b) The fitted mesh after movement (c) The unfitted mesh (d) The unfitted mesh

Figure 4.1: The fitted and unfitted meshes

The Lagrangian approach has more issues in the sensitivity computation in which one needs to compute the gradient of an objective functional with respect to the design variables, i.e., parameters describing the interface [97, 192, 194]. Indeed, the gradient of the objective functional is a necessary ingredient in many commonly used numerical optimization algorithms such as the descent methods and the trust region methods [61, 163]; hence, sensitivity is a fundamental part for applying these algorithms to a shape optimization problem. The gradient computation in shape optimization involves the shape derivatives and the velocity field. In this research, we employ the method of [50, 175] such that the velocity field is defined as derivatives of spatial variables with respect to the design variables which poses challenges for the Lagrangian approach. First, the nodes in a fitted mesh depend on the interface parameters (design variables), but it is difficult, if not impossible, to find or construct a formula for this dependence because the mesh is usually produced by an automatic mesh generator. Most, if not all, general mesh generators are not based on any explicit mathematical rules [50] and requiring such a formula to be differentiable is an even more excessive demand. Furthermore, the assumption that each node of a fitted mesh has to move in general as the interface changes in the Lagrangian framework inevitably leads to a global velocity field in the Lagrange framework, and a global velocity field and related quantities in a shape optimization are expensive to compute especially when the number of design variables is large.

In the Lagrangian framework, the velocity field is highly related to the mesh updating procedure in the shape optimization process. According to [50], the velocity field in the sensitivity analysis used to move the finite element mesh should have a few desirable features for maintaining the topology and quality of the mesh. Indeed, it was pointed out in [45] that an inappropriate choice of velocity field for mesh update will result in a distorted mesh and thus an inaccurate finite element solution, see again the illustration in the plots in Figure 4.1. The authors in [50] summarized three basic approaches to compute a suitable velocity field: (1) finite difference methods, (2) isoparametric mapping methods, and (3) boundary displacement and fictitious load methods. Except for the isoparametric mapping method, the other two lead to an approximate velocity field to be globally computed over the whole

solution domain. The isoparametric mapping method needs special decomposition of the computational domain which results in extra difficulties for complicated geometry. Also, it can not always guarantee mesh quality as pointed out in [50].

Therefore, forward problem solvers that can handle discontinuous coefficients on an unfitted mesh are desirable alternatives for shape optimization applications, and methods within this direction are referred as the Eulerian approach in some literatures [126]. Since the interface cuts edges of elements, various techniques are suggested to improve the accuracy of the evaluation of either the stiffness matrix or sensitivity on those interface elements. One group of the Eulerian approaches [11, 36, 44, 53] uses a local averaging method [37] to smooth the discontinuous coefficient such that standard finite element methods can be applied on an unfitted mesh. Another group of Eulerian approaches employs special finite difference/element methods such as the immersed interface methods (IIM) in [117] for cavity reconstruction in scalar elliptic equations and the extended finite element methods (XFEM) in [161, 170, 195] for crack detection.

The goal of this chapter is to develop an IFE-based shape optimization method for solving the interface inverse problem described by (4.1)-(4.4) on unfitted meshes. Specifically, we will use the PPIFE method [85, 148] with the linear IFE space for solving the related interface forward problems on an unfitted triangular (Cartesian) mesh. Using an IFE method in the shape optimization for solving interface inverse problems with an unfitted mesh is advantageous, below are some of its benefits.

- Because the IFE method allows us to use an interface-independent unfitted mesh in the shape optimization process, the issues caused by the mesh regeneration or movement from (large) interface changes are circumvented, see Figure 4.1 for an illustration. With an unfitted mesh, the velocity field does not need to guide the mesh movement; hence, some practical and theoretical issues for the construction of the velocity field [50] are simply avoided.

- Using an unfitted mesh in the shape optimization process admits a velocity field for the sensitivity that can be computed efficiently and accurately. With an unfitted mesh, as the interface updates in the optimization, the interface-mesh intersection points are changing but all the mesh nodes are fixed. Consequently only the points in interface elements should be considered to move according to the interface, and this allows a velocity field that is zero outside interface elements. Moreover, we can derive a function that explicitly relates the points inside interface elements and the design variables of the interface. Thus, the velocity field defined as the derivatives of this function can be computed efficiently by explicit formulas rather than any numerical approximation to be globally carried out over the whole domain.

- Since the mesh is the same in one step and the next of the iterative optimization process, the IFE discretization of the governing equations (4.1) maintains the same algebraic structure because the global degrees of freedom do not change, and this feature

facilitates the derivation of computation procedures for sensitivity. Moreover, assuming the interface does not evolve too drastically, the accuracy of an IFE discretization on an unfitted mesh can always remain optimal regardless of the location of the interface. Of course, no need to regenerate the mesh over and over again in the iterative optimization process helps to reduce the computational cost.

- Using the IFE method in the discretization of the shape optimization for solving interface inverse problems enables efficient and accurate computations for the sensitivity. First, the proposed framework allows us to derive explicit formulas for all the derivatives with respect to the design variables in the sensitivity including the velocity field and shape derivatives of IFE functions. Furthermore, almost all the computations for the sensitivity of the objective function are carried out only over interface elements because both the velocity field constructed in this framework and the shape derivatives of the IFE basis functions vanish over non-interface elements. This feature drastically decreases the computational cost for sensitivity since the number of the interface elements is only $\mathcal{O}(h^{-1})$ compared with $\mathcal{O}(h^{-2})$ for the total number of elements.

As demonstrated by numerical examples for a group of representative interface inverse problems in Section 4.6, these features can greatly benefit a successful application of a typical optimization algorithm, especially those based on the quasi-Newton descent direction, to minimize the objective function for solving the interface inverse problems.

4.2 An IFE Method for Interface Forward Problems

In this section, we employ the PPIFE method [85, 148] with the linear IFE space [79, 85, 136, 148], as an example of IFE methods, to describe the discretization of interface forward problems. In particular, we put the discretized interface forward problems into a unified matrix-vector form which facilitates both the derivation of shape sensitivities and related computations in practice.

We let $\Gamma(t, \boldsymbol{\alpha}), t \in [0, 1]$ be a parametrization of the interface Γ with the design variables as entries in the vector $\boldsymbol{\alpha} = (\alpha_j)_{j\in\mathcal{D}}$ where $\mathcal{D}$ is the index set of the chosen design variables. For example, when $\Gamma(t, \boldsymbol{\alpha})$ is a cubic spline, $\boldsymbol{\alpha}$ is the vector of all the coordinates of the control points of this cubic spline [70]. In a Cartesian triangular mesh $\mathcal{T}_h$ of Ω, let the node set be $\mathcal{N}_h = \{X_1, X_2, \cdots, X_{|\mathcal{N}_h|}\}$ and let $\mathring{\mathcal{N}}_h$ be the set of the interior nodes. Recall that $\mathcal{T}_h^i$ ($\mathcal{E}_h^i$) and $\mathcal{T}_h^n$ ($\mathcal{E}_h^n$) are the sets of interface and non-interface elements (edges), respectively.

On non-interface elements, the local IFE spaces are defined according to (1.12), but on interface elements, they are defined according to (1.22). In particular in this chapter, in the construction of IFE functions (1.14)-(1.21) on each interface element T, we employ F as the midpoint of the segment DE and $\mathbf{n}(F) = \bar{\mathbf{n}}$ where D and E are interface-mesh intersection points of Γ and ∂T and $\bar{\mathbf{n}}$ is the normal vector to DE, see the illustration in plot (b) of

Figure 1.2. In addition, we partition the two polynomial components of an IFE function on T by the line segment DE instead of the interface curve Γ for constructing piecewise polynomials. Such a set-up is a little different from the one in Section 1.2 but are equivalent to those in [136]. Then, we employ these local IFE spaces to define the following global IFE space

$$S_h(\Omega) = \big\{ v \in L^2(\Omega) : v|_T \in S_h(T), \forall T \in \mathcal{T}_h;\ v|_{T_1}(X) = v|_{T_2}(X),\ \forall X \in \mathcal{N}_h, \forall\, T_1, T_2 \in \mathcal{T}_h \\ \text{with } X \in T_1 \cap T_2 \big\}. \tag{4.5}$$

We note that this IFE space is similar to the vector IFE space in (2.43) for the elasticity system in the sense that all the functions in this space are continuous at mesh nodes. With this IFE space and its associated space $S_h^0(\Omega)$ whose elements have zero trace on $\partial\Omega$, the interface forward problems (4.1) and (4.2) can be discretized by the symmetric PPIFE (SPPIFE) method [148] as follows: find $u_h^k \in S_h(\Omega), k = 1, 2, \cdots, K$ such that

$$a_h(u_h^k, v_h) = L_f^k(v_h), \quad \forall v_h \in S_h^0(\Omega), \quad u_h^k(X) = g_D^k(X), \quad \forall X \in \mathcal{N}_h \cap \partial\Omega_D^k, \tag{4.6}$$

where the bilinear form $a_h(\cdot,\cdot)$ and the linear functional $L_f^k(\cdot)$ are given by

$$\begin{aligned} a_h(u_h, v_h) = &\sum_{T\in\mathcal{T}_h} \int_T \beta \nabla u_h \cdot \nabla v_h dX - \sum_{e\in\mathcal{E}_h^i \setminus \partial\Omega_N^k} \int_e \{\beta \nabla u_h\}_e \cdot [v_h]_e ds \\ &- \sum_{e\in\mathcal{E}_h^i \setminus \partial\Omega_N^k} \int_e \{\beta \nabla v_h\}_e \cdot [u_h]_e ds \\ &+ \sum_{e\in\mathcal{E}_h^i \setminus \partial\Omega_N^k} \frac{\rho_e^0}{|e|} \int_e [u_h]_e \cdot [v_h]_e ds, \quad \forall u_h, v_h \in S_h(\Omega), \end{aligned} \tag{4.7}$$

$$\begin{aligned} L_f^k(v_h) = &\int_\Omega f^k v_h dX + \int_{\partial\Omega_N^k} g_N^k v_h ds - \sum_{e\in\mathcal{E}_h^i \cap \partial\Omega_D^k} \int_e \beta g_D^k \nabla v_h \cdot \mathbf{n}_e ds \\ &+ \sum_{e\in\mathcal{E}_h^i \cap \partial\Omega_D^k} \frac{\rho_e^0}{|e|} \int_e g_D^k v_h ds, \quad \forall v_h \in S_h(\Omega). \end{aligned} \tag{4.8}$$

In the bilinear form $a_h(\cdot,\cdot)$, the operators $[\cdot]_e$ and $\{\cdot\}_e$ on each interior interface edge $e \in \mathring{\mathcal{E}}_h^i$ shared by elements T_1 and T_2 are such that

$$[v]_e = (v|_{T_1}\mathbf{n}_e^1 + v|_{T_2}\mathbf{n}_e^2) \quad \text{and} \quad \{\beta\nabla v\}_e = \frac{1}{2}(\beta\nabla v|_{T_1} + \beta\nabla v|_{T_2}),\ \forall v \in S_h(\Omega),$$

where the normal vector $\mathbf{n}_e^1 = -\mathbf{n}_e^2$ is from T^1 to T^2. For $e \in \mathcal{E}_h^i \cap \partial\Omega$, we define the operators $[\cdot]_e$ and $\{\cdot\}_e$ as

$$[v]_e = v|_T \mathbf{n}_e,\ \{\beta\nabla v\}_e = \beta\nabla v|_T,\ \forall v \in S_h(\Omega), \tag{4.9}$$

where T is the element that contains e and $\mathbf{n}_e$ is the outward normal vector to $\partial\Omega$. In our applications, we choose $\rho_e^0 = 10\max\{\beta^-, \beta^+\}$. We note that the edge operators in (4.9) are different from those in the literature [148] or (3.66b), but the induced penalties on interface edges in the bilinear forms are actually equivalent to each other. The purpose to use (4.9) is to facilitate a systematic matrix representation of the local penalties discussed below.

It has been shown [85, 148] that the PPIFE solutions u_h^k from (4.6) approximate the true solutions u^k, $1 \leqslant k \leqslant K$, with an optimal accuracy in both the L^2 and H^1 norms with respect to the involved polynomial degree regardless of the interface location and shape on unfitted meshes, i.e.,

$$\|u_h^k - u^k\|_{L^2(\Omega)} + h|u_h^k - u^k|_{H^1(\Omega)} \leqslant Ch^2. \tag{4.10}$$

Here the PPIFE scheme (4.7)-(4.8) can be considered as a "complete one" in the sense that it takes into account both the boundary conditions, including the Dirichlet and Neumann conditions, and the situation that interface meets the boundary.

We now put the SPPIFE method described by (4.6)-(4.8) into a matrix form. This is also important for deriving formulas of their material derivatives and the related computations in practice. We assume that $S_h(\Omega) = \mathrm{Span}\{\varphi_i(X) \mid X_i \in \mathring{\mathcal{N}}_h\}$ in which $\varphi_i(X)$ is the global IFE basis function associated with the node $X_i \in \mathring{\mathcal{N}}_h$. When the k-th ($1 \leq k \leq K$) interface forward problem has a mixed boundary condition, we let $\mathcal{N}_h^M = \{X_i \mid X_i \in \mathring{\mathcal{N}}_h \cup \partial\Omega_N\}$ such that we can denote the SPPIFE solution $u_h^k(X) \in S_h(\Omega)$ determined by (4.6)-(4.8) as follows:

$$u_h^k(X) = \sum_{i=1}^{|\mathcal{N}_h^M|} u_i^k \varphi_i(X) + \sum_{i=|\mathcal{N}_h^M|+1}^{|\mathcal{N}_h|} g_D^k(X_i)\varphi_i(X), \tag{4.11}$$

where, without loss of generality, we have assumed that nodes in $\mathcal{N}_h^M$ are ordered first. Here and from now on, the superscript M means that the boundary condition in the k-th interface forward problem is of a mixed type.

To simplify the notations, we only use $\phi_{p,T}$ to denote local IFE shape functions without distinguishing interface or non-interface elements, i.e., on each element T, $\phi_{p,T}$ is the IFE shape function associated with the p-th vertex A_p of T. Then, the stiffness matrix $\tilde{\mathbf{A}} = (a_{i,j})_{i,j=1}^{|\mathring{\mathcal{N}}_h|}$ associated with the bilinear form defined in (4.7) can be assembled from the following local matrices on elements and edges of $\mathcal{T}_h$:

$$\mathbf{K}_T = \left(\int_T \beta \nabla\phi_{p,T} \cdot \nabla\phi_{q,T} dX\right)_{p,q\in\mathcal{I}}, \qquad \forall T \in \mathcal{T}_h, \tag{4.12a}$$

$$\mathbf{E}_e^{r_1 r_2} = \left(\int_e \beta \nabla\phi_{p,T^{r_1}} \cdot (\phi_{q,T^{r_2}} \mathbf{n}_e^{r_2}) ds\right)_{p,q\in\mathcal{I}}, \qquad \forall e \in \mathcal{E}_h^i, \tag{4.12b}$$

$$\mathbf{G}_e^{r_1 r_2} = \left(\frac{\rho_e^0}{|e|}\int_e (\phi_{p,T^{r_1}} \mathbf{n}_e^{r_1}) \cdot (\phi_{q,T^{r_2}} \mathbf{n}_e^{r_2}) ds\right)_{p,q\in\mathcal{I}}, \quad \forall e \in \mathcal{E}_h^i, \tag{4.12c}$$

where the index $r_1, r_2 = 1, 2$ and the edge $e \in \mathring{\mathcal{E}}_h^i$ is shared by the two neighbor elements T^1 and T^2, but in the case $e \in \mathcal{E}_h^i \cap \partial\Omega$, we let $r_1 = r_2 = 0$, and $\mathbf{n}_e^0 = \mathbf{n}_e$ is the outward normal vector and $T^0 = T$ is the element that contains e. In (4.12) and from now on, we use p, q to represent the position of an entry in the related matrix or vector. Let

$$\tilde{\mathbf{A}}_b^{M,k} = (a_{b,i}^k)_{i=1}^{|\mathcal{N}_h|} = \tilde{\mathbf{A}} \begin{bmatrix} \mathbf{0} & \mathbf{g}_D^k \end{bmatrix}^T,$$

where $\mathbf{0}$ is the $\left|\mathcal{N}_h^M\right|$-dimensional zero vector and $\mathbf{g}_D^k = [g_D^k(X_{|\mathcal{N}_h^M|+1}), \cdots, g_D^k(X_{|\mathcal{N}_h|})]^T$. Similarly, the load vector $\tilde{\mathbf{F}}^k = (f_i^k)_{i=1}^{|\mathcal{N}_h|}$ associated with the linear form defined in (4.8) can be assembled from the following vectors:

$$\mathbf{F}_T^k = \left(\int_T f^k \phi_{p,T} dX \right)_{p \in \mathcal{I}}, \qquad \forall T \in \mathcal{T}_h, \quad (4.13a)$$

$$\mathbf{B}_e^k = \left(\int_e \beta g_D^k \nabla \phi_{p,T} \cdot \mathbf{n}_e ds \right)_{p \in \mathcal{I}}, \quad \mathbf{C}_e^k = \frac{\rho_e^0}{|e|} \left(\int_e \beta g_D^k \phi_{p,T} ds \right)_{p \in \mathcal{I}}, \quad \forall e \in \mathcal{E}_h^i \cap \partial\Omega_D, \quad (4.13b)$$

$$\mathbf{N}_e^k = \left(\int_e g_N^k \phi_{p,T} ds \right)_{p \in \mathcal{I}}, \qquad \forall e \in \mathcal{E}_h^i \cap \partial\Omega_N. \quad (4.13c)$$

Letting $\mathbf{u}_h^{M,k} = [u_1^k, u_2^k, \cdots, u_{|\mathcal{N}_h^M|}^k]^T$, we can see that the unknown vector $\mathbf{u}_h^{M,k}$ of the SPPIFE solution $u_h^k(X)$ described by (4.11) is determined by the following linear system:

$$\mathbf{A}^{M,k} \mathbf{u}_h^{M,k} = \mathbf{F}^{M,k}, \quad (4.14)$$

where $\mathbf{A}^{M,k} = (a_{i,j})_{i,j=1}^{\left|\mathcal{N}_h^M\right|}$, $\mathbf{F}^{M,k} = (f_i^k)_{i=1}^{\left|\mathcal{N}_h^M\right|} - (a_{b,i}^k)_{i=1}^{\left|\mathcal{N}_h^M\right|}$.

When the k-th ($1 \le k \le K$) interface forward problem has a Neumann boundary condition such that $\partial\Omega_N^k = \partial\Omega$, we know that $\left|\mathcal{N}_h^M\right| = |\mathcal{N}_h|$, $u_h^k(X)$ given in (4.11) does not have the second term and the related load vector $\tilde{\mathbf{F}}^k = (f_i^k)_{i=1}^{|\mathcal{N}_h|}$ is assembled by the local vectors only in (4.13a) and (4.13c). Since the solution to the interface problem is not unique, as a common practice, the normalization condition $\int_\Omega u^k dX = u_0^k$ is imposed such that the SPPIFE solution $u_h^k(X)$ described by (4.11) is determined by the following linear system:

$$\mathbf{A}^{N,k} \mathbf{u}_h^{N,k} = \mathbf{F}^{N,k}, \quad \text{with} \quad \mathbf{A}^{N,k} = \begin{bmatrix} \tilde{\mathbf{A}} & \mathbf{R} \\ \mathbf{R}^T & 0 \end{bmatrix}, \quad \begin{cases} \mathbf{u}_h^{N,k} = [u_1^k, u_2^k, \cdots, u_{|\mathcal{N}_h|}^k, \lambda]^T, \\ \mathbf{F}^{N,k} = [f_1^k, f_2^k, \cdots, f_{|\mathcal{N}_h|}^k, u_0^k]^T, \end{cases} \quad (4.15)$$

where the superscript N refers to the pure Neuman boundary condition, λ is the Lagrange multiplier, and $\mathbf{R}$ is the vector assembled with the following local vector constructed on each element:

$$\mathbf{R}_T = \left(\int_T \phi_{p,T} dX \right)_{p \in \mathcal{I}}, \quad \forall T \in \mathcal{T}_h. \quad (4.16)$$

In summary, according to (4.14) and (4.15), the SPPIFE discretization for the K interface forward problems described in (4.1) and (4.2) can be written in the following unified matrix

form:

$$\mathbf{A}^k\mathbf{u}_h^k = \mathbf{F}^k, \tag{4.17}$$

$$\text{with } \mathbf{u}_h^k = \begin{cases} \mathbf{u}_h^{M,k} \\ \mathbf{u}_h^{N,k} \end{cases} \quad \mathbf{A}^k = \begin{cases} \mathbf{A}^{M,k} \\ \mathbf{A}^{N,k} \end{cases} \quad \mathbf{F}^k = \begin{cases} \mathbf{F}^{M,k} & \text{for a mixed boundary condition,} \\ \mathbf{F}^{N,k} & \text{for a Neumann boundary condition.} \end{cases}$$

We note that the matrices $\mathbf{A}^k$s in (4.17) are symmetric positive definite, and their size and algebraic structure remain the same as the interface $\Gamma(t, \boldsymbol{\alpha}), t \in [0, 1]$ evolves in an unfitted mesh when the design variable $\boldsymbol{\alpha}$ varies.

4.3 An IFE Method for Interface Inverse Problems

We now discuss the discretization of the shape optimization method for solving the interface inverse problem (4.3) subject to the interface forward problems (4.1) and (4.2) by the SPPIFE method on an unfitted mesh. By the discussion above, we note that the local matrices (4.12a)-(4.12c), local vectors (4.13a)-(4.13c), and (4.16) are all influenced by the shape variation. Hence, we write the matrix $\mathbf{A}^k$ and vector $\mathbf{F}^k$ in the SPPIFE equation (4.17) as

$$\mathbf{A}^k = \mathbf{A}^k(\boldsymbol{\alpha}), \quad \mathbf{F}^k = \mathbf{F}^k(\boldsymbol{\alpha}), \quad k = 1, 2, \cdots, K,$$

which further imply the solution $\mathbf{u}_h^k$ to the IFE equation (4.17) depends on $\boldsymbol{\alpha}$ and so we will denote it as $\mathbf{u}_h^k(\boldsymbol{\alpha})$ from now on. In addition, as an important feature in a shape optimization problem, the spatial variables X should be considered to depend on the interface curve, i.e., they are functions of $\boldsymbol{\alpha}$. More details about this dependence will be given in Subsection 4.4.2. Therefore, the IFE solution u_h^k to the k-th ($1 \le k \le K$) interface forward problem in the form of (4.11) depends on $\boldsymbol{\alpha}$ through the IFE solution vector $\mathbf{u}_h^k(\boldsymbol{\alpha})$, the spatial variable $X(\boldsymbol{\alpha})$, and the IFE basis functions; hence, we can comprehend it as follows

$$\begin{aligned} u_h^k = u_h^k(\boldsymbol{\alpha}) &= u_h^k(\mathbf{u}_h^k(\boldsymbol{\alpha}), X(\boldsymbol{\alpha}), \boldsymbol{\alpha}) \\ &= \sum_{i=1}^{|\mathcal{N}_h^M|} u_i^k(\boldsymbol{\alpha})\varphi_i(X(\boldsymbol{\alpha}), \boldsymbol{\alpha}) + \sum_{i=|\mathcal{N}_h^M|+1}^{|\mathcal{N}_h|} g_D^k(X_i)\varphi_i(X(\boldsymbol{\alpha}), \boldsymbol{\alpha}), \end{aligned} \tag{4.18}$$

where the second variable in $\varphi_i(X(\boldsymbol{\alpha}), \boldsymbol{\alpha})$ emphasizes the fact that $\boldsymbol{\alpha}$ effects the IFE solution u_h^k through the coefficients c_i, c_0, and the function $L(X)$ in the IFE shape functions described by the formulas (1.18a)-(1.20b). More details of this dependence will be discussed in Subsection 4.4.3.

The IFE solutions $u_h^k(X) \approx u^k(X)$, $1 \le k \le K$, spatial-design-variable mapping $X = X(\boldsymbol{\alpha})$, and the interface parameterization $\Gamma(\cdot, \boldsymbol{\alpha})$ together naturally suggest the following discretization of the integrand in the objective functional defined by (4.4):

$$\begin{aligned} &J(u^1(\boldsymbol{\alpha}), u^2(\boldsymbol{\alpha}), \cdots, u^K(\boldsymbol{\alpha}); X, \Gamma(\cdot, \boldsymbol{\alpha})) \\ \approx &J(u_h^1(\boldsymbol{\alpha}), u_h^2(\boldsymbol{\alpha}), \cdots, u_h^K(\boldsymbol{\alpha}); X(\boldsymbol{\alpha}), \Gamma(\cdot, \boldsymbol{\alpha})). \end{aligned} \tag{4.19}$$

Following the explanations similar to those in the previous paragraph, the design variable $\boldsymbol{\alpha}$ can influence the approximated integrand $J(u_h^1(\boldsymbol{\alpha}), u_h^2(\boldsymbol{\alpha}), \cdots, u_h^K(\boldsymbol{\alpha}); X(\boldsymbol{\alpha}), \Gamma(\cdot, \boldsymbol{\alpha}))$ not only through $\mathbf{u}_h^k(\boldsymbol{\alpha}), 1 \leq k \leq K$, $X(\boldsymbol{\alpha})$, but also through the coefficients of IFE shape functions (1.17) represented by the last variable $\boldsymbol{\alpha}$ in the following notation for the discretized integrand J_h:

$$\begin{aligned} &J_h(\mathbf{u}_h^1(\boldsymbol{\alpha}), \mathbf{u}_h^2(\boldsymbol{\alpha}), \cdots, \mathbf{u}_h^K(\boldsymbol{\alpha}), X(\boldsymbol{\alpha}), \boldsymbol{\alpha}) \\ &\quad \coloneqq J(u_h^1(\boldsymbol{\alpha}), u_h^2(\boldsymbol{\alpha}), \cdots, u_h^K(\boldsymbol{\alpha}); X(\boldsymbol{\alpha}), \Gamma(\cdot, \boldsymbol{\alpha})). \end{aligned} \tag{4.20}$$

The discretized integrand defined in (4.20) can be then used to define a discretized objective function:

$$\mathcal{J}_h(\mathbf{u}_h^1(\boldsymbol{\alpha}), \mathbf{u}_h^2(\boldsymbol{\alpha}), \cdots, \mathbf{u}_h^K(\boldsymbol{\alpha}), \boldsymbol{\alpha}) = \int_{\Omega_0} J_h(\mathbf{u}_h^1(\boldsymbol{\alpha}), \mathbf{u}_h^2(\boldsymbol{\alpha}), \cdots, \mathbf{u}_h^K(\boldsymbol{\alpha}), X(\boldsymbol{\alpha}), \boldsymbol{\alpha}) dX. \tag{4.21}$$

In many applications such as those to be presented in Section 4.6, the approximation optimality of the IFE solution $u_h^k(X),\ 1 \leq k \leq K$ [85, 148] implies that the discretized objective function $\mathcal{J}_h$ in this IFE method is also an optimal approximation to the exact objective functional given by (4.4) regardless of the interface location in the unfitted mesh.

Therefore, we propose an IFE method on an unfitted mesh of Ω for solving the interface inverse problem formulated as a shape optimization with (4.1)-(4.4) by carrying out a constrained multi-variable optimization as follows: find the design variable $\boldsymbol{\alpha}^*$ such that

$$\begin{aligned} \boldsymbol{\alpha}^* = \text{argmin } \mathcal{J}_h(\boldsymbol{\alpha}), \quad & \mathcal{J}_h(\boldsymbol{\alpha}) = \mathcal{J}_h(\mathbf{u}_h^1(\boldsymbol{\alpha}), \mathbf{u}_h^2(\boldsymbol{\alpha}), \cdots, \mathbf{u}_h^K(\boldsymbol{\alpha}), \boldsymbol{\alpha}) \\ \text{subject to} \quad & \mathbf{A}^k(\boldsymbol{\alpha})\mathbf{u}_h^k(\boldsymbol{\alpha}) - \mathbf{F}^k(\boldsymbol{\alpha}) = \mathbf{0}, \quad k = 1, 2, \cdots, K. \end{aligned} \tag{4.22}$$

The proposed method follows the idea of discrete derivatives [194], i.e., we first discretize the whole system and then calculate the gradient of the discretized objective function with respect to the vector $\boldsymbol{\alpha}$ for optimization. This methodology has been used in many shape optimization applications, see [160, 175, 194] and references therein.

It is well known that many inverse problems discussed in the literature are ill-conditioned. By choosing a reasonably small number of control points, the proposed IFE-based shape optimization algorithm actually searches for the target interface curve in a small space on a unfitted mesh. This means that the parameterization $\Gamma(\boldsymbol{\alpha})$ in the optimization problem (4.22) can be interpreted as a "hidden" regularization for the inverse problem. Indeed, the numerical experiments presented in Section 4.6 show that the reconstructions produced by the proposed IFE-based shape optimization algorithm are quite satisfactory without additional regularization such as the geometric regularization [117], total variation regularization [53], and Tikhonov regularization [120]. We will further discuss this in more details in Section 4.7.

4.4 Sensitivity Analysis

In this section, we discuss the sensitivity analysis of the shape functional (4.21) and its computations. Due to the discussion in Section 4.3, there are two critical components in this sensitivity computation: the derivatives of spatial variables and IFE shape functions with respect to the design variables, referred as velocity field and shape derivatives of IFE functions, respectively. In the following discussions, we use the operator $\mathfrak{D}_{\alpha_j}$ to denote the total derivative operator with respect to the j-th design variable α_j, $j \in \mathcal{D}$, and $\mathfrak{D}_{\boldsymbol{\alpha}}$ is the corresponding gradient operator. Also, we will use $\frac{\partial}{\partial \alpha_j}$ and $\frac{\partial}{\partial \boldsymbol{\alpha}}$ to denote the standard partial differential operators and the gradient operator with respect to α_j and $\boldsymbol{\alpha}$, respectively.

4.4.1 Velocity at Intersection Points

By (1.17), an IFE function on an interface element depends on the interface-mesh intersection points D and E, see the illustration in Figure 4.2. Obviously, the points D and E change their locations when the interface $\Gamma(\boldsymbol{\alpha})$ evolves due to the change in the design variables $\boldsymbol{\alpha} = (\alpha_i)_{i\in\mathcal{D}}$. Hence, the objective function in the IFE method for solving the interface inverse problem essentially depends on how the interface-mesh intersection points D and E change when the design variable $\boldsymbol{\alpha}$ of the parametrization of the interface Γ varies, so that the derivatives of D and E with respect to $\boldsymbol{\alpha}$ are critical ingredients for the sensitivity analysis of the proposed IFE method, and this motivates us to derive their formulas in this subsection. According to [175], these derivatives are the velocity defined at those intersection points, and we will further use these point-wise velocity to construct the velocity field on the whole domain.

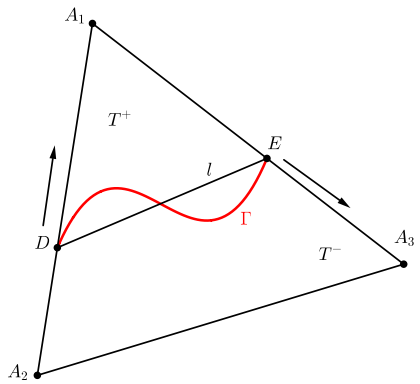

Figure 4.2: Movement of interface-mesh intersection points

To be precise, we let $\Gamma(t, \boldsymbol{\alpha}) = (x(t, \boldsymbol{\alpha}), y(t, \boldsymbol{\alpha}))$, $t \in [0, 1]$ be a certain parametrization of the interface curve and let $T = \triangle A_1A_2A_3 \in \mathcal{T}_h$ be an interface element such that $A_i =$

$(x_i, y_i)^T, i = 1, 2, 3$, as shown in Figure 4.2. Assume that $\Gamma(t, \boldsymbol{\alpha})$ intersects with the edges of T at points $D = (x_D, y_D)$ and $E = (x_E, y_E)$ corresponding to certain parameters $\hat{t}_D, \hat{t}_E \in [0, 1]$. Obviously, these two interface-mesh intersection points and their corresponding parameters $\hat{t}_D$ and $\hat{t}_E$ all vary with respect to the design variable $\boldsymbol{\alpha}$; hence, we can express them as functions of $\boldsymbol{\alpha}$ as follows:

$$D = D(\boldsymbol{\alpha}) = (x_D, y_D) = (x(\hat{t}_D), y(\hat{t}_D)) = (x(\hat{t}_D(\boldsymbol{\alpha}), \boldsymbol{\alpha}), y(\hat{t}_D(\boldsymbol{\alpha}), \boldsymbol{\alpha})),$$
$$E = E(\boldsymbol{\alpha}) = (x_E, y_E) = (x(\hat{t}_E), y(\hat{t}_E)) = (x(\hat{t}_E(\boldsymbol{\alpha}), \boldsymbol{\alpha}), y(\hat{t}_E(\boldsymbol{\alpha}), \boldsymbol{\alpha})).$$

Without loss of generality, we let the interface-mesh intersection points be $D \in \overline{A_1A_2}$ and $E \in \overline{A_1A_3}$ as illustrated in Figure 4.2. Then the following two lemmas establishes explicit formulas for computing the total derivatives of interface-mesh intersection points with respect to $\boldsymbol{\alpha}$.

Lemma 4.1. *Assume $\Gamma(t, \boldsymbol{\alpha})$ is not tangent to A_1A_2 at D. Then the function $D = D(\hat{t}_D(\boldsymbol{\alpha}), \boldsymbol{\alpha})$ is differentiable and its velocity defined as the total derivatives $\mathfrak{D}_{\alpha_j} D$ with respect to α_j, $j \in \mathcal{D}$ is determined by the following linear system:*

$$M_D(\hat{t}_D)\ \mathfrak{D}_{\alpha_j} D = b_{D,j}(\hat{t}_D), \quad \forall\ j \in \mathcal{D}, \tag{4.23}$$

where

$$M_D(\hat{t}_D) = \begin{bmatrix} y_2 - y_1 & -(x_2 - x_1) \\ \frac{\partial y}{\partial t}(\hat{t}_D) & -\frac{\partial x}{\partial t}(\hat{t}_D) \end{bmatrix} \quad \textit{and} \quad b_{D,j}(\hat{t}_D) = \begin{bmatrix} 0 \\ \frac{\partial y}{\partial t}(\hat{t}_D)\frac{\partial x}{\partial \alpha_j}(\hat{t}_D) - \frac{\partial x}{\partial t}(\hat{t}_D)\frac{\partial y}{\partial \alpha_j}(\hat{t}_D) \end{bmatrix}.$$

Proof. First, differentiating $x_D = x(\hat{t}_D(\boldsymbol{\alpha}), \boldsymbol{\alpha})$ and $y_D = y(\hat{t}_D(\boldsymbol{\alpha}), \boldsymbol{\alpha})$ with respect to α_j, we have

$$\mathfrak{D}_{\alpha_j} x_D = \frac{\partial x}{\partial t}\frac{\partial \hat{t}_D}{\partial \alpha_j} + \frac{\partial x}{\partial \alpha_j}, \qquad \mathfrak{D}_{\alpha_j} y_D = \frac{\partial y}{\partial t}\frac{\partial \hat{t}_D}{\partial \alpha_j} + \frac{\partial y}{\partial \alpha_j},$$

which leads to

$$\frac{\partial y}{\partial t}\mathfrak{D}_{\alpha_j} x_D - \frac{\partial x}{\partial t}\mathfrak{D}_{\alpha_j} y_D = \frac{\partial y}{\partial t}\frac{\partial x}{\partial \alpha_j} - \frac{\partial x}{\partial t}\frac{\partial y}{\partial \alpha_j}. \tag{4.24}$$

On the other hand, since D is on the edge A_1A_2, we have the equation

$$(y_2 - y_1)x_D - (x_2 - x_1)y_D = x_2y_1 - x_1y_2. \tag{4.25}$$

Differentiating (4.25) with respect to α_j yields

$$(y_2 - y_1)\mathfrak{D}_{\alpha_j} x_D - (x_2 - x_1)\mathfrak{D}_{\alpha_j} y_D = 0. \tag{4.26}$$

Combining (4.26) and (4.24) yields the linear system for $\mathfrak{D}_{\alpha_j} D$ in (4.23). Let $\mathbf{n}_e$ be the normal vector to the edge A_1A_2. Then we have

$$\det(M_D(\hat{t}_D) = \mathbf{n}_e \cdot \nabla\Gamma(\hat{t}_D(\boldsymbol{\alpha}), \boldsymbol{\alpha})$$

which is non-zero by the assumption that A_1A_2 is not tangent to $\Gamma(t, \boldsymbol{\alpha})$ at D. □

Note that formulas (4.23) allow us to compute $\mathfrak{D}_{\alpha_j} D$ without using $\frac{\partial \hat{t}_D}{\partial \alpha_j}$ which is cumbersome to compute because the dependence of $\hat{t}_D$ on $\boldsymbol{\alpha}$ involves the inverse function of the parametrization $\Gamma(t, \boldsymbol{\alpha})$ for the interface. By similar ideas, we can derive the formula for the point E.

Lemma 4.2. *Assume $\Gamma(t, \boldsymbol{\alpha})$ is not tangent to A_1A_3 at E. Then the function $E = E(\hat{t}_E(\boldsymbol{\alpha}), \boldsymbol{\alpha})$ is differentiable and its velocity defined as the total derivatives $\mathfrak{D}_{\alpha_j} E$ with respect to α_j, $j \in \mathcal{D}$ is determined by the following linear system:*

$$M_E(\hat{t}_E)\ \mathfrak{D}_{\alpha_j} E = b_{E,j}(\hat{t}_E), \quad \forall\ j \in \mathcal{D}, \tag{4.27}$$

where

$$M_E(\hat{t}_E) = \begin{bmatrix} y_2 - y_1 & -(x_2 - x_1) \\ \frac{\partial y}{\partial t}(\hat{t}_E) & -\frac{\partial x}{\partial t}(\hat{t}_E) \end{bmatrix} \quad \textit{and} \quad b_{E,j}(\hat{t}_E) = \begin{bmatrix} 0 \\ \frac{\partial y}{\partial t}(\hat{t}_E)\frac{\partial x}{\partial \alpha_j}(\hat{t}_E) - \frac{\partial x}{\partial t}(\hat{t}_E)\frac{\partial y}{\partial \alpha_j}(\hat{t}_E) \end{bmatrix}.$$

Also, the formulas for the derivatives of interface-mesh intersection points with respect to the design variables $\boldsymbol{\alpha}$ are valid for general parametrization $\Gamma(t, \boldsymbol{\alpha})$ in which $\partial x/\partial t$ and $\partial y/\partial t$ can be calculated directly because they are the standard partial derivatives with respect to the parameter t. But $\partial x/\partial \alpha_j$ and $\partial y/\partial \alpha_j$ depend on the specific parameterization, and we herein use a cubic spline as an example to explain how to calculate them. Let $x = x(t, \mathbf{c}_x)$ and $y = y(t, \mathbf{c}_y)$ be the cubic splines interpolating the vectors $\boldsymbol{\alpha}_x$ and $\boldsymbol{\alpha}_y$, respectively, at the sampling points with $\mathbf{c}_x$ and $\mathbf{c}_y$ being the coefficients of the involved cubic polynomials. As usual, $\boldsymbol{\alpha}_x$ and $\boldsymbol{\alpha}_y$ are the x and y coordinates of the control points for this cubic spline parameterization. According to [70], the vectors $\mathbf{c}_x$ and $\mathbf{c}_y$ are determined by two linear systems

$$\mathbf{W}_x \mathbf{c}_x = \mathbf{r}_x(\boldsymbol{\alpha}_x), \quad \mathbf{W}_y \mathbf{c}_y = \mathbf{r}_y(\boldsymbol{\alpha}_y) \tag{4.28}$$

where the matrices $\mathbf{W}_x$ and $\mathbf{W}_y$ are independent of the design variable $\boldsymbol{\alpha} = (\boldsymbol{\alpha}_x, \boldsymbol{\alpha}_y)^T$. Differentiating (4.28) with respect to α_j leads to

$$\mathbf{W}_x \frac{\partial \mathbf{c}_x}{\partial \alpha_j} = \frac{\partial \mathbf{r}_x(\boldsymbol{\alpha}_x)}{\alpha_j}, \quad \text{if} \ \ 1 \le j \le dim(\boldsymbol{\alpha}_x), \tag{4.29a}$$

$$\mathbf{W}_y \frac{\partial \mathbf{c}_y}{\partial \alpha_j} = \frac{\partial \mathbf{r}_y(\boldsymbol{\alpha}_y)}{\partial \alpha_j}, \quad \text{if} \ \ dim(\boldsymbol{\alpha}_x) + 1 \le j \le dim(\boldsymbol{\alpha}_x) + dim(\boldsymbol{\alpha}_y), \tag{4.29b}$$

from which we can solve for $\frac{\partial \mathbf{c}_x}{\partial \alpha_j}$ and $\frac{\partial \mathbf{c}_y}{\partial \alpha_j}$ to obtain

$$\partial x/\partial \alpha_j = x(t, \frac{\partial \mathbf{c}_x}{\partial \alpha_j}), \quad \partial y/\partial \alpha_j = y(t, \frac{\partial \mathbf{c}_y}{\partial \alpha_j}). \tag{4.30}$$

Remark 4.1. *We can directly verify $\mathfrak{D}_{\alpha_j} D \cdot \mathbf{n}_e = \mathbf{n}_e M_D^{-1} b_{D,j} = 0$ which means that $\mathfrak{D}_{\alpha_j} D$ is in the same direction as the edge A_1A_2 for any α_j, $j \in \mathcal{D}$. In a certain sense, this property follows from the geometry that the intersection point D can only move along the edge A_1A_2. The intersection point E has a similar property.*

4.4.2 A Velocity Field for Sensitivity Computations

As discussed at the beginning of Section 4.3, in shape optimization, the two sub-domains Ω^- and Ω^+ separated from each other by the interface $\Gamma = \Gamma(t, \boldsymbol{\alpha}), t \in [0, 1]$ change their shapes when the parametric interface moves because of a variation in the design variable $\boldsymbol{\alpha}$. Hence, Ω^- and Ω^+ can be considered as functions of $\boldsymbol{\alpha}$. Consequently, since $\Omega^- \cup \Omega^+ = \Omega \backslash \Gamma$, we can consider the spatial variable $X \in \Omega$ as a mapping from the design variables $\boldsymbol{\alpha}$ to Ω, i.e., $X = X(\boldsymbol{\alpha})$, and its derivative $\mathfrak{D}_{\boldsymbol{\alpha}} X$ is the so called velocity field [175], a key ingredient in the sensitivity analysis in shape optimizations. Therefore, in this subsection, we employ the results in Subsection 4.4.1 to develop and analyze a velocity field for the proposed IFE-based shape optimization method to solve the interface inverse problems.

Since the IFE method proposed in (4.22) is based on an unfitted mesh, the design variable $\boldsymbol{\alpha}$ for the parameterized interface $\Gamma(t, \boldsymbol{\alpha}), t \in [0, 1]$ will influence the IFE basis functions on interface elements only. Alternatively speaking, all the points located in non-interface elements can be considered as constant functions of the design variable $\boldsymbol{\alpha}$. Therefore, on such an unfitted mesh used by the proposed IFE method, the velocity field vanishes on all non-interface elements because $\mathfrak{D}_{\boldsymbol{\alpha}} X = 0$, and this suggests we need to discuss the velocity field only on interface elements.

As before, we consider a typical interface element $T = \triangle A_1 A_2 A_3$. Without loss of generality, we consider the case that the parameterized interface $\Gamma(t, \boldsymbol{\alpha}) = (x(t, \boldsymbol{\alpha}), y(t, \boldsymbol{\alpha})),\ t \in [0, 1]$ intersects with T at $D(\boldsymbol{\alpha}) \in \overline{A_1 A_2}$ and $E(\boldsymbol{\alpha}) \in \overline{A_1 A_3}$, see the illustration in Figure 4.3, but neither D nor E coincides with vertices of T. All results derived from now on are readily extended to the case in which one of the interface-mesh intersection points D and E is a vertex of T. A core idea is to find a function relating every point X in this interface element T to the design variable $\boldsymbol{\alpha}$. For this purpose, following the ideas in [184], we partition T into three sub-elements as follows: $T_1 = \triangle A_1 D E$, $T_2 = \triangle A_2 E D$, $T_3 = \triangle A_3 E A_2$, see the illustration in Figure 4.3.

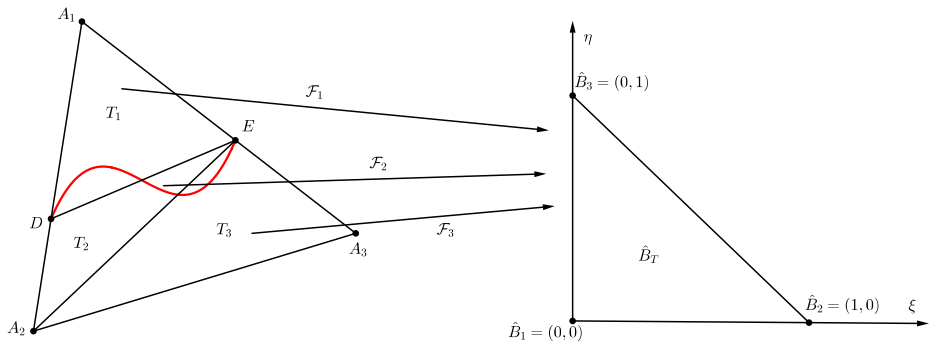

Figure 4.3: Mapping each sub-element to the reference triangle

Let $\hat{B}_T = \triangle \hat{B}_1 \hat{B}_2 \hat{B}_3$ be the usual reference element with vertices $\hat{B}_1 = (0, 0)^T$, $\hat{B}_2 =$

$(1,0)^T$, $\hat{B}_1 = (0,1)^T$. Then, the standard affine mappings from the reference element $\hat{B}_T = \triangle\hat{B}_1\hat{B}_2\hat{B}_3$ to $T_m, m = 1,2,3$ provide a relation between the points in T and the design variable $\boldsymbol{\alpha}$ as follows:

$$X(\boldsymbol{\alpha}) = \mathcal{F}_m(\boldsymbol{\alpha},\xi,\eta) = \mathbf{J}_m(\boldsymbol{\alpha})\begin{pmatrix}\xi\\ \eta\end{pmatrix} + A_m, \quad \text{for} \quad X \in T_m \subset T, \quad m = 1,2,3, \tag{4.31}$$

where the matrix $\mathbf{J}_m(\boldsymbol{\alpha})$ is the Jacobian matrix of $\mathcal{F}_m$ such that

$$\begin{aligned}
\mathbf{J}_1(\boldsymbol{\alpha}) &= \left(D(\boldsymbol{\alpha}) - A_1, E(\boldsymbol{\alpha}) - A_1\right),\\
\mathbf{J}_2(\boldsymbol{\alpha}) &= \left(E(\boldsymbol{\alpha}) - A_2, D(\boldsymbol{\alpha}) - A_2\right),\\
\mathbf{J}_3(\boldsymbol{\alpha}) &= \left(E(\boldsymbol{\alpha}) - A_3, A_2 - A_3\right).
\end{aligned} \tag{4.32}$$

By Lemma 4.1 and Lemma 4.2, these Jacobian matrices are differentiable with respect to $\boldsymbol{\alpha}$ such that $\forall j \in \mathcal{D}$ we have

$$\begin{aligned}
\mathfrak{D}_{\alpha_j}\mathbf{J}_1(\boldsymbol{\alpha}) &= \left(\mathfrak{D}_{\alpha_j}D, \mathfrak{D}_{\alpha_j}E\right),\\
\mathfrak{D}_{\alpha_j}\mathbf{J}_2(\boldsymbol{\alpha}) &= \left(\mathfrak{D}_{\alpha_j}E, \mathfrak{D}_{\alpha_j}D\right),\\
\mathfrak{D}_{\alpha_j}\mathbf{J}_3(\boldsymbol{\alpha}) &= \left(\mathfrak{D}_{\alpha_j}E, \mathbf{0}\right).
\end{aligned} \tag{4.33}$$

Therefore, for every $X \in T$, the function $X(\boldsymbol{\alpha})$ given in (4.31) is a piecewise differentiable function such that its total derivative with respect to the j-th design variable is

$$\begin{aligned}
\mathfrak{D}_{\alpha_j}X(\boldsymbol{\alpha}) &= \left(\mathfrak{D}_{\alpha_j}\mathbf{J}_m(\boldsymbol{\alpha})\right)\begin{pmatrix}\xi\\ \eta\end{pmatrix}\\
&= \left(\mathfrak{D}_{\alpha_j}\mathbf{J}_m(\boldsymbol{\alpha})\right)\mathbf{J}_m^{-1}(\boldsymbol{\alpha})(X(\boldsymbol{\alpha}) - A_m) \quad \text{for } X(\boldsymbol{\alpha}) \in T_m,\ m = 1,2,3.
\end{aligned} \tag{4.34}$$

Hence, using the formula for $X \in T$ in terms of $\boldsymbol{\alpha}$ given in (4.31), we can define a piecewise velocity field $\mathbf{V}^j$ with respect to the j-th design variable α_j, $j \in \mathcal{D}$ as follows:

$$\begin{aligned}
&\mathbf{V}^j(X) = \mathfrak{D}_{\alpha_j}X(\boldsymbol{\alpha})\\
&= \begin{cases}
\mathbf{V}_T^j(X) = \mathbf{0}, & \text{if } T \notin \mathcal{T}_h^i\ ,\\
\mathbf{V}_T^j(X) = \left(\mathfrak{D}_{\alpha_j}\mathbf{J}_m(\boldsymbol{\alpha})\right)\mathbf{J}_m^{-1}(\boldsymbol{\alpha})(X(\boldsymbol{\alpha}) - A_m), & \text{if } T \in \mathcal{T}_h^i,\ X \in T_m, m = 1,2,3.
\end{cases}
\end{aligned} \tag{4.35}$$

We now discuss some properties of the velocity field developed above.

Theorem 4.1. *For any $j \in \mathcal{D}$, the velocity $\mathbf{V}^j(X)$ defined in (4.35) has the properties:*

***P1**: on each interface element $T = \triangle A_1A_2A_3 \in \mathcal{T}_h^i$, there hold*

$$\mathbf{V}_T^j|_{A_mD} = \frac{\|X - A_m\|}{\|D - A_m\|}\mathfrak{D}_{\alpha_j}D,\ m = 1,2, \tag{4.36a}$$

$$\mathbf{V}_T^j|_{A_mE} = \frac{\|X - A_m\|}{\|E - A_m\|}\mathfrak{D}_{\alpha_j}E,\ m = 1, 2, 3, \tag{4.36b}$$

$$\mathbf{V}_T^j|_{DE} = \frac{\|X - E\|}{\|D - E\|}\mathfrak{D}_{\alpha_j}D + \frac{\|X - D\|}{\|D - E\|}\mathfrak{D}_{\alpha_j}E, \quad \mathbf{V}_T^j|_{A_2A_3} = \mathbf{0}, \tag{4.36c}$$

$$\mathrm{div}(\mathbf{V}_T^j|_{T_m}) = \mathrm{tr}\left((\mathfrak{D}_{\alpha_j}\mathbf{J}_m)\mathbf{J}_m^{-1}\right), \quad m = 1, 2, 3; \tag{4.36d}$$

P2: $\mathbf{V}^j \in H^1(\Omega)$ *and* $supp(\mathbf{V}^j) \subseteq \bigcup_{T\in\mathcal{T}_h^i} T$;

P3: *when restricted on each interface edge* e, $\mathbf{V}^j(X)$ *is in the same direction as the edge* e.

Proof. Identities in (4.36a)-(4.36c) can be verified by direct calculations, and to avoid redundancy, we only provide a proof for the first identity in (4.36c), and the proofs for the other follow similarly. Without loss of generality, we let T have the configuration shown in the right plot in Figure 4.3. Since $\mathbf{V}_T^j$ is a piecewise function, we need to prove $\mathbf{V}_T^j|_{T_m}, m = 1, 2$ are the same when they are restricted on DE. We consider $\mathbf{V}_T^j|_{T_1}$ first. For any $X \in DE$, we note that

$$X - A_1 = \frac{\|X - E\|}{\|D - E\|}(D - A_1) + \frac{\|X - D\|}{\|D - E\|}(E - A_1)$$

and $\mathbf{J}_1^{-1}(D - A_1) = (1, 0)^T$, $\mathbf{J}_1^{-1}(E - A_1) = (0, 1)^T$. Hence, by (4.35) and (4.33), for $X \in DE$, we have

$$\begin{aligned}
\mathbf{V}_T^j|_{T_1}(X) =& (\mathfrak{D}_{\alpha_j}\mathbf{J}_1)\mathbf{J}_1^{-1}(X - A_1) \\
=& \frac{\|X - E\|}{\|D - E\|}(\mathfrak{D}_{\alpha_j}\mathbf{J}_1)(1, 0)^T + \frac{\|X - D\|}{\|D - E\|}(\mathfrak{D}_{\alpha_j}\mathbf{J}_1)(0, 1)^T \\
=& \frac{\|X - E\|}{\|D - E\|}\mathfrak{D}_{\alpha_j}D + \frac{\|X - D\|}{\|D - E\|}\mathfrak{D}_{\alpha_j}E.
\end{aligned}$$

Similar arguments show that $\mathbf{V}_T^j|_{T_2}(X)$ satisfies the same identity; hence, the first identity in (4.36c) is proved.

As for **P2**, it is to see the velocity field vanishes on all the non-interface elements. Besides, we consider an arbitrary interface edge e shared by two interface elements T_1 and T_2. By (4.36a), (4.36b) and (4.23), we can see that, for every α_j, $j \in \mathcal{D}$, the velocity field $\mathbf{V}_{T_1}^j$ and $\mathbf{V}_{T_2}^j$ have the same formula on e. Thus, the velocity field defined by (4.35) are continuous across the interface edges. Similarly, (4.36b) and the first identity in (4.36c) indicates that the velocity field are also continuous across the internal sides DE and A_2E. Also, by its definition and the second identity in (4.36c), the velocity field $\mathbf{V}^j(X)$ is continuous across every non-interface edge. Furthermore, by (4.35), the velocity field $\mathbf{V}^j(X), j \in \mathcal{D}$ is a piecewise polynomial. Thus, we have that $\mathbf{V}^j(X)$ is a continuous piecewise C^1 function; therefore, $\mathbf{V}^j(X) \in H^1(\Omega)$.

P3 follows from Remark 4.1 together with (4.36a) and (4.36b). □

Remark 4.2. *According to **P3**, since a velocity field describes the movement of the spatial variables X, this means that every points on interface edges can only move along the edge.*

We note that there are other ways to express a point X in an interface element T as a function of the design variable $\boldsymbol{\alpha}$ and they can lead to different velocity fields. The advantage of the proposed formula (4.31) for X is that its derivatives can be calculated by the explicit formulas given in (4.35) instead of any approximation techniques. Furthermore, **P2** in Theorem 4.1 shows that the velocity field and other related quantities can be computed efficiently since the support of this velocity field is inside the union of interface elements whose number is proportional only to $O(h^{-1})$ while the number of all elements in the mesh is in the order of $O(h^{-2})$.

4.4.3 Shape Derivatives of IFE Shape Functions

In the proposed shape optimization problem (4.22), the IFE basis functions $\varphi_i, 1 \leq i \leq |\mathcal{N}_h|$ on the chosen unfitted mesh are directly employed in the objective function $\mathcal{J}_h$ according to (4.18)-(4.21). By their construction described in (1.17)-(1.20b), the IFE basis functions change when the interface $\Gamma(t, \boldsymbol{\alpha}), t \in [0, 1]$ moves because of the variations in the design variable $\boldsymbol{\alpha}$. Hence, the gradient of the objective function $\mathcal{J}_h$ in this IFE method inevitably involves the derivatives of the IFE basis functions with respect to $\boldsymbol{\alpha}$. By definition, each IFE basis function is a piecewise polynomial that is a linear combination of the IFE shape functions on each element according to (1.22) or (1.13) depending on whether the element is an interface element or not. Consequently, the derivative of an IFE basis function φ_i with respect to $\boldsymbol{\alpha}$ is zero on each non-interface element where all the shape functions are independent of $\boldsymbol{\alpha}$, and our focus in this subsection will be the derivative of IFE shape functions with respect to $\boldsymbol{\alpha}$ on interface elements.

Consider a typical interface element $T = \triangle A_1A_2A_3$ configured as in Figure 4.2. By (1.17) and the discussions in Section 4.3, we can express an IFE shape function $\phi_T(X)$ on T as $\phi_T(X) = \phi_T(X(\boldsymbol{\alpha}), \boldsymbol{\alpha})$ to emphasize that the design variable $\boldsymbol{\alpha}$ influences the value of ϕ_T not only through the spatial variable X which is a function of $\boldsymbol{\alpha}$ according to (4.31), but also directly through its coefficients $c_0, \mathbf{c}$, and the coefficients of $L(X)$. However, the rate of change for an IFE shape function ϕ_T with respect to $\boldsymbol{\alpha}$ through $X(\boldsymbol{\alpha})$ is readily known by the simple chain rule for differentiation because the velocity field $\mathbf{V}^j(X) = \mathfrak{D}_{\alpha_j} X$, $j \in \mathcal{D}$, can be computed by the formula prepared in Subsection 4.4.2. Therefore, we only need to discuss the rate of change for an IFE shape function ϕ_T with respect to $\alpha_j, j \in \mathcal{D}$ not through $X(\boldsymbol{\alpha})$, and this rate of change is referred as the shape derivative in the shape optimization literature [97]. We note that [160, 208] presented similar approaches to calculate the shape derivative for special finite element shape functions.

First, we recall that l is the line connecting the intersection points of the interface and element boundary, i.e., $D = (x_D, y_D)$ and $E = (x_E, y_E)$, as shown in Figure 4.2. Then, the

normal vector and the tangential vector for the line l are

$$\bar{\mathbf{n}} = \frac{1}{||D-E||}(y_D - y_E, -(x_D - x_E))^T, \quad \bar{\mathbf{t}} = \frac{1}{\|D-E\|}(x_D - x_E, y_D - y_E)^T,$$

and the equation for the line l is $L(X) = 0$ with $L(X) = \bar{\mathbf{n}} \cdot (X - D)$. Both $L(X)$ and $\bar{\mathbf{n}}$ depend on the design variable $\boldsymbol{\alpha}$ because of their dependence on the interface-mesh intersection points $D = (x_D, y_D)^T$ and $E = (x_E, y_E)^T$ that are functions of $\boldsymbol{\alpha}$. By direct calculations, we have

$$\begin{aligned} &\frac{\partial L}{\partial D} = -\frac{(X-D)^T \bar{\mathbf{t}} \bar{\mathbf{n}}^T}{\|D-E\|} - \bar{\mathbf{n}}^T, \quad \frac{\partial L}{\partial E} = \frac{(X-D)^T \bar{\mathbf{t}} \bar{\mathbf{n}}^T}{\|D-E\|}, \\ &\frac{\partial \bar{\mathbf{n}}}{\partial D} = \frac{-\bar{\mathbf{t}} \bar{\mathbf{n}}^T}{\|D-E\|}, \quad \frac{\partial \bar{\mathbf{n}}}{\partial E} = \frac{\bar{\mathbf{t}} \bar{\mathbf{n}}^T}{\|D-E\|}, \end{aligned} \tag{4.37}$$

where

$$\frac{\partial L}{\partial D} = (\frac{\partial L}{\partial x_D}, \frac{\partial L}{\partial y_D}), \quad \frac{\partial L}{\partial E} = (\frac{\partial L}{\partial x_E}, \frac{\partial L}{\partial y_E})$$

are 1-by-2 matrices, and

$$\frac{\partial \bar{\mathbf{n}}}{\partial D} = (\frac{\partial \bar{\mathbf{n}}}{\partial x_D}, \frac{\partial \bar{\mathbf{n}}}{\partial y_D}), \qquad \frac{\partial \bar{\mathbf{n}}}{\partial E} = (\frac{\partial \bar{\mathbf{n}}}{\partial x_E}, \frac{\partial \bar{\mathbf{n}}}{\partial y_E})$$

are 2-by-2 matrices. Then, by the chain rule, we can use (4.37) to calculate $\frac{\partial L(X,\boldsymbol{\alpha})}{\partial \alpha_j}$ and $\frac{\partial \bar{\mathbf{n}}}{\partial \alpha_j}$ as follows:

$$\frac{\partial L(X,\boldsymbol{\alpha})}{\partial \alpha_j} = \frac{\partial L}{\partial D}\, \mathfrak{D}_{\alpha_j} D + \frac{\partial L}{\partial E}\, \mathfrak{D}_{\alpha_j} E, \quad \frac{\partial \bar{\mathbf{n}}}{\partial \alpha_j} = \frac{\partial \bar{\mathbf{n}}}{\partial D}\, \mathfrak{D}_{\alpha_j} D + \frac{\partial \bar{\mathbf{n}}}{\partial E}\, \mathfrak{D}_{\alpha_j} E, \tag{4.38}$$

in which $\mathfrak{D}_{\alpha_j} D$ and $\mathfrak{D}_{\alpha_j} E$ are given by formulas in Lemma 4.1 and Lemma 4.2.

Remark 4.3. *According to* (4.38)*, we note that the shape derivatives of L and $\bar{\mathbf{n}}$ are decomposed into two components: their derivatives with respect to interface-mesh intersection points D and E, and the total derivatives of D and E with respect to the design variables. The derivatives of L and $\bar{\mathbf{n}}$ with respect to interface-mesh intersection points D and E given in* (4.37) *are independent of the parametrization of the interface.*

As discussed in Section 4.2, in the construction of IFE shape functions (1.17)-(1.20b), we let F be on the line l and $\mathbf{n}(F) = \bar{\mathbf{n}}$, i.e., the normal vector to l, and let the IFE functions formed by piecewise polynomials partitioned by l. So, based on Lemmas 4.1 and 4.2, on every interface element $T \in \mathcal{T}_h^i$, we have the following explicit formulas for the derivatives of the coefficients (1.18a)-(1.20b) with respect to $\boldsymbol{\alpha}$:

$$\frac{\partial c_0}{\partial \alpha_j} = \mu \left(\sum_{p \in \mathcal{I}^-} \left(\frac{\partial c_p}{\partial \alpha_j} \nabla \psi_{p,T} \cdot \bar{\mathbf{n}} + c_p \nabla \psi_{p,T} \cdot \frac{\partial \bar{\mathbf{n}}}{\partial \alpha_j} \right) + \sum_{q \in \mathcal{I}^+} v_q \nabla \psi_{q,T} \cdot \frac{\partial \bar{\mathbf{n}}}{\partial \alpha_j} \right), \tag{4.39a}$$

$$\frac{\partial \boldsymbol{\gamma}}{\partial \alpha_j} = \left(\nabla \psi_{p,T} \cdot \frac{\partial \bar{\mathbf{n}}}{\partial \alpha_j} \right)_{p \in \mathcal{I}^-}, \qquad \frac{\partial \boldsymbol{\delta}}{\partial \alpha_j} = \left(\frac{\partial L(A_p)}{\partial \alpha_j} \right)_{p \in \mathcal{I}^-}, \tag{4.39b}$$

$$\frac{\partial \mathbf{b}}{\partial \alpha_j} = \left(-\mu \frac{\partial L(A_p)}{\partial \alpha_j} \sum_{q \in \mathcal{I}^+} \nabla \psi_{q,T} \cdot \bar{\mathbf{n}} \; v_q - \mu L(A_p) \sum_{q \in \mathcal{I}^+} \nabla \psi_{q,T} \cdot \frac{\partial \bar{\mathbf{n}}}{\partial \alpha_j} \; v_q \right)_{p \in \mathcal{I}^-}. \tag{4.39c}$$

Furthermore, by (1.20a), we can compute $\frac{\partial \mathbf{c}}{\partial \alpha_j}, j \in \mathcal{D}$ with (4.39b) and (4.39c) as follows:

$$\frac{\partial \mathbf{c}}{\partial \alpha_j} = \frac{\partial \mathbf{b}}{\partial \alpha_j} - \mu \frac{\left[\left(\frac{\partial \boldsymbol{\gamma}}{\partial \alpha_j} \right)^T \mathbf{b} \boldsymbol{\delta} + \boldsymbol{\gamma}^T \frac{\partial \mathbf{b}}{\partial \alpha_j} \boldsymbol{\delta} + \boldsymbol{\gamma}^T \mathbf{b} \frac{\partial \boldsymbol{\delta}}{\partial \alpha_j} \right] (1 + \mu \boldsymbol{\gamma}^T \boldsymbol{\delta}) - \mu \boldsymbol{\gamma}^T \mathbf{b} \boldsymbol{\delta} \left[\left(\frac{\partial \boldsymbol{\gamma}}{\partial \alpha_j} \right)^T \boldsymbol{\delta} + \boldsymbol{\gamma}^T \frac{\partial \boldsymbol{\delta}}{\partial \alpha_j} \right]}{(1 + \mu \boldsymbol{\gamma}^T \boldsymbol{\delta})^2}. \tag{4.40}$$

Finally, we use (4.38), (4.39a), and (4.40) to obtain the following formula for the shape derivatives of an IFE shape function defined by (1.17): for every $j \in \mathcal{D}$,

$$\frac{\partial \phi_T(X, \boldsymbol{\alpha})}{\partial \alpha_j} = \begin{cases} \frac{\partial \phi_T^-(X, \boldsymbol{\alpha})}{\partial \alpha_j} = \frac{\partial \phi_T^+(X, \boldsymbol{\alpha})}{\partial \alpha_j} + \frac{\partial c_0}{\partial \alpha_j} L(X, \boldsymbol{\alpha}) + c_0 \frac{L(X, \boldsymbol{\alpha})}{\partial \alpha_j} & \text{if } X \in \hat{T}^-, \\ \frac{\partial \phi_T^+(X, \boldsymbol{\alpha})}{\partial \alpha_j} = \sum_{p \in \mathcal{I}^-} \frac{\partial c_p}{\partial \alpha_j} \psi_{p,T}(X) & \text{if } X \in \hat{T}^+, \end{cases} \tag{4.41}$$

where $\hat{T}^-$ and $\hat{T}^+$ are subelements of T partitioned by the line l.

4.4.4 The gradient of the Discretized Objective Function

The gradient of the objective function $\mathcal{J}_h$ is necessary for the implementation of the proposed IFE method with a common minimization algorithm based on a decent direction or trust region. We now put all the preparations in the previous subsections into a procedure for accurately and efficiently computing the gradient of the objective function $\mathcal{J}_h$ within the IFE framework, i.e., the total derivatives of $\mathcal{J}_h$ with respect to $\alpha_j, j \in \mathcal{D}$. And these total derivatives involve both the velocity field and shape derivatives discussed in the previous subsections, which are referred as the material derivatives of $\mathcal{J}_h$ in shape optimization literature [184]. As we can see later in this subsection, the material derivative of $\mathcal{J}_h$ depends on its counterparts for the matrix $\mathbf{A}^k(X(\boldsymbol{\alpha}), \boldsymbol{\alpha})$ and the vector $\mathbf{F}^k(X(\boldsymbol{\alpha}), \boldsymbol{\alpha})$. Therefore, we start from the formulas for the material derivatives with respect to $\alpha_j, j \in \mathcal{D}$ of the local matrices and local vectors which are used to construct $\mathbf{A}^k(X(\boldsymbol{\alpha}), \boldsymbol{\alpha})$ and $\mathbf{F}^k(X(\boldsymbol{\alpha}), \boldsymbol{\alpha})$, and the results are presented in the two theorems below.

Theorem 4.2. *On each interface element $T \in \mathcal{T}_h^i$ and each interface edge $e \in \mathcal{E}_h^i$ with the intersection point D, we have the following formulas for the material derivatives of $\mathbf{K}_T, \mathbf{E}_e^{r_1,r_2}, \mathbf{G}_e^{r_1,r_2}$ and $\mathbf{R}_T$ with respect to $\alpha_j, j \in \mathcal{D}$:*

$$\mathfrak{D}_{\alpha_j} \mathbf{K}_T = \left(\int_T \beta \nabla \frac{\partial \phi_{p,T}}{\partial \alpha_j} \cdot \nabla \phi_{q,T} dX \right)_{p,q \in \mathcal{I}} + \left(\int_T \beta \nabla \frac{\partial \phi_{p,T}}{\partial \alpha_j} \cdot \nabla \phi_{q,T} dX \right)_{p,q \in \mathcal{I}}^T$$

$$+\left(\sum_{m=1}^{3}\int_{T_m}\beta\nabla\phi_{p,T}\cdot\nabla\phi_{q,T}\ dX\ \mathrm{tr}\left((\mathfrak{D}_{\alpha_j}\mathbf{J}_m)\mathbf{J}_m^{-1}\right)\right)_{p,q\in\mathcal{I}}, \tag{4.42a}$$

$$\mathfrak{D}_{\alpha_j}\mathbf{E}_e^{r_1r_2}=\left(\int_e\beta\nabla\frac{\partial\phi_{p,T^{r_1}}}{\partial\alpha_j}\cdot(\phi_{q,T^{r_2}}\mathbf{n}_e^{r_2})ds\right)_{p,q\in\mathcal{I}}+\left(\int_e\beta\nabla\phi_{p,T^{r_1}}\cdot(\frac{\partial\phi_{q,T^{r_2}}}{\partial\alpha_j}\mathbf{n}_e^{r_2})ds\right)_{p,q\in\mathcal{I}}$$
$$+\left(\beta^-\nabla\phi^-_{p,T^{r_1}}\cdot(\phi^-_{q,T^{r_2}}\mathbf{n}_e^{r_2})|_D-\beta^+\nabla\phi^+_{p,T^{r_1}}\cdot(\phi^+_{q,T^{r_2}}\mathbf{n}_e^{r_2})|_D\right)_{p,q\in\mathcal{I}}\frac{\mathfrak{D}_{\alpha_j}D\cdot(A_2-A_1)}{\|A_2-A_1\|}, \tag{4.42b}$$

$$\mathfrak{D}_{\alpha_j}\mathbf{G}_e^{r_1r_2}=\frac{\rho_e^0}{|e|}\left(\int_e(\frac{\partial\phi_{p,T^{r_1}}}{\partial\alpha_j}\mathbf{n}_e^{r_1})\cdot(\phi_{q,T^{r_2}}\mathbf{n}_e^{r_2})ds+\int_e(\phi_{p,T^{r_1}}\mathbf{n}_e^{r_1})\cdot(\frac{\partial\phi_{q,T^{r_2}}}{\partial\alpha_j}\mathbf{n}_e^{r_2})ds\right)_{p,q\in\mathcal{I}}, \tag{4.42c}$$

$$\mathfrak{D}_{\alpha_j}\mathbf{R}_T=\left(\int_T\frac{\partial\phi_{p,T}}{\partial\alpha_j}dX+\int_T\nabla\phi_{p,T}\cdot\mathbf{V}^j dX\right)_{p\in\mathcal{I}}$$
$$+\left(\sum_{m=1}^{3}\int_{T_m}\phi_{p,T}\ dX\ \mathrm{tr}\left((\mathfrak{D}_{\alpha_j}\mathbf{J}_m)\mathbf{J}_m^{-1}\right)\right)_{p\in\mathcal{I}}, \tag{4.42d}$$

where $\frac{\partial\phi_{p,T}}{\partial\alpha_j}$ *and* $\frac{\partial\phi_{q,T}}{\partial\alpha_j}$ *are the shape derivatives of the IFE shape functions given by the formula* (4.41) *for each* $T\in\mathcal{T}_h^i$.

Proof. For each $T\in\mathcal{T}_h^i$, according to the material derivative formula given in Lemma 3.3 of [97], we have

$$\begin{aligned}\mathfrak{D}_{\alpha_j}\mathbf{K}_T&=\left(\mathfrak{D}_{\alpha_j}\int_T\beta\nabla\phi_{p,T}\cdot\nabla\phi_{q,T}dX\right)_{p,q\in\mathcal{I}}\\&=\left(\int_T\beta\nabla\frac{\partial}{\partial\alpha_j}\phi_{p,T}\cdot\nabla\phi_{q,T}dX+\int_T\beta\nabla\phi_{p,T}\cdot\nabla\frac{\partial}{\partial\alpha_j}\phi_{q,T}dX\right)_{p,q\in\mathcal{I}}\\&+\left(\int_T\frac{\partial}{\partial X}\left(\beta\nabla\phi_{p,T}\cdot\nabla\phi_{q,T}\right)\cdot\mathbf{V}_T^j dX\right)_{p,q\in\mathcal{I}}\\&+\left(\int_T\beta\nabla\phi_{p,T}\cdot\nabla\phi_{q,T}\ \mathrm{div}(\mathbf{V}_T^j)\ dX\right)_{p,q\in\mathcal{I}},\end{aligned} \tag{4.43}$$

where $\frac{\partial\phi_{p,T}}{\partial\alpha_j}, p\in\mathcal{I}$ are the shape derivatives of the IFE shape functions with respect to α_j given by the formula in (4.41). Since $\nabla\phi_{p,T}\cdot\nabla\phi_{q,T}$ are constants for any $p,q\in\mathcal{I}$, we have $\frac{\partial}{\partial X}\left(\beta\nabla\phi_{p,T}\cdot\nabla\phi_{q,T}\right)=0$; hence, (4.42a) follows from (4.43) together with (4.36d). And the formula (4.42d) for the material derivatives of $\mathbf{R}_T$ can be derived similarly.

For the material derivatives of $\mathbf{E}_e^{r_1r_2}$, let $e=\overline{A_1A_2}$ be an interface edge with the intersection point D of an interface element T, as configured in Figure 4.2, without loss of generality. According to Remark 4.2, the geometry change restricted on interface edges can be viewed

as the 1-D shape change with the two ending points fixed. Hence, applying the material derivative formula given in Lemma 3.3 of [97] to $\mathbf{E}_e^{r_1 r_2}$ given in (4.12b), we have

$$\begin{aligned}
\mathfrak{D}_{\partial_j}\mathbf{E}_e^{r_1 r_2} &= \mathfrak{D}_{\alpha_j}\left(\int_e \beta\nabla\phi_{p,T^{r_1}}\cdot(\phi_{q,T^{r_2}}\mathbf{n}_e^{r_2})ds\right)_{p,q\in\mathcal{I}} \\
&= \left(\int_e \frac{\partial}{\partial\alpha_j}\left(\beta\nabla\phi_{p,T^{r_1}}\cdot(\phi_{q,T^{r_2}}\mathbf{n}_e^{r_2})\right)ds\right)_{p,q\in\mathcal{I}} \qquad (4.44)\\
&+ \left(\beta^-\nabla\phi^-_{p,T^{r_1}}\cdot(\phi^-_{q,T^{r_2}}\mathbf{n}_e^{r_2})|_D\mathbf{V}_T^j(D)\cdot\mathbf{t}_e\right)_{p,q\in\mathcal{I}} \\
&- \left(\beta^+\nabla\phi^+_{p,T^{r_1}}\cdot(\phi^+_{q,T^{r_2}}\mathbf{n}_e^{r_2})|_D\mathbf{V}_T^j(D)\cdot\mathbf{t}_e\right)_{p,q\in\mathcal{I}} \qquad (4.45)\\
&- \left(\beta\nabla\phi_{p,T^{r_1}}\cdot(\phi_{q,T^{r_2}}\mathbf{n}_e^{r_2})|_{A_1}\mathbf{V}_T^j(A_1)\cdot\mathbf{t}_e\right)_{p,q\in\mathcal{I}} \\
&+ \left(\beta\nabla\phi_{p,T^{r_1}}\cdot(\phi_{q,T^{r_2}}\mathbf{n}_e^{r_2})|_{A_2}\mathbf{V}_T^j(A_2)\cdot\mathbf{t}_e\right)_{p,q\in\mathcal{I}}, \qquad (4.46)
\end{aligned}$$

where $\mathbf{t}_e$ is the unit direction vector from A_1 to A_2. Then, (4.42b) follows from applying (4.36a) and the fact $\mathbf{V}_T^j(A_1)=\mathbf{V}_T^j(A_2)=\mathbf{0}$ to (4.46). The formula (4.42c) for the material derivative of $\mathbf{G}_e^{r_1,r_2}$ can be derived similarly. □

Theorem 4.3. *On each interface element $T\in\mathcal{T}_h^i$ and each interface edge $e\in\mathcal{E}_h^i$ with the intersection point D, we have the following formulas for the total derivatives of $\mathbf{F}_T,\mathbf{B}_e,\mathbf{C}_e$ and $\mathbf{N}_e$ with respect to $\alpha_j, j\in\mathcal{D}$:*

$$\begin{aligned}
\mathfrak{D}_{\alpha_j}\mathbf{F}_T^k &= \left(\int_T f^k\frac{\partial\phi_{p,T}}{\partial\alpha_j}dX\right)_{p\in\mathcal{I}} + \left(\int_T\nabla(f^k\phi_{p,T})\cdot\mathbf{V}_T^j dX\right)_{p\in\mathcal{I}} \\
&\quad + \left(\sum_{m=1}^3\int_{T_m} f^k\phi_{p,T}\ dX\ \mathrm{tr}\left((\mathfrak{D}_{\alpha_j}\mathbf{J}_m)\mathbf{J}_m^{-1}\right)\right)_{p\in\mathcal{I}}, \qquad (4.47a)\\
\mathfrak{D}_{\partial_j}\mathbf{B}_e^k &= \left(\int_e \beta g_D^k\nabla\frac{\partial\phi_{p,T}}{\partial\alpha_j}\cdot\mathbf{n}_e ds\right)_{p\in\mathcal{I}} \\
&\quad + \left(\beta^- g_D^k\nabla\phi^-_{p,T}\cdot\mathbf{n}_e|_D - \beta^+ g_D^k\nabla\phi^+_{p,T}\cdot\mathbf{n}_e|_D\right)_{p\in\mathcal{I}}\frac{\mathfrak{D}_{\alpha_j}D\cdot(A_2-A_1)}{\|A_2-A_1\|}, \qquad (4.47b)\\
\mathfrak{D}_{\partial_j}\mathbf{C}_e^k &= \frac{\rho_e^0}{|e|}\left(\int_e\beta g_D^k\frac{\partial\phi_{p,T}}{\partial\alpha_j}ds\right)_{p\in\mathcal{I}} + \frac{\rho_e^0}{|e|}\left(\beta^- g_D^k\phi^-_{p,T}|_D - \beta^+ g_D^k\phi^+_{p,T}|_D\right)_{p\in\mathcal{I}}\frac{\mathfrak{D}_{\alpha_j}D\cdot(A_2-A_1)}{\|A_2-A_1\|}, \qquad (4.47c)
\end{aligned}$$

$$\mathfrak{D}_{\partial_j}\mathbf{N}_e^k = \left(\int_e g_N^k \frac{\partial \phi_{p,T}}{\partial \alpha_j} ds\right)_{p\in\mathcal{I}} + \left(g_N^k \phi_{p,T}^-|_D - g_N^k \phi_{p,T}^+|_D\right)_{p\in\mathcal{I}} \frac{\mathfrak{D}_{\alpha_j} D \cdot (A_2 - A_1)}{\|A_2 - A_1\|}, \tag{4.47d}$$

where $\frac{\partial \phi_{p,T}}{\partial \alpha_j}$ *are the shape derivatives of IFE shape functions given by the formula* (4.41) *for each* $T \in \mathcal{T}_h^i$

Proof. The proof follows from applying arguments similar to those for Theorem 4.2 to the local vectors defined in (4.13a)-(4.13c). □

Now, by Lemma 3.3 in [97] again, we have the following standard formula of the objective functional for the material derivative associated to the j-th design variable α_j:

$$\begin{aligned}
&\mathfrak{D}_{\alpha_j}\mathcal{J}_h = \int_{\Omega_0} \mathfrak{D}_{\alpha_j} J_h dX + \int_{\Omega_0} J_h \ \mathrm{div}\left(\mathbf{V}^j\right) dX \\
=&\sum_{k=1}^K \left(\int_{\Omega_0} \left(\frac{\partial J_h}{\partial \mathbf{u}_h^k}\right) \cdot \mathfrak{D}_{\alpha_j}\mathbf{u}_h^k dX\right) + \int_{\Omega_0} \left(\frac{\partial J_h}{\partial X}\right)^T \mathbf{V}^j dX + \int_{\Omega_0} \frac{\partial J_h}{\partial \alpha_j} dX + \int_{\Omega_0} J_h \ \mathrm{div}\left(\mathbf{V}^j\right) dX \\
=&\sum_{k=1}^K \left(\frac{\partial \mathcal{J}_h}{\partial \mathbf{u}_h^k} \cdot \mathfrak{D}_{\alpha_j}\mathbf{u}_h^k\right) + \int_{\Omega_0} \frac{\partial J_h}{\partial \alpha_j} dX + \int_{\Omega_0} \nabla J_h \cdot \mathbf{V}^j dX + \int_{\Omega_0} J_h \ \mathrm{div}\left(\mathbf{V}^j\right) dX
\end{aligned} \tag{4.48}$$

in which we have used the fact that

$$\frac{\partial \mathcal{J}_h}{\partial \mathbf{u}_h^k} = \int_{\Omega_0} \frac{\partial J_h}{\partial \mathbf{u}_h^k} dX. \tag{4.49}$$

The terms $\frac{\partial J_h}{\partial \alpha_j}$ are derivatives of J_h with respect to its last variable $\boldsymbol{\alpha}$ specified in the generic formula (4.20), not through other variables $\mathbf{u}_h^k(\boldsymbol{\alpha})$s and $X(\boldsymbol{\alpha})$ of J_h , and the computations for $\frac{\partial J_h}{\partial \alpha_j}$ essentially rely on the shape derivatives of IFE shape functions given in (4.41), a typical example to further explain this is given by (4.56) in the next section. Furthermore, as demonstrated by examples presented in the next section, in this fundamental formula for $\mathfrak{D}_{\alpha_j}\mathcal{J}_h$, the terms $\frac{\partial \mathcal{J}_h}{\partial \mathbf{u}_h^k}, \nabla J_h, \frac{\partial J_h}{\partial \alpha_j}$, and J_h are problem dependent, but they are easy to calculate for many applications by explicit formulas. Also, we note that $\mathbf{V}^j$ is given in (4.35) and $\mathrm{div}\left(\mathbf{V}^j\right)$ is given in (4.36d); hence, we proceed to derive the formula for $\left(\frac{\partial \mathcal{J}_h}{\partial \mathbf{u}_h^k}\right) \cdot \mathfrak{D}_{\alpha_j}\mathbf{u}_h,\ j \in \mathcal{D}$ which can be directly used in (4.48).

For $\mathfrak{D}_{\alpha_j}\mathbf{u}_h^k, 1 \le k \le K, j \in \mathcal{D}$, by differentiating the IFE system in (4.17) with respect to α_j, we have

$$\mathfrak{D}_{\alpha_j}\mathbf{A}^k(X(\boldsymbol{\alpha}), \boldsymbol{\alpha})\ \mathbf{u}_h^k(\boldsymbol{\alpha}) + \mathbf{A}^k(X(\boldsymbol{\alpha}), \boldsymbol{\alpha})\ \mathfrak{D}_{\alpha_j}\mathbf{u}_h^k = \mathfrak{D}_{\alpha_j}\mathbf{F}^k(X(\boldsymbol{\alpha}), \boldsymbol{\alpha}),$$

which leads to the linear system for $\mathfrak{D}_{\alpha_j}\mathbf{u}_h^k$:

$$\mathbf{A}^k(X(\boldsymbol{\alpha}), \boldsymbol{\alpha})\ \mathfrak{D}_{\alpha_j}\mathbf{u}_h^k = \left(\mathfrak{D}_{\alpha_j}\mathbf{F}^k(X(\boldsymbol{\alpha}), \boldsymbol{\alpha}) - \mathfrak{D}_{\alpha_j}\mathbf{A}^k(X(\boldsymbol{\alpha}), \boldsymbol{\alpha})\ \mathbf{u}_h^k(\boldsymbol{\alpha})\right), \quad 1 \le k \le K. \tag{4.50}$$

Then, by (4.50) and the standard process in the discretized adjoint method [73], we obtain the following formula to compute $\left(\frac{\partial \mathcal{J}_h}{\partial \mathbf{u}_h^k}\right) \cdot \mathfrak{D}_{\alpha_j} \mathbf{u}_h^k$ efficiently (especially when $|\mathcal{D}|$ is large):

$$\left(\frac{\partial \mathcal{J}_h}{\partial \mathbf{u}_h^k}\right) \cdot \mathfrak{D}_{\alpha_j} \mathbf{u}_h^k = \mathbf{Y}^k \cdot \left(\mathfrak{D}_{\alpha_j} \mathbf{F}^k(X(\boldsymbol{\alpha}), \boldsymbol{\alpha}) - \mathfrak{D}_{\alpha_j} \mathbf{A}^k(X(\boldsymbol{\alpha}), \boldsymbol{\alpha})\ \mathbf{u}_h^k(\boldsymbol{\alpha})\right), \quad 1 \le k \le K, \tag{4.51}$$

where $\mathbf{Y}^k$ is obtained by solving

$$\left(\mathbf{A}^k\right)^T \mathbf{Y}^k = \frac{\partial \mathcal{J}_h}{\partial \mathbf{u}_h^k}, \tag{4.52}$$

and $\mathbf{A}^k$ is the matrix for the k-th IFE equation described in (4.17). We further note that the formula (4.51) involves the material derivatives of the global stiffness matrix and load vector with respect to $\alpha_j, j \in \mathcal{D}$, i.e., $\mathfrak{D}_{\alpha_j} \mathbf{A}^k(\boldsymbol{\alpha})$ and $\mathfrak{D}_{\alpha_j} \mathbf{F}^k(\boldsymbol{\alpha})$ which can be assembled with the material derivatives of the local matrices for $\mathbf{A}^k$ and the material derivatives of local vectors for $\mathbf{F}^k$ according to the same standard assemblage procedure as that for assembling matrix $\mathbf{A}^k$ and vector $\mathbf{F}^k$. However, the assemblage for $\mathfrak{D}_{\alpha_j} \mathbf{A}^k(\boldsymbol{\alpha})$ and $\mathfrak{D}_{\alpha_j} \mathbf{F}^k(\boldsymbol{\alpha})$ only needs to be performed over the interface elements/edges since the material derivatives of the local matrices and local vectors all vanish on the non-interface elements/edges.

4.5 Implementation

For the implementation of the proposed IFE-based shape optimization method, we put the discretization of forward/inverse problems and the sensitivity computation together into an algorithm as follows.

Algorithm The IFE-based Shape Optimization Algorithm

1: Generate an unfitted mesh and choose an initial design variable $\boldsymbol{\alpha}$.
2: Loop until convergence.
3: Prepare data:
   a: use the design variables to generate the parametric curve $\Gamma(\boldsymbol{\alpha})$ as the numerical interface;
   b: find the interface-mesh intersection points, interface edges and interface elements.
4: Prepare matrices and vectors for the IFE systems and compute the objective function:
   a: use (4.12) and (4.13) and the IFE spaces given in (1.13) and (1.22) to assemble matrices and vectors $\mathbf{A}^k, \mathbf{F}^k, 1 \leq k \leq K$ for the IFE systems (4.17);
   b: compute the PPIFE solutions $\mathbf{u}^k, 1 \leq k \leq K$ by (4.17) and the objective function $\mathcal{J}_h(\boldsymbol{\alpha})$ in (4.22).
5: Compute the shape sensitivities:
   a: form the material derivatives of local matrices and vectors according to Theorems 4.2, 4.3, and use them to assemble the global matrices $\mathfrak{D}_{\alpha_j}\mathbf{A}^k(\boldsymbol{\alpha})$ and vectors $\mathfrak{D}_{\alpha_j}\mathbf{F}^k(\boldsymbol{\alpha})$;
   b: compute $\frac{\partial \mathcal{J}_h}{\partial \mathbf{u}_h^k} \cdot \mathfrak{D}_{\alpha_j}\mathbf{u}_h^k$ for $k = 1, \cdots, K$, according to (4.51);
   c: compute the terms $\int_{\Omega_0} \frac{\partial J_h}{\partial \alpha_j} dX$, $\int_{\Omega_0} \nabla J_h \cdot \mathbf{V}^j dX$ and $\int_{\Omega_0} J_h \mathrm{div}(\mathbf{V}^j) dX$ according to the given shape functional;
   d: compute the material derivatives of $\mathcal{J}_h(\boldsymbol{\alpha})$ according to (4.48).
6: Use $\mathcal{J}_h(\boldsymbol{\alpha})$ and its material derivatives to update the design variable $\boldsymbol{\alpha}$ by a chosen gradient-based optimization algorithm.
7: End loop

In this proposed IFE-based Shape Optimization Algorithm, we note that the mesh can be fixed during the optimization process, and the only mesh information needed to be updated are those interface-mesh intersection points and interface elements/edges. Consequently, the sizes and algebraic structures of the global matrices $\mathbf{A}^k$ and vectors $\mathbf{F}^k$ in step 4 remain the same on this fixed unfitted mesh, which is beneficial for implementation. Also, they do not need to be completely re-assembled in each iteration, because only those global basis functions whose supports overlap with the interface elements/edges in two consecutive iterations are changed. As a result, their assemblage can be done very efficiently by just updating those entries corresponding to the global basis functions whose supports overlap with the interface elements/edges in the previous and the current iteration.

In step 5 above (computing the shape sensitivities), we emphasize that the velocity fields and the shape derivatives of IFE shape functions are only needed on interface elements, which can be implemented according to the analytical formulas (4.35) and (4.41). These two quantities vanishing over all the non-interface elements make the whole procedure of shape sensitivity computation remarkably efficient. Firstly, the integration for the terms $\int_{\Omega_0} \nabla J_h \cdot \mathbf{V}^j dX$ and $\int_{\Omega_0} J_h \mathrm{div}(\mathbf{V}^j) dX$ in the material derivative of the objective functional (4.48) only needs to be done on those interface elements intersecting with Ω_0 because the involved integrands

vanish on all the non-interface elements. Secondly, assembling the matrices $\mathfrak{D}_{\alpha_j}\mathbf{F}^k(\boldsymbol{\alpha})$ and $\mathfrak{D}_{\alpha_j}\mathbf{A}^k(\boldsymbol{\alpha})$, i.e., the material derivatives of global matrices $\mathbf{A}^k$ and $\mathbf{F}^k$, is also a very efficient process since it is only performed over the interface elements/edges by the explicit formulas given in Theorems 4.2 and 4.3. In summary, the computations of shape sensitivity in this algorithm only need to be carried out over interface elements whose number is in the order of $O(h^{-1})$ versus the number of all elements in the order of $O(h^{-2})$ in the mesh. In contrast, preparing $\mathfrak{D}_{\alpha_j}\mathbf{F}^k(\boldsymbol{\alpha})$ and $\mathfrak{D}_{\alpha_j}\mathbf{A}^k(\boldsymbol{\alpha})$ is usually expensive within the Lagrange framework where a global velocity field requires to carry out the assemblages over all elements in a mesh [50], and $\mathfrak{D}_{\alpha_j}\mathbf{F}^k(\boldsymbol{\alpha})$ and $\mathfrak{D}_{\alpha_j}\mathbf{A}^k(\boldsymbol{\alpha})$ are usually prepared approximately in methods in the Eullerian framework, see the related discussions in [64, 198, 208].

Finally, we note that the proposed IFE-based shape optimization algorithm is highly parallelizable because computing the velocity fields $\mathbf{V}^j$ (4.35), shape derivatives of IFE shape functions $\frac{\partial \phi_T}{\partial \alpha_j}$ (4.41) and the material derivatives of stiffness matrices and vectors $\mathfrak{D}_{\alpha_j}\mathbf{A}^k(\boldsymbol{\alpha})$ and $\mathfrak{D}_{\alpha_j}\mathbf{F}^k(\boldsymbol{\alpha})$, i.e., the material derivatives of objective functions (4.48) with respect to each individual design variable α_j, are independent with each other. Hence these computations can be done very efficiently with an easy implementation on modern parallel computers.

Therefore, we believe these properties together with the optimal accuracy of PPIFE solutions (4.10) and the resulted optimal accuracy of discretized objective functions, regardless of the interface location, make the proposed IFE-based shape optimization algorithm advantageous compared with those in the literature.

4.6 Some Applications

In this section, we demonstrate how the general IFE-based shape optimization method proposed in the previous section can use an unfitted mesh to solve a spectrum of interface inverse problems posed in the format of (4.1)-(4.4) by applying this method to, but not limited to, three representative interface inverse/design problems: (1). an output-least-squares problem [40, 43, 74]; (2). a Dirichlet-Neumann problem [27, 110, 179]; and (3). a heat dissipation minimization problem [69, 135, 210]. The first problem uses the interior data available on the whole or a portion of Ω to reconstruct/design the interface, the second one recovers the interface from the data only available on $\partial\Omega$, and the last one is an application for an optimal design of heat conduction fields. These examples also serve as hints/suggestions how the proposed IFE method can be implemented efficiently.

All numerical examples to be presented are posed on the domain $\Omega = (-1,1)\times(-1,1)$ with an unfitted Cartesian mesh that is formed by partitioning Ω into congruent rectangles and then partitioning each rectangle into two triangles along its diagonal line. The parameterized interface $\Gamma(\boldsymbol{\alpha})$ in the shape optimization is expressed by a cubic spline. This choice of parametrization for the interface Γ is based on the accuracy, versatility, and popularity of the cubic spline, and we emphasize that the algorithm developed here can be readily extended

to other parameterizations.

4.6.1 An Output-Least-Squares Problem

In this example, we consider an interface inverse/design problem associated to the interface forward problem described by (4.1) and (4.2) with $K = 1$, in which we assume an observation data (or a target function in an optimal design application) $\bar{u}$ for the solution u^1 to the forward problem described by (4.1)-(4.2) with a pure Dirichlet boundary condition g_D^1 on $\partial\Omega$ is available on a sub-domain $\Omega_0 \subseteq \Omega$, and we need to recover/design the location and the shape of the interface from $\bar{u}$ by solving an output-least-squares problem [43, 117], i.e., by optimizing the following shape functional

$$\mathcal{J}(\Gamma) = \int_{\Omega_0} (u^1 - \bar{u})^2 dX. \tag{4.53}$$

This problem arises from oil/underwater reservoirs [67, 205] and optimal designing of cooling elements in battery systems [168]. Applying the IFE method proposed in (4.22) to the inverse problem formulated in (4.53) suggests to seek the design variable $\boldsymbol{\alpha}^*$ by solving the following constrained optimization problem:

$$\begin{aligned} \boldsymbol{\alpha}^* = \text{argmin } \mathcal{J}_h(\boldsymbol{\alpha}), \qquad \mathcal{J}_h(\boldsymbol{\alpha}) &= \int_{\Omega_0} J_h(\mathbf{u}_h^1(\boldsymbol{\alpha}), X(\boldsymbol{\alpha}), \boldsymbol{\alpha}) dX, \\ \text{subject to} \qquad \mathbf{A}^1(\boldsymbol{\alpha})\mathbf{u}_h^1(\boldsymbol{\alpha}) &- \mathbf{F}^1(\boldsymbol{\alpha}) = \mathbf{0}, \end{aligned} \tag{4.54}$$

where, expressing the IFE solution $u_h^1(\boldsymbol{\alpha}) = u_h^1(\mathbf{u}_h^1(\boldsymbol{\alpha}), X(\boldsymbol{\alpha}), \boldsymbol{\alpha})$ in the format given in (4.18), we have

$$\begin{aligned} &J_h(\mathbf{u}_h^1(\boldsymbol{\alpha}), X(\boldsymbol{\alpha}), \boldsymbol{\alpha}) = \left(\tilde{J}_h(\mathbf{u}_h^1(\boldsymbol{\alpha}), X(\boldsymbol{\alpha}), \boldsymbol{\alpha})\right)^2, \\ \text{with } \ &\tilde{J}_h(\mathbf{u}_h^1(\boldsymbol{\alpha}), X(\boldsymbol{\alpha}), \boldsymbol{\alpha}) = \sum_{i=1}^{|\mathring{\mathcal{N}}_h|} u_i^1(\boldsymbol{\alpha})\varphi_i(X(\boldsymbol{\alpha}), \boldsymbol{\alpha}) + \sum_{i=|\mathring{\mathcal{N}}_h|+1}^{|\mathcal{N}_h|} g_D^1(X_i)\varphi_i(X(\boldsymbol{\alpha}), \boldsymbol{\alpha}) - \bar{u}. \end{aligned} \tag{4.55}$$

It is easy to see that the discrete objective function $\mathcal{J}_h(\boldsymbol{\alpha})$ has the optimal second order accuracy to approximate the continuous objective functional $\mathcal{J}(\Gamma(\boldsymbol{\alpha}))$ regardless of the interface location and shape on an unfitted mesh. According to (4.55), the evaluation of $J_h(\mathbf{u}_h^1(\boldsymbol{\alpha}), X(\boldsymbol{\alpha}), \boldsymbol{\alpha})$ is straightforward and it is obvious that

$$\begin{aligned} \nabla J_h &= 2\tilde{J}_h(\mathbf{u}_h^1(\boldsymbol{\alpha}), X(\boldsymbol{\alpha}), \boldsymbol{\alpha}) \\ &\quad \cdot \left(\sum_{i=1}^{|\mathring{\mathcal{N}}_h|} u_i^1(\boldsymbol{\alpha}) \nabla\varphi_i(X(\boldsymbol{\alpha}), \boldsymbol{\alpha}) + \sum_{i=|\mathring{\mathcal{N}}_h|+1}^{|\mathcal{N}_h|} g_D^1(X_i) \nabla\varphi_i(X(\boldsymbol{\alpha}), \boldsymbol{\alpha}) - \nabla\bar{u} \right), \\ \frac{\partial J_h}{\partial \alpha_j} &= 2\tilde{J}_h(\mathbf{u}_h^1(\boldsymbol{\alpha}), X(\boldsymbol{\alpha}), \boldsymbol{\alpha}) \left(\sum_{i=1}^{|\mathring{\mathcal{N}}_h|} u_i^1(\boldsymbol{\alpha}) \frac{\partial\varphi_i(X(\boldsymbol{\alpha}), \boldsymbol{\alpha})}{\partial\alpha_j} + \sum_{i=|\mathring{\mathcal{N}}_h|+1}^{|\mathcal{N}_h|} g_D^1(X_i) \frac{\partial\varphi_i(X(\boldsymbol{\alpha}), \boldsymbol{\alpha})}{\partial\alpha_j} \right), \end{aligned} \tag{4.56}$$

where $\bar{u}$ is assumed to be optimization independent, $\nabla\varphi_i(X(\boldsymbol{\alpha}),\boldsymbol{\alpha})$ is the standard gradient with respect to X, and $\frac{\partial\varphi_i(X(\boldsymbol{\alpha}),\boldsymbol{\alpha})}{\partial\alpha_j}, j\in\mathcal{D}$ are the shape derivatives of the global IFE basis functions which are zero on all the non-interface elements or computed by (4.41) on interface elements. Furthermore, a direct calculation leads to

$$\mathcal{J}_h = \begin{pmatrix} \mathbf{u}_h^1 \\ \mathbf{g}_D^1 \end{pmatrix}^T \mathbf{M} \begin{pmatrix} \mathbf{u}_h^1 \\ \mathbf{g}_D^1 \end{pmatrix} - 2\begin{pmatrix} \mathbf{u}_h^1 \\ \mathbf{g}_D^1 \end{pmatrix}^T \bar{\mathbf{u}} + \int_{\Omega_0} \bar{u}^2 dX, \tag{4.57}$$

$$\frac{\partial \mathcal{J}_h}{\partial \mathbf{u}_h^1} = 2\mathbf{M}_0 \begin{pmatrix} \mathbf{u}_h^1 \\ \mathbf{g}_D^1 \end{pmatrix} - 2\bar{\mathbf{u}}_0, \tag{4.58}$$

$$\text{where } \mathbf{M} = \left(\int_{\Omega_0} \phi_i\phi_j dX\right)_{i=1,j=1}^{|\mathcal{N}_h|,|\mathcal{N}_h|} \in \mathbb{R}^{|\mathcal{N}_h|\times|\mathcal{N}_h|},\ \bar{\mathbf{u}} = \left(\int_{\Omega_0} \bar{u}\phi_i dX\right)_{i=1}^{|\mathcal{N}_h|} \in \mathbb{R}^{|\mathcal{N}_h|\times 1}, \tag{4.59}$$

and $\mathbf{M}_0$, $\bar{\mathbf{u}}_0$ are formed by the first $|\mathring{\mathcal{N}}_h|$ rows of $\mathbf{M}$ and $\bar{\mathbf{u}}$, respectively. Formulas above confirm that the computations for $\frac{\partial \mathcal{J}_h}{\partial \mathbf{u}_h^k}, \nabla J_h, \frac{\partial J_h}{\partial \alpha_j}$ and J_h itself are problem dependent but they are usually straightforward to calculate within the IFE framework. These preparations can then be utilized in the proposed IFE-based Shape Optimization Algorithm presented in Subsection 4.4.4.

Cases	β	Interface S and initial guess	Data $\bar{u}$
Case 1	$\beta^- = 1$ $\beta^+ = 20$	$S = (x^2+y^2)^2(1+0.8\sin(6\arctan(y/x))) - 0.1$ $S_0 = (x+0.6)^2 + (y+0.2)^2 - (\pi/9)^2$	$\bar{u} = S/\beta^s$ in Ω^s $s = \pm$
Case 2	$\beta^1 = 1 \quad \beta^2 = 10$ $\beta^3 = 100$	$S = 4\sin(\pi x)\cos(\pi y + \pi/2) - 2$ $S_0^1 = 64x^2 + 144(y+0.5)^2 - \pi^2$ $S_0^2 = 64x^2 + 144(y-0.5)^2 - \pi^2$	$\bar{u} = S/\beta^i$ in Ω^i $i = 1,2,3$
Case 3	$\beta^- = 1$ $\beta^+ = 10$ or 1000	$S = r - 1$, where $r = (16x^2 + 64(y-0.4)^2)/\pi^2$ $S_0 = (x-0.4)^2 + (y-0.2)^2 - (\pi/6.28)^2$	$\bar{u} = \frac{1024}{\pi^4\beta^s}(r^{\frac{5}{2}} - 1)$ $+ \frac{1024}{\pi^4\beta^-}$ in Ω_0^s, $s = \pm$.

Table 4.1: Configuration for the Output-Least-Squares Problem

We now present three specific cases for this interface inverse/design problem whose key data are described in Table 4.1. In this table, $S(x,y) = 0$ is the target curve Γ to be recovered that is plotted as a dotted curve (in red color) in the related figures. We use the BFGS optimization algorithm [163] in step 6 of the IFE-based Shape Optimization Algorithm presented in Section 4.5, for which, $S_0(x,y) = 0$ is the initial curve that is plotted as a solid curve (in blue color) in the first plot of related figures as all other presented approximate

curves in shape optimization by the BFGS iterations.

Case 1: The data $\bar{u}(X)$ is given on the whole Ω, i.e., $\Omega_0 = \Omega$. The numerical curve is a parametric cubic spline with 20 control points, and the target curve has a star shape representing a certain complexity in the convexity. Some approximate curves generated in the BFGS iterations are presented in Figure 4.4 from which we can see a quick evolution of the numerical curve towards to the target curve with a complicated geometry for this inverse/design problem.

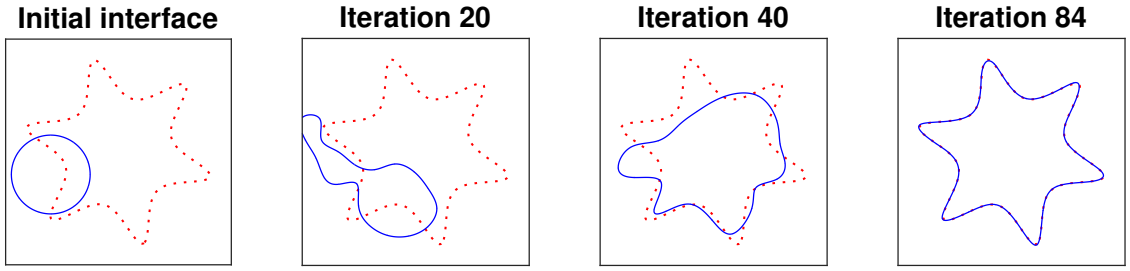

Figure 4.4: Reconstruction process for case 1 with interior data

Case 2: We demonstrate how the proposed algorithm can handle an interface inverse/design problem whose target interface consists of multiple components. For this purpose and for simplicity, we consider the case in which the interface Γ consists of two simple curves. We denote the sub-domain inside the upper-left dotted curve (in red color) by Ω^1, the sub-domain inside the lower-right dotted curve (in red color) by Ω^2, and denote the sub-domain outside these two closed dotted curves by Ω^3, see Figure 4.5, and the corresponding parameter is given by β^i, $i = 1, 2, 3$. Each numerical curve component is a parametric cubic spline with 15 control points and 30 control points in total. We notice that the numerical curve component started from S_0^1 converges to the exact curve component much faster than that started from S_0^2. We believe the objective function is more sensitive to the design variables for the first numerical curve component than the second because the jump β^3/β^1 is much larger than β^3/β^2 in this example, and the gradient in the proposed algorithm seems to be capable to capture this kind of subtle dependence of the objective function on the design variables.

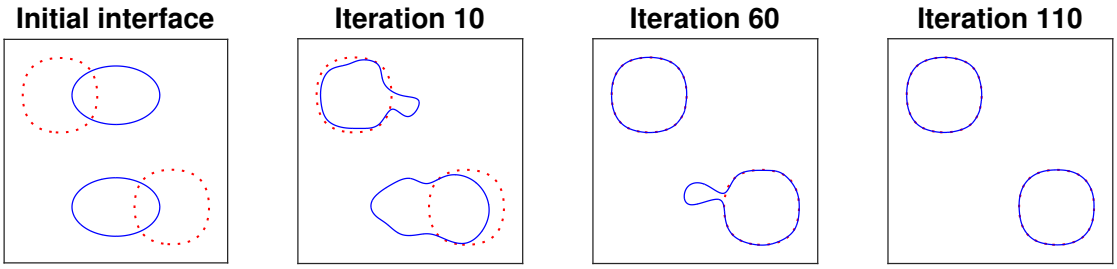

Figure 4.5: Reconstruction process for case 2 with interior data

Case 3: The data function $\bar{u}$ is given on a proper sub-domain $\Omega_0 = [-0.5, 1] \times [0, 1]$ in the upper-right of Ω illustrated in Figure 4.6. In Figure 4.6, we observe that the converged numerical curve is a much better approximation to the target interface curve Γ inside Ω_0 than outside, and we believe this is a reasonable consequence of the available data function $\bar{u}$ given only on Ω_0. In addition, we also test this example with a larger jump case, i.e., β^-=1, $\beta^+ = 1000$. The numerical results are presented in Figure 4.7 which also shows a better reconstruction.

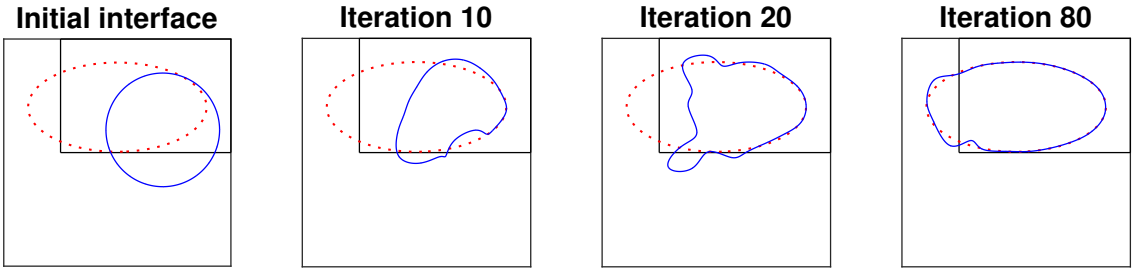

Figure 4.6: Reconstruction process for case 3 with interior data and $\beta^- = 1$, $\beta^+ = 10$

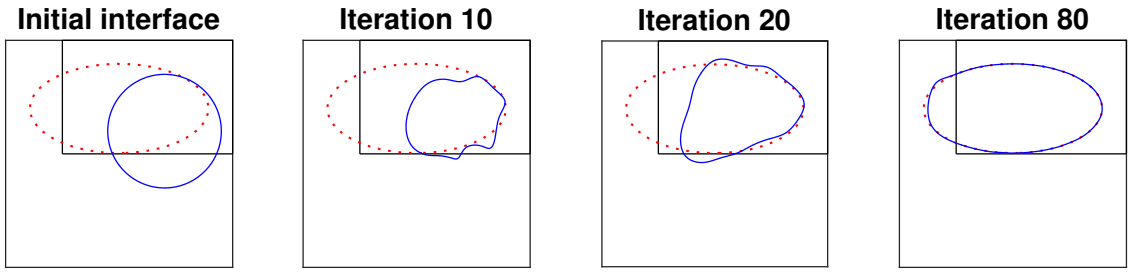

Figure 4.7: Reconstruction process for case 3 with interior data and $\beta^- = 1$, $\beta^+ = 1000$

4.6.2 The Dirichlet-Neumann Problem with a Single Measurement

In this group of numerical examples, we apply the proposed IFE-based shape optimization algorithm to the well-known and challenging Dirichlet-Neumann inverse problem in which we try to recover the interface Γ from a single pair of Dirichlet-Neumann data, i.e., g_D and g_N, provided on the boundary for an interface forward problem of the elliptic equation described by (4.1)-(4.2). This type of inverse problems has a wide range of applications in electronic impedance tomography (EIT) [27, 110, 154] where one wishes to detect a material interface by injecting the voltage potential g_D on $\partial\Omega$ and measuring the current density g_N on (or a portion of) $\partial\Omega$. When the charge source $f = 0$, it is referred as the Calderón's inverse conductivity problem [38] which is well-known ill-conditioned since only the data on the boundary $\partial\Omega$ is available for the reconstruction of Γ.

This problem relates to the so called Dirichlet-to-Neumann operator $\Lambda_\beta : H^{\frac{1}{2}}(\partial\Omega) \rightarrow H^{-\frac{1}{2}}(\partial\Omega)$ with

$$\Lambda_\beta : u|_{\partial\Omega} \rightarrow \frac{\partial u}{\partial \mathbf{n}}|_{\partial\Omega}, \tag{4.60}$$

where u satisfies the elliptic equation with the coefficient β. In [127], Kohn and Vogelius proved that the operator (4.60) can uniquely determine the piecewise analytical coefficients β. Then the analyticity assumption was weakened by a series of articles [159, 189]. Recently, the authors in [17] proved the uniqueness by only assuming $\beta^s \in L^\infty(\Omega^s)$, $s = \pm$ and bounded away from zero and infinity. If β is assumed to be piecewise C^2 functions and only the coefficient β^- of the inclusion Ω^- is unknown, the uniqueness of Γ and β^+ can be also guaranteed from the operator (4.60) [115]. Besides, a more challenging problem is to recover the interface and coefficients β as piecewise constants in general from only a single pair of Dirichlet-Neumann measurement. However there are no complete solutions to the issue of uniqueness in this case. When the coefficients β are known, the global uniqueness can only be obtained for several classes of the inclusion Ω^-, such as the convex cylinders, unions of discs in [114], and convex polyhedrons in [24]. But if β^- is also an unknown, even a two or three dimensional ball may not be identified uniquely by one single measurement [125].

Here we consider the construction of the interface by a single pair of Dirichlet-Neumann measurement and assuming $\beta^\pm$ are known. In particular, we formulate this inverse problem as a shape optimization problem with a Kohn-Vogelius type functional [27, 128, 164]:

$$\mathcal{J}(\Gamma) = \int_\Omega (u^1 - u^2)^2 dX, \tag{4.61}$$

where u^1 and u^2 are the solutions of the following interface forward problems:

$$\begin{cases} -\nabla\cdot(\beta\nabla u^1) = f, \\ [u^1]|_\Gamma = 0, \\ [\beta\nabla u^1\cdot\mathbf{n}]|_\Gamma = 0, \\ u^1 = g_D^1 = g_D, \quad \text{on } \partial\Omega, \end{cases} \qquad \begin{cases} -\nabla\cdot(\beta\nabla u^2) = f, \\ [u^2]|_\Gamma = 0, \\ [\beta\nabla u^2\cdot\mathbf{n}]|_\Gamma = 0, \\ u^2 = g_D^2 = g_D, \quad \text{on } \partial\Omega_D, \quad \frac{\partial u^2}{\partial\mathbf{n}} = g_N^2, \quad \text{on } \partial\Omega_N, \end{cases}$$

and $\int_\Omega u^2 dx = u_0$ needs to be imposed when $\partial\Omega_N = \partial\Omega$. With the IFE-based Shape Optimization Algorithm, we solve this interface inverse problem by seeking the design variable $\boldsymbol{\alpha}^*$ from the following constrained optimization problem:

$$\begin{aligned} \boldsymbol{\alpha}^* = \text{argmin } \mathcal{J}_h(\boldsymbol{\alpha}), \qquad & \mathcal{J}_h(\boldsymbol{\alpha}) = \int_{\Omega_0} J_h(\mathbf{u}_h^1(\boldsymbol{\alpha}), \mathbf{u}_h^2(\boldsymbol{\alpha}), X(\boldsymbol{\alpha}), \boldsymbol{\alpha}) dX, \\ \text{subject to} \qquad & \mathbf{A}^k(\boldsymbol{\alpha})\mathbf{u}_h^k(\boldsymbol{\alpha}) - \mathbf{F}^k(\boldsymbol{\alpha}) = \mathbf{0}, \quad k = 1, 2, \end{aligned} \tag{4.62}$$

where $J_h(\mathbf{u}_h^1(\boldsymbol{\alpha}), \mathbf{u}_h^2(\boldsymbol{\alpha}), X(\boldsymbol{\alpha}), \boldsymbol{\alpha}) = \left(\tilde{J}_h(\mathbf{u}_h^1(\boldsymbol{\alpha}), \mathbf{u}_h^2(\boldsymbol{\alpha}), X(\boldsymbol{\alpha}), \boldsymbol{\alpha})\right)^2$ with

$$\begin{aligned} & \tilde{J}_h(\mathbf{u}_h^1(\boldsymbol{\alpha}), \mathbf{u}_h^2(\boldsymbol{\alpha}), X(\boldsymbol{\alpha}), \boldsymbol{\alpha}) \\ = \quad & \sum_{i=1}^{|\mathring{\mathcal{N}}_h|} u_i^1 \varphi_i(X(\boldsymbol{\alpha}), \boldsymbol{\alpha}) + \sum_{i=|\mathring{\mathcal{N}}_h|+1}^{|\mathcal{N}_h|} g_D^1(X_i)\varphi_i(X(\boldsymbol{\alpha}), \boldsymbol{\alpha}) \\ & - \sum_{i=1}^{|\mathcal{N}_h^M|} u_i^2 \varphi_i(X(\boldsymbol{\alpha}), \boldsymbol{\alpha}) - \sum_{i=|\mathcal{N}_h^M|+1}^{|\mathcal{N}_h|} g_D^2(X_i)\varphi_i(X(\boldsymbol{\alpha}), \boldsymbol{\alpha}). \end{aligned} \tag{4.63}$$

Again, we note that the discrete objective function $\mathcal{J}_h(\mathbf{u}_h^1(\boldsymbol{\alpha}), \mathbf{u}_h^2(\boldsymbol{\alpha}), \boldsymbol{\alpha})$ approximates the objective functional $\mathcal{J}(\Gamma(\boldsymbol{\alpha}))$ with an optimal second order independent of interface location and shape, and this objective function can be evaluated quickly by matrix-vector operations as follows:

$$\mathcal{J}_h(\mathbf{u}_h^1(\boldsymbol{\alpha}), \mathbf{u}_h^2(\boldsymbol{\alpha}), \boldsymbol{\alpha}) = \left[\begin{pmatrix} \mathbf{u}_h^1 \\ \mathbf{g}_D^1 \end{pmatrix} - \begin{pmatrix} \mathbf{u}_h^2 \\ \mathbf{g}_D^2 \end{pmatrix}\right]^T \mathbf{M} \left[\begin{pmatrix} \mathbf{u}_h^1 \\ \mathbf{g}_D^1 \end{pmatrix} - \begin{pmatrix} \mathbf{u}_h^2 \\ \mathbf{g}_D^2 \end{pmatrix}\right], \tag{4.64}$$

where $\mathbf{g}_D^1 = (g_D(X_i))_{i=|\mathring{\mathcal{N}}_h|+1}^{|\mathcal{N}_h|}$, $\mathbf{g}_D^2 = (g_D(X_i))_{i=|\mathcal{N}_h^M|+1}^{|\mathcal{N}|_h}$, and $\mathbf{M}$ is the global mass matrix on the whole domain Ω:

$$\mathbf{M} = \left(\int_\Omega \phi_i\phi_j dX\right)_{i=1,j=1}^{|\mathcal{N}_h|,|\mathcal{N}_h|}. \tag{4.65}$$

Also, formulas similar to those in (4.56) can be easily derived to compute $\frac{\partial J_h}{\partial X}$ and $\frac{\partial J_h}{\partial \alpha_j}, j \in \mathcal{D}$. Furthermore, by direct calculations, we have

$$\frac{\partial \mathcal{J}_h}{\partial \mathbf{u}_h^1} = 2\mathbf{M}_1 \left[\begin{pmatrix} \mathbf{u}_h^1 \\ \mathbf{g}_D^1 \end{pmatrix} - \begin{pmatrix} \mathbf{u}_h^2 \\ \mathbf{g}_D^2 \end{pmatrix}\right], \quad \text{and} \quad \frac{\partial \mathcal{J}_h}{\partial \mathbf{u}_h^2} = 2\mathbf{M}_2 \left[\begin{pmatrix} \mathbf{u}_h^2 \\ \mathbf{g}_D^2 \end{pmatrix} - \begin{pmatrix} \mathbf{u}_h^1 \\ \mathbf{g}_D^1 \end{pmatrix}\right], \tag{4.66}$$

where $\mathbf{M}_1$ and $\mathbf{M}_2$ are the mass matrices formed by the first $|\mathring{\mathcal{N}}_h|$ and $|\mathcal{N}_h^M|$ rows of $\mathbf{M}$, respectively. These derivations together confirm again that formulas for J_h, ∇J_h, $\frac{\partial J_h}{\partial \alpha_j}, j \in \mathcal{D}$ as well as $\frac{\partial \mathcal{J}_h}{\partial \mathbf{u}_h^k}, k = 1, 2$ in general can be easily derived explicitly and efficiently implemented in the IFE framework. These preparations can then be used in the proposed IFE-based Shape Optimization Algorithm presented in Section 4.5.

For the Dirichlet-Neumann inverse problem, we report 3 experiments that are configured with the target curve $S(x, y) = 0$ and one of the exact solutions $u(X)$ given in Table 4.2 corresponding to the interface $S(x, y) = 0$ for the interface forward problem. We emphasize that $u(X)$ given in the third column of this table is used only to generate the Dirichlet and Neumann boundary data, i.e., g_D and g_N on $\partial\Omega$, for the related inverse problem. As before, the BFGS algorithm [163] is employed to carry out the shape optimization described by (4.62) according to the proposed IFE-based Shape Optimization Algorithm. In Table 4.2, $S_0(x, y) = 0$ is the initial curve that is plotted as a solid curve (in blue color) in the related figures as all other presented approximate curves in the BFGS iterations and the dotted curve (in red color) is the target curve to be recovered.

Cases	β	Interface S and initial guess	Exact u
Case 1	$\beta^- = 1$ $\beta^+ = 10$	$S = r - 1$, where $r = (100(x - 0.4)^2 + 36(y + 0.3)^2)/\pi^2$ $S_0 = (x - 0.1)^2 + y^2 - (\pi/4)^2$	$u = \frac{3600}{\pi^4 \beta^s}(r^{\frac{5}{2}} - 1)$ $+ \frac{3600}{\pi^4 \beta^-}$ in Ω^s $s = \pm$
Case 2	$\beta^- = 1$ $\beta^+ = 2$	$S = (2((x + 0.5)^2 + y^2) - x - 0.2)^2 - ((x + 0.5)^2 + y^2) + 0.3$ $S_0 = 64(x - 0.5)^2 + 16y^2 - \pi^2$	$u = S/\beta^s$ in Ω^s, $s = \pm$
Case 3	$\beta^- = 1$, $\beta^+ = 2$	$S = \sin(\pi x) + \frac{\pi}{1.5} y + 0.1$ $S_0 = y + 0.15/\pi$	$u = S/\beta^s$ in Ω^s, $s = \pm$

Table 4.2: Configuration for the Dirichlet-Neumann Problem

Case 1: The Neumann data is given on the whole $\partial\Omega$, and the numerical curve is a parametric cubic spline with 20 control points. These numerical results demonstrate that the proposed IFE method can handle a large shape change, as illustrated in Figure 4.8 from the initial interface to the one generated by the third iteration. We note that such a large shape change often causes mesh distortion when body fitting mesh is used, but the proposed IFE method circumvents this issue by using an unfitted mesh. The numerical curve quickly converges to the target curve after about 80 iterations.

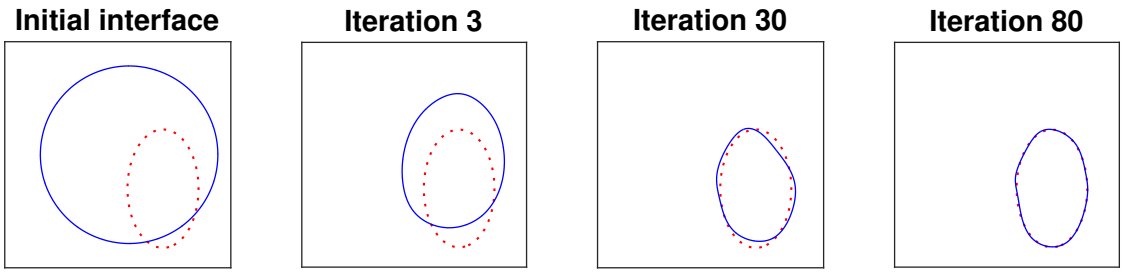

Figure 4.8: Reconstruction process for case 1 with boundary data

Case 2: We now consider a more difficult Dirichlet-Neumann interface inverse problem whose exact solution interface curve Γ has a non-conical and non-convex kidney-like shape, and, to the best of our knowledge, there is no general theory to guarantee the uniqueness of the solution to this inverse problem with only a single pair of Dirichelt and Neumann data given on the whole $\partial\Omega$. The numerical curve is a parametric cubic spline with 20 control points. We note this example takes far more iterations to converge and we believe this is caused by the challenging nature of this interface inverse problem whose exact solution is non-convex; nevertheless, the proposed IFE method still produces an approximate solution quite satisfactory. Furthermore, it is interesting to note that the portion of the target interface curve close to the center of the domain is more difficult to retrieve than the portion near the boundary. In our extensive numerical experiments, we have also observed such a phenomenon. This is a well-known issue due to the ill-conditioning nature of the considered inverse problems which has already been observed in the literature through different methods [121] that the portion of the target curve in the center of the domain is much harder to recover by the boundary data.

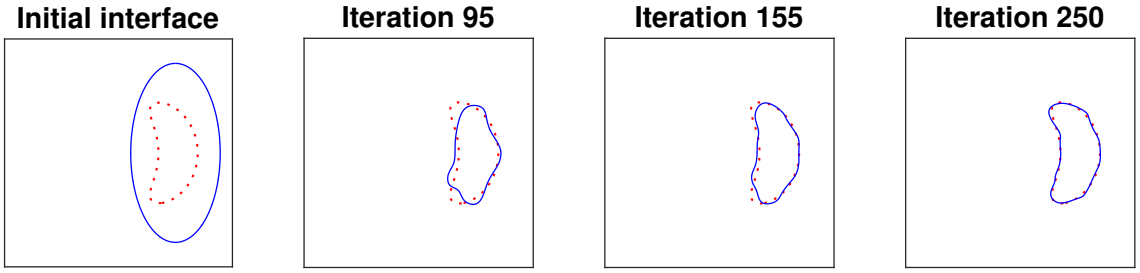

Figure 4.9: Reconstruction process for case 2 with boundary data

Case 3: In this case, the Neumann data is provided only on a proper subset of the boundary $\partial\Omega$. Specifically, the true interface Γ is the level set $S(x, y) = 0$ plotted as the dotted curve (in red color) in Figure 4.10 that partitions Ω into two sub-domains Ω^- and Ω^+ below and above Γ, and the Neumann data function g_N is given only on the lower and upper edges of the square domain Ω. The numerical interface is a 1-D cubic spline $y = y(t)$, $t \in [-1, 1]$ with 10

control points whose end points match the exact interface. The last plot in Figure 4.10 shows that the numerical curve after 140 iterations matches the exact curve well. This demonstrates that the proposed IFE method can handle a Dirichlet-Naumann interface inverse problem that has a limited Neumann data measured on part of the boundary of Ω. We also test the case in which the Neumann data is on the left and right boundary of Ω instead of the lower and upper boundary, but the result is not as satisfactory as the one presented here.

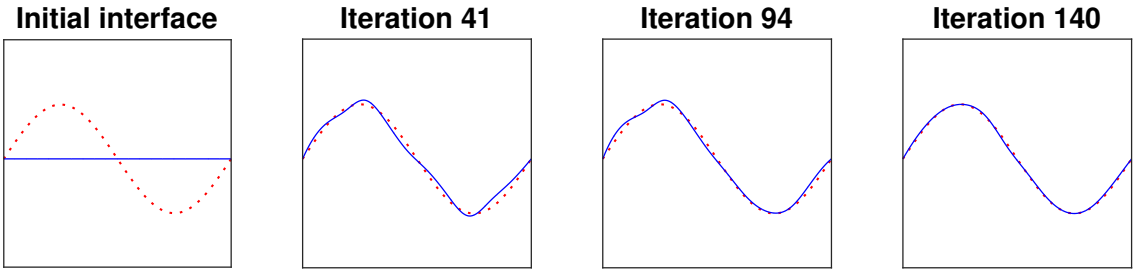

Figure 4.10: Reconstruction process for case 3 with boundary data

4.6.3 The Heat Dissipation Problem

We now consider the application of the proposed IFE method to an optimal design problem for a heat system in which the goal is to minimize the overall heat dissipation by optimally distributing two materials in a domain [69, 71, 210]. This thermal design problem has wide applications such as cooling fins [18, 178] and high-conductivity channel of electronic components [26].

In the steady heat conduction situation, this design problem is to find an optimal curve Γ^* separating two chosen materials that can minimize the following objective functional [69]:

$$\mathcal{J}(\Gamma) = \int_\Omega \nabla u^1 \cdot (\beta \nabla u^1) dX \quad \text{subject to} \quad |\Omega^-| \leqslant \theta |\Omega|, \tag{4.67}$$

where u^1 is the solution to the interface problem described by (4.1)-(4.2) with $K = 1$ and a Dirichlet boundary condition, Ω^- is the sub-domain filled with the high conductivity material, and $\theta \in (0, 1)$ is a prescribed design parameter. By the proposed IFE method (4.22), we seek a design variable $\boldsymbol{\alpha}^*$ by solving the following constrained optimization problem:

$$\begin{aligned} \boldsymbol{\alpha}^* = \operatorname{argmin} \mathcal{J}_h(\boldsymbol{\alpha}), \qquad & \mathcal{J}_h(\boldsymbol{\alpha}) = \int_{\Omega_0} J_h(\mathbf{u}_h^1(\boldsymbol{\alpha}), X(\boldsymbol{\alpha}), \boldsymbol{\alpha}) dX, \\ \text{subject to} \qquad & \mathbf{A}^1(\boldsymbol{\alpha}) \mathbf{u}_h^1(\alpha) - \mathbf{F}^1(\boldsymbol{\alpha}) = \mathbf{0} \ \text{ and } \ |\Omega^-| \leqslant \theta |\Omega|, \end{aligned} \tag{4.68}$$

where

$$J_h(\mathbf{u}_h^1(\boldsymbol{\alpha}), X(\boldsymbol{\alpha}), \boldsymbol{\alpha}) = \beta \left| \sum_{i=1}^{|\mathring{\mathcal{N}}_h|} u_i^1 \nabla \varphi_i(X(\boldsymbol{\alpha}), \boldsymbol{\alpha}) + \sum_{i=|\mathring{\mathcal{N}}_h|+1}^{|\mathcal{N}_h|} g_D(X_i) \nabla \varphi_i(X(\boldsymbol{\alpha}), \boldsymbol{\alpha}) \right|^2. \tag{4.69}$$

It is easy to show that the discrete objective function can approximate the true shape functional (4.67) with an optimal first order accuracy independent of the interface shape and location. Also, similar to (4.56)-(4.59) again, formulas can be easily derived for $\mathcal{J}_h(\boldsymbol{\alpha})$, $\frac{\partial J_h}{\partial \alpha_j}, j \in \mathcal{D}$ and $\frac{\partial \mathcal{J}_h}{\partial \mathbf{u}_h^1}$ that can be implemented efficiently within the IFE framework. In particular, we have $\nabla J_h = \mathbf{0}$, and

$$\mathcal{J}_h(\mathbf{u}_h^1(\boldsymbol{\alpha}), \boldsymbol{\alpha}) = \begin{pmatrix} \mathbf{u}_h^1 \\ \mathbf{g}_D \end{pmatrix}^T \mathbf{K} \begin{pmatrix} \mathbf{u}_h^1 \\ \mathbf{g}_D \end{pmatrix} \tag{4.70}$$

where

$$\mathbf{K} = \begin{pmatrix} \mathbf{K}_{11} & \mathbf{K}_{12} \\ \mathbf{K}_{12} & \mathbf{K}_{22} \end{pmatrix} \in \mathbb{R}^{|\mathcal{N}_h| \times |\mathcal{N}_h|} \tag{4.71}$$

is the global stiffness matrix in block form according to the vector partition in (4.70). Since $\varphi_i, 1 \le i \le |\mathcal{N}_h|$ are linear IFE basis functions, and a formula similar to the one in (4.56) can be easily derived to compute $\frac{\partial J_h}{\partial \alpha_j}, j \in \mathcal{D}$. Furthermore, by direct calculations, we have

$$\frac{\partial \mathcal{J}_h}{\partial \mathbf{u}_h^1} = \mathbf{K}_{11}\mathbf{u}_h^1 + \mathbf{K}_{12}\mathbf{g}_D. \tag{4.72}$$

These preparations can then be employed in the proposed IFE-based Shape Optimization Algorithm together with the SQP (sequential quadratic programming) method [163] to carry out the constrained optimization numerically.

We test the proposed IFE method on a specific design problem configured in the domain Ω that contains a design independent heat source $f = -1$ on a center square $[-0.1, 0.1] \times [-0.1, 0.1]$, and the boundary temperature is fixed to be $u = 0$ and $\theta = 0.5$, see the illustration in Figure 4.11. The two materials separated by the curve Γ are such that $\beta^- = 1$ and $\beta^+ = 10^{-3}$. We start the SQP iteration from a circle $x^2 + y^2 = 0.82^2$ plotted as a solid curve (in blue color) in Figure 4.11(a), and the numerical curve in the optimization is a parametric cubic spline with 20 control points. After 28 iterations, the algorithm generates a design shown in Figure 4.11(b) whose patten is very similar to the one reported in [69].

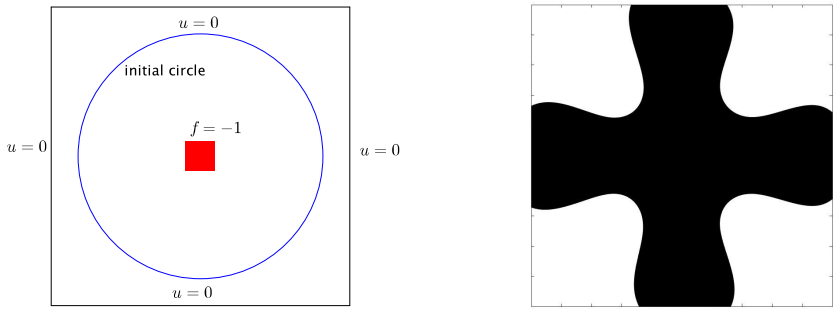

(a) The heating conditions and initial guess

(b) The optimal design

Figure 4.11: The heat dissipation problem

4.7 Some Conclusions on Numerical Experiments

First of all, for solving the interface forward problems in each iteration, our numerical experience demonstrate that the IFE method is robust with respect to how interface cuts elements, i.e., there is no ill-conditioning issue when some interface elements contain small sub-elements because the two polynomial components in every IFE function are constructed collectively capturing the jump conditions and behaving close to a standard polynomial. This important property for moving interface problems follows from the analysis in [148].

In addition, in our numerical experiments, we have observed that the proposed algorithm can produce a reasonably good reconstruction within a relatively small number of iterations. We believe this is the consequence of two main features in the proposed algorithm. Firstly, in this IFE-Based Shape Optimization Algorithm, the involved forward problems and the objective functional are discretized optimally by the IFE method, and the formula for the discrete gradient is not only derived explicitly but also can be implemented in the IFE framework without any further approximation. All these computations are executed on an unfitted mesh independent of the interface movement which circumvents extra errors induced by the mesh movement process and the related velocity computation. Secondly, the proposed algorithm actually searches the interface curve to be recovered in a small space, for instance, 20 control points are used in the numerical curve for the presented examples which lead to a 40-dimensional searching space. Besides, extensive numerical experiments suggest that the numerical interface curve converges diffeomorphically to the target interface curve in the shape optimization. All these features suggest our algorithm searches the target interface in a small set which can quickly locate the target interface. As mentioned in Section 4.3, this feature can be considered as a regularization mechanism "hidden" in the proposed algorithm to enhance its robustness. Shape optimization methods with similar regularization features can be found in [59, 96, 107, 166, 167]. This is in contrast to the explicit regularization methods, such as the geometric regularization [117], total variation regularization [53], and the Tikhonov regularization [120] in level-set type methods for some inverse problems [44, 53, 95, 117, 177] which search for the interface in a much larger space.

Finally, it is interesting to mention that the Kohn-Vogelius type functional (4.61) is used for shape optimization when there is only boundary data available for reconstruction rather than a least squares functional imposed on the boundary. We make this choice because the boundary integration of finite element solutions will lose order in general. Indeed, according to our numerical experience, we have the impression that in the proposed algorithm the Kohn-Vogelius type functional in general can produce a better result for data only available on boundary. We also think this may be due to the self-regularizing features of this type functional as mentioned in [98]. However, we note that, in order to use the Kohn-Vogelius type functional (4.61), we need to solve two interface problems for each iteration and each pair of Dirichlet-Neumann data.

Chapter 5

Conclusions

In this dissertation, we have discussed the design, analysis, and application of IFE methods on two types of interface problems and the related inverse problems. In this chapter, we summarize our main contributions in this dissertation and make some conclusions.

In Chapter 2, we have extended the current IFE framework in the literature [79, 85, 148] from the scalar elliptic interface problems to the elasticity interface problems with a vector unknown. In particular, we have proposed a new construction approach such that the bilinear and rotated Q_1 vector IFE functions can be uniquely determined by their nodal values at element vertices. This result improves those in [153] in which the existence of IFE functions can only be guaranteed conditionally. We have extended the multipoint Taylor expansions from scalar functions to vector functions, by which, we have proved the optimal approximation capabilities of the proposed vector IFE spaces through the Lagrange type interpolation operator. Furthermore, we have proposed a PPIFE method for solving the elasticity interface problems with these vector IFE spaces. We have established the trace inequalities for the vector IFE functions which are further used to analyze the stability of the proposed PPIFE scheme. Finally, we have proved the optimal convergence of the PPIFE solutions. This chapter is the first work to analyze IFE methods for elasticity interface problems.

In Chapter 3, we have proposed the first systematic framework for arbitrary p-th degree IFE methods to solve elliptic interface problem including both the construction and analysis. We have constructed IFE functions by solving local Cauchy problems on interface elements, and this procedure yields the so called Cauchy mapping. In this framework, various key results in the analysis can be traced back to some properties of this Cauchy mapping. In particular, we have shown that the existence of IFE functions is universally guaranteed regardless of interface element configuration, and the proof simply reduces to showing the bijectivity of the Cauchy mapping on polynomial spaces. This approach completely avoids the tedious discussion used in the literature for the lower-degree IFE methods based on different polynomial spaces and interface element configuration. In addition, we have proved the optimal approximation capabilities of the proposed IFE spaces through a new interpolation operator based

on Sobolev extension, projections, and the Cauchy mapping illustrated by the Diagram in Figure 3.9. This is rather different from the Lagrange interpolation used in the literature for the lower-degree IFE methods and avoids the complicated derivation of multipoint Taylor expansions. We have also established the trace inequalities for the proposed IFE functions, and the argument is based on the stability of the Cauchy mapping in terms of the semi-H^1 norm. This technique also circumvents the tedious direct calculus employed in the literature for the lower-degree IFE functions. All these analysis techniques are applicable for IFE functions with arbitrary polynomial degree p. Using these results, we have proved the optimal convergence of DGIFE solutions based on the proposed IFE space. By this method, we have achieved what the conventional construction/analysis techniques in the literature for macro polynomials cannot offer, and we believe it may be useful for other finite element methods based on unfitted meshes.

In Chapter 4, we have developed an IFE-based shape optimization algorithm to solve a group of interface inverse and optimal design problems on unfitted meshes. In this algorithm, we parameterize the interface curve by a cubic spline and use the coordinates of control points as the design variables for optimization. This parameterization, we believe, also acts as a geometric regularization mechanism to reduce the searching space. Besides, we have discretized both the interface forward problems and shape dependent functionals optimally by a linear IFE method on unfitted meshes. In addition, we have derived exact formulas to calculate the velocity field and shape derivatives of IFE shape functions which are further used to calculate the shape sensitivities of the discretized shape functions accurately through a discretized adjoint method. The computation of the shape sensitivities is efficient in the sense that almost all the computations are only performed on interface elements. All these properties enable the proposed algorithm to reconstruct the target interface curve quickly and satisfactorily as illustrated by numerical examples presented in Section 4.6.

Bibliography

[1] Amel B. Abda, Hend B. Ameur, and Mohamed Jaoua. Identification of 2D cracks by elastic boundary measurements. *Inverse Problems*, 15:67, 1999.

[2] R. A. (Robert Alexander) Adams and John J. F. Fournier. *Sobolev spaces*, volume 140. London, Amsterdam, 2003.

[3] Slimane Adjerid, Mohamed Ben-Romdhane, and Tao Lin. Higher degree immersed finite element methods for second-order elliptic interface problems. *Int. J. Numer. Anal. Model.*, 11(3):541–566, 2014.

[4] Slimane Adjerid, Mohamed Ben-Romdhane, and Tao Lin. Higher-order immersed finite element spaces for second-order elliptic interface problems with quadratic interface. *Adv. Appl. Math.*, 87, 2014.

[5] Slimane Adjerid, Mohamed Ben-Romdhane, and Tao Lin. Higher degree immersed finite element spaces constructed according to the actual interface. *Comput. Math. Appl.*, 75(6):1868–1881, 2018.

[6] Slimane Adjerid, Nabil Chaabane, and Tao Lin. An immersed discontinuous finite element method for stokes interface problems. *Comput. Methods Appl. Mech. Engrg.*, 293:170–190, 2015. in press.

[7] Slimane Adjerid, Nabil Chaabane, Tao Lin, and Pengtao Yue. An immersed discontinuous finite element method for the stokes problem with a moving interface. *Journal of Computational and Applied Mathematics*, 2018.

[8] Slimane Adjerid, Ruchi Guo, and Tao Lin. High degree immersed finite element spaces by a least squares method. *Int. J. Numer. Anal. Model.*, 14:604–626, 2016.

[9] Slimane Adjerid and Tao Lin. A p-th degree immersed finite element for boundary value problems with discontinuous coefficients. *Appl. Numer. Math.*, 59(6):1303–1321, 2009.

[10] Lekbir Afraites, Marc Dambrine, and Djalil Kateb. Shape methods for the transmission problem with a single measurement. *Numerical Functional Analysis and Optimization*, 28(5-6):519–551, 2007.

[11] J. P. Agnelli, A. De Cezaro, A. Leitão, and M. Marques Alves. On the identification of piecewise constant coefficients in optical diffusion tomography by level set. *ESAIM: Control, Optimisation and Calculus of Variations*, 23(2):663–683, 2017.

[12] G. Alessandrini, V. Isakov, and J. Powell. Local uniqueness in the inverse conductivity problem with one measurement. *Transactions of the American Mathematical Society*, 347(8):3031–3041, 1995.

[13] G. Allaire, C. Dapogny, and P. Frey. Shape optimization with a level set based mesh evolution method. *Comput. Methods Appl. Mech. Engrg.*, 282:22–53, 2014.

[14] Carlos J. S. Alves and Tuong Ha-Duong. Inverse scattering for elastic plane cracks. *Inverse Problems*, 15:91, 1999.

[15] Hend B. Ameur, Martin Burger, and Benjamin Hackl. Level set methods for geometric inverse problems in linear elasticity. *Inverse Problems*, 20(3):673–696, 2004.

[16] Luca Antiga, Joaquim Peiró, and David A. Steinman. *From image data to computational domains*, pages 123–175. Springer Milan, Milano, 2009.

[17] Kari Astala and Lassi Päivärinta. Calderón's inverse conductivity problem in the plane. *Annals of Mathematics*, 163(1):265–299, 2006.

[18] A. V. Attetkov, I. K. Volkov, and E. S. Tverskaya. The optimum thickness of a cooled coated wall exposed to local pulse-periodic heating. *J. Eng. Phys. Thermophys.*, 74(6):1467–1474, 2001.

[19] I. Babuška and J. E. Osborn. Generalized finite element methods: their performance and their relation to mixed methods. *SIAM J. Numer. Anal.*, 20(3):510–536, 1983.

[20] Ivo Babuška. The finite element method for elliptic equations with discontinuous coefficients. *Computing (Arch. Elektron. Rechnen)*, 5:207–213, 1970.

[21] Ivo Babuška, Gabriel Caloz, and John E. Osborn. Special finite element methods for a class of second order elliptic problems with rough coefficients. *SIAM J. Numer. Anal.*, 31(4):945–981, 1994.

[22] Ivo Babuška and John E. Osborn. Can a finite element method perform arbitrarily badly? *Math. Comp.*, 69(230):443–462, 2000.

[23] Robert Banasiak and Manuchehr Soleimani. Shape based reconstruction of experimental data in 3D electrical capacitance tomography. *NDT and E International*, 43(3):241–249, 2010.

[24] Bartolomé Barceló, Eugene Fabes, and Jin K. Seo. The inverse conductivity problem with one measurement: Uniqueness for convex polyhedra. *Proceedings of the American Mathematical Society*, 122(1):183–189, 1994.

[25] Roland Becker, Erik Burman, and Peter Hansbo. A Nitsche extended finite element method for incompressible elasticity with discontinuous modulus of elasticity. *Comput. Methods Appl. Mech. Engrg.*, 198(41-44):3352–3360, 2009.

[26] Adrian Bejan. Constructal-theory network of conducting paths for cooling a heat generating volume. *Int. J. Heat Mass Transfer*, 40(4):799,813–811,816, 1997.

[27] Z. Belhachmi and H. Meftahi. Shape sensitivity analysis for an interface problem via minimax differentiability. *Appl. Math. Comput.*, 219(12):6828, 2013.

[28] Martin P. Bendsøe. *Optimization of structural topology, shape, and material*. Springer-Verlag, Berlin, 1995.

[29] J. A. Bennett and M. E. Botkin. Structural shape optimization with geometric description and adaptive mesh refinement. *AIAA Journal*, 23(3):458–464, 1985.

[30] Elena Beretta, Stefano Micheletti, Simona Perotto, and Matteo Santacesaria. Reconstruction of a piecewise constant conductivity on a polygonal partition via shape optimization in EIT. *Journal of Computational Physics*, 353:264 – 280, 2018.

[31] Charles K. Birdsall and A. Bruce Langdon. *Plasma Physics via Computer Simulation (Series in Plasma Physics)*. Institute of Physisc Publishing, 1991.

[32] Pavel B. Bochev and Max D. Gunzburger. *Least-squares finite element methods*, volume 166. Springer, New York, 1. aufl. edition, 2009.

[33] Dietrich Braess. *Finite elements*. Cambridge University Press, Cambridge, second edition, 2001. Theory, fast solvers, and applications in solid mechanics, Translated from the 1992 German edition by Larry L. Schumaker.

[34] V. Braibant and C. Fleury. Shape optimal design using B-splines. *Computer Methods in Applied Mechanics and Engineering*, 44(3):247–267, 1984.

[35] Susanne C. Brenner and L. Ridgway Scott. *The mathematical theory of finite element methods*, volume 15 of *Texts in Applied Mathematics*. Springer, New York, third edition, 2008.

[36] Martin Burger. Levenberg-marquardt level set methods for inverse obstacle problems. *Inverse Problems*, 20(1):259–282, 2004.

[37] Martin Burger and Stanley J. Osher. A survey on level set methods for inverse problems and optimal design. *European J. Appl. Math.*, 16(2):263–301, 2005.

[38] Alberto P. Calderón. On an inverse boundary value problem. *Comput. Appl. Math*, 25(2-3), 2006.

[39] Brian Camp, Tao Lin, Yanping Lin, and Weiwei Sun. Quadratic immersed finite element spaces and their approximation capabilities. *Adv. Comput. Math.*, 24(1-4):81–112, 2006.

[40] Alejandro Cantarero and Tom Goldstein. A fast method for interface and parameter estimation in linear elliptic PDEs with piecewise constant coefficients. 2013.

[41] Waixiang Cao, Xu Zhang, and Zhimin Zhang. Superconvergence of immersed finite element methods for interface problems. *Advances in Computational Mathematics*, pages 1–27, 2017.

[42] S. Chaabane, M. Masmoudi, and H. Meftahi. Topological and shape gradient strategy for solving geometrical inverse problems. *Journal of Mathematical Analysis and Applications*, 400(2):724–742, 2013.

[43] Tony F. Chan and Xue-Cheng Tai. Identification of discontinuous coefficients in elliptic problems using total variation regularization. *SIAM J. Sci. Comput*, 25(3):881–904, 2003.

[44] Tony F. Chan and Xue-Cheng Tai. Level set and total variation regularization for elliptic inverse problems with discontinuous coefficients. *Journal of Computational Physics*, 193(1):40–66, 2004.

[45] Kuang-Hua Chang and Kyung K. Choi. A geometry-based parameterization method for shape design of elastic solids. *Mechanics of Structures and Machines*, 20(2):215–252, 1992.

[46] Long Chen, Huayi Wei, and Min Wen. An interface-fitted mesh generator and virtual element methods for elliptic interface problems. *Journal of Computational Physics*, 334(1):327–348, 2017.

[47] Zhiming Chen and Jun Zou. Finite element methods and their convergence for elliptic and parabolic interface problems. *Numer. Math.*, 79(2):175–202, 1998.

[48] Zhiming Chen and Jun Zou. An augmented lagrangian method for identifying discontinuous parameters in elliptic systems. *SIAM J. Control Optim.*, 37(3), 1999.

[49] Xue cheng Tai, Tony, F. Chan, and Communicated Yanping Lin. A survey on multiple level set methods with applications for identifying piecewise constant functions. *Int. J. Numer. Anal. Model*, 1:25–48, 2004.

[50] Kyung K. Choi and Kuang-Hua Chang. A study of design velocity field computation for shape optimal design. *Finite Elem. Anal. Des.*, 15(4):317–341, 1994.

[51] S. Chow and R. S. Anderssen. Determination of the transmissivity zonation using a linear functional strategy. *Inverse Problems*, 7:841, 1991.

[52] C.-C. Chu, I. G. Graham, and T.-Y. Hou. A new multiscale finite element method for high-contrast elliptic interface problems. *Math. Comp.*, 79(272):1915–1955, 2010.

[53] Eric T. Chung, Tony F. Chan, and Xue-Cheng Tai. Electrical impedance tomography using level set representation and total variational regularization. *Journal of Computational Physics*, 205(1):357–372, 2005.

[54] Eric T. Chung, Yalchin Efendiev, and Shubin Fu. Generalized multiscale finite element method for elasticity equations. *GEM Int. J. Geomath.*, 5(2):225–254, 2014.

[55] Philippe G. Ciarlet. *The finite element method for elliptic problems*. North-Holland Publishing Co., Amsterdam-New York-Oxford, 1978. Studies in Mathematics and its Applications, Vol. 4.

[56] Ray. W. Clough and James L. Tocher. Finite element stiffness matrices for analysis of plate bending. In *Matrix Methods in Structual Mechanics*, pages 515–545, 1966.

[57] Bernardo Cockburn, Dominik Schötzau, and Jing Wang. Discontinuous Galerkin methods for incompressible elastic materials. *Comput. Methods Appl. Mech. Engrg.*, 195(25-28):3184–3204, 2006.

[58] M. Crouzeix and P.-A. Raviart. Conforming and nonconforming finite element methods for solving the stationary Stokes equations. I. *Rev. Française Automat. Informat. Recherche Opérationnelle Sér. Rouge*, 7(R-3):33–75, 1973.

[59] Marc Dambrine and Djalil Kateb. Conformal mapping and inverse conductivity problem with one measurement. *ESAIM: Control, Optimisation and Calculus of Variations*, 13(1):163–177, 2007.

[60] F. Dassi, S. Perotto, L. Formaggia, and P. Ruffo. Efficient geometric reconstruction of complex geological structures. *Mathematics and Computers in Simulation*, 106:163–184, 2014. Applied Scientific Computing X: Advanced Meshing and Simulations Approaches - Edited by: Angel Plaza and Rosa Maria Spitaleri and Applied Scientific Computing XI: Effective Numerical approaches for complex problems - Edited by Rosa Maria Spitaleri.

[61] J.E. Dennis and Robert B. Schnabel. *Numerical Methods for Unconstrained Optimization and Nonlinear Equations*, volume 16 of *Classics Appl. Math.* SIAM, 1996.

[62] Jorgen S. Dokken, Simon W. Funke, August Johansson, and Stephan Schmidt. Shape optimization using the finite element method on multiple meshes. *arXiv:1806.09821*, 2018.

[63] John Dolbow, Nicolas Moës, and Ted Belytschko. An extended finite element method for modeling crack growth with frictional contact. *Comput. Methods Appl. Mech. Engrg.*, 190(51-52):6825–6846, 2001.

[64] Peter D. Dunning, H. A. Kim, and Glen Mullineux. Investigation and improvement of sensitivity computation using the area-fraction weighted fixed grid fem and structural optimization. *Finite Elem. Anal. Des.*, 47(8):933–941, 2011.

[65] Yalchin Efendiev and Thomas Y. Hou. *Multiscale finite element methods*, volume 4 of *Surveys and Tutorials in the Applied Mathematical Sciences*. Springer, New York, 2009. Theory and applications.

[66] Yekaterina Epshteyn and Béatrice Rivière. Estimation of penalty parameters for symmetric interior penalty galerkin methods. *Journal of Computational and Applied Mathematics*, 206(2):843 – 872, 2007.

[67] Richard E. Ewing, Society for Industrial, and Applied Mathematics. *The Mathematics of reservoir simulation*, volume 1. SIAM, Philadelphia, 1983.

[68] F. Fogolari, A. Brigo, and H. Molinari. The Poisson-Boltzmann equation for biomolecular electrostatics: a tool for structural biology. *Journal of Molecular Recognition*, 15(6):377–392, 2002.

[69] T. Gao, W. H. Zhang, J. H. Zhu, Y. J. Xu, and D. H. Bassir. Topology optimization of heat conduction problem involving design-dependent heat load effect. *Finite Elem. Anal. Des.*, 44(14):805–813, 2008.

[70] Walter Gautschi. *Numerical analysis*. Springer, New York, 2nd edition, 2012.

[71] A. Gersborg-Hansen, M. P. Bendsøe, and O. Sigmund. Topology optimization of heat conduction problems using the finite volume method. *Struct. Multidiscip. Optim.*, 31(4):251–259, 2006.

[72] David Gilbarg and Neil S. Trudinger. *Elliptic partial differential equations of second order*, volume 224. Springer, New York, 2 edition, 2001.

[73] Michael B. Giles and Niles A. Pierce. An introduction to the adjoint approach to design. *Flow Turbul. Combust.*, 65(3):393–415, 2000.

[74] Mark S. Gockenbach and Akhtar A. Khan. An abstract framework for elliptic inverse problems: Part 2. an augmented lagrangian approach. *Math. Mech. Solids*, 14(6):517–539, 2009.

[75] Yan Gong. *Immersed-interface finite-element methods for elliptic and elasticity interface problems*. PhD thesis, North Carolina State University, 2007.

[76] Yan Gong, Bo Li, and Zhilin Li. Immersed-interface finite-element methods for elliptic interface problems with nonhomogeneous jump conditions. *SIAM J. Numer. Anal.*, 46(1):472–495, 2008.

[77] Yan Gong and Zhilin Li. Immersed interface finite element methods for elasticity interface problems with non-homogeneous jump conditions. *Numer. Math. Theory Methods Appl.*, 3(1):23–39, 2010.

[78] Ruchi Guo. A linear immersed finite element space defined by actual interface curve on triangular meshes. Master's thesis, Virginia Polytechnic Institute and State University, 2017.

[79] Ruchi Guo and Tao Lin. A group of immersed finite element spaces for elliptic interface problems. *IMA J.Numer. Anal.*, page drx074, 2017.

[80] Ruchi Guo and Tao Lin. A higher degree immersed finite element method based on a cauchy extension. *SIAM J. Numer. Anal. (accepted)*, 2019.

[81] Ruchi Guo, Tao Lin, and Yanping Lin. Approximation capabilities of the immersed finite element spaces for elasticity interface problems. *Numer. Methods Partial Differential Equations*, 35(3):1243–1268, 2018.

[82] Ruchi Guo, Tao Lin, and Yanping Lin. Error estimates for a partially penalized immersed finite element method for elasticity interface problems. *Submitted*, 2018.

[83] Ruchi Guo, Tao Lin, and Yanping Lin. A fixed mesh method with immersed finite elements for solving interface inverse problems. *J. Sci. Comput.*, 79(1):148–175, 2018.

[84] Ruchi Guo, Tao Lin, and Xu Zhang. Nonconforming immersed finite element spaces for elliptic interface problems. *Comput. Math. Appl.*, 75(6):2002 – 2016, 2018.

[85] Ruchi Guo, Tao Lin, and Qiao Zhuang. Improved error estimation for the partially penalized immersed finite element methods for elliptic interface problems. *Int. J. Numer. Anal. Model.*, 16(4):575–589, 2018.

[86] Johnny Guzmán, Manuel A. Sánchez, and Marcus Sarkis. Higher-order finite element methods for elliptic problems with interfaces. *ESAIM Math. Model. Numer. Anal.*, 50(5):1561–1583, 2016.

[87] Johnny Guzmán, Manuel A. Sánchez, and Marcus Sarkis. A finite element method for high-contrast interface problems with error estimates independent of contrast. *J. Sci. Comput.*, 73(1):330–365, 2017.

[88] Johnny Guzmán, Manuel A. Sánchez, and Marcus Sarkis. A finite element method for high-contrast interface problems with error estimates independent of contrast. *J. Sci. Comput.*, 73(1):330–365, 2017.

[89] Jacques Hadamard. *Lectures on Cauchy's Problem in Linear Partial Differential Equations*. Dover, New York, 1952.

[90] Daoru Han, Pu Wang, Xiaoming He, Tao Lin, and Joseph Wang. A 3D immersed finite element method with non-homogeneous interface flux jump for applications in particle-in-cell simulations of plasma–lunar surface interactions. *Journal of Computational Physics*, 321:965–980, 2016.

[91] Anita Hansbo and Peter Hansbo. An unfitted finite element method, based on Nitsche's method, for elliptic interface problems. *Comput. Methods Appl. Mech. Engrg.*, 191(47-48):5537–5552, 2002.

[92] Anita Hansbo and Peter Hansbo. A finite element method for the simulation of strong and weak discontinuities in solid mechanics. *Comput. Methods Appl. Mech. Engrg.*, 193(33-35):3523–3540, 2004.

[93] Peter Hansbo and Mats G. Larson. Discontinuous Galerkin and the Crouzeix-Raviart element: application to elasticity. *M2AN Math. Model. Numer. Anal.*, 37(1):63–72, 2003.

[94] Peter Hansbo, Mats G. Larson, Högskolan i Jönköping, Tekniska Högskolan, and JTH. Forskningsmiljö Produktutveckling. Discontinuous Galerkin methods for incompressible and nearly incompressible elasticity by Nitsche's method. *Comput. Methods Appl. Mech. Engrg.*, 191(17):1895–1908, 2002.

[95] Eduard Harabetian and Stanley Osher. Regularization of ill-posed problems via the level set approach. *SIAM Journal on Applied Mathematics*, 58(6):1689–1706, 1998.

[96] Helmut Harbrecht and Johannes Tausch. On the numerical solution of a shape optimization problem for the heat equation. *SIAM J. Sci. Comput.*, 35(1):A.104–A121, 2013.

[97] J. Haslinger and R. A. E. Mäkinen. *Introduction to shape optimization: theory, approximation, and computation*. SIAM, Society for Industrial and Applied Mathematics, Philadelphia, 2003.

[98] Maatoug Hassine and Imen Kallel. Kohn-Vogelius formulation and topological sensitivity analysis based method for solving geometric inverse problems. *Arab Journal of Mathematical Sciences*, 24(1):43 – 62, 2018.

[99] Xiaoming He. *Bilinear immersed finite elements for interface problems*. PhD thesis, Virginia Polytechnic Institute and State University, 2009.

[100] Xiaoming He, Tao Lin, and Yanping Lin. Approximation capability of a bilinear immersed finite element space. *Numer. Methods Partial Differential Equations*, 24(5):1265–1300, 2008.

[101] Xiaoming He, Tao Lin, and Yanping Lin. A bilinear immersed finite volume element method for the diffusion equation with discontinuous coefficient. *Commun. Comput. Phys.*, 6(1):185–202, 2009.

[102] Xiaoming He, Tao Lin, and Yanping Lin. Immersed finite element methods for elliptic interface problems with non-homogeneous jump conditions. *Int. J. Numer. Anal. Model.*, 8(2):284–301, 2011.

[103] Xiaoming He, Tao Lin, and Yanping Lin. The convergence of the bilinear and linear immersed finite element solutions to interface problems. *Numer. Methods Partial Differential Equations*, 28(1):312–330, 2012.

[104] Xiaoming He, Tao Lin, and Yanping Lin. A selective immersed discontinuous Galerkin method for elliptic interface problems. *Math. Methods Appl. Sci.*, 37(7):983–1002, 2014.

[105] Xiaoming He, Tao Lin, Yanping Lin, and Xu Zhang. Immersed finite element methods for parabolic equations with moving interface. *Numer. Methods Partial Differential Equations*, 29(2):619–646, 2013.

[106] Jan Hegemann, Alejandro Cantarero, Casey L. Richardson, and Joseph M. Teran. An explicit update scheme for inverse parameter and interface estimation of piecewise constant coefficients in linear elliptic pdes. *SIAM J. Sci. Comput.*, 35(2), 2013.

[107] R. Hiptmair and A. Paganini. Shape optimization by pursuing diffeomorphisms. *Computational Methods in Applied Mathematics*, 15(3):291–305, 2015.

[108] R. W. Hockney and J. W. Eastwood. *Computer Simulation Using Particles*. Taylor & Francis, Inc., Bristol, PA, USA, 1988.

[109] Cosmina Hogea, Christos Davatzikos, and George Biros. An image-driven parameter estimation problem for a reaction–diffusion glioma growth model with mass effects. *J. Math. Biol.*, 56(6):793–825, 2008.

[110] David Holder and Institute of Physics (Great Britain). *Electrical impedance tomography: methods, history, and applications*. Institute of Physics Pub, 2005.

[111] Songming Hou, Zhilin Li, Liqun Wang, and Wei Wang. A numerical method for solving elasticity equations with interfaces. *Commun. Comput. Phys.*, 12(2):595–612, 2012.

[112] Xiaozhe Hu, Lin Mu, and Xiu Ye. A simple finite element method of the Cauchy problem for poisson equation. *Int. J. Numer. Anal. Model.*, 1(1):1–12, 2017.

[113] Jianguo Huang and Jun Zou. Some new a priori estimates for second-order elliptic and parabolic interface problems. *J. Differential Equations*, 184(2):570 – 586, 2002.

[114] V. Isakov and J. Powell. On the inverse conductivity problem with one measurement. *Inverse Problems*, 6:311, 1990.

[115] Victor Isakov. On uniqueness of recovery of a discontinuous conductivity coefficient. *Communications on Pure and Applied Mathematics*, 41(7):865–877, 1988.

[116] Kazufumi Ito and Karl Kunisch. The augmented Lagrangian method for parameter estimation in elliptic systems. *SIAM J. Control Optim.*, 28(1):113–136, 1990.

[117] Kazufumi Ito, Karl Kunisch, and Zhilin Li. Level-set function approach to an inverse interface problem. *Inverse Problems*, 17:1225, 2001.

[118] Finn B. Jensen, William A. Kuperman, Michael B. Porter, Henrik Schmidt, Finn B. Jensen, William A. Kuperman, and Michael B. Porter. *Wave Propagation Theory*, chapter 2, pages 65–153. Springer New York, New York, NY, 2011.

[119] Lin Ji, Joyce R. McLaughlin, Daniel Renzi, and Jeong-Rock Yoon. Interior elastodynamics inverse problems: shear wave speed reconstruction in transient elastography. *Inverse Problems*, 19(6):S1–S29, 2003.

[120] Bangti Jin and Peter Maass. An analysis of electrical impedance tomography with applications to Tikhonov regularization. *ESAIM: COCV*, 18(4):1027–1048, 2012.

[121] Bangti Jin, Yifeng Xu, and Jun Zou. A convergent adaptive finite element method for electrical impedance tomography. *IMA J. Numer. Anal.*, 37(1):1520–1550, 2017.

[122] H. J. Jou, Perry H. Leo, and John S. Lowengrub. Microstructural evolution in inhomogeneous elastic media. *J. Comput. Phys.*, 131(1):109–148, 1997.

[123] R. Kafafy, J. Wang, and T. Lin. A hybrid-grid immersed-finite-element particle-in-cell simulation model of ion optics plasma dynamics. *Dyn. Contin. Discrete Impuls. Syst. Ser. B Appl. Algorithms*, 12(Suppl. Vol. 12b):1–16, 2005.

[124] Raed Kafafy and Joseph Wang. Whole ion optics gridlet simulations using a hybrid-grid immersed-finite-element particle-in-cell code. *J. Propulsion Power*, 23(1):59–68, 2007.

[125] Hyeonbae Kang and Jin Keun Seo. Note on uniqueness and stability for the inverse conductivity problems with one measurement. *J. Korean Math. Soc*, pages 781–792, 2001.

[126] Nam H. Kim and Youngmin Chang. Eulerian shape design sensitivity analysis and optimization with a fixed grid. *Comput. Methods Appl. Mech. Engrg.*, 194(30):3291–3314, 2005.

[127] Robert Kohn and Michael Vogelius. Determining conductivity by boundary measurements. *Communications on Pure and Applied Mathematics*, 37(3):289–298, 1984.

[128] Robert V. Kohn and Michael Vogelius. Relaxation of a variational method for impedance computed tomography. *Commun. Pure Appl. Anal.*, 40(6):745–777, 1987.

[129] Do Y. Kwak, Kye T. Wee, and Kwang S. Chang. An analysis of a broken P_1-nonconforming finite element method for interface problems. *SIAM J. Numer. Anal.*, 48(6):2117–2134, 2010.

[130] Hae S. Lee, Cheon J. Park, and Hyun W. Park. Identification of geometric shapes and material properties of inclusions in two-dimensional finite bodies by boundary parameterization. *Comput. Methods Appl. Mech. Engrg.*, 181(1):1–20, 2000.

[131] D. Leguillon and E. Sanchez-Palencia. *Computation of singular solutions in elliptic problems and elasticity*. Wiley, New York, 1987.

[132] Perry H. Leo, John S. Lowengrub, and Qing Nie. Microstructural evolution in orthotropic elastic media. *J. Comput. Phys.*, 157(1):44–88, 2000.

[133] Randall J. LeVeque and Zhilin Li. The immersed interface method for elliptic equations with discontinuous coefficients and singular sources. *SIAM J. Numer. Anal.*, 31(4):1019–1044, 1994.

[134] Randall J. LeVeque and Zhilin Li. Immersed interface methods for Stokes flow with elastic boundaries or surface tension. *SIAM J. Sci. Comput.*, 18(3):709–735, 1997.

[135] Qing Li, Grant P. Steven, Y. M. Xie, and Osvaldo M. Querin. Evolutionary topology optimization for temperature reduction of heat conducting fields. *Int. J. Heat Mass Transfer*, 47(23):5071–5083, 2004.

[136] Z. Li, T. Lin, Y. Lin, and R. C. Rogers. An immersed finite element space and its approximation capability. *Numer. Methods Partial Differential Equations*, 20(3):338–367, 2004.

[137] Z-C. Li, T-T. Lu, H-Y. Hu, and A. H-D. Cheng. *Trefftz and Collocation Methods*. WIT Press, 2008.

[138] Zhilin Li. Immersed interface methods for moving interface problems. *Numer. Algorithms*, 14(4):269–293, 1997.

[139] Zhilin Li and Kazufumi Ito. *The immersed interface method*, volume 33 of *Frontiers in Applied Mathematics*. Society for Industrial and Applied Mathematics (SIAM), Philadelphia, PA, 2006. Numerical solutions of PDEs involving interfaces and irregular domains.

[140] Zhilin Li and Ming-Chih Lai. The immersed interface method for the Navier-Stokes equations with singular forces. *J. Comput. Phys.*, 171(2):822–842, 2001.

[141] Zhilin Li, Tao Lin, and Xiaohui Wu. New Cartesian grid methods for interface problems using the finite element formulation. *Numer. Math.*, 96(1):61–98, 2003.

[142] Zhilin Li and Xingzhou Yang. An immersed finite element method for elasticity equations with interfaces. In T. Tang Z.-C. Shi, Z. Chen and D. Yu, editors, *Recent advances in adaptive computation*, volume 383 of *Contemporary Mathematics*, pages 285–298. Amer. Math. Soc., Providence, RI, 2005.

[143] Min Lin, Tao Lin, and Huili Zhang. Error analysis of an immersed finite element method for Euler-Bernoulli beam interface problems. *Int. J. Numer. Anal. Mod.*, 14:822–841, 2017.

[144] T. Lin, Y. Lin, W.-W. Sun, and Z. Wang. Immersed finite element methods for 4th order differential equations. *J. Comput. Appl. Math.*, 235(13):3953–3964, 2011.

[145] Tao Lin, Yanping Lin, Robert Rogers, and M. Lynne Ryan. A rectangular immersed finite element space for interface problems. In Peter Minev and Yanping Lin, editors, *Scientific computing and applications (Kananaskis, AB, 2000)*, volume 7 of *Advances In Computation: Theory And Practice*, pages 107–114. Nova Sci. Publ., Huntington, NY, 2001.

[146] Tao Lin, Yanping Lin, and Weiwei Sun. Error estimation of a class of quadratic immersed finite element methods for elliptic interface problems. *Discrete Contin. Dyn. Syst. Ser. B*, 7(4):807–823, 2007.

[147] Tao Lin, Yanping Lin, and Xu Zhang. A method of lines based on immersed finite elements for parabolic moving interface problems. *Adv. Appl. Math. Mech.*, 5(4):548–568, 2013.

[148] Tao Lin, Yanping Lin, and Xu Zhang. Partially penalized immersed finite element methods for elliptic interface problems. *SIAM J. Numer. Anal.*, 53(2):1121–1144, 2015.

[149] Tao Lin, Dongwoo Sheen, and Xu Zhang. A locking-free immersed finite element method for planar elasticity interface problems. *J. Comput. Phys.*, 247:228–247, 2013.

[150] Tao Lin, Dongwoo Sheen, and Xu Zhang. A nonconforming immersed finite element method for elliptic interface problems. *J. Sci. Comput.*, 79(1):442–463, 2019.

[151] Tao Lin and Joseph Wang. An immersed finite element electric field solver for ion optics modeling. In *Proceedings of AIAA Joint Propulsion Conference*, Indianapolis, IN, Jul 2002. AIAA.

[152] Tao Lin, Qing Yang, and Xu Zhang. *A Priori* error estimates for some discontinuous Galerkin immersed finite element methods. *J. Sci. Comput.*, 2015. in press.

[153] Tao Lin and Xu Zhang. Linear and bilinear immersed finite elements for planar elasticity interface problems. *J. Comput. Appl. Math.*, 236(18):4681–4699, 2012.

[154] W. R. B. Lionheart. Boundary shape and electrical impedance tomography. *Inverse Problems*, 14:139, 1998.

[155] Ralf Massjung. An unfitted discontinuous Galerkin method applied to elliptic interface problems. *SIAM J. Numer. Anal.*, 50(6):3134–3162, 2012.

[156] Joyce R. McLaughlin, Ning Zhang, and Armando Manduca. Calculating tissue shear modulus and pressure by 2D log-elastographic methods. *Inverse Problems*, 26, 2010.

[157] J. M. Melenk and I. Babuška. The partition of unity finite element method: basic theory and applications. *Comput. Methods Appl. Mech. Engrg.*, 139(1-4):289–314, 1996.

[158] Kihyo Moon. *Immersed Discontinuous Galerkin Methods for Acoustic Wave Propagation in Inhomogeneous Media*. PhD thesis, Virginia Tech, 2016.

[159] Adrian I. Nachman. Global uniqueness for a two-dimensional inverse boundary value problem. *Annals of Mathematics*, 143(1):71–96, 1996.

[160] Ahmad R. Najafi, Masoud Safdari, Daniel A. Tortorelli, and Philippe H. Geubelle. A gradient-based shape optimization scheme using an interface-enriched generalized fem. *Comput. Methods Appl. Mech. Engrg.*, 296:1–17, 2015.

[161] S. S. Nanthakumar, T. Lahmer, and T. Rabczuk. Detection of flaws in piezoelectric structures using extended FEM. *International Journal for Numerical Methods in Engineering*, 96(6):373–389, 2013.

[162] L.K. Nielsen, X.-C. Tai, S.I. Aanonsen, and M. Espedal. A binary level set model for elliptic inverse problems with discontinuous coefficients. *Int. J. Numer. Anal. Model.*, 4:74–99, 2007.

[163] J. Nocedal and S. Wright. *Numerical optimization*. Springer Series in Operations Research. Springer, second edition, 2006.

[164] Antonio André Novotny, Alfredo Canelas, and Antoine Laurain. A non-iterative method for the inverse potential problem based on the topological derivative. In *Technical Report for Mini-Workshop: Geometries, Shapes and Topologies in PDE-based Applications, 57/2012, edited by Michael Hintermüller and Günter Leugering and Jan Sokołowski*, pages 3383–3387, Mathematisches Forschungsinstitut Oberwolfach, Oberwolfach, Germany, 2012.

[165] Antonio André Novotny and Jan Sokołowski. *Topological derivatives in shape optimization*. Springer, Heidelberg, 2013.

[166] A. Paganini. *Approximate Shape Gradients for Interface Problems*, pages 217–227. Springer International Publishing, Cham, 2015.

[167] A. Paganini, F. Wechsung, and P. Farrell. Higher-order moving mesh methods for PDE-constrained shape optimization. *SIAM Journal on Scientific Computing*, 40(4):A2356–A2382, 2018.

[168] X. Peng, K. Niakhai, and B. Protas. A method for geometry optimization in a simple model of two-dimensional heat transfer. *SIAM J. Sci. Comput.*, 35(5):B.1105–B1131, 2013.

[169] Mauro Perego, Alessandro Veneziani, and Christian Vergara. A variational approach for estimating the compliance of the cardiovascular tissue: An inverse fluid-structure interaction problem. *SIAM J. Sci. Comput.*, 33(3):1181–1211, 2011.

[170] Daniel Rabinovich, Dan Givoli, and Shmuel Vigdergauz. XFEM-based crack detection scheme using a genetic algorithm. *International Journal for Numerical Methods in Engineering*, 71(9):1051–1080, 2007.

[171] R. Rannacher and S. Turek. Simple nonconforming quadrilateral Stokes element. *Numer. Methods Partial Differential Equations*, 8(2):97–111, 1992.

[172] Satish C. Reddy and Lloyd N. Trefethen. Stability of the method of lines. *Numer. Math.*, 62(2):235–267, 1992.

[173] Xiaofeng Ren and Juncheng Wei. On a two-dimensional elliptic problem with large exponent in nonlinearity. *Transactions of the American Mathematical Society*, 343(2):749–763, 1994.

[174] Béatrice Rivière. *Discontinuous Galerkin methods for solving elliptic and parabolic equations*, volume 35 of *Frontiers in Applied Mathematics*. Society for Industrial and Applied Mathematics (SIAM), Philadelphia, PA, 2008. Theory and implementation.

[175] J. J. Ródenas, F. J. Fuenmayor, and J. E. Tarancón. A numerical methodology to assess the quality of the design velocity field computation methods in shape sensitivity analysis. *Internat. J. Numer. Methods Engrg.*, 59(13):1725–1747, 2004.

[176] Mohamed Ben Romdhane. *Higher-degree immersed finite elements for second-order elliptic interface problems*. PhD thesis, Virginia Polytechnic Institute and State University, 2011.

[177] Fadil Santosa. A level-set approach for inverse problems involving obstacles. *ESAIM: Control, Optimisation and Calculus of Variations*, 1:17–33, 1996.

[178] M. Sasikumar and C. Balaji. Optimization of convective fin systems: a holistic approach. *Heat Mass Transf.*, 39(1):57–68, 2002.

[179] David H. Sattinger, C. A. Tracy, and S. Venakides. *Inverse scattering and applications*, volume 122. American Mathematical Society, Providence, R.I, 1991.

[180] D. S. Schnur and Nicholas Zabaras. An inverse method for determining elastic material properties and a material interface. *Internat. J. Numer. Methods Engrg.*, 33(10):2039–2057, 1992.

[181] A. P. S. Selvadurai. *Partial Differential Equations in Mechanics 2: The Biharmonic Equation, Poisson's Equation*. Springer Berlin Heidelberg, Berlin, Heidelberg, 1 edition, 2000.

[182] Ruben Sevilla and Sonia Fernández-Méndez. Numerical integration over 2D NURBS-shaped domains with applications to NURBS-enhanced FEM. *Finite Elements in Analysis & Design*, 47(10):1209–1220, 2011.

[183] Khosro Shahbazi. An explicit expression for the penalty parameter of the interior penalty method. *Journal of Computational Physics*, 205(2):401–407, 2005.

[184] Jan Sokolowski and Jean-Paul Zolésio. *Introduction to shape optimization : shape sensitivity analysis*, volume 16 of *Springer Series in Computational Mathematics*. Springer, 1992.

[185] M. Soleimani, W. R. B. Lionheart, and O. Dorn. Level set reconstruction of conductivity and permittivity from boundary electrical measurements using experimental data. *Inverse Problems in Science and Engineering*, 14(2):193–210, 2006.

[186] N. Sukumar, D. L. Chopp, N. Moës, and T. Belytschko. Modeling holes and inclusions by level sets in the extended finite-element method. *Comput. Methods Appl. Mech. Engrg.*, 190(46-47):6183–6200, 2001.

[187] N. Sukumar, Z. Y. Huang, J. H. Prévost, and Z. Suo. Partition of unity enrichment for bimaterial interface cracks. *Internat. J. Numer. Methods Engrg*, 59(8):1075–1102, 2004.

[188] Katsuyuki Suzuki and Noboru Kikuchi. A homogenization method for shape and topology optimization. *Comput. Methods Appl. Mech. Engrg.*, 93(3):291–31, 1991.

[189] John Sylvester and Gunther Uhlmann. A global uniqueness theorem for an inverse boundary value problem. *Annals of Mathematics*, 125(1):153–169, 1987.

[190] Xue-Cheng Tai and Hongwei Li. A piecewise constant level set method for elliptic inverse problems. *Applied Numerical Mathematics*, 57(5):686–696, 2007.

[191] Daniel A. Tortorelli, John A. Tomasko, Timothy E. Morthland, and Jonathan A. Dantzig. Optimal design of nonlinear parabolic systems. part ii: Variable spatial domain with applications to casting optimization. *Computer Methods in Applied Mechanics and Engineering*, 113(1):157–172, 1994.

[192] Daniel A. Tortorelli and Wang Zixian. A systematic approach to shape sensitivity analysis. *International Journal of Solids and Structures*, 30(9):1181–1212, 1993.

[193] Sylvain Vallaghé and Théodore Papadopoulo. A trilinear immersed finite element method for solving the electroencephalography forward problem. *SIAM J. Sci. Comput.*, 32(4):2379–2394, 2010.

[194] F. van Keulen, R. T. Haftka, and N. H. Kim. Review of options for structural design sensitivity analysis. part 1: Linear systems. *Computer Methods in Applied Mechanics and Engineering*, 194(30):3213–3243, 2005.

[195] Haim Waisman, Eleni Chatzi, and Andrew W. Smyth. Detection and quantification of flaws in structures by the extended finite element method and genetic algorithms. *International Journal for Numerical Methods in Engineering*, 2009.

[196] Fei Wang, Yuanming Xiao, and Jinchao Xu. High-order extended finite element methods for solving interface problems. *arXiv:1604.06171v1*, 2016.

[197] T. Warburton and J. S. Hesthaven. On the constants in *hp*-finite element trace inverse inequalities. *Comput. Methods Appl. Mech. Engrg.*, 192(25):2765–2773, 2003.

[198] Peng Wei, Michael Y. Wang, and Xianghua Xing. A study on X-FEM in continuum structural optimization using a level set model. *Comput. Aided Des.*, 42(8):708–719, 2010.

[199] Thomas P. Wihler. Locking-free adaptive discontinuous Galerkin FEM for linear elasticity problems. *Math. Comp.*, 75(255):1087–1102, 2006.

[200] Kelin Xia, Meng Zhan, and G.-W Wei. The matched interface and boundary (MIB) method for multi-domain elliptic interface problems. *J. Comput. Phys.*, 230:8231–8258, 01 2011.

[201] Dexuan Xie and Jinyong Ying. A new box iterative method for a class of nonlinear interface problems with application in solving Poisson-Boltzmann equation. *Journal of Computational and Applied Mathematics*, 307:319–334, 2016. 1st Annual Meeting of SIAM Central States Section, April 11–12, 2015.

[202] Xingzhou Yang. *Immersed interface method for elasticity problems with interfaces*. PhD thesis, North Carolina State University, 2004.

[203] Xingzhou Yang, Bo Li, and Zhilin Li. The immersed interface method for elasticity problems with interfaces. *Dyn. Contin. Discrete Impuls. Syst. Ser. A Math. Anal.*, 10(5):783–808, 2003. Progress in partial differential equations (Pullman, WA, 2002).

[204] Tse-Min Yao and Kyung K. Choi. 3-D shape optimal design and automatic finite element regridding. *International Journal for Numerical Methods in Engineering*, 28(2):369–384, 1989.

[205] William W. Yeh. Review of parameter identification procedures in groundwater hydrology: The inverse problem. *Water Resources Research*, 22(2):95–108, 1986.

[206] Sining Yu and G.W. Wei. Three-dimensional matched interface and boundary (MIB) method for treating geometric singularities. *Journal of Computational Physics*, 227(1):602 – 632, 2007.

[207] Sining Yu, Yongcheng Zhou, and G.W. Wei. Matched interface and boundary (MIB) method for elliptic problems with sharp-edged interfaces. *Journal of Computational Physics*, 224(2):729 – 756, 2007.

[208] J. Zhang, W. H. Zhang, J. H. Zhu, and L. Xia. Integrated layout design of multi-component systems using XFEM and analytical sensitivity analysis. *Comput. Methods Appl. Mech. Engrg.*, 245-246:75–89, 2012.

[209] Xu Zhang. *Nonconforming Immersed Finite Element Methods for Interface Problems*. PhD thesis, Virginia Polytechnic Institute and State University, 2013.

[210] Yongcun Zhang, Shutian Liu, and Heting Qiao. Design of the heat conduction structure based on the topology optimization. *Dev. Heat Transf.*, 2011.

[211] Shan Zhao and G W Wei. Matched interface and boundary (MIB) for the implementation of boundary conditions in high-order central finite differences. *International journal for numerical methods in engineering*, 77:1690–1730, 03 2009.

[212] Y. C. Zhou and G. W. Wei. On the fictitious-domain and interpolation formulations of the matched interface and boundary (MIB) method. *J. Comput. Phys.*, 219(1):228–246, 2006.

[213] Y. C. Zhou, Shan Zhao, Michael Feig, and G. W. Wei. High order matched interface and boundary method for elliptic equations with discontinuous coefficients and singular sources. *J. Comput. Phys.*, 213(1):1–30, 2006.

[214] Qiao Zhuang and Ruchi Guo. High degree Discontinuous Petrov-Galerkin immersed finite element methods using fictitious elements for elliptic interface problems. *J. Comput. Appl. Math. (in press)*, 2018.

[215] Miloš Zlámal. Curved elements in the finite element method. I. *SIAM J. Numer. Anal.*, 10(1):229–240, 1973.